THE UNIVERSITY
of ADELAIDE

A study on a single-tether spherical point absorber with an asymmetric mass distribution

Fantai Meng

School of Mechanical Engineering
The University of Adelaide
Adelaide, Australia

Thesis submitted in partial fulfillment of the requirements for the degree of Doctor of Philosophy in March, 2020.

Ph. D. Thesis

13th March 2020

School of Mechanical Engineering
The University of Adelaide
Adelaide, Australia

Typeset by the author using LaTeX.
Printed in Australia.

Abstract

The adoption of renewable energy has long been regarded as an effective solution to fulfil the growing demand for electricity and reduce greenhouse gas emissions. Ocean wave energy is a promising and reliable resource in the renewable energy mix, which exhibits higher power density and continuity than solar and wind energy. Furthermore, the overall potential of ocean wave energy is estimated as being much as 3.7 terawatts, which is double the current global demand for electricity.

Although the first wave energy converter (WEC) design appeared as early as 1790, the technology of wave energy conversion is still at an early stage of commercialisation. Compared with solar and wind energy plants, the existing WEC systems have relatively small power generation capacity and exhibit greater costs associated with investment, infrastructure and maintenance. Consequently, wave energy conversion is currently at an economic disadvantage in the renewable energy mix.

This thesis studies the efficiency improvement of a single-tether submerged spherical point absorbing wave energy converter by utilising an asymmetric mass distributed buoy. The spherical point absorber with asymmetric mass distribution is referred to as SPAMD in the thesis. The main contribution lies in frequency-domain modal analysis, parametric optimisation and high-fidelity modelling of the system. This Ph.D. research answers three questions: (i) What effect does mass distribution have on the dynamics of a submerged spherical buoy; (ii) how does the mass distribution of the buoy affect the power output of the SPAMD in irregular waves; and (iii) do the nonlinear hydrodynamic effects compromise the performance of the SPAMD?

To understand the working principle and evaluate the efficiency improvement of the SPAMD, a frequency-domain modal analysis is conducted over typical wave frequencies. The influence of a power take-off device on the performance of the SPAMD is discussed on the basis of a modal analysis. The efficiency improvement over a generic point absorber for regular waves

is assessed over different frequency regimes. Recommendations pertaining to the application of an asymmetric mass distributed buoy in wave energy harvesting are provided.

The design considerations of the mass distribution of the buoy are also investigated under irregular waves characterised by the Pierson-Moskowitz spectrum. A spectral-domain model, including viscous drag effects, is developed to evaluate the performance of the SPAMD efficiently. Attention is given to the power absorption bandwidth, the mean power output and the dynamic mooring loading caused by the configuration of mass distribution. Suggestions regarding the configuration of the mass distribution of the buoy are provided according to the facility cost and the system performance.

The final part of this thesis explores the trajectory and power analysis of the SPAMD in a high-fidelity simulation. A numerical wave tank has been developed from the Navier-Stokes equations, to simulate the fluid-structure interface during the operation of the SPAMD. It was found that the nonlinear hydrodynamics significantly modify the trajectory of the device as the wave height grows. The large change in the motion trajectory of the buoy decreases the efficiency of the converter in terms of wave energy harvesting. The efficiency improvement of the SPAMD in comparison with the generic point absorber is demonstrated in the numerical wave tank experiment.

Declaration

I certify that this work contains no material which has been accepted for the award of any other degree or diploma in my name, in any university or other tertiary institution and, to the best of my knowledge and belief, contains no material previously published or written by another person, except where due reference has been made in the text. In addition, I certify that no part of this work will, in the future, be used in a submission in my name, for any other degree or diploma in any university or other tertiary institution without the prior approval of the University of Adelaide and where applicable, any partner institution responsible for the joint-award of this degree.

I acknowledge that copyright of published works contained within this thesis resides with the copyright holder(s) of those works.

I also give permission for the digital version of my thesis to be made available on the web, via the University's digital research repository, the Library Search and also through web search engines, unless permission has been granted by the University to restrict access for a period of time.

_____

Fantai Meng

Acknowledgements

First of all I would like to thank my principal supervisor Professor Benjamin Cazzolato, who accepted me as his Ph.D. student and who has patiently cultivated my ability to become an independent researcher. His outstanding leadership, rich expertise in the field of vibration and control, and gentle personality have influenced me deeply and made me determined to be such a person.

Next, I owe huge thanks to my co-supervisor Dr Boyin Ding, for his emotional and technical support which helped me get through the hardship of my first two years. I would also like to thank Dr Nataliia Sergiienko, Associate Professor Maziar Arjomandi, Dr Ashkan Rafiee, Ms Dorothy Missingham and Dr Alison-Jane Hunter, who have provided great support during my candidature.

Special thanks go to my father and mother, for their selfless love and support over the past eight years, which gave me great courage and faith to face challenges. Furthermore, I believe my deceased grandfather and grandmother would be proud of my achievement today.

Finally, I wish to thank my colleagues and friends who have contributed to the dynamic and motivating atmosphere in my life over the past five years.

Author's Comments

All publications included in this thesis are identical to the original articles as published or submitted, with the following exceptions:

1. The typesetting and referencing have been changed to keep the format consistent throughout the entire thesis.
2. The positions of the figures and tables have been re-arranged to improve the overall readability of the thesis.
3. The tables, figures and equations of each publication have been re-numbered with the prefix of the number of the chapter.

Glossary of symbols

Symbol	SI unit	Quantity
α	rad/deg	Mooring point angle
β	rad/deg	Tether angle
δ	-	Phase function indicator
η	m	Wave elevation
θ_y	rad	Pitch displacement of buoy
κ	-	Air-water interface curvature
λ	m	Wavelength
μ	m^2/s	Dynamic viscosity
ν	m^2/s	Water kinematic viscosity
ϕ	m^2/s	Velocity potential
ϕ_s	m^2/s	Velocity potential for scattered wave
ϕ_0	m^2/s	Velocity potential for incident wave
ϕ_d	m^2/s	Velocity potential for diffracted wave
ϕ_r	m^2/s	Velocity potential for radiated wave
φ	rad/deg	Mass offset angle
ω	rad/s	Wave frequency
ω_x	rad/s	Natural frequency of buoy's surge mode
ω_z	rad/s	Natural frequency of buoy's heave mode
ρ	kg/m^3	Water density
σ	-	Coefficient of water surface tension
$\mathbf{A}$	kg	Hydrodynamic added mass matrix
$\mathbf{B}$	kg	Hydrodynamic damping matrix
$\mathbf{K}$	N/m	Stiffness matrix
$\mathbf{M}$	kg	Mass matrix
$\mathbf{F}_{exe}$	N	Wave excitation force
$\mathbf{F}_{rad}$	N	Wave radiation force
$\mathbf{F}_{buoy}$	N	Net buoyancy force
$\mathbf{F}_{vis}$	N	Viscous drag

Symbol	SI unit	Quantity
$\mathbf{F}_{pto}$	N	PTO force
$\mathbf{F}_{hydro}$	N	Total hydrodynamic force
$\mathbf{F}_{re}$	N	Hydrodynamic restoring force
$\mathbf{Z}$	N·s/m	Radiation impedance
$\mathbf{x}$	m	Displacement vector
$\mathbf{v}$	kg	Matrix of eigenvectors
B_{pto}	N/m	PTO damping coefficient
C_D	-	Viscous drag coefficient
d	m	Submergence depth
g	m/s^2	Gravitational acceleration
H	m	Wave height
h	m	Water depth
J	kW/m	Wave energy flux
J^{-1}	-	Inverse Jacobian matrix
K_{pto}	N/m	PTO stiffness
k	m^{-1}	Wavenumber
L	m	Initial tether length
m	kg	Mass of buoy
m_1	kg	Mass of spherical hull
m_2	kg	Additional offset mass
m/m_w	-	Weight-to-buoyancy ratio
m_1/m_2	-	Weight-to-buoyancy ratio
$\vec{n}$	-	Surface normal vecotor
P	kW	Power
p	Pa	Pressure
q	-	Efficiency improvement ratio
r	m	Radius of buoy
r_{gy}	m	Mass offset radius
$S(\omega)$	W/rad	Spectral variance density
S_B	-	Moving body surface
T	s	Wave period
$\vec{u}$	m/s	Velocity vector of a body surface along its surface normal
V	m^3	Volume of buoy
V_s	m^3	Maximum swept volume of buoy
$\vec{v}$	m/s	Water particle velocity vector
x	m	Surge displacement of buoy
z	m	Heave displacement of buoy
(u, v, w)	m/s	Particle velocity in Cartesian coordinate

Contents

List of Figures

List of Tables

Acronyms

BEM	Boundary element method
CFD	Computational Fluid Dynamics
DOF	Degree of freedom
FRF	Frequency response function
IRF	Impulse response function
LCoE	Levelised cost of electricity
MPC	Model predictive control
OWC	Oscillating water column
OWSC	Oscillating wave surge converter
PA	Point absorber
PTO	Power take-off
RAO	Response amplitude operator
RCW	Relative capture width
SPAMD	Spherical point absorber with asymmetric mass distribution
WEC	Wave energy converter

Chapter 1

Introduction

1.1 Background of global energy production

Energy is a fundamental requirement for the operation of contemporary society. The global primary energy mix (2018) is shown in Figure 1.1.

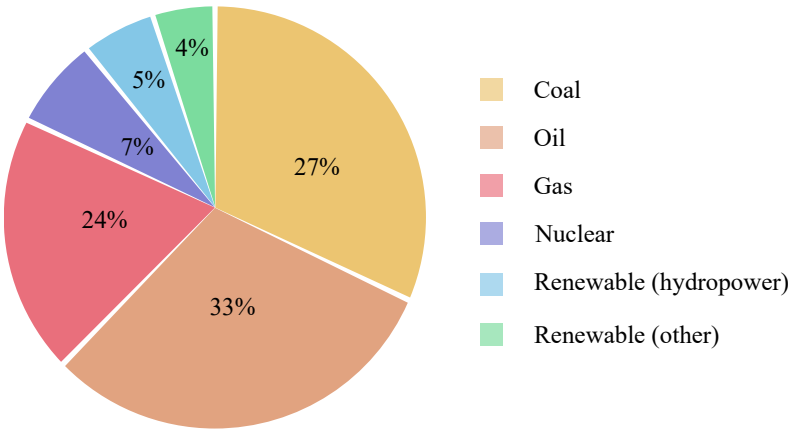

Figure 1.1: The division of primary energy, adapted from [4].

- **Fossil fuels** are the main primary energy source, with a more than 84% share because it is abundant and reliable. Coal resources are widespread and found throughout the Asia-Pacific region, North America, Europe and parts of Eurasia. Oil and natural gas are unevenly distributed in North and South America, the Middle East and parts of Eurasia. Among fossil fuels, natural gas has the largest growth rate (1.6%) due to concerns about air pollution and greenhouse gas emissions brought on by coal and oil burning.

- **Hydropower** is the largest exploited and most economical clean energy resource. Hydropower originates from the kinematic energy contained in falling water or steams. Hydropower resources are pre-dominantly found in Asia, North and South America, and the share of hydropower has remained steady at around 6% of the global primary energy mix for many years.

- **Nuclear energy** is generally used to produce steam for turbines to generate electricity. Nuclear power can fulfill intensive electricity demands with low carbon emissions. However, the management of nuclear waste and the potential for accidents in nuclear plants is a of significant concern to the public. Since Japan's Fukushima nuclear accident, many countries have cancelled or suspended the development of nuclear plants, and consequently the share of nuclear energy has decreased to 5% of the primary energy demand.

- **Renewable energy (other)** includes solar, wind, marine energy and biomass etc, accounting for less than 5% of the share in the primary energy demand. The potential of renewable energy is that it is incredibly abundant and everlasting. For example, the annual solar energy that can be easily harvested is estimated to be 5×10^4 EJ [16]. The annual growth rate of renewable energy is around 7.5%, which is the fastest in the primary energy mix [4].

The current energy mix is faced with a crucial challenge. On the one hand, due to continuous prosperity in fast-growing economies (e.g. China and India), the global primary energy demand is increasing at about 7% annually, and there will be a significantly large demand gap by 2040 [4]. On the other hand, the global warming caused by widespread use of fossil fuels has become an increasing threat to the sustainability of society, which means that carbon reduction is an essential task. According to the Paris Agreement in 2015 [27], 175 countries should make efforts to constrain the global temperature to 2°C above the pre-industrial period and realise zero net carbon emission in the latter half of this century. Therefore, renewable energy has been regarded as a solution to mitigate global warming and decouple economic growth from fossil fuels. Among the renewable energy mix, ocean wave energy is relatively continuous and predictable, and consequently it has received increasing attention from the scientific and industrial communities. The potential of global ocean wave energy is estimated to be 32,000 (TW·h) annually, which is the same order of magnitude as for electricity demand [20]. Considering the efficiency of exploitability is around 10% - 25% [1], the

amount of ocean wave energy which might be converted into electricity can potentially fulfill a significant amount of our future energy needs.

1.2 Ocean wave energy

Ocean wave energy originates from solar energy. As solar radiation is unevenly delivered over the surface of the earth, the resulting atmospheric pressure difference creates winds that blow over an area of the surface of ocean and thus ocean surface waves are formed [22]. Although the rate of solar energy input to waves is less than 1 W/m^2, the wave energy flux can continuously accumulate to 100 kW/m as the waves travel over oceanic distances. It should be noted that there are few energy losses after wind-generated waves travel thousands of kilometres in deep water.

As oceanic waves are generated by local and distant winds, the ocean wave energy resource is mainly distributed between 40° to 60° of the northern and southern hemispheres, belonging to the mid to high-latitude temperate storm belt. Figure 1.2 shows the global annual mean wave power estimates. It can be seen that high wave power regions include the west coast of the British Isles, the western Pacific coast of the US and Canada, the coast of Southern Chile and Southern Africa, and the south coasts of Australia and New Zealand. It should also be noted that the wave energy resources of the Atlantic and the Pacific ocean have remarkable seasonal variability in the northern hemisphere [32].

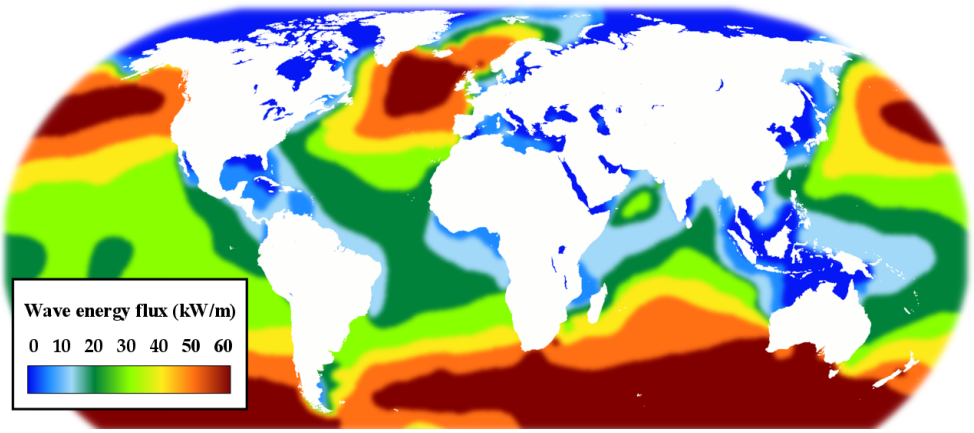

Figure 1.2: The global annual average wave energy flux, adapted from [2].

Australia has a world-class wave energy resource off its coast, where the average instantaneous wave power is approximately 3.47 PW [14]. Figure 1.3 illustrates the time-averaged wave power across the Australian shelf waters.

The largest annual mean wave power is 48 kW/m [19], appearing off the coast of Western Australia. This is mainly because Western Australia has a steep continental shelf and therefore merely 3.4% of wave power loss occurs when the wave power propagates from deep water to the coastline. The entire southern Australian margin is a potential area for the wave energy industry (35-65 kW/m annual average wave power) because the southern Australian margin is dominated by temperate storms from west to east [12]. The eastern Australian margin has a moderate wave power level of 26.7 kW/m annual mean wave power, which is regarded as another suitable area for wave energy harvesting [28]. Hughes and Heap [14] suggested that northern Australia is not suitable for current wave energy technology because of the low wave power density (< 10 kW/m annual average wave power) and the significant seasonal variability.

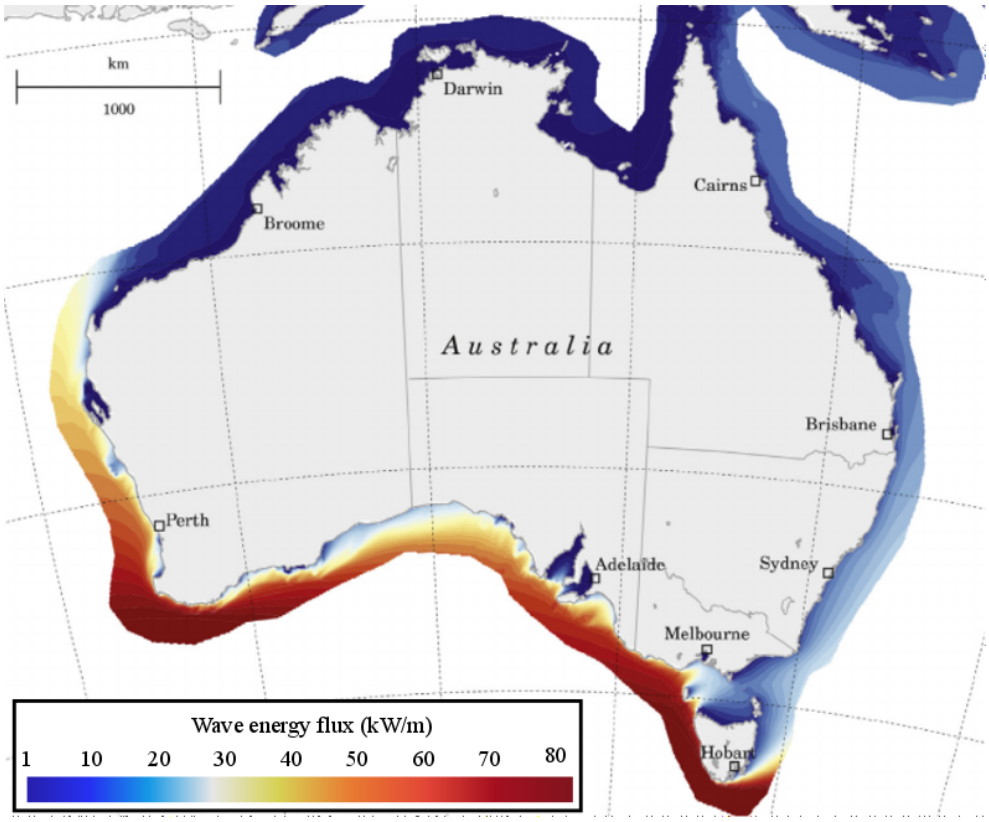

Figure 1.3: Mean wave energy flux off the Australian coast over the period from 1979 to 2010, adapted from [13].

1.3 Primary considerations for wave energy technology

Since the Oil Crisis in the 1970s, more than 1,000 conceptual wave energy converters (WECs) have been proposed by the scientific and industrial communities. Despite several decades of development, the current wave energy technology is still in the early stage of commercialisation. This is partially because the development of wave energy technology is an interdisciplinary problem, involving consideration of economic viability, survivability in extreme wave conditions and environmental impact.

- **Economics** of wave energy technology is the main consideration for potential investors to support this industry. The profitability and competitiveness of wave energy projects are generally quantified by the levelized cost, which is defined as the ratio of the cost to income over the lifespan of project [24]. The cost of deploying wave energy technology mainly consists of pre-operating expenses, construction expenses, operational expenditure and decommissioning costs [1]. Specifically, the operational expenditure can be considerably reduced by employing techno-economic development strategies in the design of wave energy converters [22]. The main income of a wave farm comes from the sale of electricity. The estimated electrical power of a wave farm is equal to the sum of the power output of each single wave device with the absence of hydrodynamic interaction among the units. However, there is no prior experience of running a large-scale wave farm, which means the published economic analyses might be inaccurate [3, 10, 11].

- **Survivability** is closely associated with the commercial viability of wave energy technology. The WECs are expected to operate efficiently in small to intermediate wave conditions and to avoid damage in extreme wave conditions. Although it is difficult to estimate real-time wave loading in energetic sea states precisely, the knowledge and approaches of maritime engineering can be migrated to the wave energy industry [8, 21, 29]. Furthermore, submergence and self-protecting controls are also important approaches to ensure the safety of the devices [9, 23, 25, 33].

- **Environmental impacts** of deploying wave energy technology in marine environments are still unknown to regulators. Although a few small arrays have already been tested in real marine environments (e.g. Pelamis Wave Energy Converter [31] and CETO 5 [17]), the impact of

deploying WECs in large wave arrays remains unknown. The potential environmental impact includes biotic habitat loss due to installation [15], electromagnetic effects from electric cables [30], underwater noise and vibration during operation [5, 18, 26], toxic material leakage [7] and the negative visual impact of floating or fixed WECs, etc. It should be noted that the low-frequency noise and vibration generated by the operation of WECs, have been proven to be a significant disturbance for marine mammal communication [5].

1.4 Thesis

1.4.1 Thesis aims and scope

A point absorbing wave energy converter, or point absorber for short, is defined as a wave device that is much smaller in size than an incident wavelength. Point absorbers are able to extract incident wave energy in the vicinity of devices and have the capacity to generate in the order of MW [6]. The Cylindrical Energy Transfer Oscillator (Carnegie owned CETO) is an example of a single-tether point absorber, which is one of the wave energy technologies approaching commercialisation [22]. However, as a heaving point absorber, the CETO system is significantly less efficient than multi-mode ones (see Chapter 2), which weakens the applicability and economics of the CETO device.

This thesis is dedicated to improving the efficiency of submerged single-tether spherical point absorbers for small wave amplitudes by employing a buoy with asymmetric mass distribution. The main objectives of this study include:

(i) to investigate the dynamics and working principle of a submerged single-tether spherical point absorber with asymmetric mass distribution (SPAMD), and to compare the power output of the SPAMD with generic single-tether point absorbers.

(ii) to investigate the impact of mass distribution of the spherical buoy on the performance of the SPAMD;

(iii) to assess the mean annual power output of the SPAMD in real sea states;

(iv) to investigate the trajectory and power variability of the SPAMD due to hydrodynamic nonlinearities caused by large motion of the SPAMD.

1.4.2 Thesis outline

With the exception of Chapters 2, 3 and 7, this thesis is organised as a collection of papers that have been published for peer-review in high-ranked journals and conference proceedings. Note that the papers presented in this thesis have been reproduced as published, with the exception of format, page and section numbering, trivial grammatical corrections, typographical corrections, along with minor changes to a number of symbols/parameters to ensure consistency throughout the thesis.

Chapter 2 provides a broad literature review survey of existing wave energy conversion technologies, especially for wave activated bodies. The theory of wave power absorption and the design factors that have impact on the performance of the converters are also presented. The scientific research contributions are specified through this critical literature review and detailed in the following Chapters 4-6.

Chapter 3 summarises the fundamental knowledge of linear wave theory and relevant governing equations for wave-structure interaction. Based on linear wave theory, the modelling approaches for wave-structure interaction in frequency-domain and spectral-domain modelling are presented. Furthermore, the numerical modelling method based on the Navier-Stokes equations is also presented and employed for nonlinear hydrodynamic analysis of the wave energy converters.

A novel coupled resonant multi-mode point absorber prototype (i.e. SPAMD) is proposed in Chapter 4. The dynamic governing equations, working principle and power assessment are investigated in the frequency-domain.

Asymmetric mass-distribution optimisation of the proposed coupled resonant prototype is conducted for maximising the power output in real sea states. In Chapter 5, the impact of mass-distribution on the kinematic and power absorption bandwidth of the system are also investigated to provide a guideline for the wave energy industry when designing such devices.

A nonlinear hydrodynamic analysis of the proposed coupled resonant prototype is presented in Chapter 6. The hydrodynamics of the coupled resonant prototype is modelled numerically, based on the Navier-Stokes equations, to investigate the performance of the system due to nonlinear hydrodynamics.

Finally, the contributions to the research field are concluded in Chapter 7, along with the recommendations for future work.

1.4.3 List of publications included as part of the thesis

1. Meng, F., Ding, B., Cazzolato, B. S. and Arjomandi, M. (2019). "Modal analysis of a submerged spherical point absorber with asymmetric mass distribution". *Renewable Energy* 93, pp. 223 - 237.

2. Meng, F., Cazzolato, B. S., Li, Y., Ding, B. and Arjomandi, M. (2019). "A sensitivity study on the effect of mass distribution of a single-tether spherical point absorber". *Renewable Energy* 141, pp. 583 - 595.

3. Meng, F., Rafiee, A., Cazzolato, B. S., Ding, B.,and Arjomandi, M. (2019). "Nonlinear hydrodynamics analysis of a submerged spherical point absorber with asymmetric mass distribution". Accepted by Renewable Energy.

1.4.4 Additional publications relevant to the thesis but not forming part of it

1. Meng, F., Rafiee, A., Cazzolato, B. S., Ding, B., Arjomandi, M., Piper, J., Sergiienko, N., and Hu, Q. (2017). "Numerical simulation of a submerged spherical point absorber with asymmetric mass distribution". In: *Proceedings of the 12th European Wave and Tidal Energy Conference*. Ed. by A. Lewis. Cork, Ireland, pp. 1128-1–1128-8.

2. Ding, B., da Silva, L. S. P., Sergiienko, N., Meng, F., Piper, J. D., Bennetts, L., Wagner, M., Cazzolato, B. and Arjomandi, M. (2017). "Study of fully submerged point absorber wave energy converter-modelling, simulation and scaled experiment". In: *The 32nd International Workshop on Water Waves and Floating Bodies (IWWWFB)*. Dalian, China. pp. 1 - 4.

3. Schubert, B., Meng, F., Sergiienko, N., Robertson, W., Cazzolato, B. S., Ghayesh, M., Rafiee, A., Ding, B., and Arjomandi, M. (2018). "Pseudo-nonlinear hydrodynamic coefficients for modelling point absorber wave energy converters". In: *Proceedings of the 4th Asian Wave and Tidal Energy Conference*. Ed. by J. Chen. Taipei, Taiwan, China. pp. 1 - 10.

4. Ding, B., Sergiienko, N., Meng, F., Cazzolato, B. S., Hardy, P. and Arjomandi, M. (2018). "Enhancing the relative capture width of submerged point absorbing wave energy converters". In: *Proceedings of the 4th Asian Wave and Tidal Energy Conference*. Ed. by J. Chen. Taipei, Taiwan, China. pp. 1 - 10.

5. Ding, B., Sergiienko, N., Meng, F., Cazzolato, B. S., and Arjomandi, M. (2019). "The application of modal analysis to the design of multi-mode point absorber wave energy converters". *Ocean Engineering* 171, pp. 603 - 618.

6. Ding, B., Wuillaume, P., Meng, F., Babarit, A., Schubert, B., Sergiienko, N., Cazzolato, B. (2019). "Comparison of wave-body interaction modelling methods for the study of reactively controlled point absorber wave energy converter". In: *The 34nd International Workshop on Water Waves and Floating Bodies (IWWWFB)*. Newcastle, Australia. pp. 1 - 4.

References

[1] Astariz, S. and Iglesias, G. (2015). "The economics of wave energy: A review". In: *Renewable and Sustainable Energy Reviews* 45, pp. 397–408.

[2] Barstow, S., Mørk, G., Mollison, D. and Cruz, J. (2008). *Ocean Wave Energy*. Springer.

[3] Beels, C., Troch, P., Kofoed, J. P., Frigaard, P., Kringelum, J. V., Kromann, P. C., Donovan, M. H., De Rouck, J. and De Backer, G. (2011). "A methodology for production and cost assessment of a farm of wave energy converters". In: *Renewable Energy* 36.12, pp. 3402–3416.

[4] BP (2018). *Statistical review of world energy*. Report. BP.

[5] Brooke, J. (2003). *Wave energy conversion*. Vol. 6. Elsevier.

[6] Budar, K. and Falnes, J. (1975). "A resonant point absorber of ocean-wave power". In: *Nature* 256.5517, p. 478.

[7] Chambers, L. D., Stokes, K. R., Walsh, F. C. and Wood, R. J. (2006). "Modern approaches to marine antifouling coatings". In: *Surface and Coatings Technology* 201.6, pp. 3642–3652.

[8] Coe, R. G., Neary, V. S. et al. (2014). "Review of methods for modeling wave energy converter survival in extreme sea states". In: *Proceedings of the 2nd Marine Energy Technology Symposium*. Ed. by A. Lewis. Seattle, Washington, USA: TETHYS, pp. 1–8.

[9] Cornett, A., Hecimovich, M. and Nistor, I. (2015). "Extreme wave loads on submerged water intakes in shallow water". In: *Journal of Hydrodynamics* 27.1, pp. 38 –51.

[10] Dalton, G., Alcorn, R and Lewis, T (2012). "A 10 year installation program for wave energy in Ireland: A case study sensitivity analysis on financial returns". In: *Renewable Energy* 40.1, pp. 80–89.

[11] Deane, J., Dalton, G. and Gallachóir, B. Ó. (2012). "Modelling the economic impacts of 500 MW of wave power in Ireland". In: *Energy Policy* 45, pp. 614–627.

[12] Hemer, M., Simmonds, I. and Keay, K. (2008). "A classification of wave generation characteristics during large wave events on the Southern Australian margin". In: *Continental Shelf Research* 28.4-5, pp. 634–652.

[13] Hemer, M. A., Zieger, S., Durrant, T., O'Grady, J., Hoeke, R. K., McInnes, K. L. and Rosebrock, U. (2017). "A revised assessment of Australia's national wave energy resource". In: *Renewable Energy* 114, pp. 85–107.

[14] Hughes, M. G. and Heap, A. D. (2010). "National-scale wave energy resource assessment for Australia". In: *Renewable Energy* 35.8, pp. 1783–1791.

[15] Johnson, K., Kerr, S. and Side, J. (2012). "Accommodating wave and tidal energy - Control and decision in Scotland". In: *Ocean and Coastal Management* 65, pp. 26–33.

[16] Kabir, E., Kumar, P., Kumar, S., Adelodun, A. A. and Ki Hyun, K. (2018). "Solar energy: Potential and future prospects". In: *Renewable and Sustainable Energy Reviews* 82, pp. 894 –900.

[17] Kofoed, J. P. (2017). "The wave energy sector". In: *Handbook of Ocean Wave Energy*. Springer, Cham, pp. 17–42.

[18] Koschinski, S., Culik, B. M., Henriksen, O. D., Tregenza, N., Ellis, G., Jansen, C. and Kathe, G. (2003). "Behavioural reactions of free-ranging porpoises and seals to the noise of a simulated 2 MW windpower generator". In: *Marine Ecology Progress Series* 265, pp. 263–273.

[19] Lemm, A., Hegge, B. and Masselink, G. (1999). "Offshore wave climate, Perth (Western Australia), 1994–1996". In: *Marine and Freshwater Research* 50.2, pp. 95–102.

[20] Mork, G., Barstow, S., Kabuth, A. and Pontes, M. T. (2010). "Assessing the global wave energy potential". In: *ASME 2010 29th International conference on ocean, offshore and arctic engineering*. American Society of Mechanical Engineers, pp. 447–454.

[21] Muliawan, M. J., Gao, Z. and Moan, T. (2013). "Application of the contour line method for estimating extreme responses in the mooring lines of a two-body floating wave energy converter". In: *Journal of Offshore Mechanics and Arctic Engineering* 135.3, pp. 031301–031301–10.

[22] Pecher, A. and Kofoed, J. P. (2017). *Handbook of ocean wave energy*. Springer.

[23] Pecher, A., Kofoed, J. P. and Larsen, T. (2012). "Design specifications for the Hanstholm WEPTOS wave energy converter". In: *Energies* 5.4, pp. 1001–1017.

[24] *Projected Costs of Generating Electricity – 2015 Edition* (2015). Tech. rep. International Energy Agency, Nuclear Energy Agency.

[25] Ren, N., Gao, Z., Moan, T. and Wan, L. (2015). "Long-term performance estimation of the Spar Torus Combination (STC) system with different survival modes". In: *Ocean Engineering* 108, pp. 716 –728.

[26] Richardson, J., Greene, C., Malme, C. and Thomson, D. (2013). *Marine mammals and noise*. Academic press.

[27] Rogelj, J., Den Elzen, M., Höhne, N., Fransen, T., Fekete, H., Winkler, H., Schaeffer, R., Sha, F., Riahi, K. and Meinshausen, M. (2016). "Paris Agreement climate proposals need a boost to keep warming well below 2 C". In: *Nature* 534.7609, p. 631.

[28] Short, A. D. and Trenaman, N. (1992). "Wave climate of the Sydney region, an energetic and highly variable ocean wave regime". In: *Marine and Freshwater Research* 43.4, pp. 765–791.

[29] Veritas, N. (2000). *Environmental conditions and environmental loads*. Det Norske Veritas.

[30] Wilson, S. and Downie, A. (2003). *A review of possible marine renewable energy development projects and their natural heritage impacts from a Scottish perspective*. Scottish Natural Executive.

[31] Yemm, R., Pizer, D., Retzler, C. and Henderson, R. (2012). "Pelamis: experience from concept to connection". In: *Philosophical Transactions of the Royal Society A: Mathematical, Physical and Engineering Sciences* 370.1959, pp. 365–380.

[32] Young, I. (1999). "Seasonal variability of the global ocean wind and wave climate". In: *International Journal of Climatology* 19.9, pp. 931–950.

[33] Yu, Y. and Li, Y. (2011). "Preliminary results of a RANS simulation for a floating point absorber wave energy system in extreme wave conditions". In: *Proceedings of the 30th International Conference on Ocean, Offshore and Arctic Engineering*. Rotterdam, The Netherlands: American Society of Mechanical Engineers.

Chapter 2

Wave energy conversion: A literature review

This thesis is focused on improving the efficiency of single-tether spherical point absorbers by using a submerged buoy with asymmetric mass distribution (referred to as SPAMD). The aims of this chapter are to review the efficiency of existing wave energy prototypes, identify the considerations in WEC design optimisation, introduce the nonlinear hydrodynamics acting on WECs and clarify the research motivation of this thesis.

2.1 Categories of wave energy converters

Wave energy has the potential to be a high-quality renewable energy resource for electricity generation because of the outstanding energy density in ocean waves. However, the reciprocating nature of the water flows poses a challenge for conventional mechanical energy converters like stream turbines, which can only operate efficiently under constant uni-directional flows. This is one of the main reasons why wave energy technology is still at the initial stage of commercialisation. Since the Oil Crisis in the 1970s, more than 1000 wave energy converter patents have been proposed to address the difficulty of wave energy absorption, pioneered by the likes of the Cockerell raft [15], the Salter duck [50], the Bristol cylinder [17] and NEL oscillating water column (OWC) [33].

According to the operating principles summarised by IEA–Ocean Energy Systems [40], existing WECs can be classified into oscillating water columns, wave activated bodies, overtopping and submerged pressure differential devices. Each of the categories includes fixed and floating types.

Oscillating water column devices (OWCs) utilise an air column that is

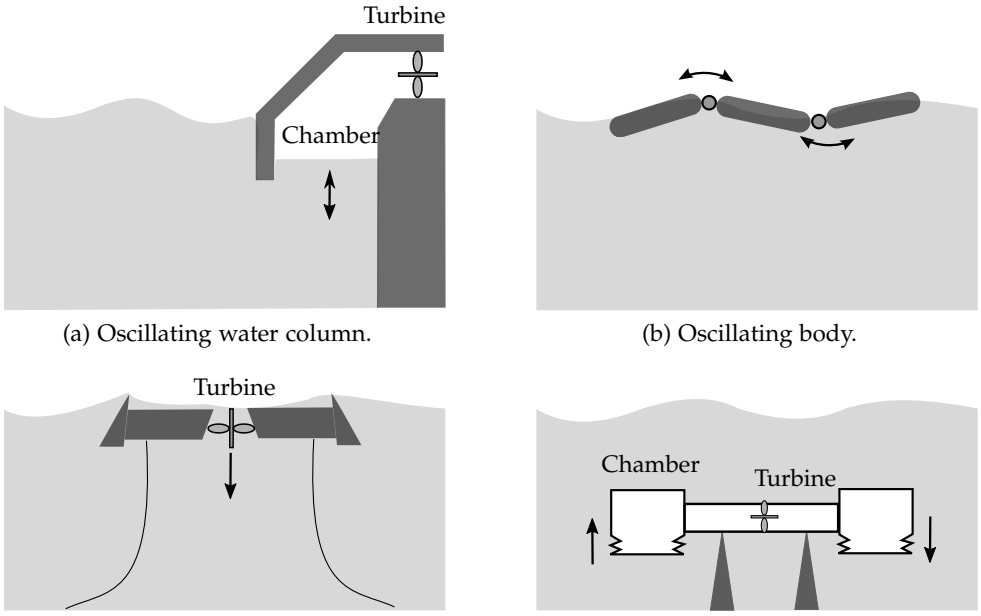

(a) Oscillating water column.

(b) Oscillating body.

(c) Overtopping device.

(d) Submerged pressure differential.

Figure 2.1: The operating principle of existing WECs, adapted from [40].

periodically compressed and decompressed by incident waves, to drive an air turbine through ducts to generate electricity. The air column is usually sealed in one or more partly submerged oscillating chambers, as shown in Figure 2.1a. The design of the chamber plays an important role in the performance of the OWC device because the energy conversion from the slow oscillating internal water column to high-speed airflow happens in the chamber. The early chamber designs were vertical columns with a constant cross section, which cannot effectively compress the airflow to drive the turbine of OWC [41]. Therefore, the inclined oscillating chamber with shrinking cross-section area is now widely applied to improve the efficiency of the OWC [8].

As the high-speed air flow in the enclosed chamber of OWCs is bidirectional, the turbines are required to self-rectify the changing flow to keep a certain rotational direction. For example, Wells type turbines use symmetrical aerofoils that are insensitive to the air flow direction to address this challenge. This technology has been tested in the Azores Pico Plant [23] and LIMPET [1].

Wave activated bodies utilise one or more oscillating bodies induced by wave loads to deliver the mechanical power to a power take-off device, as shown in Figure 2.1b. An efficient wave activated body must be a good wave

generator, which interacts destructively with the incident waves [11, 12, 21]. In general, fully submerged devices have poorer wave generation capability as compared to their surface-piercing counterparts as the wave power decays exponentially with submergence depth. However, the submerged bodies can be good candidates for wave power applications if they operate in close proximity to the water surface and take advantage of multiple motion modes [12, 54]. More details on the efficiency of this WEC type are presented in Section 2.2.

Hydraulic and direct-drive PTOs are the most commonly used PTO types for wave activated bodies. A hydraulic PTO is suitable for large wave activated bodies because this system can handle heavy wave loads at most wave frequencies [26]. However, the containment of hydraulic fluid might be a threat to the marine environment, which might restrict the application of hydraulic PTOs. Conversely, a direct-drive PTO system is generally applied to small to medium-sized wave activated bodies (e.g. the single-tether floating point absorber by Uppsala University [19]), because it simplifies the transformation from the oscillation of a body into the movement of an electrical generator, and tends to be more efficient, responsive and compact.

Overtopping devices collect the water of incident waves by using a reservoir above the water surface, to drive low head turbines which generate electricity (see Figure 2.1c). The advantage of the overtopping device is that the efficiency of the system is almost independent of incident wave periods. To achieve a certain level of power capacity, the size of the overtopping device is usually as large as the wavelength, which results in the challenge of controlling and stabilising the structure. Furthermore, exceeding overtopping rate can degrade the performance of the system, which is another engineering challenge in this field [27, 34]. Hydro turbines are generally employed as low-head turbines in overtopping devices, converting the potential energy of the collected seawater in the reservoir into usable electricity. A hydro turbine has the benefit of more than 90% energy conversion efficiency and low maintenance requirements [57]. Therefore it has been widely applied in many overtopping devices such as Wave Dragon [35], Tapchan [38] and Floating Wave Power Vessel [3].

Submerged pressure differential devices utilise the pressure difference between the environment and system internals to develop the relative motion of PTO units or drive air turbines. It mainly consists of a base (seabed-situated or bottom-referenced) and a flexible structure. The structure can be designed as one or multiple deformable air chambers, which are expended to the environment and squeezed under the varying hydrodynamic pressure from wave crest to trough such as Bombora [2] and M3 wave (see Figure 2.1d)

[6]. Another design of a flexible structure is a movable rigid cylinder, which allows the enclosed air chamber to be compressed and released for electricity generation, such as Archimedes Wave Swing [59].

Most of the first and second generation of WEC systems (e.g. Salter duck) were designed for onshore or nearshore, with consideration for low capital cost and accessibility for maintenance [45]. However, there is considerable wave energy loss when incident waves travel from deep water to shallow water, resulting in a reduction in the harvesting potential. Therefore, most of the third generation of WEC systems (e.g. CETO 5) are sited in intermediate or deep water, even though the systems are subjected to greater wave loads in extreme sea states.

2.2 Oscillating bodies

2.2.1 Wave energy absorption principles

Wave activated bodies are designed to extract the incident wave energy through wave-structure interaction. The wave-structure interaction results in the diffraction and radiation of water waves. The capability of radiating waves determines the efficiency of wave activated bodies. From the perspective of wave interaction, the incident wave energy is completely extracted only if the reflected waves (for short waves) or transmitted waves (for long waves) are diminished. In other words, the body should radiate waves with optimum amplitudes and phases that can cancel the upstream reflected waves or downstream transmitted waves [24]. It should be noted that the pattern of radiated wave is determined by the motion modes of the oscillating body: heave motion generates monopole-type radiated waves which are symmetrically circular; while the surge or pitch motion leads to dipole-type radiated waves which are asymmetric [16].

The terminator has the largest theoretical capture width, which is defined as the ratio of the mean absorbed wave power to incident wave power resource [24]. Figure 2.2 illustrates perfect incident wave destruction by using an infinite long terminator oscillating vertically and horizontally. Conversely a single-mode terminator with a symmetrical cross-section can only achieve up to 50% wave energy absorption through one motion mode (i.e. heave, surge and pitch), because it only cancels 50% of the upstream wave elevation [24]. It is interesting to note that there is no additional benefit for oscillating bodies to use three modes (i.e. heave, surge and pitch) to extract wave energy because both surge and pitch can generate dipole radiated waves. It should be noted that a body with asymmetric cross-section might have the potential to

generate radiated waves that perfectly destroy the incident waves. Therefore, it is possible to extract the majority of incident wave energy by only using one motion mode, e.g. Salter duck [20].

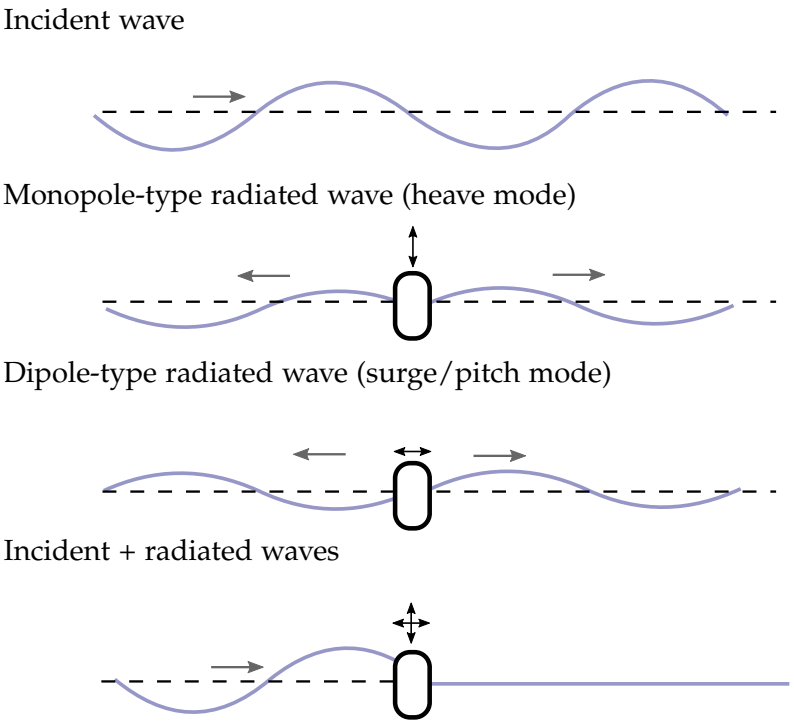

Figure 2.2: Incident wave cancellation by a 2D-body, adapted from [24].

For axisymmetric point absorbers, the theoretical maximum power extracted from sinusoidal waves from each mode, P_A, is defined by the radiation property of the body, given by [21]:

$$P_A = \begin{cases} \frac{\lambda}{2\pi} J & \text{heave mode} \\ \frac{\lambda}{\pi} J & \text{surge\pitch mode} \end{cases} \tag{2.1}$$

where J is the wave energy flux, λ is the wavelength.

However, the capacity factor poses another power limit for the oscillating body. For submerged wave energy converters oscillating in deep water, the power limit due to the PTO constraint, P_B, is given by [10, 25, 58]:

$$P_B = \frac{8\pi^3}{3T^3} e^{-2kr} \rho V_s H r, \qquad \text{surge\heave mode} \tag{2.2}$$

where T is the wave period, k is wavenumber, r is the radius of body, ρ is the water density, V_s is the maximum swept volume of the buoy, which is the function of oscillation amplitude and the cross-section area of the

buoy, H is the wave height. It can be seen that the power limit presented in Equation (2.1) is independent of the shape of the body. In contrast, P_B is a function of the geometry of the oscillating body [54].

Equation (2.1) and Equation (2.2) define the upper bounds on the maximum wave energy absorption of the oscillating body with finite dimension for low and high wave frequencies. The graph of these two upper power bounds is known as Budal's diagram (see Figure 2.3) [11], which is frequently used to evaluate the design of prototypes and the performance of control algorithm. Figure 2.3 shows the upper power absorption limits of a submerged spherical point absorber oscillating in surge and heave. It can be seen that the heave and surge modes have distinct power absorption limits over the wave periods of interest. For short waves, the dipole radiation pattern caused by the surge motion results in a higher power limit P_A; while for long waves, the heave motion of the oscillating body is not likely to be saturated by the PTO constraint and therefore the heave mode has a higher power limit P_B.

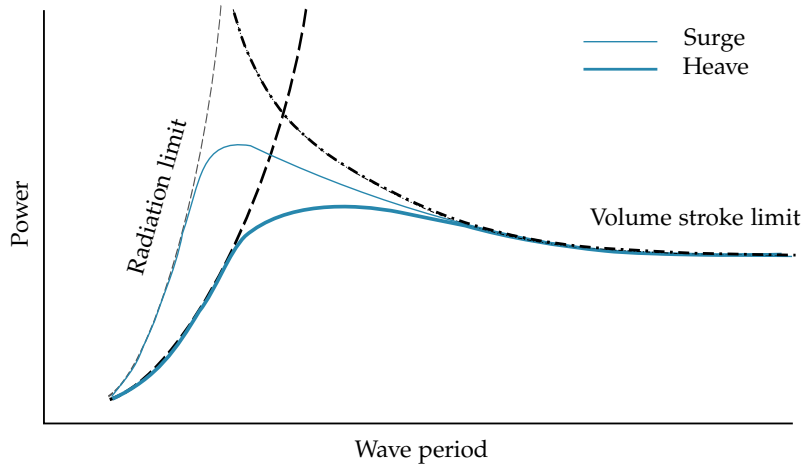

Figure 2.3: An example of the upper power absorption limits of a submerged spherical point absorber oscillating in surge and heave, adapted from [54]. The solid lines represent the absorbed power by the WEC under optimal control, which are limited by the radiation property of the system at low wave periods and the volume stroke of the PTO at high wave periods

.

It can be concluded that oscillating WECs can increase wave power absorption from multiple oscillation modes compared with a single mode. However, multi-mode WECs require multiple PTO units to couple and control the motion of the buoy, which complicates the system and reduces the overall reliability. Therefore, there are still a considerable number of oscillating WEC designs predominantly utilising a single mode to extract wave energy. In

Chapter 4, a new coupled resonant concept is proposed, where only one external PTO unit is employed to extract 100% of the wave power for a selected frequency range.

2.2.2 Design optimisation

Although wave activated bodies have the potential to absorb 100% of the incident wave power for certain wave frequencies, the efficiency of the system is still unsatisfactory in realistic sea states (irregular waves) because the wave activated body usually has a narrow bandwidth in comparison with the wave spectrum [25]. Therefore, it is necessary to optimise the design of the WECs to improve their performance for the candidate deployment sites.

Prior to design optimisation, the wave climate of candidate deployment sites should be surveyed in terms of the annual statistics of the wavelength, wave height, wave periods and wave direction distribution. The information about the wave climate is usually integrated in a scatter diagram, together with the corresponding probability of occurrence. The scatter diagram is used to determine the operational sea states for design optimisation according to the corresponding wave energy contribution. It is recommended that the amount of selected operational sea states should be fewer than 10 and each contributes 5-25% wave energy of the total. Furthermore, each of the operational sea states should have a probability of occurrence of more than 0.5% [41].

The **geometrical shape** is an important aspect for an optimisation study, because it determines the hydrodynamic efficiency and absorption bandwidth of wave activated bodies, especially for heaving devices. One objective of geometrical optimisation is to select optimal shapes, mainly among axisymmetric geometries. This is because the performance of axisymmetric buoys are insensitive to the wave direction. For example, Goggins and Finnegan [29] benchmarked 12 candidate cylindrical buoys with different bottoms to maximise the efficiency of a floating point absorber for the Atlantic marine energy test site. Backer [18] compared hydrodynamic efficiency between a cylinder with a conical bottom and a cylinder with a hemispherical bottom. Another objective of geometrical optimisation is to determine the optimum dimension for a given geometry. For example, Soulard et al. [56] determined the optimum radii of a two-body spherical heaving point absorber through a statistical analysis. Barbarit and Clement [5] and McCabe [36] employed genetic algorithm to determine the optimal diameter and drafts of the SEAREV device, to achieve an increase in power and a decrease in structural cost. It should be noted that the absorbed power is calculated from the response

amplitude operator (RAO), which might be overestimated due to the tether slack caused by the large motion of the buoy. Therefore, it is suggested the geometrical shape should be optimised with consideration of motion constraint to avoid exaggerating the result [22, 29, 36, 55].

PTO configuration is an essential part of the design optimisation because it can improve the power extraction efficiency of wave activated bodies. One objective of PTO optimisation is to improve the coupling between PTO units and the oscillating body. For example, Sergiienko et al. [53] presented an optimisation on the inclination angle of the mooring system, to improve power output and controllability of a three-tether point absorber. Moretti et al. [39] employed dual parallelogram-shaped soft dielectric elastomers to obtain more controllability of a sea-bottom referenced surging converter. Furthermore, the power absorption bandwidth can be broadened via PTO optimisation. For conventional hydraulic PTO systems, Schlemmer et al. [51] proposed a hydraulic transformer circuit to enlarge the power capacity of the Wavebob point absorber, where dual hydraulic motors were employed to provide two operational modes for high and low sea states. Studies with similar outcomes were also reported by Henderson [31], Falcão [4] and Ricci et al. [47], etc. For direct drive generators, Zhang et al. [68] and Xiao et al. [65] installed mechanical springs or magnets to the ends of a generator, to create a bistable condition that allows the PTO system to achieve a wider absorption bandwidth.

The **mass-related parameters** are the dominant optimisation mechanisms for coupled resonant converters because they determine the natural frequency and motion of the coupled system. For a coupled resonant system with an internal pendulum-type PTO, the efficiency of the converter is mainly affected by the natural frequency of the pendulum. Therefore, the tuning parameter is the distance from the mass to the centre of gyration [9, 14, 48]. In contrast, for a coupled resonant system with external PTOs, the tuning parameter is the mass distribution of the whole oscillating body. In Chapter 5, a sensitivity study is presented to investigate the impact of mass distribution on the performance of a coupled resonant system with an external PTO.

Increasing attention is paid to multi-objective design optimisation because the hydrodynamic efficiency cannot demonstrate the commercial viability of the prototype, e.g. Salter's duck and the Bristol cylinder. The additional objectives of optimisation include the cost of system design, construction, transportation, installation, maintenance, and decommissioning, etc. For example, Cordonnier et al. [14] developed an economic model considering energy production, capital expenditures, operational expenditures and lifetime, to guide the design optimisation of the coupled resonant device SEAREV.

It was found that the latest generation shows significant improvement in commercial viability with respect to the former ones. Another example is the optimisation study presented by Piscopo et al. [44], where the radii of a two-body spherical point absorber was optimised with consideration of the annualised energy production per unit area of the buoy's surface and the Levelised Cost of Energy (LCoE). However, multi-objective optimisation is usually time-consuming for personal computers due to the considerable computational loads. Therefore, various evolutionary algorithms have been employed to accelerate the optimisation procedure, e.g. the genetic algorithm [36] and the random hill-climbing algorithm (1+1)-EA [64].

2.3 Nonlinear hydrodynamics for WECs

The mathematical dynamic models widely used in power production assessment and design optimisation are usually developed from linear potential theory which assumes the motion of structure is small relative to the wave height in order to linearise the boundary conditions. This is because the computational load is heavy due to the considerable number of study cases, whilst the accuracy is not paramount. As is the case with real-time model-based control, the linear potential model is also the first option for initial modelling of controller performance. However, the assumptions of linear potential theory are only valid for traditional offshore engineering applications rather than WECs, due to the fact that the wave activated body is designed to have large motion amplitudes for maximising power absorption. It has been demonstrated that the linear models overestimate the response of heaving and surging converters [7, 42, 67].

Some efforts have been made to improve the accuracy of the linear models within the framework of potential theory. McCabe et al. [37] developed a time-varying parameter model for a pitching point absorber at resonance, in which the hydrodynamic coefficients were linearly interpolated according to the immersed surface of the oscillating body. It was found that response of the time-varying parameter model is more accurate than the conventional time-invariant models with respect to experiment data. Penalba et al. suggested the modelling approaches can be determined through the perspective of operation conditions, as shown in Figure 2.4 [43, 49]. Since the power production mode of the wave energy converter might be characterised by an intermediate system response and wave loadings, a weakly nonlinear model should be employed for an accurate response of the system. For example, Retes et al. [42] implemented nonlinear Froude-Krylov forces and restoring forces derived from an instantaneous wetted surface to model a resonant

submerged heaving point absorber, resulting in good agreement with the experimental results. Gilloteaux et al. [28] modelled the high-order diffraction and radiation to obtain a reasonable response of the prototype SEAREV at resonance. However, although the partly or fully nonlinear potential theory can address the problem of response overestimate in certain cases, some nonlinear hydrodynamics can not be modelled using potential theory due to its inherent assumptions (see Chapter 3).

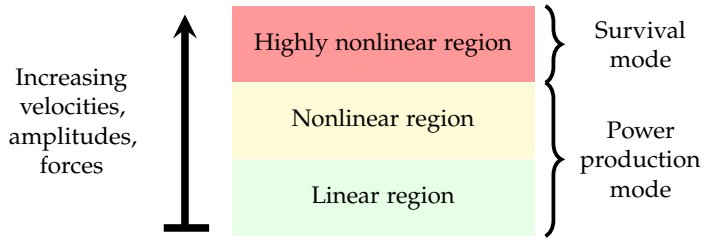

Figure 2.4: Operating modes of a wave energy converter and corresponding hydrodynamic nonlinearity extent, adapted from [49].

The numerical wave tank (NWT) implemented by solving Navier-Stokes equations provides a relatively low-cost option for simulating and visualising a nonlinear wave-structure interaction in a full scale prototype. Therefore, the NWT experiment is widely used to identify and understand the dominant nonlinear hydrodynamics acting on the WEC prototypes, such as slamming, vortex shedding and extreme wave loads.

Slamming is generally observed from near shore OWSCs when re-entering the water. Henry et al. [32] identified that wave slamming is likely to happen to the OWSC when the trough of incident waves leads to a drying-out side of the flap. The resulting impulsive pressure imbalance then accelerates the flap to slam into the water. Wei et al. [61] investigated the pressure distribution on the flap by using a 2D NWT experiment. It was found that the peak pressure appears at the centre of the flap when the flap surface moves up to the water surface.

Vortex shedding is a periodic oscillating flow which is induced when water flow travels through a blunt body at a particular velocity range. Wei et al. [60] demonstrated that the vortex shedding at the edge of the OWSCs only exists in half of the wave period. It appears when the flap and incident waves are proceeding in the same direction and disappears once the wave flow reverses. The resulting viscous drag force is usually approximated by the Morison equation where the viscous coefficients can be determined by using a free oscillation in a NWT experiment [46]. Since vortex shedding has a greater negative impact on the performance of OWSCs than heaving

converters, the viscous force should be modelled in the dynamic equation of OWSCs [43].

Extreme wave loads are key design concerns that are necessarily examined in the development of WECs. Yu et al. [66] found that the extreme wave loads do not always result from the largest waves. Instead, extreme loads are randomly triggered by specific wavetrains, together with instantaneous WEC positions. In order to create such short lived extreme scenarios, WECs are generally tested in various extreme sea states, such as large monochromatic waves [52, 63, 67], energetic stochastic waves [13, 30] and focused waves [62].

Surface piercing is another significant nonlinear hydrodynamic process that restricts the motion of WECs. The effect of surface piercing is represented simply by the position-dependent Froude-Krylov force and restoring force in the dynamic equation of point absorbers [43]. However, in Chapter 6, it is demonstrated that surface piercing is a complicated process, where a high-pressure area on the top of the buoy stops the device breaching the water surface. The impact of surface piercing on the performance of multi-DOF point absorbers is investigated via a NWT experiment.

2.4 Concluding remarks and perspectives

The literature related to this thesis is broadly reviewed in this chapter, including an overview of the existing wave energy technology focusing on wave activated bodies, considerations of design optimisation that influence the performance of wave energy converters, and nonlinear hydrodynamics acting on wave energy converters.

The majority of wave activated bodies are designed as single-mode devices that operate in either heave mode or surge/pitch mode around the water free surface. This is because multi-mode WECs (e.g. Bristol cylinder and WaveSub) require multiple PTO units to couple and control the dynamics of the buoy, which increases the system complexity and capital cost. However, as discussed in Section 2.2.1, the multi-mode WECs have been shown to be more hydrodynamically efficient than the uni-mode ones. The concept of a coupled resonant device is proposed to provide an alternative low-cost way for multi-mode WECs to extract wave power using a single PTO unit. Additionally, most coupled resonant devices tend to relocate the PTO unit inside the WEC to enhance the survivability of the whole system. The internal PTO arrangement significantly constrains the wave cancellation ability of the coupled resonant devices and consequently the maximum theoretical efficiency reduces significantly. A novel coupled resonant device that achieves

100% power absorption for some wave frequencies is proposed in Chapter 4, using a spherical buoy with asymmetric mass distribution which is connected to an external PTO unit.

For coupled resonant devices, the mass-related parameters are the primary factors affecting the design optimisation. This is because the mass-related parameters determine the absorption bandwidth of the system. As reviewed in Section 2.2.2, most proposed coupled resonant devices utilise an internal pendulum-type PTO to extract wave power, consequently the tuning parameters are the weight and the distance from the bob to the centre of gyration, instead of the mass-distribution of the whole buoy. In Chapter 5, the impact of the mass distribution of a system with an external PTO unit is investigated in terms of the response of system and the power absorption bandwidth. Furthermore, the performance of the proposed coupled resonant device is assessed in real sea states.

As discussed in Section 2.2.2, by using linear wave theory and the principle of superposition, the annual power calculated for design optimisation can be quickly solved for given sea states. However, linear wave theory neglects the nonlinear hydrodynamic effects and therefore tends to overestimate the response of the system. The numerical modelling methods based on Navier-Stokes equations are widely used for optimal design validation in terms of survivability, mooring system test and power output. For submerged multi-mode WECs, the nonlinear hydrodynamic effects might be more significant than for floating ones because of the larger wetted surface. In Chapter 6, the nonlinear hydrodynamics induced by large motions of the buoy, especially when the buoy breaches the water surface, are investigated.

References

[1] Alcorn, R., Beattie, W. et al. (2001). "Power quality assessment from the LIMPET wave-power station". In: *Proceedings of the 11th International Offshore and Polar Engineering Conference*. International Society of Offshore and Polar Engineers.

[2] Algie, C., Ryan, S. and Fleming, A. (2017). "Predicted power performance of a submerged membrane pressure-differential wave energy converter". In: *International Journal of Marine Energy* 20, pp. 125–134.

[3] Almeida, A. T. and Moura, P. S. (2007). "Desalination with wind and wave power". In: *Solar Desalination for the 21st Century*. Springer, pp. 305–325.

[4] António, F. d. O. (2008). "Phase control through load control of oscillating-body wave energy converters with hydraulic PTO system". In: *Ocean Engineering* 35.3-4, pp. 358–366.

[5] Babarit, A. and Clément, A. (2006). "Shape optimisation of the SEAREV wave energy converter". In: *Proceedings of World Renewable Energy Congress IX*. Floransa, Italy: Elsevier.

[6] Babarit, A., Wendt, F., Yu, Y.-H. and Weber, J. (2017). "Investigation on the energy absorption performance of a fixed-bottom pressure-differential wave energy converter". In: *Applied Ocean Research* 65, pp. 90 –101.

[7] Babarit, A., Mouslim, H., Clément, A. and Laporte-Weywada, P. (2009). "On the numerical modelling of the non linear behaviour of a wave energy converter". In: *Proceedings of the 28th International Conference on Ocean, Offshore and Arctic Engineering*. American Society of Mechanical Engineers, pp. 1045–1053.

[8] Boake, C. B., Whittaker, T. J., Folley, M., Ellen, H. et al. (2002). "Overview and initial operational experience of the LIMPET wave energy plant". In: *Proceedings of the 12th International Offshore and Polar Engineering Conference*. International Society of Offshore and Polar Engineers.

[9] Bracco, G., Giorcelli, E. and Mattiazzo, G. (2010). "ISWEC: Design of a prototype model for wave tank test". In: *Proceedings of the 10th Biennial Conference on Engineering Systems Design and Analysis*. Istanbul, Turkey: American Society of Mechanical Engineers, pp. 25–31.

[10] Budal, K. and Falnes, J. (1980). "Interacting point absorbers with controlled motion". In: *Power from sea waves*. Ed. by B. Count. London: UK: Academic Press, pp. 381–399.

[11] Budal, K. and Falnes, J. (1982). "Wave power conversion by point absorbers: a Norwegian project". In: *International Journal of Ambient Energy* 3.2, pp. 59–67.

[12] Budar, K. and Falnes, J. (1975). "A resonant point absorber of ocean-wave power". In: *Nature* 256.5517, p. 478.

[13] Chen, W., Dolguntseva, I., Savin, A., Zhang, Y., Li, W., Svensson, O. and Leijon, M. (2017). "Numerical modelling of a point-absorbing wave energy converter in irregular and extreme waves". In: *Applied Ocean Research* 63, pp. 90–105.

[14] Cordonnier, J., Gorintin, F., De Cagny, A., Clément, A. and Babarit, A. (2015). "SEAREV: Case study of the development of a wave energy converter". In: *Renewable Energy* 80, pp. 40–52.

[15] Count, B. (1979). "Exploiting wave power: To realize the promise, engineers must deal with unique power-transfer modes, erratic seas, and unfavorable economics". In: *IEEE Spectrum* 16.9, pp. 42–49.

[16] Cruz, J. (2007). *Ocean wave energy: current status and future prespectives*. Springer Science and Business Media.

[17] Davis, J. (1990). "Wave energy absorption by the Bristol Cylinder: linear and non-linear effects". In: *Institution of Civil Engineers Proceedings* 89, pp. 317–40.

[18] De Backer, G. (2009). "Hydrodynamic design optimization of wave energy converters consisting of heaving point absorbers". Ph.D. thesis. Department of Civil Engineering, Ghent University.

[19] Eriksson, M. (2007). "Modelling and experimental verification of direct drive wave energy conversion: Buoy-generator dynamics". PhD thesis. Acta Universitatis Upsaliensis.

[20] Evans, D. V. and Porter, R. (1997). "Efficient calculation of hydrodynamic properties of OWC-type devices". In: *Journal of Offshore Mechanics and Arctic Engineering* 119.4, pp. 210–218.

[21] Evans, D. (1976). "A theory for wave-power absorption by oscillating bodies". In: *Journal of Fluid Mechanics* 77.1, pp. 1–25.

[22] Faizal, M., Ahmed, M. R. and Lee, Y.-H. (2014). "A design outline for floating point absorber wave energy converters". In: *Advances in Mechanical Engineering* 6, pp. 1–18.

[23] Falcão, A (2000). "The shoreline OWC wave power plant at the Azores". In: *Proceedings of the 4th European Wave Energy Conference*. Aalborg, Denmark, pp. 4–6.

[24] Falnes, J. (2002). *Ocean waves and oscillating systems: linear interactions including wave-energy extraction*. Cambridge University Press.

[25] Falnes, J. and Hals, J. (2012). "Heaving buoys, point absorbers and arrays". In: *Philosophical Transactions of the Royal Society A: Mathematical, Physical and Engineering Sciences* 370.1959, pp. 246–277.

[26] Ferri, F. and Kracht, P. (2013). "Implementation of a hydraulic power take-off for wave energy applications". Ph.D. thesis. Department of Civil Engineering, Aalborg University.

[27] Franco, L., De Gerloni, M. and Meer, J. Van der (1995). "Wave overtopping on vertical and composite breakwaters". In: *Coastal Engineering 1994*, pp. 1030–1045.

[28] Gilloteaux, J.-C., Bacelli, G. and Ringwood, J. (2007). "A non-linear potential model to predict large-amplitudes-motions: Application to a multi-body wave energy converter". In: *Proceedings of the 22nd International Workshop on Water Waves and Floating Bodies*, pp. 1–10.

[29] Goggins, J. and Finnegan, W. (2014). "Shape optimisation of floating wave energy converters for a specified wave energy spectrum". In: *Renewable Energy* 71, pp. 208–220.

[30] Göteman, M., Engström, J., Eriksson, M., Hann, M., Ransley, E., Greaves, D., Leijon, M. et al. (2015). "Wave loads on a point-absorbing wave energy device in extreme waves". In: *The Twenty-fifth International Ocean and Polar Engineering Conference*. International Society of Offshore and Polar Engineers.

[31] Hansen, R. H., Andersen, T. O. and Pedersen, H. C. (2011). "Model based design of efficient power take-off systems for wave energy converters". In: *Proceedings of the 12th Scandinavian International Conference on Fluid Power, SICFP 2011*. Tampere University Press, pp. 35–49.

[32] Henry, A., Schmitt, P., Whittaker, T., Rafiee, A. and Dias, F. (2013). "The characteristics of wave impacts on an oscillating wave surge converter". In: *The Twenty-third International Offshore and Polar Engineering Conference*. International Society of Offshore and Polar Engineers. Rhodes, Greece.

[33] Hunter, R. (1982). *Future possibilities for the NEL oscillating water column wave energy converter–Experimental measurements and theoretical predictions of the phase control in regular waves*. Report. Department of Energy, National Engineering Laboratory, East Kilbride, Glasgow.

[34] Kofoed, J. P. (2002). "Wave overtopping of marine structures: utilization of wave energy". PhD thesis. Hydraulics and Coastal Engineering Laboratory, Department of Civil Engineering, Aalborg University.

[35] Kofoed, J. P., Frigaard, P., Friis-Madsen, E. and Sørensen, H. C. (2006). "Prototype testing of the wave energy converter wave dragon". In: *Renewable Energy* 31.2, pp. 181–189.

[36] McCabe, A. (2013). "Constrained optimization of the shape of a wave energy collector by genetic algorithm". In: *Renewable Energy* 51, pp. 274–284.

[37] McCabe, A., Aggidis, G. A. and Stallard, T. (2006). "A time-varying parameter model of a body oscillating in pitch". In: *Applied Ocean Research* 28.6, pp. 359–370.

[38] Mehlum, E. (1986). "Tapchan". In: *Hydrodynamics of Ocean Wave-Energy Utilization*. Springer, pp. 51–55.

[39] Moretti, G., Fontana, M. and Vertechy, R. (2015). "Model-based design and optimization of a dielectric elastomer power take-off for oscillating wave surge energy converters". In: *Meccanica* 50.11, pp. 2797–2813.

[40] Ocean Energy System. [Online] https://www.ocean-energy-systems.org, accessed 07 Sep 2018.

[41] Pecher, A. and Kofoed, J. P. (2017). *Handbook of ocean wave energy*. Springer.

[42] Penalba, M., Mérigaud, A., Gilloteaux, C. and Ringwood, J. (2015). "Nonlinear Froude-Krylov force modelling for two heaving wave energy point absorbers". In: *Proceedings of the 11th European Wave and Tidal Energy Conference*. European Wave and Tidal Energy Conference. Nante, France.

[43] Penalba, M., Giorgi, G. and Ringwood, J. V. (2017). "Mathematical modelling of wave energy converters: A review of nonlinear approaches". In: *Renewable and Sustainable Energy Reviews* 78, pp. 1188–1207.

[44] Piscopo, V., Benassai, G., Cozzolino, L., Della Morte, R. and Scamardella, A. (2016). "A new optimization procedure of heaving point absorber hydrodynamic performances". In: *Ocean Engineering* 116, pp. 242–259.

[45] Price, A. A. (2009). "New perspectives on wave energy converter control". Ph.D. thesis. The University of Edinburgh.

[46] Rafiee, A. and Fiévez, J. (2015). "Numerical prediction of extreme loads on the CETO wave energy converter". In: *11th European Wave and Tidal Energy Conference*. Nantes, France.

[47] Ricci, P., Lopez, J., Santos, M., Villate, J., Ruiz-Minguela, P., Salcedo, F. and Falcao, A (2009). "Control strategies for a simple point-absorber connected to a hydraulic power take-off". In: *Proceedings of the 8th European Wave and Tidal Energy Conference, Uppsala, Sweden*, pp. 7–10.

[48] Rinaldi, G., Fontanella, A., Sannino, G., Bracco, G., Giorcelli, E., Mattiazzo, G. and Bludszuweit, H. (2016). "Development of a simplified analytical model for a passive inertial system solicited by wave motion". In: *International Journal of Marine Energy* 13, pp. 45–61.

[49] Ringwood, J. V., Bacelli, G. and Fusco, F. (2014). "Energy-maximizing control of wave-energy converters: The development of control system technology to optimize their operation". In: *IEEE Control Systems* 34.5, pp. 30–55.

[50] Salter, S., Jeffery, D. and Taylor, J. (1976). "The architecture of nodding duck wave power generators". In: *The Naval Architect* 1, pp. 21–24.

[51] Schlemmer, K., Fuchshumer, F., Böhmer, N., Costello, R. and Villegas, C. (2011). "Design and control of a hydraulic power take-off for an axisymmetric heaving point absorber". In: *Proceedings of the 9th European Wave and Tidal Energy Conference*. Southampton, UK.

[52] Schmitt, P. M. (2014). "Investigation of the near flow field of bottom hinged flap type wave energy converters". PhD thesis. Queen's University Belfast.

[53] Sergiienko, N., Cazzolato, B., Ding, B. and Arjomandi, M. (2016). "An optimal arrangement of mooring lines for the three-tether submerged point-absorbing wave energy converter". In: *Renewable Energy* 93, pp. 27–37.

[54] Sergiienko, N., Cazzolato, B., Ding, B., Hardy, P. and Arjomandi, M. (2017). "Performance comparison of the floating and fully submerged quasi-point absorber wave energy converters". In: *Renewable Energy* 108, pp. 425–437.

[55] Shadman, M., Estefen, S. F., Rodriguez, C. A. and Nogueira, I. C. (2018). "A geometrical optimization method applied to a heaving point absorber wave energy converter". In: *Renewable Energy* 115, pp. 533 –546.

[56] Soulard, T., Alves, M., Sarmento, A. et al. (2009). "Force reacting principle applied to a heave point absorber wave energy converter". In: *Proceedings of the 19th International Offshore and Polar Engineering Conference*. International Society of Offshore and Polar Engineers.

[57] Têtu, A. (2017). "Power take-off systems for WECs". In: *Handbook of ocean wave energy*. Ed. by A. Pecher and J. P. Kofoed. Cham: Springer International Publishing, pp. 203–220.

[58] Todalshaug, J. H. (2013). "Practical limits to the power that can be captured from ocean waves by oscillating bodies". In: *International Journal of Marine Energy* 3, e70–e81.

[59] Valerio, D., Beirao, P. and Costa, J. (2007). "Optimisation of wave energy extraction with the Archimedes Wave Swing". In: *Ocean Engineering* 34.17, pp. 2330–2344.

[60] Wei, Y., Rafiee, A., Henry, A. and Dias, F. (2015). "Wave interaction with an oscillating wave surge converter. Part I: Viscous effects". In: *Ocean Engineering* 104, pp. 185–203.

[61] Wei, Y., Abadie, T., Henry, A. and Dias, F. (2016). "Wave interaction with an oscillating wave surge converter. Part II: Slamming". In: *Ocean Engineering* 113, pp. 319–334.

[62] Westphalen, J. (2011). "Extreme wave loading on offshore wave energy devices using CFD". Ph.D. thesis. University of Plymouth.

[63] Windt, C., Ringwood, J., Davidson, J., Ransley, E., Jakobsen, M. and Kramer, M. (2018). "Validation of a CFD-based numerical wave tank of the Wavestar WEC". In: *Proceedings of Advances in Renewable Energies Offshore*. CRC Press. Lisbon, Portugal, pp. 439–447.

[64] Wu, J., Shekh, S., Sergiienko, N. Y., Cazzolato, B. S., Ding, B., Neumann, F. and Wagner, M. (2016). "Fast and effective optimisation of arrays of

submerged wave energy converters". In: *Proceedings of the Genetic and Evolutionary Computation Conference 2016*. ACM, pp. 1045–1052.

[65] Xiao, X., Xiao, L. and Peng, T. (2017). "Comparative study on power capture performance of oscillating-body wave energy converters with three novel power take-off systems". In: *Renewable Energy* 103, pp. 94–105.

[66] Yu, H., Van, J., Coe, R. and Lawson, M. (2015). "Preliminary wave energy converters extreme load analysis". In: *The 34th International Conference on Ocean, Offshore and Arctic Engineering*. American Society of Mechanical Engineers, pp. 22–26.

[67] Yu, Y.-H. and Li, Y. (2013). "Reynolds-Averaged Navier-Stokes simulation of the heave performance of a two-body floating-point absorber wave energy system". In: *Computers and Fluids* 73, pp. 104 –114.

[68] Zhang, X., Yang, J. and Xiao, L. (2016). "An oscillating wave energy converter with nonlinear snap-through power take-off systems in regular waves". In: *China Ocean Engineering* 30.4, pp. 565–580.

Chapter 3

Background theory

This chapter aims to introduce the modelling methods for the wave-structure interaction that are used throughout the thesis. Computational demands and model accuracy are the two main considerations for the wave-structure modelling task. In this thesis, linear potential theory has been employed for the WEC conceptual development (Chapter 4) and parametric optimisation (Chapter 5) because it can provide qualified model accuracy with a low computational load for these purposes. In contrast, a computational fluid dynamics (CFD) model based on the Navier-Stokes equations, which requires massive computational resources for high accuracy results, has been used to validate the performance of the proposed WEC in fully nonlinear hydrodynamics (Chapter 6).

3.1 Description of ocean waves

Regular waves

The profile of a regular wave is determined by the wave period (T), wavelength (λ), wave height (H) and water depth (h). The nonlinearity of the profile is generally determined by wave steepness ($s = H/\lambda$), and is affected by the seabed effect amongst other factors. Le Méhauté [10] summarised the suitability of wave profile model for deep, intermediate and shallow water scenarios, as shown in Figure 3.1. For deep water ($h > \frac{\lambda}{2}$), the seabed effect on surface elevation can be neglected and therefore the profile of a regular wave with a wave steepness of less than 0.01 can be approximated as a sinusoidal function. When the incident wave travels to intermediate water, the wave profile tends to be increasingly nonlinear due to the effect of the seabed. Therefore, higher-order wave theories, such as Stokes' wave theory, are essential to describe the nonlinearity of the wave profile. In Chapter 6, an

incident wavetrain with a 5th-order Stokes' wave profile is produced in the NWT experiment, to check the mesh convergence near the water surface.

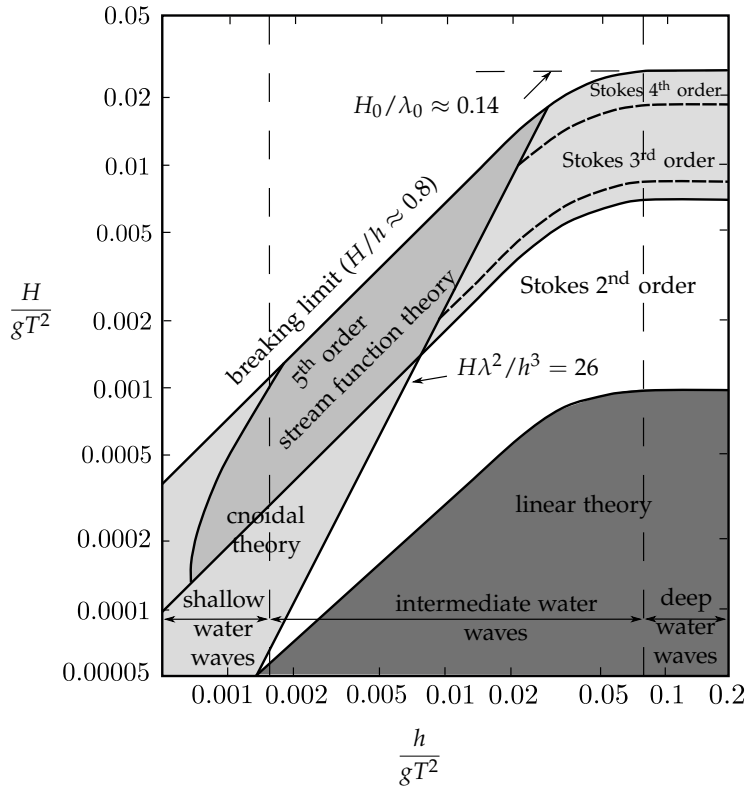

Figure 3.1: Wave model suitability, adapted from [10].

Irregular waves

The irregular waves (real sea states) develop from small ripples which are induced by local winds. With sustained wind energy input, the small ripples grow to be fully developed waves when the wind energy input is balanced out by the energy loss due to white-capping and wave breaking. The development of the sea state is mainly affected by the local wind speed and wind blowing distance (fetch). When the fully developed waves travel beyond the range of the wind, they becomes swell waves which can travel thousands of kilometres with little energy loss in deep water.

The short-term sea state is usually characterised by a spectrum, where it is assumed that the wave surface elevation can be represented as the linear superposition of sinusoidal waves over various wave frequencies, amplitudes, phases and distributions. It should be noted that this assumption is invalid for steep waves, breaking waves and shallow water waves [15]. A wave spectrum

is mainly defined by two parameters, namely the significant wave height H_s (the average of the third largest wave height) and the peak wave frequency of the spectrum ω_p.

The commonly used wave spectrum for testing wave energy converters includes [21]:

JONSWAP spectrum (the Joint North Sea Wave Observation Project) is the representative of developing sea states, where the fetch length is finite [8]. The spectral shape of JONSWAP (see Figure 3.2a) is relatively narrow in comparison with the fully developed sea states, which indicates the wave energy is concentrated over a small frequency range. The bandwidth of the spectrum is determined by the peak enhancement factor γ ($1 < \gamma < 7$). The spectral variance density is given by [8]

$$S(\omega) = \frac{\alpha g^2}{\omega^5} \exp\left[-\frac{5}{4}\left(\frac{\omega_p}{\omega}\right)^4\right] \gamma^{\exp[-\frac{(\omega-\omega_p)^2}{2\sigma^2\omega_p^2}]}, \tag{3.1}$$

with the three parameters α, ω_p and σ given by

$$\begin{aligned} \alpha &= 0.076\left(\frac{U_{10}^2}{Fg}\right)^{0.22}, \\ \omega_p &= 22\left(\frac{g^2}{U_{10}F}\right)^{1/3}, \\ \sigma &= \begin{cases} 0.07, & \omega < \omega_p. \\ 0.09, & \omega > \omega_p. \end{cases}, \end{aligned} \tag{3.2}$$

where g is the gravitational acceleration, U_{10} is the wind speed at a height of 10 m , which is equal to the wave crest phase velocity [rad/s], F is the fetch length [m] and ω is the wave component frequency.

Pierson-Moskowitz spectrum describes a typical fully developed sea state generated by sufficiently long wind blowing on a sufficiently large area of water (Figure 3.2b). The spectral variance density is given by [18]

$$S(\omega) = \frac{c_1 g^2}{\omega^5} \exp\left[-c_2\left(\frac{\omega_p}{\omega}\right)^4\right], \tag{3.3}$$

with three parameters c_1, c_2 and ω_p given by

$$\begin{aligned} c_1 &= 0.0081, \\ c_2 &= 0.74, \\ \omega_p &= \frac{g}{U_{19.5}}, \end{aligned} \tag{3.4}$$

where $U_{19.5}$ is the wind speed at a height of 19.5 m [rad/s].

Ochi-Hubble spectrum represents a bimodal sea-state, which is developed from swell waves (low-frequency dominant) and local wind-generated waves (high-frequency dominant) (see Figure 3.2c). The relevant spectral variance density is derived in [14].

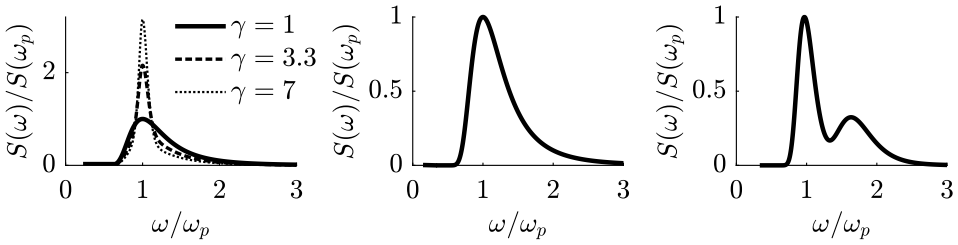

(a) JONSWAP spectrum. (b) Pierson-Moskowitz spectrum. (c) Ochi-Hubble spectrum.

Figure 3.2: The most commonly used wave spectra for testing wave energy converters [20].

The long-term sea state of a particular sea site is usually summarised by a scatter diagram (see Figure 3.3a), which shows the occurrence probability of a significant wave height and peak wave period. Furthermore, a polar plot called a wave rose diagram is collaborated with the scatter diagram to illustrate the directional distribution of the significant wave height (see Figure 3.3b). The scatter diagram and corresponding wave rose diagram provide essential information for wave farm resource assessment and annual mean power production estimations of WEC prototypes.

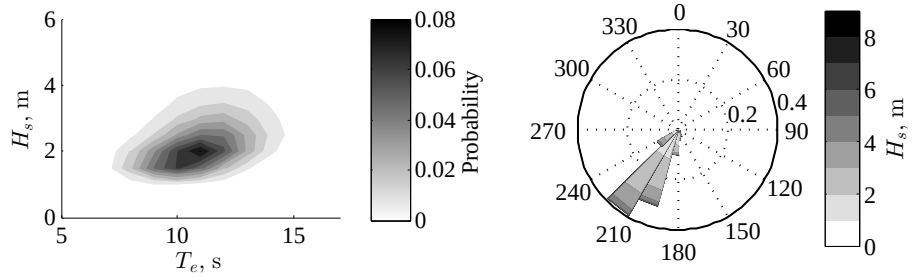

(a) Scatter diagram. (b) Wave rose of significant wave height.

Figure 3.3: An example of a scatter diagram and a wave rose diagram at a particular location [20].

In Chapter 5, the scatter diagrams characterised by the Pierson-Moskowitz spectrum have been employed to benchmark the performance of the SPAMD

with a generic single-tether point absorber.

3.2 Modes of body motion

In this thesis, body motion is defined in Cartesian coordinates, with the origin located at the centre of the gravity of the body, as shown in Figure 3.4. The translational modes (i.e. sway, surge, heave) are numbered from 1 to 3, and the rotational modes (i.e. roll, pitch, yaw) are 4 to 6.

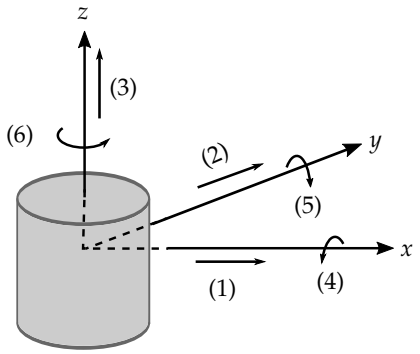

Figure 3.4: The motion modes of a rigid body with six degrees of freedom, adapted from [6].

Assuming the velocity vector of the centre of the geometry is $(\vec{U}, \vec{\Theta})$, where $\vec{U}$ is the translational component and $\vec{\Theta}$ is the rotational component. The velocity of any body surface element dS is given by

$$\vec{u} = \vec{U} + \vec{\Theta} \times \vec{s}. \tag{3.5}$$

where the vector $\vec{s}$ indicates the location of dS.

As the water particle can not penetrate the physical boundary of the buoy, the fluid velocity $\vec{v}$ should be equal to the velocity of the body surface element $\vec{u}$ in the direction of the surface normal $\vec{n}$. Therefore, the boundary condition on the surface of a moving body S_B is given by

$$v_n = \vec{n} \cdot \vec{u} = \vec{U} \cdot \vec{n} + \vec{\Theta} \cdot \vec{s} \times \vec{n} \quad \text{on } S_B. \tag{3.6}$$

Since $\vec{n} = (n_1, n_2, n_3)$ and $\vec{s} \times \vec{n} = (n_4, n_5, n_6)$, the boundary condition can be re-written as

$$v_n = \sum_{j=1}^{6} u_j n_j \quad \text{on } S_B, \tag{3.7}$$

where u_j is the velocity component in the jth mode.

3.3 Linear potential theory

Linear potential theory, which is also known as Airy wave theory, provides a linearised approximation of wave-body interaction. The theory assumes that the fluid is inviscid, incompressible and irrotational. The basic equations are derived from the conservation of mass (i.e., continuity condition) and conversation of momentum (i.e., Navier-Stokes equations) [6], given by

$$\nabla \cdot \vec{v} = 0, \tag{3.8}$$

$$\frac{\partial \vec{v}}{\partial t} + (\vec{v} \cdot \nabla)\vec{v} = -\frac{1}{\rho}\nabla p_{\text{tot}} + \nu \nabla^2 \vec{v} + \frac{1}{\rho}\vec{f}, \tag{3.9}$$

where ρ is the fluid density which is uniform throughout the fluid domain, $\vec{v} = \vec{v}(x, y, z, t)$ is the particle velocity, p_{tot} is the total pressure of the fluid, ν is the kinematic viscosity constant which is zero as the fluid is inviscid, and $\vec{f}$ is an external force per unit volume.

If gravitational force is the only external force, $\vec{f} = \rho\vec{g}$, Equations (3.8) and (3.9) become:

$$\frac{\partial \vec{v}}{\partial t} + \vec{v} \cdot \nabla \vec{v} = -\frac{1}{\rho}\nabla p_{\text{tot}} + \vec{g}. \tag{3.10}$$

As $\vec{v} \times (\nabla \times \vec{v}) = \frac{1}{2}\nabla \vec{v}^2 - \vec{v} \cdot \nabla \vec{v}$, Equation (3.10) can be simplified to

$$\frac{\partial}{\partial t}(\nabla \times \vec{v}) = \nabla \times [\vec{v} \times (\nabla \times \vec{v})]. \tag{3.11}$$

From Equation (3.11), it can be seen that the velocity vector $\vec{v}$ must satisfy $\nabla \times \vec{v} = 0$. As water particles are irrotational, the velocity can be written as a gradient of a scalar, which is denoted as velocity potential $\phi(x, y, z, t)$. Hence,

$$\nabla^2 \phi = 0. \tag{3.12}$$

The boundary conditions for solving the Laplace equation (3.12) consider the structure surface, the dynamic free water surface, the kinematic free water surface, and the sea bottom. The fluid domain is illustrated in Figure 3.5 for the two-dimensional scenario. The domain is described by the Cartesian coordinate system, where the z-axis points upwards and x-axis is along the mean water level. The air-water interface presented by the wave elevation $\eta(x, y, t)$.

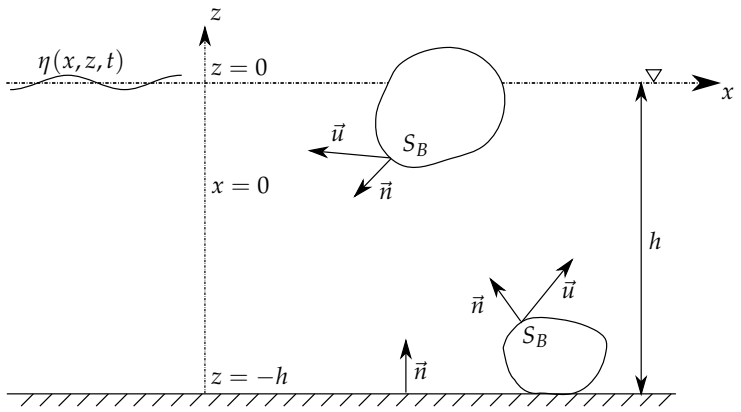

Figure 3.5: Fluid domain considered in linear potential theory, adapted from [6]. η is the incident wave elevation, $\vec{n}$ is the unit normal vector on a wetted body surface S and seabed, $\vec{u}$ is the velocity vector of an arbitrary point on S.

As derived in Equation (3.7), the boundary condition on the surface of a moving body is given by,

$$v_n = \frac{\partial \phi}{\partial n} = u_n = \sum_{j=1}^{6} u_j n_j. \quad \text{on } S_B. \tag{3.13}$$

For the sea bottom which can be considered as a fixed structure, the vertical component of the water particle velocity is zero at the surface of the sea bottom, $u_n = 0$. The boundary condition on the sea bottom is

$$\left[\frac{\partial \phi}{\partial z}\right]_{z=-h} = 0. \tag{3.14}$$

If only the gravitational force is considered, the boundary condition on the dynamic free water surface is derived from the Bernoulli equation,

$$g\eta + \left[\frac{\partial \phi}{\partial t} + \frac{1}{2}\nabla\phi \cdot \nabla\phi\right]_{z=\eta} = 0. \tag{3.15}$$

Assuming that the water particle on the surface follows the wave motion, the kinematic boundary condition on the air-water interface is derived as,

$$\left[\frac{\partial \phi}{\partial z}\right]_{z=0} = \frac{\partial \eta}{\partial t} + \frac{\partial \phi}{\partial x}\frac{\partial \eta}{\partial x}. \tag{3.16}$$

As it is assumed that the wave amplitude is relatively small in comparison with the wavelength, Equations (3.15) and (3.16) can be linearised by neglecting the higher-order differential terms, given by,

$$g\eta + \frac{\partial \phi}{\partial t} = 0, \tag{3.17}$$

$$\left[\frac{\partial \phi}{\partial z}\right]_{z=0} = \frac{\partial \eta}{\partial t}, \tag{3.18}$$

which gives the general free surface boundary condition,

$$\left[\frac{\partial^2 \phi}{\partial t^2} + g\frac{\partial \phi}{\partial z}\right]_{z=0} = 0. \tag{3.19}$$

As the water wavetrain can be approximated as a sinusoidal function if the water depth is sufficiently large and wave amplitude is small, the corresponding velocity potential satisfying all aforementioned boundary conditions can be decoupled into spatial and temporal parts [7], given by

$$\phi = \phi(x, y, z, t) = \Re\{\hat{\phi}(x, y, z)e^{i\omega t}\}, \tag{3.20}$$

where $\hat{\phi}(x, y, z)$ is the complex amplitude of the velocity potential and ω is the wave frequency.

Therefore, the Laplace equation can be re-written as

$$\nabla^2 \hat{\phi} = 0 \tag{3.21}$$

The boundary condition on the body surface becomes

$$\frac{\partial \hat{\phi}}{\partial n} = \hat{u}_n, \tag{3.22}$$

on the sea bottom surface,

$$\left[\frac{\partial \hat{\phi}}{\partial z}\right]_{z=-h} = 0, \tag{3.23}$$

and on the free water surface,

$$\left[-\omega^2 \hat{\phi} + g\frac{\partial \hat{\phi}}{\partial z}\right]_{z=0} = 0. \tag{3.24}$$

Once the complex velocity potential $\hat{\phi}(x, y, z)$ is determined, other physical variables such as particle velocity $\hat{v}$, dynamic pressure $\hat{p}$ and wave elevation $\hat{\eta}$ can be easily derived as [6],

$$\hat{v} = \nabla \hat{\phi} \tag{3.25}$$

$$\hat{p} = -i\omega\rho\hat{\phi} \tag{3.26}$$

$$\hat{\eta} = -\frac{i\omega}{g}[\hat{\phi}]_{z=0} \tag{3.27}$$

According to the linear superposition principle, the velocity potential can be separated into the scattered velocity potential $\hat{\phi}_s$ and radiated velocity potential $\hat{\phi}_r$,

$$\hat{\phi} = \hat{\phi}_s + \hat{\phi}_r. \tag{3.28}$$

Scattering problem

The scattered potential $\hat{\phi}_s$ can be further separated into incident velocity potential $\hat{\phi}_0$ and diffracted velocity potential $\hat{\phi}_d$,

$$\hat{\phi}_s = \hat{\phi}_0 + \hat{\phi}_d. \tag{3.29}$$

The solution for the scattering problem must satisfy an additional boundary condition on the body surface,

$$-\frac{\partial \hat{\phi}_d}{\partial n} = \frac{\partial \hat{\phi}_0}{\partial n} \quad \text{on } S_B. \tag{3.30}$$

To ensure the solution represents the diffracted waves propagating away from the body, the radiation condition must be satisfied [12], given by

$$\lim_{kx \to \pm\infty} \left(\frac{\partial \hat{\phi}_d}{\partial x} \mp ik\hat{\phi}_d\right) = 0 \tag{3.31}$$

The resulting excitation force in the jth mode is given by

$$\hat{F}_{exe,j} = i\omega\rho \iint_{S_B} (\hat{\phi}_0 + \hat{\phi}_d) n_j dS. \tag{3.32}$$

Noting that when the wavelength is five times greater than the width of the body, the diffracted velocity potential can be neglected and the excitation force converges to the Froude-Krylov force.

Radiation problem

According to the superposition principle, the radiated velocity potential is equal to the sum of the radiated potentials induced by each mode of oscillation [6],

$$\hat{\phi}_{rad} = \sum_{j=1}^{6} \hat{\varphi}_j \hat{u}_j \quad \text{on } S_B, \tag{3.33}$$

where $\varphi_j = \varphi_j(x, y, z)$ is the coefficient of proportionality for the unit velocity in mode j. The coefficient φ_j is defined as

$$\frac{\partial \varphi_j}{\partial n} = n_j \quad \text{on } S_B. \tag{3.34}$$

The term φ_j also satisfies the Laplace equation in the fluid domain and the boundary condition on the body surface, seabed surface and free water surface. Furthermore, to ensure the solution represents the radiated waves propagating away from the body, the aforementioned radiation condition must be satisfied.

The resulting radiation force acting on the body in the j'th mode is given by

$$\hat{F}_{rad,j'} = i\omega\rho \iint_{S_B} \varphi_j \hat{u}_j n_{j'} dS. \tag{3.35}$$

Since $\hat{u}_j$ is independent of the body surface S_B, the radiation force can be written as,

$$\hat{F}_{rad,j'} = -Z_{j'j}\hat{u}_j, \tag{3.36}$$

where $Z_{j'j}$ is the $j'j$ element of the radiation impedance matrix $\hat{\mathbf{Z}}(\omega)$, given by,

$$Z_{j'j} = -\omega\rho \iint_{S_B} \varphi_j n_{j'} dS \tag{3.37}$$

The radiation impedance element $Z_{j'j}$ can be decomposed into real and imaginary parts,

$$Z_{j'j} = R_{j'j} + i\omega m_{j'j}, \tag{3.38}$$

where $R_{j'j}$ is the $j'j$ element of hydrodynamic radiation resistance matrix $\hat{\mathbf{R}}(\omega)$, and $m_{j'j}$ is the $j'j$ element of hydrodynamic added mass matrix $\mathbf{m}(\omega)$.

The derived Laplace equation in the fluid domain, together with the corresponding boundary conditions can be solved analytically and numerically. For the simple geometries whose edges can be perfectly represented by a Cartesian or cylindrical coordinate system, the velocity potential can be expressed as a sum of infinite eigenfunctions [12]. Otherwise, the solution is approximated as the result of several singularities (multipoles) placed in the computational domain. For complex geometries, the velocity potential is usually solved numerically by using boundary element methods (BEM). The relevant toolboxes, such as ANSYS AQWA [1], NEMOH [2] and WAMIT [11], mainly utilise the Green's Theorem that treats the velocity potential on the surface of the structure as the result of the disturbance of sources in the fluid domain.

3.4 Reynolds-averaged Navier-Stokes equations

The Reynolds-averaged Navier-Stokes equations (RANS), which are derived from the instantaneous Navier-Stokes equations by using Reynolds decomposition, are generally used to describe the time-averaged motion of turbulent flows. Assuming that the velocity of an incompressible control volume situated in the fluid domain is $(u, v, w) = (u(x, y, z, t), v(x, y, z, t), w(x, y, z, t))$ with respect to the Cartesian coordinate, the instantaneous Navier-Stokes equations in the x-direction is given by [4]

$$\rho\left[\frac{\partial u}{\partial t}+\frac{\partial}{\partial x}(u^2)+\frac{\partial}{\partial y}(uv)+\frac{\partial}{\partial z}(uw)\right]=-\frac{\partial p}{\partial x}+\mu\left[\frac{\partial^2 u}{\partial x^2}+\frac{\partial^2 u}{\partial y^2}+\frac{\partial^2 u}{\partial z^2}\right], \tag{3.39}$$

in the y-direction

$$\rho\left[\frac{\partial v}{\partial t}+\frac{\partial}{\partial x}(uv)+\frac{\partial}{\partial y}(v^2)+\frac{\partial}{\partial z}(vw)\right]=-\frac{\partial p}{\partial y}+\mu\left[\frac{\partial^2 v}{\partial x^2}+\frac{\partial^2 v}{\partial y^2}+\frac{\partial^2 v}{\partial z^2}\right], \tag{3.40}$$

and in the z-direction

$$\rho\left[\frac{\partial w}{\partial t}+\frac{\partial}{\partial x}(uw)+\frac{\partial}{\partial y}(vw)+\frac{\partial}{\partial z}(w^2)\right]=-\frac{\partial p}{\partial z}+\mu\left[\frac{\partial^2 w}{\partial x^2}+\frac{\partial^2 w}{\partial y^2}+\frac{\partial^2 w}{\partial z^2}\right]-\rho g, \tag{3.41}$$

where μ is the fluid dynamic viscosity.

Assuming that the turbulent velocity can be split into a time-averaged velocity and a fluctuating velocity via Reynolds decomposition, then, for example, the velocity in x-direction can be presented as

$$u(x, y, z, t) = \bar{u}(x, y, z) + u'(x, y, z, t), \tag{3.42}$$

where $\bar{u}$ is the time-averaged component and u' is the fluctuating component.

As a result, the differential terms on the left-hand side of the Equation (3.39) can be expressed as

$$\begin{aligned}
\frac{\partial u}{\partial t} &= \frac{\partial \bar{u}}{\partial t}+\frac{\partial u'}{\partial t}=\frac{\partial u'}{\partial t},\\
\frac{\partial}{\partial x}(u^2) &= \frac{\partial}{\partial x}(\bar{u}+u')^2=\frac{\partial}{\partial x}(\bar{u}^2+2\bar{u}u'+u'^2),\\
\frac{\partial}{\partial x}(uv) &= \frac{\partial}{\partial x}(\bar{u}+u')(\bar{v}+v')=\frac{\partial}{\partial x}(\bar{u}^2+\bar{u}v'+\bar{v}u'+v'^2),\\
\frac{\partial}{\partial x}(uw) &= \frac{\partial}{\partial x}(\bar{u}+u')(\bar{w}+w')=\frac{\partial}{\partial x}(\bar{u}^2+\bar{u}w'+\bar{w}u'+w'^2).
\end{aligned} \tag{3.43}$$

The unsteady forms of the Navier-Stokes equations should be time-averaged to derive the RANS equations. As the time-averaged fluctuating

velocities are zero, so are the cross-products in Equation (3.43), as illustrated in Figure 3.6. Therefore, the resulting time-averaged Equation (3.43) is derived as

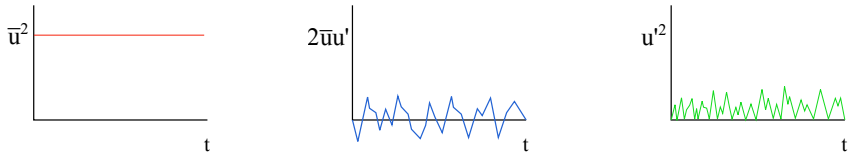

(a) Square of time-averaged velocity. (b) Cross product of velocity. (c) Square of fluctuating velocity.

Figure 3.6: Illustration of the receptive terms in Equation (3.43), adapted from [4].

$$
\begin{aligned}
\overline{\frac{\partial u}{\partial t}} &= \overline{\frac{\partial \bar{u}}{\partial t} + \frac{\partial u'}{\partial t}} = \overline{\frac{\partial u'}{\partial t}} = 0, \\
\overline{\frac{\partial}{\partial x}(u^2)} &= \overline{\frac{\partial}{\partial x}(\bar{u}^2 + 2\bar{u}u' + u'^2)} = \frac{\partial}{\partial x}(\bar{u}^2 + \bar{u'}^2), \\
\overline{\frac{\partial}{\partial x}(uv)} &= \overline{\frac{\partial}{\partial x}\left[(\bar{u}^2 + \bar{u}v' + \bar{v}u' + u'^2)\right]} = \frac{\partial}{\partial x}(\bar{u}\bar{v} + \bar{u'}\bar{v'}), \\
\overline{\frac{\partial}{\partial x}(uw)} &= \overline{\frac{\partial}{\partial x}\left[(\bar{u}^2 + \bar{u}w' + \bar{v}w' + w'^2)\right]} = \frac{\partial}{\partial x}(\bar{u}\bar{w} + \bar{u'}\bar{w'}).
\end{aligned}
\tag{3.44}
$$

By applying the Reynolds decomposition and time averaging, the right-hand side of Equation (3.39) can be presented as:

$$
-\frac{\partial \bar{p}}{\partial x} + \mu\left[\frac{\partial^2 \bar{u}}{\partial x^2} + \frac{\partial^2 \bar{u}}{\partial y^2} + \frac{\partial^2 \bar{u}}{\partial z^2}\right]. \tag{3.45}
$$

Thus, the RANS equation can be assembled from Equations (3.44) and (3.45), given by

$$
\begin{aligned}
&\rho\left[\frac{\partial}{\partial x}(\bar{u}^2) + \frac{\partial}{\partial y}(\bar{u}\bar{v}) + \frac{\partial}{\partial z}(\bar{u}\bar{w})\right] \\
&\quad = -\frac{\partial \bar{p}}{\partial x} + \left[\frac{\partial}{\partial x}(\mu\frac{\partial \bar{u}}{\partial x} - \rho\bar{u'}^2) + \frac{\partial \bar{u}}{\partial y}(\mu\frac{\partial \bar{u}}{\partial y} - \rho\bar{u'}\bar{v}) + \frac{\partial u}{\partial z}(\mu\frac{\partial \bar{u}}{\partial z} - \rho\bar{u'}\bar{w'})\right],
\end{aligned}
\tag{3.46}
$$

where $\mu\frac{\partial \bar{u}}{\partial x}$, $\mu\frac{\partial \bar{u}}{\partial y}$ and $\mu\frac{\partial \bar{u}}{\partial z}$ represent the viscous normal stresses in a laminar flow, while $-\rho\bar{u'}^2$, $-\rho\bar{u'}\bar{v}$ and $-\rho\bar{u'}\bar{w}$ are designated as the Reynolds stresses

which specify the normal stresses due to the turbulence. Assuming that turbulence is isotropic, the Reynolds stresses can be re-defined as

$$\begin{aligned}\rho\overline{u'}^2 &= \mu_t\frac{\partial\bar{u}}{\partial x} = \tau'_{xx},\\ \rho\overline{u'}^2 &= \mu_t\frac{\partial\bar{u}}{\partial x} = \tau'_{xy},\\ \rho\overline{u'}^2 &= \mu_t\frac{\partial\bar{u}}{\partial x} = \tau'_{xz},\end{aligned} \tag{3.47}$$

where μ_t is referred to as the turbulent viscosity. However, μ_t actually represents the features of turbulent momentum rather than viscosity. It should be noted that the definition in Equation (3.47) is only valid for the locations far away from walls. For near wall scenarios, turbulence models such as the $k-\omega$ turbulence model [22] and the $k-\epsilon$ turbulence model [9] are usually employed as the closures for RANS equations.

A more general RANS equation is formulated with the effective viscosity $\mu_{eff} = \mu + \mu_t$, given by

$$\begin{aligned}&\rho\left[\frac{\partial}{\partial x}(\bar{u}^2) + \frac{\partial}{\partial y}(\bar{u}\bar{v}) + \frac{\partial}{\partial z}(\bar{u}\bar{w})\right]\\ &\quad= -\frac{\partial\bar{p}}{\partial x} + \left[\frac{\partial}{\partial x}\left[(\mu+\mu_t)\frac{\partial\bar{u}}{\partial x}\right] + \frac{\partial}{\partial x}\left[(\mu+\mu_t)\frac{\partial\bar{u}}{\partial y}\right] + \frac{\partial}{\partial x}\left[(\mu+\mu_t)\frac{\partial\bar{u}}{\partial z}\right]\right].\end{aligned} \tag{3.48}$$

In Chapter 6, a numerical wave tank (NWT) based on Equation (3.48) is developed by using the computational fluid dynamic toolbox OpenFOAM, to determine the dominant nonlinear hydrodynamic effect that degrades the performance of the SPAMD.

3.5 WEC modelling approaches

The equation of motion of a wave energy converter is derived from Newton's second law. The total external hydrodynamic force, which is the integral of the hydrodynamic pressure over the surface of the body, is the key quantity to be calculated. For the WEC models developed from the RANS equation, the total hydrodynamic force can be solved only by discretising the RANS equation (i.e. Equation (3.48)) in both the time-domain and the spatial-domain, which results in considerable computational complexity. In contrast, the WEC models based on linear potential theory allow the total hydrodynamics to be decomposed into excitation, radiation, buoyancy and viscous forces, which

significantly simplifies the calculation. In this section, only the modelling approaches based on linear potential theory are introduced.

The equation of motion in the time-domain for a wave energy converter with six degrees of freedom, can be written as

$$\mathbf{M}\frac{\partial^2}{\partial t^2}\mathbf{x}(t) = \mathbf{F}_{exe}(t) + \mathbf{F}_{rad}(t) + \mathbf{F}_{buoy}(t) + \mathbf{F}_{vis}(t) + \mathbf{F}_{pto}(t), \tag{3.49}$$

where $\mathbf{M}$ is the 6×6 mass matrix of the buoy, $\mathbf{x}$ is the 6×1 vector describing the displacement of the device, $\mathbf{F}_{exe}$, $\mathbf{F}_{rad}$, $\mathbf{F}_{buoy}$, $\mathbf{F}_{vis}$, $\mathbf{F}_{pto}$ are the 6×1 hydrodynamic excitation, hydrodynamic radiation, net buoyancy, viscous drag and PTO forces respectively.

The corresponding frequency-domain equation of motion is given by,

$$-\mathbf{M}\omega^2\hat{\mathbf{x}}(\omega) = \hat{\mathbf{F}}_{exe}(\omega) + \hat{\mathbf{F}}_{rad}(\omega) + \hat{\mathbf{F}}_{buoy}(\omega) + \hat{\mathbf{F}}_{vis}(\omega) + \hat{\mathbf{F}}_{pto}(\omega). \tag{3.50}$$

Excitation force

As the excitation force is the result of the interaction between the incident wave and the fixed structure, the wave elevation can be treated as the input to the identification of excitation force. The reference position (x_0, y_0), where the excitation force acting on the body is calculated, is usually the projection of the centre of the geometry on the water surface. The complex excitation force vector $\hat{\mathbf{F}}_{exe}(\omega)$ is given by [6]

$$\hat{\mathbf{F}}_{exe}(\omega) = \hat{\mathbf{f}}_{exe}(\omega)\hat{\eta}(x_0, y_0, \omega), \tag{3.51}$$

where $\hat{\mathbf{f}}_{exe}(\omega)$ is the complex excitation coefficient vector that represents the excitation force for a unit incident wave elevation, and $\hat{\eta}(x_0, y_0, \omega)$ is the wave elevation measured at the reference position.

The corresponding equation in time-domain is formulated as a convolution:

$$\mathbf{F}_{exe}(t) = \mathbf{f}_{exe}(t) * \eta(x_0, y_0, t) = \int_{-\infty}^{\infty} \mathbf{f}_{exe}(t)\eta(x_0, y_0, t-\tau)d\tau, \tag{3.52}$$

where $\mathbf{f}_{exe}(t)$ is the inverse Fourier transform of $\hat{\mathbf{f}}_{exe}(\omega)$, acting as the excitation impulse in the convolution. In Equation (3.52), the calculation of excitation force $\mathbf{F}_{exe}(t)$ requires the future information of the wave elevation in the time domain. This is because the excitation impulse $\mathbf{f}_{exe}(t)$ is non-zero for $t \leq 0$, which means it is non-causal in the time series. Future information can be obtained by measuring the upstream wave elevation [5], which modifies Equation (3.52) into

$$\mathbf{F}_{exe}(t) = \int_{-\infty}^{\infty} \mathbf{f}_{exe}(t)\eta(x_0 - L_m, y_0, t-\tau)e^{-ikL_m}d\tau, \tag{3.53}$$

where L_m is the distance from (x_0, y_0) to the upstream measurement point.

Radiation force

The frequency-domain radiation force due to the oscillation in six degrees of freedom is given by [6]:

$$\hat{\mathbf{F}}_{rad}(\omega) = -\mathbf{Z}(\omega)\hat{\dot{\mathbf{x}}}(\omega) = \hat{\mathbf{F}}'_{rad}(\omega) - i\omega\mathbf{m}(\infty)\hat{\dot{\mathbf{x}}}(\omega), \tag{3.54}$$

where $\mathbf{m}(\infty) = \lim_{\omega\to\infty} \mathbf{m}(\omega)$ and the $\hat{\mathbf{F}}'_{rad}(\omega)$ represents the memory effect of hydrodynamic radiation, given by

$$\hat{\mathbf{F}}'_{rad}(\omega) = -\mathbf{K}(\omega)\hat{\dot{\mathbf{x}}}(\omega), \tag{3.55}$$

where $\mathbf{K}(\omega)$ is the transfer function between the memory effect and the body's velocity.

The radiation force in the time-domain is formulated as

$$\mathbf{F}_{rad}(t) = \mathbf{F}'_{rad}(t) - \mathbf{m}(\infty)\ddot{\mathbf{x}}(t) \tag{3.56}$$

$$= \int_0^t \mathbf{k}(t-\tau)\dot{\mathbf{x}}(\tau)d\tau - \mathbf{m}(\infty)\ddot{\mathbf{x}}(t), \tag{3.57}$$

where the inverse Fourier transform $\mathbf{k}(t) = \mathfrak{F}^{-1}\{K(\omega)\}$. The convolution term in Equation (3.57) can be approximated in state-space form to facilitate the calculation [17]. In Chapter 4, the time-domain radiation problem of a single-tether WEC is solved by using the Matlab toolbox MSS-FDI [17], which is able to adjust the order of the state-space model automatically to guarantee the fitting accuracy.

Viscous forces

The kinetic energy of the oscillating body is not only dissipated due to the hydrodynamic radiation damping effect but also the viscous effects of the fluid flow. Therefore, it is recommended to account for the viscous force in the conventional time-domain equation of motion [16]. The viscous forces in mode j due to the relative motion between the buoy and the fluid flow, can be modelled by the drag term of the Morison equation for the moving body in an oscillating flow [13], given by

$$F_{vis,j}(t) = -\frac{1}{2}\rho C_{d,j} A'_j(\dot{x}_j(t) - v_j(t))|\dot{x}_j(t) - v_j(t)|, \tag{3.58}$$

where $u_j(t) - v_j(t)$ is the relative velocity between the body and the fluid flow, A'_j is the cross section area of the buoy perpendicular to the flow, and $C_{d,j}$ is the viscous drag coefficient which is a function of the geometry of the buoy, its orientation, surface roughness, fluid properties and flow regime. The coefficient $C_{d,j}$ of a full scale WEC is generally determined by free-decay tests in NWT for a given scenario, such as the studies by Bhinder et al. [3] and Rafiee and Fievez [19].

As Equation (3.58) is a quadratic function of relative velocity, it should be linearised to fit the frequency-domain equation of motion. In Chapter 4, an iterative method is employed to determine the frequency-domain viscous drag force acting on the SPAMD over the wave frequency of interest.

Net buoyancy force

For fully submerged devices, the net buoyancy force is constant and can be formulated as

$$F_{buoy}(t) = \rho V g - mg, \tag{3.59}$$

where V is the volume of the submerged body and m is the mass.

For floating devices, it is assumed that the weight of the buoy is initially balanced. Therefore, the net buoyancy force due to the heave displacement is equal to the additional weight of displaced water, given by

$$F_{buoy}(t) = -\rho g A'_3 x_3(t), \tag{3.60}$$

where A'_3 is the cross section area on the water plane, and $x_3(t)$ is the heave displacement. This equation is only valid when the buoy oscillates in small amplitudes or has a constant cross section area A'_3. The term $-\rho g A'_3$ is denoted as the hydrostatic stiffness.

3.6 Concluding remarks

This chapter briefly introduces the widely used modelling approaches for wave-structure interaction in terms of computational complexity, model fidelity and applications. It can be concluded that the frequency and time-domain models developed from linear potential theory may be used for power production assessment, design optimization and real-time model-based control. While for device response simulation in extreme sea states, only CFD models based on the Navier-Stokes equation are capable of capturing the highly nonlinear wave-structure interactions.

References

[1] ANSYS Inc. (2015). *AQWA Theory Manual, Release 16.0*.

[2] Babarit, A. and Delhommeau, G. (2015). "Theoretical and numerical aspects of the open source BEM solver NEMOH". In: *Proceedings of the 11th European Wave and Tidal Energy Conference*. Nantes, France.

[3] Bhinder, M. A., Babarit, A., Gentaz, L. and Ferrant, P. (2015). "Potential time domain model with viscous correction and CFD analysis of a generic surging floating wave energy converter". In: *International Journal of Marine Energy* 10, pp. 70–96.

[4] Eph, S., Charlie, B., Srikar, C., Reid, L. et al. (2019). *The RANS Equations The Basis of Turbulence Modeling*. Accessed on 29 November 2018. URL: `http://www.me.umn.edu/courses/me5341/handouts/essay%201.pdf`.

[5] Falnes, J. (1995). "On non-causal impulse response functions related to propagating water waves". In: *Applied Ocean Research* 17.6, pp. 379–389.

[6] Falnes, J. (2002). *Ocean waves and oscillating systems: Linear interactions including wave energy extraction*. Cambridge University Press.

[7] Folley, M. (2017). "The wave energy resource". In: *Handbook of ocean wave energy*. Ed. by A. Pecher and J. P. Kofoed. Cham: Springer International Publishing, pp. 43–79.

[8] Hasselmann, K., Barnett, T., Bouws, E., Carlson, H., Cartwright, D., Enke, K., Ewing, J., Gienapp, H., Hasselmann, D., Kruseman, P. et al. (1973). "Measurements of wind-wave growth and swell decay during the Joint North Sea Wave Project (JONSWAP)". In: *Ergänzungsheft*, pp. 8–12.

[9] Launder, B. E. and Spalding, D. B. (1983). "The numerical computation of turbulent flows". In: *Numerical Prediction of Flow, Heat Transfer, Turbulence and Combustion*. Elsevier, pp. 96–116.

[10] Le Méhauté, B. (1976). *An introduction to hydrodynamics and water waves*. New York: Springer.

[11] Lee, C.-H. (1995). *WAMIT Theory Manual*.

[12] Linton, C. M. and McIver, P. (2001). *Handbook of mathematical techniques for wave/structure interactions*. CRC Press.

[13] Morison, J., Johnson, J. and Schaaf, S. (1950). "The force exerted by surface waves on piles". In: *Journal of Petroleum Technology* 2.05, pp. 149–154.

[14] Ochi, M. and Hubble, N. (1977). "Six-parameter wave spectra". In: *Coastal Engineering 1976*, pp. 301–328.

[15] Pecher, A. and Kofoed, J. P. (2017). *Handbook of ocean wave energy*. Springer.

[16] Penalba, M., Giorgi, G. and Ringwood, J. V. (2017). "Mathematical modelling of wave energy converters: A review of nonlinear approaches". In: *Renewable and Sustainable Energy Reviews* 78, pp. 1188–1207.

[17] Perez, T. and Fossen, T. I. (2009). "A Matlab toolbox for parametric identification of radiation-force models of ships and offshore structures". In: *Modeling, Identification and Control* 30.1, pp. 1–15.

[18] Pierson, W. and Moskowitz, L. (1964). "A proposed spectral form for fully developed wind seas based on the similarity theory of SA Kitaigorodskii". In: *Journal of geophysical research* 69.24, pp. 5181–5190.

[19] Rafiee, A. and Fiévez, J. (2015). "Numerical prediction of extreme loads on the CETO wave energy converter". In: *11th European Wave and Tidal Energy Conference*. Nantes, France.

[20] Sergiienko, N. "Three-tether wave energy converter: Hydrodynamic modelling, performance assessment and control". Ph.D. thesis. University of Adelaide.

[21] The Specialist Committee on Waves (2002). "Final report and recommendations to the 23rd ITTC". In: *Proceedings of the 23rd International Towing Tank Conference*. Vol. II, pp. 505–736.

[22] Wilcox, D. (2008). "Formulation of the kw turbulence model revisited". In: *AIAA journal* 46.11, pp. 2823–2838.

Chapter 4

Modal analysis of a submerged spherical point absorber with asymmetric mass distribution

The aim of this thesis is to investigate a low-cost solution to improve the efficiency of a submerged single-tether point absorber. As discussed in Section 2, multi-mode WECs are able to absorb more energy than the single-mode ones. However, multi-mode WECs also require multiple PTO units to collect the energy arising from the multi-mode motions, which leads to an increase in the total cost of the system. Therefore, this chapter proposes a new design of submerged single-tether point absorber that utilises motion coupling to efficiently absorb the wave energy arising from its heave, surge and pitch motion. Modal analysis was conducted to answer the following research questions: *1. What are the tuning parameters that affect the performance of the proposed design? 2. What are the operation regimes of the proposed design over the wave frequencies of interest?*

This chapter consists of the following published journal article:
Meng, F., Ding, B., Cazzolato, B. S. and Arjomandi, M. (2019). "Modal analysis of a submerged spherical point absorber with asymmetric mass distribution". ***Renewable Energy*** **93, pp. 223 - 237.**

The article in its published format is available at `https://doi.org/10.1016/j.renene.2018.06.014`.

Statement of Authorship

Title of Paper	Modal analysis of a submerged spherical point absorber with asymmetric mass distribution
Publication Status	☑ Published ☐ Accepted for Publication ☐ Submitted for Publication ☐ Unpublished and Unsubmitted work written in manuscript style
Publication Details	Meng, F., Ding, B., Cazzolato, B. S. and Arjomandi, M. (2019). "Modal analysis of a submerged spherical point absorber with asymmetric mass distribution". *Renewable Energy* 93, pp. 223 – 237.

Principal Author

Name of Principal Author (Candidate)	Fantai Meng
Contribution to the Paper	Developed the idea and concepts, developed the mathematical model, wrote the code of simulations and optimisations, interpreted the results, wrote the manuscript and acted as a corresponding author.
Overall percentage (%)	75%
Certification:	This paper reports on original research I conducted during the period of my Higher Degree by Research candidature and is not subject to any obligations or contractual agreements with a third party that would constrain its inclusion in this thesis. I am the primary author of this paper.
Signature	Date: 21/8/19

Co-Author Contributions

By signing the Statement of Authorship, each author certifies that:

i. the candidate's stated contribution to the publication is accurate (as detailed above);

ii. permission is granted for the candidate in include the publication in the thesis; and

iii. the sum of all co-author contributions is equal to 100% less the candidate's stated contribution.

Name of Co-Author	Boyin Ding
Contribution to the Paper	Encouraged to perform the power analysis of the mechanism, participated in developing ideas and concepts, supervised the work, helped in interpretation of obtained results, and provided a critical revision of the manuscript.
Signature	Date: 21/8/19

Name of Co-Author	Benjamin S. Cazzolato
Contribution to the Paper	Encouraged to perform the modal analysis of the mechanism, participated in developing ideas and concepts, supervised the work, helped in interpretation of obtained results, and provided a critical revision of the manuscript.
Signature	Date: 21/8/19

Name of Co-Author	Maziar Arjomandi		
Contribution to the Paper	Supervised the work and provided a critical revision of the manuscript.		
Signature		Date	21/08/2019

Please cut and paste additional co-author panels here as required.

Modal analysis of a submerged spherical point absorber with asymmetric mass distribution

F. Meng, B. Ding, B. S. Cazzolato, M. Arjomandi

Abstract

Of all the wave energy converter (WEC) categories, the single-tether point absorber (PA) is one of the most widely used in the ocean renewable energy industry. In most published research, only the heave motion of the buoy is considered in the motion equation for the analysis. This is because the heave motion of the buoy strongly couples to the power take-off device (PTO), whereas the surge and pitch motions barely couple to the PTO. As a result, only the power arising from heave motion of the buoy can be efficiently absorbed when a single-tether PTO is used, leading to deficiency of the design in absorbing the power arising from its surge and pitch motion. In this paper, the deficiencies of single-tether PAs are addressed by simply shifting the center of gravity of the buoy away from its geometric centre. A spherical buoy with asymmetric mass is used in this paper for its simplicity. The asymmetric mass distribution of the buoy causes motion coupling across surge, heave and pitch motions, which enables strong coupling between the buoy's surge motion and the PTO movement. The operation principle and power generation of the spherical point absorber with asymmetric mass distribution (SPAMD) are investigated via a modal analysis conducted on a validated frequency-domain model. The results show that the SPAMD can be up to three times more efficient than the generic PAs when subjected to regular waves in the frequency range from 0.34 to 1.4 rad/s.

4.1 Introduction

Since the Oil Crisis of the 1970s, ocean wave energy has been regarded as a potential source of renewable power. Compared with solar and wind, the power carried by ocean waves is more continuous and predictable. However, it is difficult to extract the energy from the reciprocating ocean wave motion efficiently by using conventional electricity generators. Consequently, commercial-scale wave energy conversion still does not exist.

The single-tether point absorber (PA) is one wave energy converter (WEC) that has commercial potential and has received significant attention from the

research community. In most published work, single-tether PAs are typically modelled as single degree-of-freedom (DOF) heaving devices, even though in reality the devices move in multiple DOFs (e.g. surge, heave and pitch). This is because, for single-tether PAs, the heave motion of the buoy strongly couples to the power take-off device (PTO) and therefore this motion can be fully converted to the PTO extension. In contrast, the surge and pitch motions barely couple to the PTO and only a tiny fraction of these motions are converted to useful energy. Figure 4.1 illustrates the contribution of the PTO extension from pure heave and surge motions respectively for a single-tether PA. It is clear that the heave displacement of the buoy results in an equivalent PTO extension, whereas the surge displacement leads to negligible PTO extension. Therefore, for single-tether PAs, only the heave motion can result in effective power absorption.

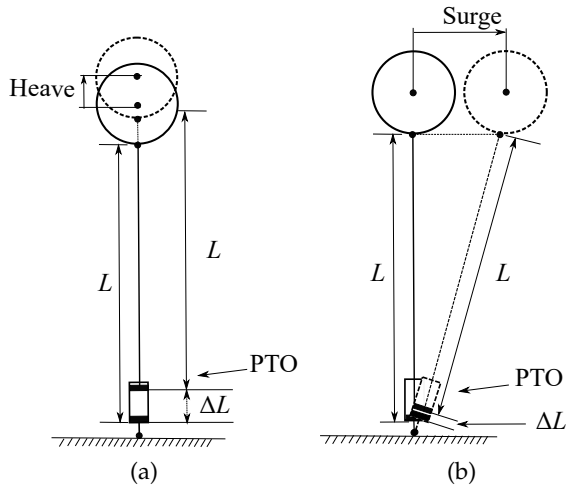

Figure 4.1: Comparison of the PTO extension caused by the heave and surge motions of the buoy: (a) the heave displacement is fully converted to the PTO extension; (b) only a tiny fraction of the surge displacement is converted to the PTO extension. L is the nominal tether length when the buoy is at equilibrium, ΔL is the tether length change.

Considering the theoretical capture width of a 3DOF (i.e., surge, heave and pitch) PA can be three times greater than a heave-only PA [4], several conceptual designs have been proposed to maximize the absorption efficiency of the PA by harvesting the energy arising from its surge and pitch motions. One typical solution is to attach multiple PTO tethers to the buoy, which couple to the orthogonal degrees of freedom. It has been shown that a three-cable PTO [15] is capable of absorbing three times more power than a

single-tether heaving PA over a broad frequency range [13], at the expense of increased captial cost from two additional PTOs and mooring points. A similar solution is to use two decoupled PTOs in alignment with the heave and pitch directions to capture more wave energy [10]. The theoretical capture width of this approach is equivalent to that of the PA with a three-cable PTO. However, the PA with two decoupled PTOs is sensitive to wave direction, since the PTO must be aligned to the incoming wavefront.

In this paper, a more effective solution that allows a single-tether PA to harvest energy arising from surge motion of a submerged spherical buoy is proposed. The approach is based on simply offsetting the mass from the centre of the buoy, such that when the buoy is excited in surge, heave motion is also enhanced. A submerged 3DOF (i.e., surge, heave and pitch) PA is employed because it can more efficiently use the surge motion to capture wave energy than an equivalent floating device [14]. It should be noted that although there are some prototypes (e.g. Salter's Duck [5] and the parametric pendulum based wave energy converter [16]) which use an asymmetric mass buoy to harvest wave energy, this is the first study which utilises the motion coupling caused by the asymmetric mass distribution to address the poor PTO coupling of a single-tether PA in surge motion. In Section 4.2, the system of spherical point absorber with asymmetric mass distribution (SPAMD) is described, with the settings of operating environment, the asymmetric mass buoy and the PTO clarified. In Section 4.3, the static stability condition of the SPAMD is investigated. Furthermore, the equations of motion are derived in the frequency domain for the subsequent modal analysis. In Section 4.4, the methodology for analysing the oscillation modes and assessing the power output of the SPAMD are presented. In Section 4.5, a modal analysis is presented, with the aim of understanding the operation principles of the SPAMD and evaluating its power generation capability. The paper is concluded in Section 4.6.

4.2 System description

For simplicity, a submerged spherical asymmetric mass buoy with a positive buoyancy is considered in this work. The buoy is tethered by a linear spring-damper PTO to be immersed below the free water surface. The PTO is anchored to the sea bottom via a ball-joint which allows the PTO to align with the mooring tether under tension when the buoy is excited by incident waves. The tether is assumed to be non-elastic and massless. The incident waves are set to be linear monochromatic waves aligned with the vertical XZ-plane of the Cartesian space, propagating along the positive X-axis, as

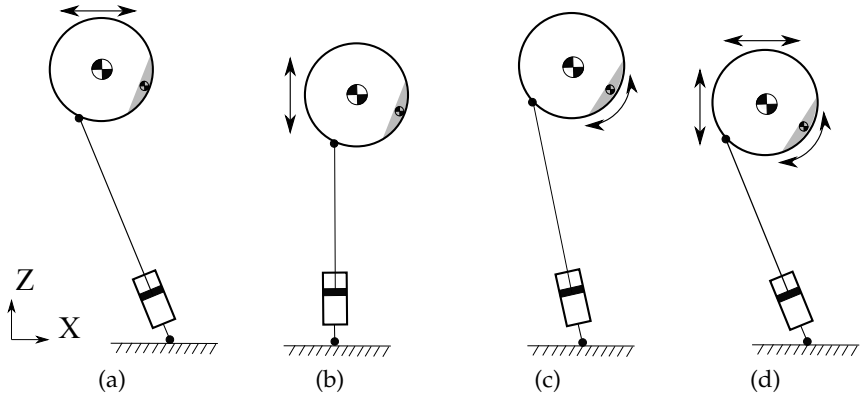

Figure 4.2: Illustration of the motions of a 3DOF SPAMD subjected to plane waves in the vertical XZ-plane. The larger centre of mass represents the mass of the hollow spherical buoy m_1, the smaller one is the centre of the gravity of the offset mass m_2: (a) surge motion, (b) heave motion, (c) pitch motion, (d) combined 3DOF motion.

shown in Figure 4.2. As the SPAMD is designed to be symmetric about the XZ-plane, it is assumed that the buoy only moves in the plane with surge, heave and pitch motion when excited by the plane waves.

The detailed descriptions of the operating environment, the asymmetric mass buoy, and the PTO are presented below.

Operating environment

The SPAMD operates in a finite depth water column. In this paper, the water depth is assumed to be 60 m. The submergence depth of the buoy is 3 m from top of the buoy to the sea surface, chosen as a compromise between maximum hydrodynamic coefficients and mitigating surface piercing. The frequency of incident monochromatic waves ranges from 0.34 to 1.4 rad/s, covering the major wave frequencies off the Australian coasts [1]. The wave amplitude was set to 0.1 m, which is sufficiently small to meet the linear wave assumption and small displacement assumption used in the modelling. It should be noted that an increase in wave amplitude above 0.1 m compromises the linear wave assumption and leads to an increase in viscous drag and kinematic nonlinearities. Figure 4.3 shows the hydrodynamic coefficients for the defined operating environment [7].

Asymmetric mass buoy configuration

Figure 4.4 shows the free-body diagram of SPAMD buoy in the vertical XZ-plane in the Cartesian space. The buoy coordinates are defined in a body-

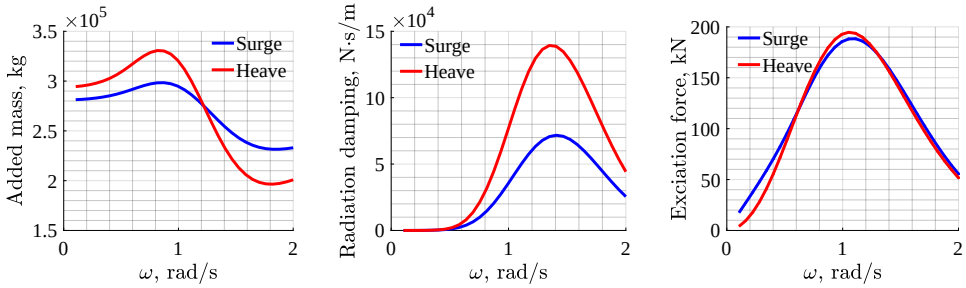

Figure 4.3: Hydrodynamic coefficients for the defined operating environment: (a) added mass; (b) radiation damping coefficient; (c) excitation force.

fixed frame with an origin located at the centre of the buoy. The SPAMD buoy consists of a spherical hull with a smooth surface of mass m_1, and an additional mass of m_2 offset from the centre of the buoy on the XZ-plane. The total mass is $m = m_1 + m_2$.

The buoy is assumed to be formed from a hollow spherical buoy of radius r. The mass of the hollow spherical body can be simplified as a point mass, m_1, located at the geometric centre of the body, with a moment of inertia about the centre of the buoy, $I_1 = \frac{2}{3}m_1r^2$.

The offset mass, m_2, is formed by the intersection of a plane with the spherical buoy and is attached on the inner surface of the spherical hull. Its centre of gravity is offset from the centre of the buoy by an offset distance, r_{gy}, and an offset angle, φ. The angle φ is measured from the positive X-axis to the offset mass, as shown in Figure 4.4. The centre of the gravity of the offset mass is denoted as (x_2, z_2). In the subsequent modelling in Section 4.3, the offset mass m_2 can be simplified as an offset point mass m_2, with the moment of inertia about the centre of the buoy $I_2 = m_2r_{gy}^2$.

In this work, the mass distribution of the SPAMD is determined by the weight-to-buoyancy ratio, m/m_w, the mass ratio, m_1/m_2 and the mass-offset position, defined by the mass offset radius r_{gy} and mass offset angle φ. Noting that the behavior of the SPAMD is affected by the weight-to-buoyancy ratio, mass ratio and mass-offset position, which might be considered as tuning parameters. Table 4.1 lists the buoy's parameters used in the analysis. The weight-to-buoyancy ratio is set to 0.5, and the mass ratio to 1. The radius of the buoy is 5 m, to be consistent with previous research on point absorbers [14]. It has been assumed that the mass offset radius, r_{gy}, is 4.5 m. In this study, the offset angle φ is set to be 30 deg, which means the offset mass m_2 is below the centre of the buoy. The values of the weight-to-buoyancy

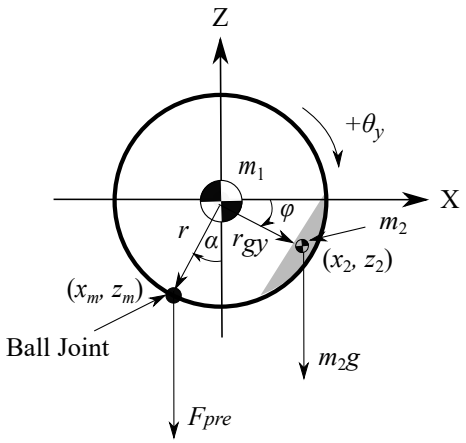

Figure 4.4: Free body diagram of the asymmetric mass buoy in the vertical XZ-plane. The origin is at the centre of the buoy.

ratio, mass ratio and mass-offset position were chosen from an unpublished optimisation study on the SPAMD.

Table 4.1: Parameters of the SPAMD buoy and bathymetry

Description	Parameter	Value/Unit
Weight-to-buoyancy ratio	m/m_w	0.5
Mass ratio	m_1/m_2	1
Radius of buoy	r	5 m
Mass offset angle	φ	30 deg
Mass offset radius	r_{gy}	4.5 m
Water depth	h	60 m
Submergence depth (from the top of the buoy)	d	3 m

Since the offset mass, m_2, causes an additional moment at the centre of the buoy, the tether attachment point on the buoy needs to be adjusted to the opposite side of the buoy to maintain the static stability of the system. The coordinate of the mooring attachment point is denoted as (x_m, z_m). The mooring point angle, which is measured from the Z-axis to the tether attachment point, is denoted as α, as shown in Figure 4.4.

PTO

A linear PTO is connected to the buoy via a mooring tether with nominal length of L. It consists of a linear spring with stiffness of K_{pto}, a linear damper with damping coefficient of B_{pto} and a pretension force of F_{pre} to balance the

net buoyancy of the buoy, as shown in Figure 4.5. The PTO does not contain any hard-stop motion constraints.

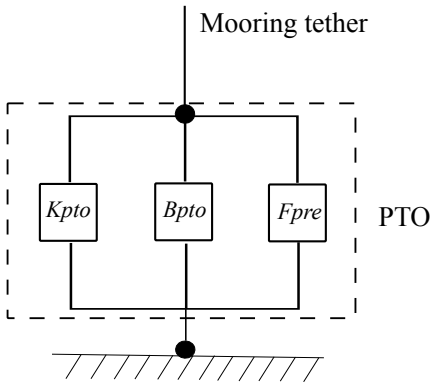

Figure 4.5: Schematic of the PTO.

Assuming harmonic motion, the time-averaged power output of the system is equal to the power consumed by the linear PTO damper, given by

$$P_{total} = \frac{1}{2} B_{pto} |\Delta \hat{\dot{L}}|^2 \tag{4.1}$$

where $\Delta \hat{\dot{L}}$ is the complex PTO extension velocity.

K_{pto}, B_{pto} and L are the key parameters affecting the efficiency of the SPAMD. These coefficients are optimized to achieve maximum power output in the modal analysis presented in Section 4.5.

4.3 Equation of motion

In this section, the system stability condition is presented and a frequency-domain model is developed. The system stability condition determines the acceptable mass-offset that maintains stability and prevents the tether from reeling on the planar constrained buoy during system operation. The frequency-domain model of the SPAMD is formulated as a basis for the subsequent modal analysis. The model is built upon linear potential theory and small displacement assumption (see Appendix 4.B for justification), with the consideration of viscous drag forces.

In practice, the viscous drag forces are the dominant forces that dissipate kinetic energy from the buoy's motion. Therefore, it is necessary to model the viscous drag forces in the motion equation of 3DOF single-tether PAs,

otherwise the PA will experience excessive motion, in particular at resonance, where power absorption efficiency of the SPAMD will be overestimated [12]. As commonly expressed in a quadratic form, the viscous drag forces need to be linearised to be used in the frequency-domain model, which leads to a hybrid frequency-domain model. This hybrid frequency-domain model has been validated against an equivalent time-domain model [8], and is shown to be accurate, even at resonance.

4.3.1 System stability condition

In this study, it is assumed that the torque generated by the offset mass m_2 is balanced by the torque generated by the PTO pretension force when buoy is at rest. The offset mass is assumed to be located in the right hemisphere of the buoy ($-\pi/2 \leq \varphi \leq \pi/2$) and the mooring attachment point is in the left hemisphere ($0 \leq \alpha \leq \pi/2$). For $0 \leq \varphi \leq \pi/2$, the SPAMD can always maintain stability during its operation; while for $-\pi/2 \leq \varphi < 0$, the system is stable only if the following condition is satisfied

$$\frac{r_{gy}}{r} < \left(\frac{m_w - m}{m_2}\right) \quad , \tag{4.2}$$

in which the m_w is the mass of water displaced by the submerged spherical buoy, $m_1 + m_2 = m$ is the total mass of the buoy. The detailed derivation of the system stability condition is presented in Appendix 4.A.

In this work, according to the mass distribution defined in Table 4.1, $0 \leq \varphi \leq \pi/2$. Therefore, the system is stable.

4.3.2 Frequency-domain modelling

The motion of the SPAMD can be described by a frequency-domain motion equation formulated at the centre of the buoy, given by

$$(\mathbf{M} + \mathbf{A}(\omega))\hat{\dot{\mathbf{x}}} + (\mathbf{B}(\omega))\hat{\mathbf{x}} = \hat{\mathbf{F}}_{exc} + \hat{\mathbf{F}}_{re} + \hat{\mathbf{F}}_{pto} + \hat{\mathbf{F}}_{vis} \quad , \tag{4.3}$$

in which $\mathbf{M}$ is the mass matrix of the asymmetric mass buoy, $\mathbf{A}(\omega)$ is the hydrodynamic added mass matrix, $\mathbf{B}(\omega)$ is the hydrodynamic damping coefficient matrix, which are calculated by using the method described in [7] (see Section 4.2), $\hat{\mathbf{x}}$ is the complex buoy velocity vector $(\hat{\dot{x}}, \hat{\dot{z}}, \hat{\dot{\theta}}_y)^{\mathbf{T}}$, where $\hat{\dot{x}}$ is the complex surge velocity, $\hat{\dot{z}}$ is the complex heave velocity and $\hat{\dot{\theta}}_y$ is the complex pitch angular velocity, $\hat{\mathbf{F}}_{exc}$ is the wave excitation force vector, which is also calculated by using the method described in [7], $\hat{\mathbf{F}}_{re}$ is the net restoring force vector, $\hat{\mathbf{F}}_{pto}$ is the PTO control force vector and $\hat{\mathbf{F}}_{vis}$ is the viscous force vector.

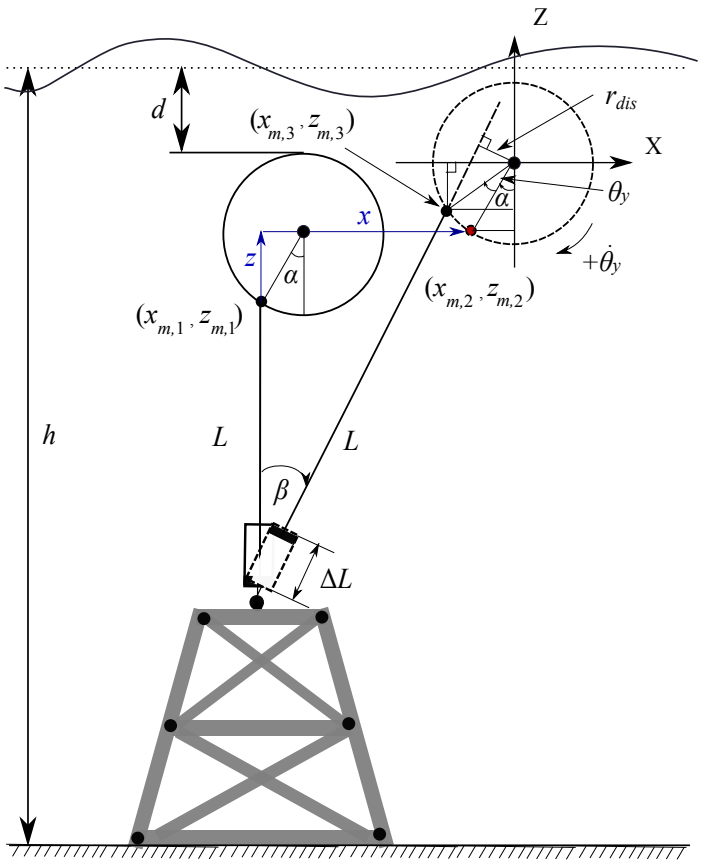

Figure 4.6: Coordinate change of tether attachment point from its rest pose ($x_{m,1}$, $z_{m,1}$) to ($x_{m,3}$, $z_{m,3}$) when the buoy moves to an arbitrary position (indicated by dashed circle).

The mass matrix of spherical buoy

According to Lee [6], for a 3DOF (i.e., surge, heave and pitch) spherical buoy with an additional offset mass m_2, the mass matrix with respect to the geometric centre of the buoy is given by

$$\mathbf{M} = \begin{pmatrix} m_1 + m_2 & 0 & m_2 z_2 \\ 0 & m_1 + m_2 & -m_2 x_2 \\ m_2 z_2 & -m_2 x_2 & I_{yy} \end{pmatrix} \quad , \tag{4.4}$$

in which the total moment of inertia $I_{yy} = I_1 + I_2 = \frac{2}{3} m_1 r^2 + m_2 r_{gy}^2$. From Figure 4.4, as small displacement is assumed, the coordinate of the offset mass is given by $(x_2, z_2) = (r_{gy}\cos(\varphi + \theta_y), r_{gy}\sin(\varphi + \theta_y)) \approx (r_{gy}\cos(\varphi), r_{gy}\sin(\varphi))$.

The net hydrostatic restoring force vector

The net hydrostatic restoring force vector consists of hydrostatic restoring forces in the heave direction and restoring torque generated by the gravity of the offset mass m_2 in the pitch direction, given by

$$\begin{aligned}\hat{\mathbf{F}}_{re} &= \begin{pmatrix} 0 \\ \rho V g - (m_1 + m_2)g \\ m_2 g r_{gy} \cos(\varphi - \theta_y) \end{pmatrix} \\ &\approx \begin{pmatrix} 0 \\ \rho V g - (m_1 + m_2)g \\ m_2 g r_{gy} (\cos(\varphi) + \sin(\varphi)\theta_y) \end{pmatrix} \end{aligned} \quad , \tag{4.5}$$

where $V = \frac{4}{3}\pi r^3$ is the volume displaced by the buoy, and g is gravitational acceleration.

The excitation force vector

The excitation force vector applied to the fully submerged spherical buoy is given by

$$\hat{\mathbf{F}}_{exc} = \begin{pmatrix} \hat{F}_{exc,x} \\ \hat{F}_{exc,z} \\ 0 \end{pmatrix} \quad , \tag{4.6}$$

in which $\hat{F}_{exc,x}$ and $\hat{F}_{exc,z}$ are calculated by using the equations given by [7]. The pitch excitation moment is negligible because the spherical buoy is axisymmetric about the pitch axis.

The PTO control force vector

According to Section 4.2, the PTO control force along the tether is the sum of the PTO spring force, the PTO damping force and the pretension force. By mapping the PTO control force to the Cartesian axes, the PTO control force vector is given by

$$\hat{\mathbf{F}}_{pto} = (-F_{pre} - B_{pto}\Delta\hat{\dot{L}} - K_{pto}\Delta\hat{L})\mathbf{T} \quad , \tag{4.7}$$

in which the transformation vector $\mathbf{T}$ converts the PTO control force to the Cartesian axes.

As illustrated in Figure 4.6, when the buoy moves to an arbitrary position, the motion of the tether attachment point can be decomposed into

a translation from $(x_{m,1}, z_{m,1})$ to $(x_{m,2}, z_{m,2})$ and a rotation from $(x_{m,2}, z_{m,2})$ to $(x_{m,3}, z_{m,3})$. Assuming small θ_y such that $\sin\theta_y \approx \theta_y$ and $\cos\theta_y \approx 1$, the change in PTO length ΔL is given by

$$\Delta L = \sqrt{(L + z + r\sin(\alpha)\theta_y)^2 + (x - r\cos(\alpha)\theta_y)^2} - L \quad , \tag{4.8}$$

in which x and z represent the surge and heave displacement of the centre of the buoy respectively, as shown in Figure 4.6.

Using the small displacement assumption, Equation (4.8) can be further linearised by a first order Taylor series expansion giving

$$\Delta L \approx z + r\sin(\alpha)\theta_y = \begin{pmatrix} 0 & 1 & r\sin(\alpha) \end{pmatrix} \begin{pmatrix} x \\ z \\ \theta_y \end{pmatrix} \quad , \tag{4.9}$$

in which the inverse Jacobian matrix that converts the buoy's motion in the Cartesian space to the PTO elongation is given by

$$\mathbf{J}^{-1} = \begin{pmatrix} 0 & 1 & r\sin(\alpha) \end{pmatrix} \quad . \tag{4.10}$$

It can be seen from Equation (4.10) that only heave and pitch motion directly couple to the PTO for small motion.

The transformation vector $\mathbf{T}$ is given by

$$\mathbf{T} = \begin{pmatrix} \sin(\beta) \\ \cos(\beta) \\ r_{dis} \end{pmatrix} \quad , \tag{4.11}$$

in which β is tether angle, r_{dis} is instantaneous lever arm between the geometric centre of the buoy to the PTO control force vector, as shown in Figure 4.6.

For small displacement, the term $\cos(\beta)$ is approximated as unity. The term $\sin(\beta)$ is approximated by a first order Taylor series expansion giving

$$\sin(\beta) \approx \frac{x - r\cos(\alpha)\theta_y}{L} \quad . \tag{4.12}$$

From Figure 4.6, the instantaneous lever arm from the centre of the buoy to the tether projection is given by

$$\begin{aligned} r_{dis} &= r\sin(\alpha + \theta_y - \beta) \\ &\approx r\Big(\sin(\alpha) + \cos(\alpha)\theta_y - \cos(\alpha)\frac{x - r\cos(\alpha)\theta_y}{L}\Big) \quad . \end{aligned} \tag{4.13}$$

The viscous drag force vector

According to the Morison equation [9], the viscous drag force is expressed as a quadratic function of the body's velocity. For a smooth spherical buoy, the viscous drag force vector is given by

$$\hat{\mathbf{F}}_{vis} = -0.5\rho C_D S \begin{pmatrix} |\hat{\dot{x}}|\hat{\dot{x}} \\ |\hat{\dot{z}}|\hat{\dot{z}} \\ 0 \end{pmatrix} \quad , \tag{4.14}$$

in which C_D is the viscous drag coefficient (C_D = 0.18 for the $5 \times 10^6 < Re < 1 \times 10^7$ [2], where the Re was estimated using an equivalent time-domain simulation) and S is the nominal cross-section area of the spherical buoy ($S = \pi r^2$). It should be noted that for a smooth spherical buoy, the viscous drag coefficient in the pitch direction is negligible.

Equation (4.14) represents a nonlinear time-domain expression. In order to consider the viscous drag forces in the frequency-domain model, the quadratic viscous drag forces must be linearised. The essence of the linearisation is to use a linear term $|\hat{\dot{x}}_{iter}|\hat{\dot{x}}$ (or $|\hat{\dot{z}}_{iter}|\hat{\dot{z}}$) to approach to the quadratic term $|\hat{\dot{x}}|\hat{\dot{x}}$ (or $|\hat{\dot{z}}|\hat{\dot{z}}$) iteratively, whereby $\hat{\dot{x}}_{iter}$ and $\hat{\dot{z}}_{iter}$ are iterative variables. This is because the velocity at which the quadratic viscous drag is linearised is known. However, the calculation of the system response requires the linearised viscous drag. Therefore, an iterative process with a reasonable initial guess is essential to solve system response in frequency-domain. Figure 4.7 shows the flow chart of the linearisation process in the surge direction, whereby $\hat{\dot{x}}_{iter,k}$ is the value of the iterative variable in the k-th iteration, and $\hat{\dot{x}}_k$ is the system response in the surge direction. Although the initial value of the $\hat{\dot{x}}_{iter}$ does not affect the final results, in this study, the initial value of $\hat{\dot{x}}_{iter}$ was set to 1 m/s. The viscous drag force in surge is linearised as $\hat{F}_{vis,surge} = -0.5\rho C_D S|\hat{\dot{x}}_{iter,k-1}|\hat{\dot{x}}$. Then the motion equation is solved to obtain the surge response of the system $\hat{\dot{x}}_1$. When the convergence criteria $\frac{|\text{Real}\{\hat{\dot{x}}_k - \hat{\dot{x}}_{iter,k-1}\}|}{|\text{Real}\{\hat{\dot{x}}_k\}|} < 1\%$ and $\frac{|\text{Imag}\{\hat{\dot{x}}_k - \hat{\dot{x}}_{iter,k-1}\}|}{|\text{Imag}\{\hat{\dot{x}}_k\}|} < 1\%$, are met, $\hat{\dot{x}}_{iter}$ and $\hat{\dot{x}}$ are regarded to be equivalent and the iteration stops. Otherwise, $\hat{\dot{x}}_{iter}$ will be updated to $\hat{\dot{x}}_{iter,k} = \frac{\hat{\dot{x}}_{iter,k-2} + \hat{\dot{x}}_{k-1}}{2}$ which will be used in next iteration. Noting that the same linearisation process was applied to the heave direction simultaneously with surge.

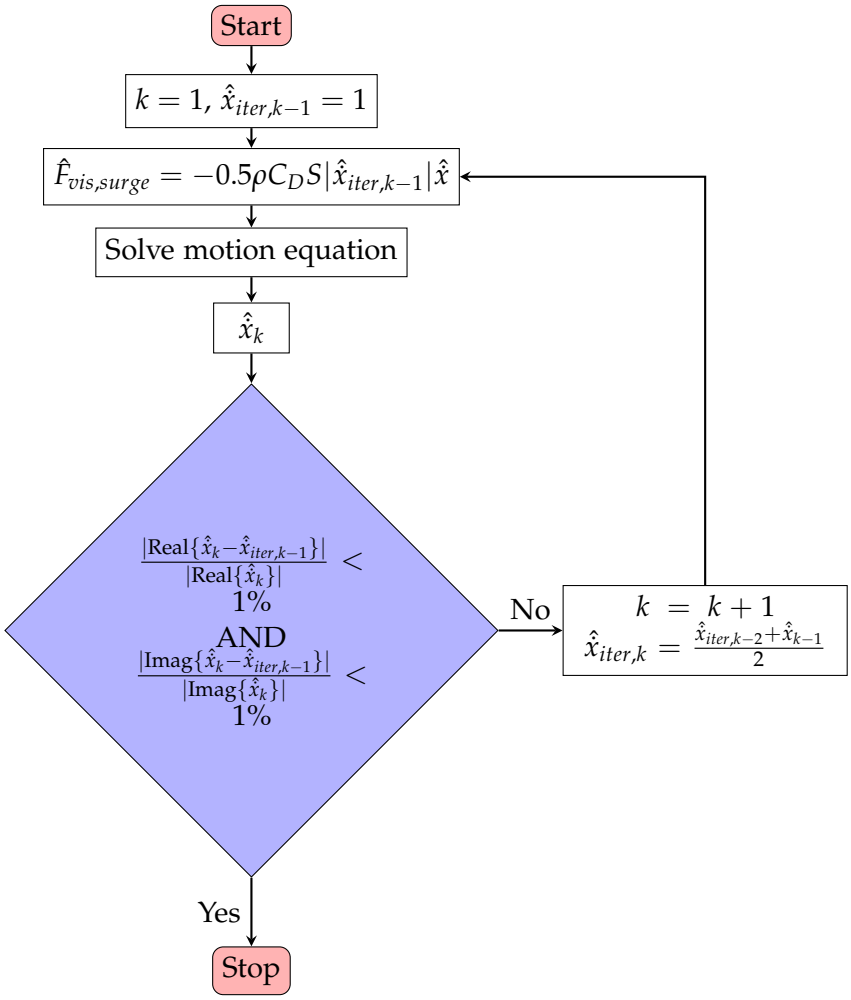

Figure 4.7: Flow chart illustrating the process of linearising the surge viscous drag force in the frequency domain.

4.4 Methodology

In this work, a modal analysis was conducted to understand the operating principles of the single-tether SPAMD, via the system natural frequencies and mode shapes. Furthermore, an efficiency analysis and a power analysis were conducted to explain the efficiency improvement of the SPAMD. The approach and governing equations applied in the modal analysis, efficiency analysis and power analysis are presented below.

4.4.1 Natural frequencies of the decoupled system

The motion of the 3DOF single-tether generic PA can be decomposed into three independent vibration modes, namely the surge mode, heave mode and pitch mode. The heave mode is induced by the up and down motion of the buoy along the vertical axis. Therefore, the natural frequency of the buoy's heave mode ω_z is governed by the PTO stiffness K_{pto} and is independent of the nominal tether length L. It is given by

$$\omega_z = \sqrt{\frac{K_{pto}}{(m + A_z(\omega))}} \quad , \tag{4.15}$$

in which $A_z(\omega)$ is the hydrodynamic added mass in the heave direction.

For small displacement, the natural frequency of the surge mode can be approximated as that of an inverted pendulum, which is inversely proportional to the square root of the nominal tether length L, given by

$$\omega_x = \sqrt{\frac{g(\rho V - m)}{(L + r)(m + A_x(\omega))}} \quad , \tag{4.16}$$

in which $A_x(\omega)$ is the hydrodynamic added mass in the surge direction.

The natural frequency of the pitch mode has little impact on the power absorption of the system. This is because the natural frequency of the buoy's pitch mode tends to be significantly higher than the wave frequencies of interest, as illustrated in Section 4.5.2. Therefore, natural frequency of the pitch mode is not discussed in this work.

In this study, Equation (4.15) and (4.16) were only used to provide initial estimates for the search of the optimal PTO stiffness and nominal tether length that maximises the efficiency of the PAs in Section 4.5. A more precise way to calculate the natural frequencies of the system is presented below.

4.4.2 Mode shapes and natural frequencies of the fully coupled system

The eigenvectors (mode shapes) and corresponding eigenvalues (natural frequencies) are calculated by solving the characteristic equation of the system

$$[(\mathbf{M} + \mathbf{A}(\omega))^{-1}\mathbf{K} - \lambda\mathbf{I}]\mathbf{v} = 0 \quad , \tag{4.17}$$

in which λ are the eigenvalues, $\mathbf{M}$ is the mass matrix , $\mathbf{A}(\omega)$ is the hydrodynamic added mass matrix, given by Equation (4.4), $\mathbf{I}$ is the identity

matrix, **v** is the matrix of eigenvectors, **K** is the stiffness matrix, derived by substituting Equations (4.4)-(4.14) into Equation (4.3) and given by

$$\mathbf{K} = \begin{pmatrix} \frac{F_{pre}}{L} & 0 & -\frac{F_{pre} r \cos\alpha}{L} \\ 0 & K_{pto} & K_{pto} r \sin\alpha \\ -\frac{F_{pre} r \cos\alpha}{L} & K_{pto} r \sin\alpha & \begin{bmatrix} F_{pre} r \cos\alpha \\ -m_2 g r_{gy} \sin\varphi \\ +\frac{F_{pre}(r\cos\alpha)^2}{L} \\ +K_{pto}(r\sin\alpha)^2 \end{bmatrix} \end{pmatrix}. \tag{4.18}$$

Unlike Equation (4.15) and Equation (4.16) that provide an estimation of the natural frequencies, Equation (4.17) was used to compute the natural frequencies of the oscillation modes for both the decoupled system and fully coupled system in Section 4.5.

By solving Equation (4.17) , the resulting matrix **v** of the eigenvectors is given by

$$\mathbf{v} = \begin{pmatrix} v_{1,x} & v_{2,x} & v_{3,x} \\ v_{1,z} & v_{2,z} & v_{3,z} \\ v_{1,\theta_y} & v_{2,\theta_y} & v_{3,\theta_y} \end{pmatrix} \quad , \tag{4.19}$$

in which the three columns correspond to Mode 1, Mode 2 and Mode 3 respectively. The rows of the matrix represent the projections of the oscillation modes along the surge, heave and pitch axis of the buoy in the Cartesian space.

In Section 4.5.2, the matrix **v** is used to determine the orientations of the buoys' oscillation modes in the Cartesian space. Furthermore, for the given response $\hat{\mathbf{x}}$ in the Cartesian space, the matrix **v** was used to calculate the complex modal response vector $\hat{\mathbf{X}}$,

$$\hat{\mathbf{X}} = \mathbf{v}^{-1}\hat{\mathbf{x}} \quad . \tag{4.20}$$

Moreover, in Section 4.5.2, the motion trajectories of the buoy are investigated over the frequencies of interest. For the given response of the buoy $\hat{\mathbf{x}}$ in the Cartesian space, the resulting motion trajectory of the buoy in the XZ plane is described by

$$\begin{cases} x(t) = \text{Real}\{\hat{x}e^{i\omega t}\} \\ z(t) = \text{Real}\{\hat{z}e^{i\omega t}\} \end{cases} \quad , \tag{4.21}$$

where the j is an imaginary operator.

4.4.3 PTO extension velocities arsing from oscillation modes

In Section 4.5.1, the PTO extension velocities arsing from oscillation modes are presented to demonstrate impact of nominal tether length on the efficiency of the SPAMD (see Figure 4.8c and 4.10c). From Equation (4.9) where the PTO extension velocity is given by $\Delta\hat{\dot{L}} = \mathbf{J}^{-1}\hat{\dot{\mathbf{x}}}$, for a given modal velocity response $\hat{\dot{\mathbf{X}}} = (\hat{\dot{X}}_1, \hat{\dot{X}}_2, \hat{\dot{X}}_3)^T$, the resulting PTO extension velocity can be re-written as

$$\begin{aligned} \Delta\hat{\dot{L}} &= \mathbf{J}_{\mathrm{M}}^{-1}\hat{\dot{\mathbf{X}}} \quad , \\ \mathbf{J}_{\mathrm{M}}^{-1} &= \mathbf{J}^{-1}\mathbf{v} \quad , \end{aligned} \tag{4.22}$$

in which $\mathbf{J}_{\mathrm{M}}^{-1} = (J_{M,1}, J_{M,2}, J_{M,3})$ is the inverse Jacobian matrix that converts modal response to PTO extension. Equation (4.22) can be re-written as

$$\Delta\hat{\dot{L}} = \underbrace{J_{M,1}\hat{\dot{X}}_1}_{\Delta\hat{\dot{L}}_1} + \underbrace{J_{M,2}\hat{\dot{X}}_2}_{\Delta\hat{\dot{L}}_2} + \underbrace{J_{M,3}\hat{\dot{X}}_3}_{\Delta\hat{\dot{L}}_3} \quad , \tag{4.23}$$

in which $\Delta\hat{\dot{L}}_1$, $\Delta\hat{\dot{L}}_2$ and $\Delta\hat{\dot{L}}_3$ are the PTO extension velocities arsing from oscillation Mode 1, 2 and 3 respectively.

4.4.4 Relative capture width

In this work, relative capture width (RCW) is used to evaluate the efficiency of the single-tether PAs. According to [4], the relative capture width is defined as

$$RCW = \frac{P_{total}}{2rJ} \quad , \tag{4.24}$$

in which J is the power transport per unit width of the wave frontage, given by [4]

$$\begin{aligned} J &= \frac{\rho g^2 D(kh)}{4\omega}|A|^2 \quad , \\ D(kh) &= \left(1 + \frac{2kh}{\sinh(2kh)}\right)\tanh(kh) \quad , \end{aligned} \tag{4.25}$$

where ρ is the water density, k is the wavenumber, and h is the water depth.

In this paper, the efficiency of the SPAMD was compared with a generic buoy with a uniformly distributed mass m across the spherical hull. Although often used in wave energy conversion of arrays, herein the q factor is re-

defined as the ratio of the RCW of the SPAMD to the RCW of the generic buoy, implying the efficiency improvement, given by

$$q = \frac{RCW_{SPAMD}}{RCW_{generic}} \quad . \tag{4.26}$$

4.4.5 Power output

As mentioned in Section 4.2, the time-averaged power output of the SPAMD is equal to the time-averaged power consumed by the PTO damper, which can be decomposed into power components arising from buoy motion in each DOF by substituting Equation (4.9) into Equation (4.1), leading to

$$\begin{aligned} P_{total} &= \frac{1}{2} B_{pto} |\hat{\dot{z}} + r \sin(\alpha) \hat{\dot{\theta}}_y|^2 \\ &= \underbrace{\frac{1}{2} B_{pto} \hat{\dot{z}} \hat{\dot{z}}^*}_{P_{heave}} + \underbrace{\frac{1}{2} B_{pto} (r \sin\alpha)^2 \hat{\dot{\theta}}_y \hat{\dot{\theta}}_y^*}_{P_{pitch}} + \underbrace{\frac{1}{2} B_{pto} r \sin\alpha (\hat{\dot{z}} \hat{\dot{\theta}}_y^* + \hat{\dot{z}}^* \hat{\dot{\theta}}_y)}_{P_{cross}} \end{aligned} \quad , \tag{4.27}$$

in which the $\hat{\dot{z}}^*$ and $\hat{\dot{\theta}}_y^*$ are the conjugates of $\hat{\dot{z}}$ and $\hat{\dot{\theta}}_y$.

In Equation (4.27), it can be seen that the power output P_{total} consists of three components, namely the power arising from the heave motion P_{heave}, the power arising from the pitch motion P_{pitch} and a cross term arising from the heave-pitch coupled motion P_{cross}, which indicates the energy flow between the two motions. At the limit as $\alpha \to 0$ (i.e., offset mass located directly above the tether attachment point), the power is only generated from heave motion, which is similar to the generic buoy).

In Section 4.5.2, Equation (4.27) is used to understand the contributions of buoy's motion to the power output of the system.

4.5 Result

In this section, the working principle of the SPMAD was investigated and corresponding efficiency was compared against the generic PAs, over the frequencies of interest.

4.5.1 Modal analysis as a function of nominal tether length

In this section, the modal analysis considers the impact of the nominal tether length on the efficiency of the SPAMD at a typical wave frequency of ω = 0.48 rad/s ($T = 13$ s), which is a common peak wave frequency off the coast

of Perth [1]. The nominal tether length ranges from 1 to 9 times the buoy's radius ($r < L < 9r$), over 500 sampled nominal tether lengths. It should be noted that in order to realise an optimal tether length for the SPAMD, it might be necessary to raise the tether mooring above the sea floor as shown in Figure 4.6. At each sampled nominal tether length, the optimal PTO stiffness K_{pto} and PTO damping coefficient B_{pto} that maximise the RCW of the system are determined by using the MATLAB optimization function *fmincon*, within the defined range of tether length L.

The analysis on the nominal tether length is firstly conducted for the generic symmetric mass PA as a benchmark. Figure 4.8 illustrates the natural frequencies (see Figure 4.8a), mode shapes (see Figure 4.8b), PTO extension velocities arising from the oscillation modes under forced excitation (see Figure 4.8c) and RCW (see Figure 4.8d) respectively, versus the ratio of the nominal tether length to the buoy radius. As shown in Figure 4.8a, the natural frequency of the surge-dominant Mode 1 declines as the nominal tether length increases. Conversely, the natural frequency of the heave-dominant Mode 2 remains constant and equal to the excitation frequency over various nominal tether lengths. Furthermore, as the generic PA is a decoupled system, it can be seen that natural frequencies of Mode 1 and 2 almost perfectly match the natural frequencies given by Equations (4.15) and (4.16). The oscillation Mode 3 is pitch-dominant and its natural frequency is considerably higher than the incident wave frequency. Therefore, Mode 3 is not shown in Figure 4.8a. From the eigenvector plots shown in Figure 4.8b, it can be seen that Mode 1 only contains surge motion, which means Mode 1 oscillates purely along the surge. In contrast, Mode 2 oscillates purely along the heave. The mode shapes of the generic buoy in the Cartesian space are illustrated in Figure 4.9. Figure 4.8c shows the PTO extension velocity arising from the two oscillation modes, which is mapped from the mode shapes via inverse Jacobian matrix. As the surge motion of the generic buoy is poorly coupled to the single-tether PTO, it can be seen that only Mode 2, which oscillates purely along the heave, can contribute to the PTO extension, and thus to power output. Consequently, the resulting RCW remains constant over various nominal tether lengths, as shown in Figure 4.8d.

The same analysis is then undertaken for the SPAMD. Figure 4.10 illustrates natural frequencies (see Figure 4.10a), mode shapes (see Figure 4.10b), PTO extension velocities arising from oscillation modes under forced excitation (see Figure 4.10c) and RCW (see Figure 4.10d) of the SPAMD respectively, versus the ratio of nominal tether length to buoy radius. In regards to Figure 4.10a, it should be noted that when calculating the natural frequencies of the decoupled modes using Equations (4.15) and (4.16), the

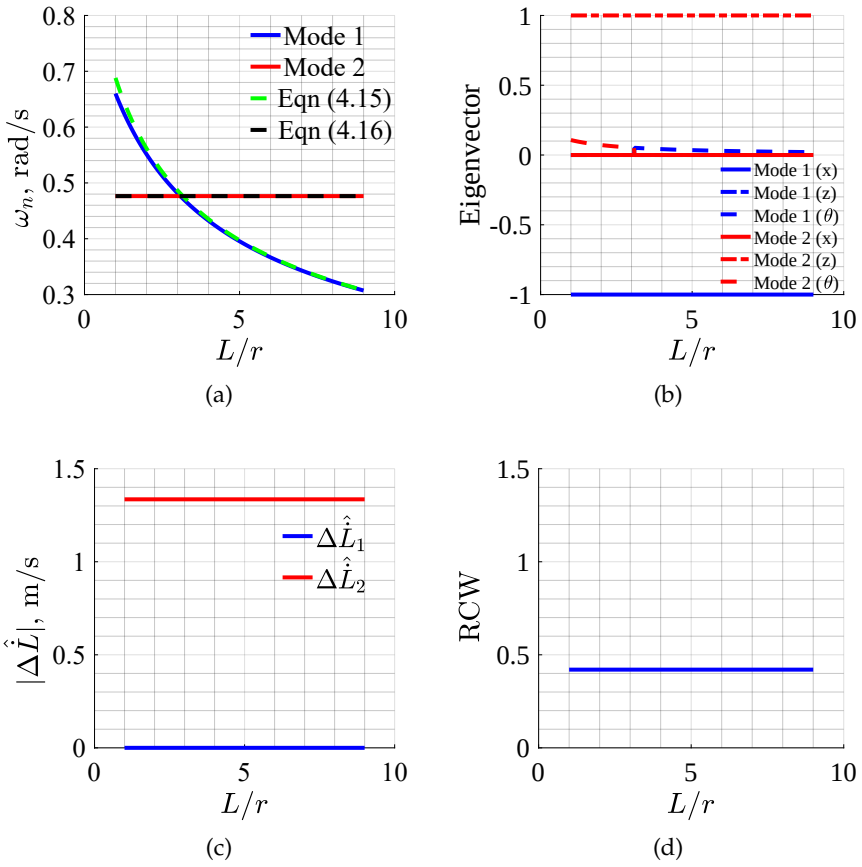

Figure 4.8: Analysis of the generic spherical PA for various ratios of nominal tether length to buoy radius, for ω = 0.48 rad/s: (a) natural frequencies of Mode 1 and 2, compared against the natural frequencies of the decoupled modes given by Equations (4.15) and (4.16); (b) eigenvectors of Mode 1 and 2; (c) PTO extension velocity arising from Mode 1 and 2; (d) RCW of the generic PA.

optimal parameters (stiffness, damping coefficient and nominal tether length) of the SPAMD were used. This results in a small difference in the natural frequencies compared to those displayed in Figure 4.8a. In comparison to the generic PA, the oscillation modes of the SPAMD contain motions along multiple Cartesian DOFs because of the strong motion coupling arising from offsetting the centre of mass. From Figure 4.10a and 4.10b, it can be seen that for very small and very large tether length ratios, L/r, there exists a surge-dominant mode and a heave-dominant mode. It should be noted that since the surge and heave motions are coupled in the SPAMD, the natural

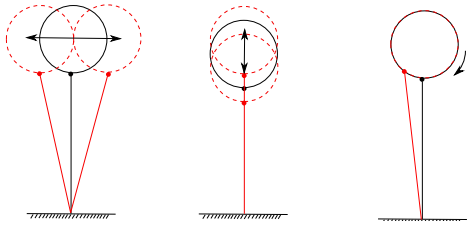

Figure 4.9: Mode shapes of the generic PA: (a) surge-dominant Mode 1; (b) heave-dominant Mode 2; (c) pitch-dominant Mode 3.

frequencies of Mode 1 and 2 deviate from the natural frequencies given by Equations (4.15) and (4.16) at small tether length to buoy radius ratios. When the SPAMD operates at optimal nominal tether lengths ($3 \leq L/r \leq 4$, the shaded range in Figure 4.10), the natural frequencies of Mode 1 and Mode 2 are approximately equal and approach the natural frequencies given by Equations (4.15) and (4.16). For the greatest tether length to buoy radius ratios, the eigenvectors of the Mode 1 and 2 are similar to the generic case, where the surge and heave motions of the PA are weakly coupled. The oscillation Mode 3 is pitch-dominant and its natural frequency is considerably higher than the incident wave frequency, and consequently is not shown in Figure 4.10a.

From Figure 4.10b, it can be seen that Mode 1 and 2 contain both surge and heave motions. When the motion of the system becomes the most strongly coupled (the shaded range in Figure 4.10b), the surge and heave motion contribute equally to Mode 1 and 2 of the buoy. For Mode 1, surge and heave are out of phase, which means the buoy oscillates -45° to the Cartesian X-axis as shown in Figure 4.11a. For Mode 2, surge and heave motion are in phase, and thus the buoy oscillates 45° to the Cartesian X-axis, as shown in Figure 4.11b. Figure 4.10c shows the PTO extension velocities arising from Mode 1 and 2 respectively. It can be seen that Mode 1 and Mode 2 result in almost equal contribution to the PTO extension at the optimal tether lengths. Furthermore, under the optimal condition the temporal phase difference between Mode 1 and 2 is around -105° at low frequencies (see Figure 4.12d), and therefore the phase difference between the PTO extension velocities, $\angle(\Delta\hat{\dot{L}}_1/\Delta\hat{\dot{L}}_2)$, is also approximately -105°. Figure 4.10d shows the change in RCW for the SPAMD versus the ratio of the nominal tether length to the buoy radius. As the surge motion can drive the PTO via surge-heave motion coupling (see Section 4.5.3), the RCW of the SPAMD (see Figure 4.10d) is significantly higher in comparison to RCW of the generic PA (see Figure

4.8d). When the SPAMD operates with the optimal nominal tether length, the RCW of the SPAMD is up to three times that of the generic PAs (see Section 4.5.2). This is because the capture width of the additional surge motion can be theoretically twice that of the heave motion [4]. It is also interesting to note that under the optimal conditions, the PTO velocity (and therefore PTO extension) is minimised, despite maximal RCW.

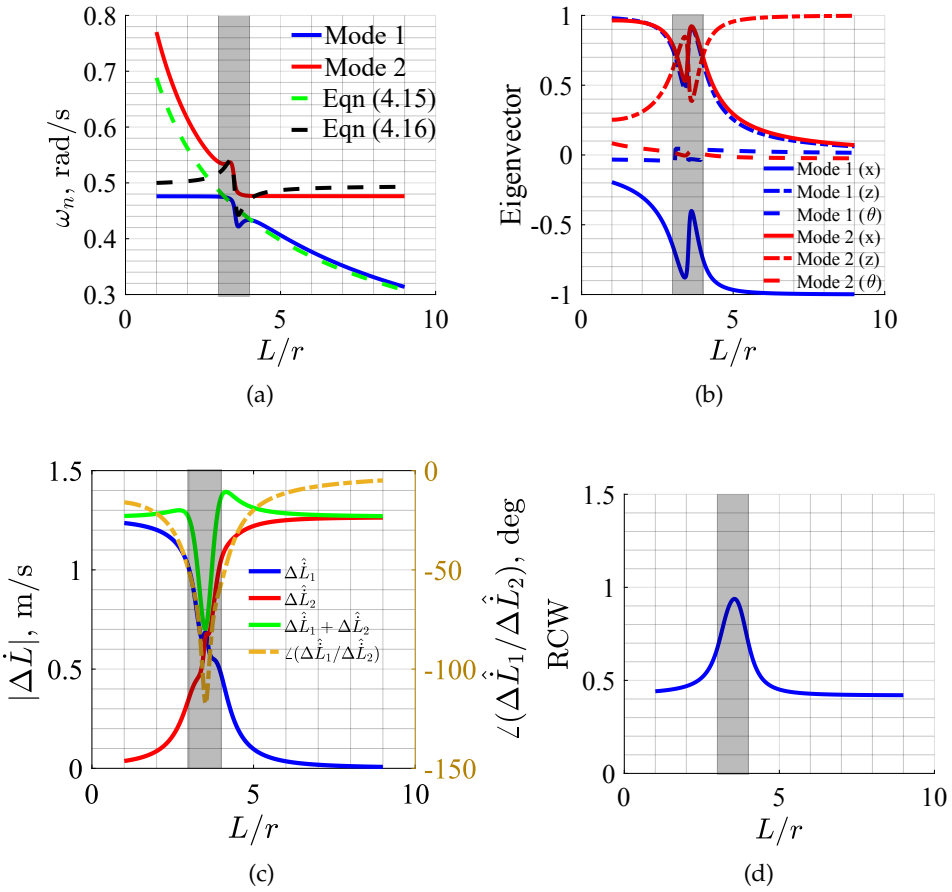

Figure 4.10: Analysis of the SPAMD for various ratios of nominal tether length to buoy radius, when the wave frequency is 0.48 rad/s: (a) natural frequencies of Mode 1 and 2, compared against the natural frequencies of the decoupled modes given by Equations (4.15) and (4.16); (b) eigenvectors of Mode 1 and 2; (c) PTO extension velocities arising from Mode 1 and 2, and relative phase difference $\angle(\Delta\hat{\dot{L}}_1/\Delta\hat{\dot{L}}_2)$, and total PTO velocity; (d) RCW of the SPAMD.

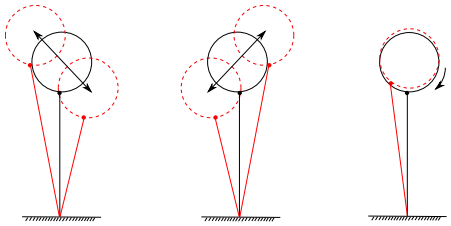

Figure 4.11: Mode shapes of the SPAMD under the optimal condition of nominal tether length: (a) Mode 1 oscillating at -45° in the Cartesian space; (b) Mode 2 oscillating at 45° in the Cartesian space; (c) Mode 3 pitching in the Cartesian space.

4.5.2 Modal analysis as a function of wave frequency

The modal analysis of the SPAMD was extended to understand the operation principles of the PA at optimal working conditions over the wave frequencies of interest. The wave frequencies ranged from 0.34 to 1.4 rad/s, and the system was analysed by using 30 discrete frequencies within this range. For each sampled wave frequency, the optimal PTO stiffness, the optimal PTO damping coefficient and the optimal nominal tether length were found by using the MATLAB optimization function "fmincon", within the defined range of tether length L.

Figure 4.12 illustrates the natural frequencies (see Figure 4.12a), mode shapes (see Figures 4.12b and 4.12c), phase difference, ψ, between Mode 1 and 2 under forced excitation (see Figure 4.12d), optimal nominal tether length (see Figure 4.12e) and wave energy harvesting efficiency (see Figure 4.12f) of the SPAMD respectively, over the wave frequencies of interests. The SPAMD operates under three different regimes (i.e., I, II and III) throughout the frequencies of interest, which are discussed in the following.

Regime I ($\omega < 0.5$ rad/s)

In this regime, Mode 1 and 2 both oscillate in resonance with the incident waves. From Figure 4.12a, it can be seen that the natural frequencies of Modes 1 and 2 match the wave frequencies, which implies that these two modes are resonant. Note that the oscillation Mode 3, which is pitch-dominant, has a significantly higher natural frequency in comparison to the wave frequency range of interest. Figures 4.12b and 4.12c show that Mode 1 and 2 contain almost equal surge and heave motions in Regime I, which implies these two modes oscillate at $\pm 45^\circ$ with respect to the Cartesian space. Figure 4.13

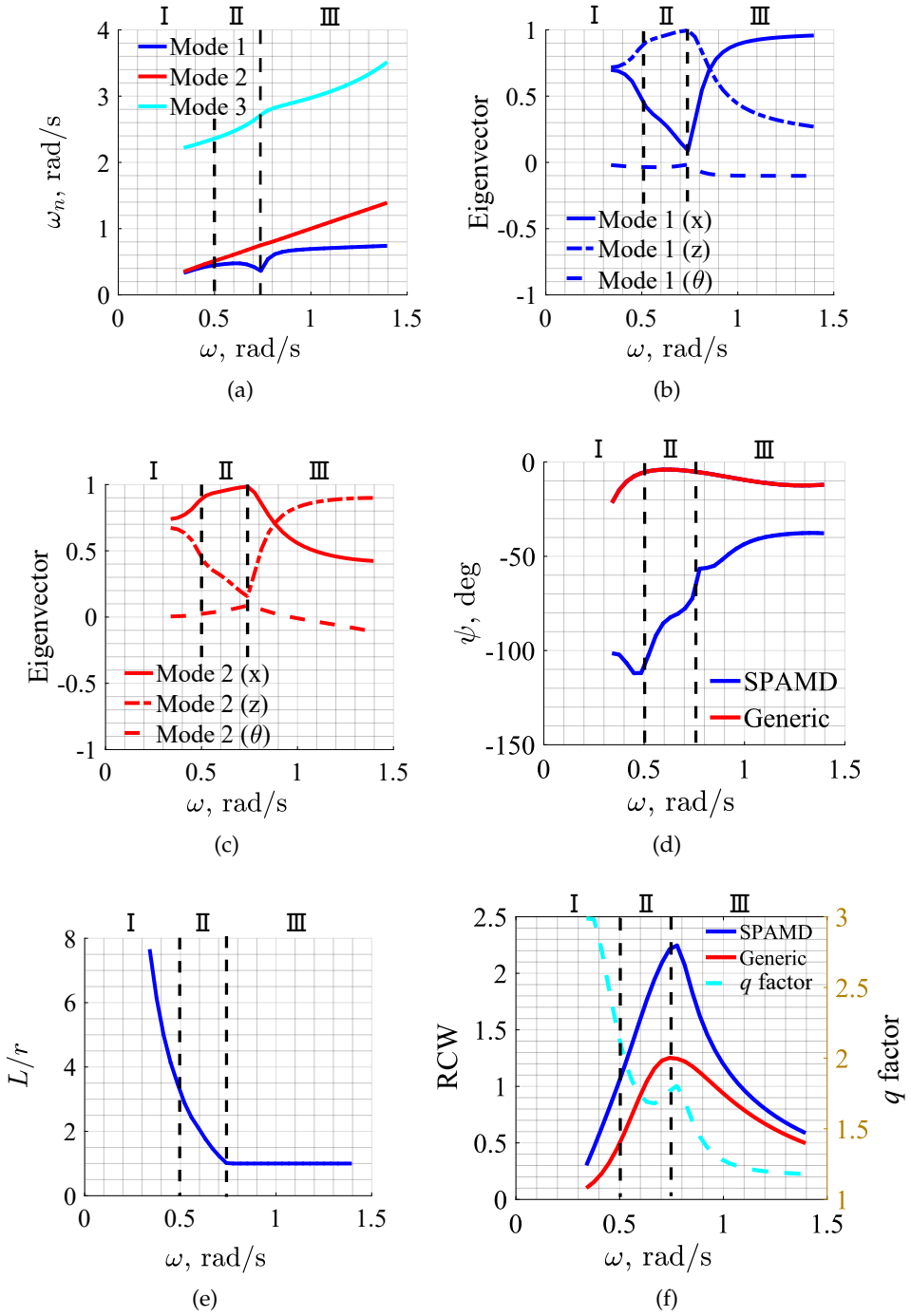

Figure 4.12: Analysis of the SPAMD buoy with optimal PTO configurations (i.e. K_{pto}, B_{pto} and L) for wave frequencies ranging from 0.34 to 1.4 rad/s: (a) the natural frequencies of three modes; (b) eigenvectors of Mode 1; (c) eigenvectors of Mode 2; (d) phase difference between Mode 1 and 2 under forced excitation; (e) the optimal nominal tether length; (f) RCW and the q factor.

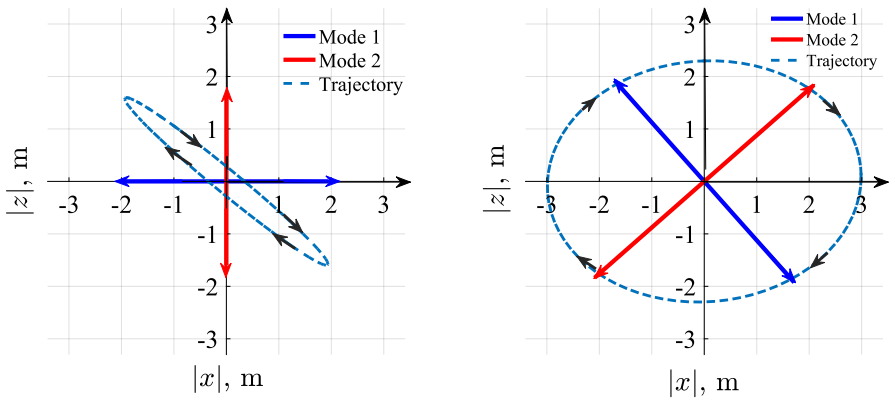

Figure 4.13: Trajectory and mode shape for ω = 0.4 rad/s: (a) generic PA; (b) SPAMD.

compares the orientations and amplitudes of oscillation modes (Mode 1 and 2), as well as resulting motion trajectory between the generic PA and the SPAMD at the wave frequency ω =0.4 rad/s. It can be seen that for the SPAMD, Mode 1 and 2 have equal amplitudes and orientate to $\pm 45^{\circ}$ in the Cartesian space, while the modes of the generic PA purely oscillate along X and Z axis. For the generic PA, the phase difference between Mode 1 and 2, ψ, approaches zero (see Figure 4.12d), which means the oscillation modes reach their peaks and troughs almost simultaneously. As a result, the aspect ratio of the elliptical trajectory of the generic PA is considerably high (i.e., a thin ellipse). In contrast, the phase difference of the oscillation modes of the SPAMD remain approximately -105°, and therefore the trajectory of the SPAMD tends to be circular. Noting that the circular trajectory can drive the PTO more efficiently than the highly elliptical one. The significance of the circular trajectory to PAs is discussed at the end of this section.

In Figure 4.12e, the optimal nominal tether length declines as the wave frequency increases in order to match the natural frequencies of Mode 1 and Mode 2 to the wave frequency. As the wave energy is captured by surge and heave motion of the buoy, the RCW of the SPAMD is improved up to three times in comparison to the generic PA, as shown in Figure 4.12f. The threefold efficiency improvement reflects the Falnes' theory that the point absorber utilizing 3DOF motion (surge, heave and pitch) to harvest wave energy can be theoretically three times more efficient than the point absorber using heave-only [4].

Regime II (0.5 rad/s $< \omega <$ 0.74 rad/s)

In Regime II, only Mode 2 (surge-dominant) oscillates in resonance with the incident waves. From Figure 4.12a, it can be seen that only the natural frequency of Mode 2 matches the wave frequency, whereas the natural frequency of Mode 1 increasingly deviates from the wave frequency. The natural frequency curve of Mode 1 reaches a notch at the wave frequency of 0.74 rad/s when the minimum tether limit is reached. The factors that determine the shape of the notch are investigated in next chapter. Figures 4.12b and 4.12c show that Mode 1 tends to be heave-dominant, whereas Mode 2 tends to be surge-dominant until the wave frequency of 0.74 rad/s. Figure 4.14 compares the orientations and amplitudes of oscillation modes (Mode 1 and 2), and resulting motion trajectory between the generic PA and the SPAMD at the wave frequency ω =0.6 rad/s. It can be seen that for the SPAMD, the orientations of Mode 1 and 2 approach Z and X axis. Furthermore, since only surge-dominant Mode 2 oscillates in resonance with the incident waves, the trajectory of the SPAMD becomes a horizontal ellipse.

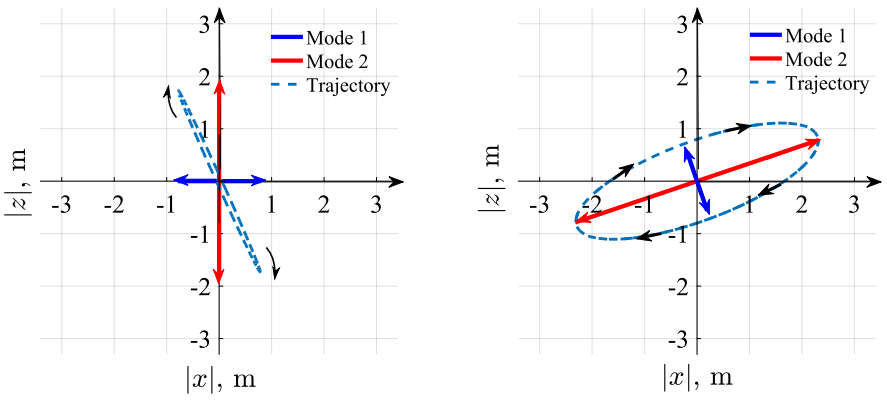

(a) (b)

Figure 4.14: Trajectory and mode shape for ω = 0.6 rad/s: (a) generic PA; (b) SPAMD.

In this regime, since the SPAMD is no longer resonant in heave, the maximum RCW of the SPAMD declines from 3 times to 1.8 times that of the generic PA, as shown in Figure 4.12f. This is to be expected given that the SPAMD is essentially operating in surge which can deliver a two-fold

increase in RCW.

Regime III (0.74 rad/s $< \omega$)

In Regime III, only Mode 2 (heave-dominant) oscillates in resonance with the incident waves. From Figure 4.12a, it can be seen that only the natural frequency of Mode 2 can match the wave frequency. In contrast, the natural frequency of Mode 1 is much lower than the wave frequency. For wave frequencies over 0.74 rad/s, the length of the tether reaches its lower limit (L_{min} = 5 m), which also provides a limit on the surge mode natural frequency. Consequently, the SPAMD is no longer resonant in surge, which limits the amount of wave energy via the surge motion. From Figure 4.12c, it can be seen that Mode 2 contains motion in both translational degree of freedoms (i.e., surge and heave), but the SPAMD mainly uses resonant heave motion to capture the wave energy, especially in higher frequencies. Figure 4.15 compares the orientations and amplitudes of oscillation modes (Mode 1 and 2), and resulting motion trajectory between the generic PA and the SPAMD at the wave frequency ω =0.88 rad/s. It can be seen that for the SPAMD, the orientations of Mode 1 and 2 tend to rotate towards X and Z axis as the frequency increases. Furthermore, since the phase difference between Mode 1 and 2 approaches zero, the trajectory of the SPAMD tends to be highly elliptical as for the generic PA. As a result, the RCW of the SPAMD starts to converge to that of the generic PA, as shown in Figure 4.12f.

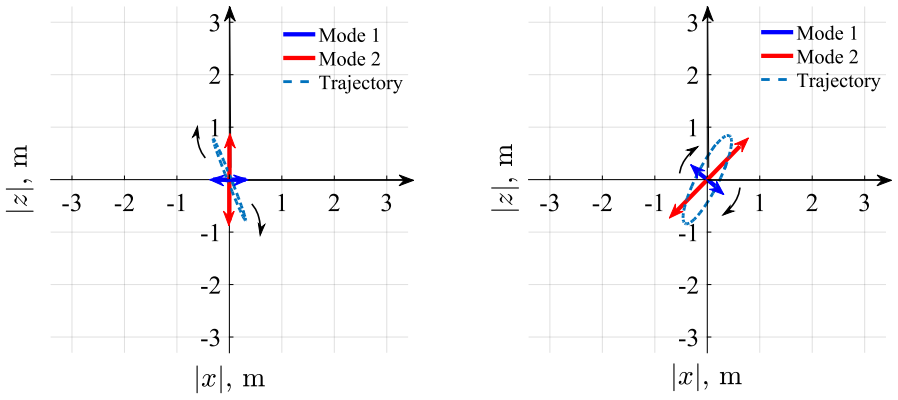

(a) (b)

Figure 4.15: Trajectory and mode shape for ω = 0.88 rad/s: (a) generic PA; (b) SPAMD.

It can be concluded that the efficiency of the SPAMD depends highly on the shape of the buoy's trajectory. The circular trajectory of the SPAMD which occurs at low frequencies was found to be the most productive. As shown in Figure 4.13b and 4.12d, the circular trajectory requires that the modes of the SPAMD are equal in amplitude with a phase difference around $\pm 90^{\circ}$. A similar behaviour was found with the Bristol Cylinder [3], where a circular trajectory was found to maximise power production. This knowledge can be used to design the potential control algorithm for the SPAMD, in which the amplitudes and phases of the oscillation modes are controlled to achieve the circular trajectory.

4.5.3 Power analysis

The surge motion of the SPAMD buoy couples to the PTO via motion coupling (surge-heave or surge-pitch) arising from offsetting the centre of mass of the buoy. A power analysis has been performed to understand the contributions of the buoy motions to the power output of the system. Figure 4.16 shows the power output contribution from the motion of the buoy calculated from Equation (4.27) (see Figure 4.16a) and the corresponding velocity amplitude of the heave, surge and pitch movements (see Figure 4.16b, 4.16c and 4.16d) across the three operation regimes. From Figure 4.16a, in Regime I, the entire power output of the SPAMD directly arises from the buoy's heave motion. This is because the heave oscillation of the buoy is enhanced by the surge motion via surge-heave motion coupling, as shown in Figure 4.16c. As it is the low frequency surge (and sway) motion that defines the buoy's mooring watch circle, such surge suppression is an advantage. In contrast, the power arising from the heave-pitch coupled motion is negative, which implies that a part of the power returns to the environment via this coupled motion. This phenomenon will be investigated in the future. In Regime II, the pitch motion of the buoy is enhanced by the resonant surge motion via surge-pitch motion coupling, as evident in Figure 4.16d. Consequently, from Figure 4.16a, it can be seen that the power arising from the heave motion declines, whereas the power arising from the pitch and the heave-pitch coupled motion increase. In Regime III, the power arising from the heave motion increasingly becomes dominant, whereas the power from the pitch motion and from the heave-pitch coupled motion declines. This is because the SPAMD mainly uses the resonant heave motion of Mode 2 to capture the wave energy in Regime III.

In Figure 4.17, the optimal PTO stiffness and damping coefficient of the SPAMD and the generic PAs are compared over the three regimes. In Regime I, as the SPAMD mainly harvests the power arising from the buoy's

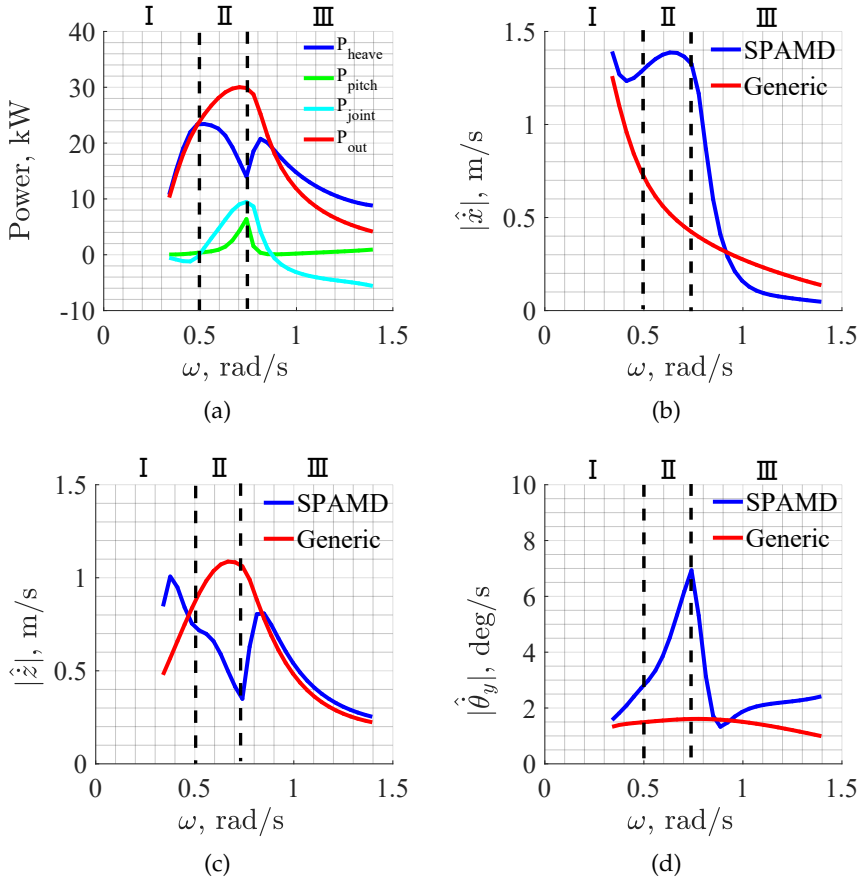

Figure 4.16: Power analysis of the SPAMD and velocity amplitudes in the surge, heave and pitch directions over the wave frequencies of interest: (a) power output analysis of the SPAMD; (b) surge velocity amplitude; (c) heave velocity amplitude; (d) pitch velocity amplitude.

heave motion, the optimal PTO stiffness is identical to that of the generic PA. Whereas, the optimal PTO damping coefficient of the SPAMD is significantly greater than that of the generic PA because the heave motion of the SPAMD is enhanced by the surge motion via surge-heave motion coupling. In Regime II, as SPAMD mainly harvests the power arising from the buoy's surge motion, the optimal PTO stiffness and damping coefficient are distinct from these of the generic PA. In Regime III, although the SPAMD mainly utilizes resonant heave motion to capture wave energy, the optimal PTO configuration of the SPAMD still significantly differs from that of the generic PA for the wave frequency $\omega > 1.2$ rad/s. This is because the heave and pitch motion of the SPAMD tend to be strongly coupled at very high frequencies, which will be

investigated in future work.

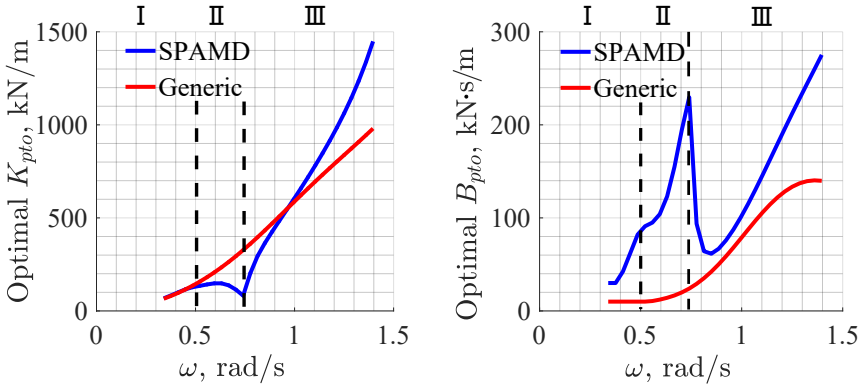

Figure 4.17: The comparison of optimal PTO stiffness and damping coefficient between the SPAMD and the generic PAs across the three regimes: (a) optimal PTO stiffness; (b) optimal PTO damping coefficient.

4.6 Conclusion

In this paper, an asymmetric mass buoy is employed to improve the efficacy of fully submerged single-tether spherical point absorbers by harvesting the wave energy from both surge and heave directions. The results of the modal analysis show that the efficiency of the SPAMD is significantly affected by the nominal tether length, unlike the generic PA. Furthermore, the SPAMD operates under three different operation regimes over the wave frequencies of interest. In Regime I, Modes 1 and 2 oscillate in resonance with the incident waves; in Regime II, only surge-dominant Mode 2 oscillates in resonance with the incident waves; in Regime III, only the heave-dominant Mode 2 oscillates in resonance with the incident waves. The maximum efficiency of the SPAMD can be three times higher than the generic PAs for low frequencies (see Figure 4.12f), which implies that the SPAMD has significant commercial potential. Given that this work used the assumption of small wave amplitudes, to assess the efficiency improvement of the SPAMD in large wave amplitudes (e.g. >1 m typical wave amplitudes), a numerical wave tank test is required and forms future work. Furthermore, since the efficiency of the SPAMD is affected by the nominal tether length, the mechanism for achieving the optimal tether length must be considered in practice. The steel-frame riser employed to achieve the optimal tether length in this work might be the dominant cost

driver in the system design. Deploying the device in shallow water or sharing the underwater structure with offshore platforms might be two potential solutions to reduce the cost of the SPAMD.

Acknowledgement

This research is supported by China Scholarship Council (CSC), Australia Research Council (ARC) Linkage Grant (LP130100117) and the Research Training Program (RTP). We also thank Nataliia Sergiienko, Alison-Jane Hunter and Jonathan David Piper for their comments that greatly improved the manuscript.

Appendix 4.A

With reference to the geometric centre of the buoy in Figure 4.4, the torque generated by the offset mass m_2 should be balanced by the torque generated by the PTO pretension force F_{pre} when the buoy is at rest, hence

$$F_{pre} r \sin(\alpha) = m_2 g r_{gy} \cos(\varphi) \quad , \tag{4.A.1}$$

for $-\pi/2 \leq \varphi \leq \pi/2$ and $0 \leq \alpha \leq \pi/2$.

When the buoy rotates a small pitch angle θ_y, the net moment M_{net} can be calculated by

$$M_{net} = m_2 g r_{gy} \cos(\varphi + \theta_y) - F_{pre} r \sin(\alpha + \theta_y) \quad , \tag{4.A.2}$$

which can be simplified to

$$M_{net} = -\sin(\theta_y)[F_{pre} r \cos(\alpha) + m_2 g r_{gy} \sin(\varphi)] \quad . \tag{4.A.3}$$

For the system to be stable in the pitch direction, the derivative of the net moment with respect to the pitch angle must be negative, hence

$$\frac{\partial M_{net}}{\partial \theta_y} = -\cos(\theta_y)[F_{pre} r \cos(\alpha) + m_2 g r_{gy} \sin(\varphi)] < 0 \quad . \tag{4.A.4}$$

For the small angle assumption, $\cos(\theta_y) > 0$, and therefore the following condition must hold

$$F_{pre} r \cos(\alpha) + m_2 g r_{gy} \sin(\varphi) > 0 \quad . \tag{4.A.5}$$

For $0 \leq \varphi \leq \pi/2$, Equation (4.A.5) is always true; For $-\pi/2 \leq \varphi \leq 0$, since $r\cos(\alpha) = |z_m|$ and $r_{gy}\sin(\varphi) = -|z_2|$, Equation (4.A.5) can be simplified as

$$F_{pre}|z_m| - m_2 g|z_2| > 0 \quad . \tag{4.A.6}$$

As $r^2 = x_m^2 + z_m^2$ and $F_{pre}|x_m| = m_2 g|x_2|$, Equation (4.A.6) can be expressed as

$$F_{pre}\sqrt{r^2 - (\frac{m_2 g|x_2|}{F_{pre}})^2} > m_2 g|z_2| \quad . \tag{4.A.7}$$

As both sides are positive, squaring both sides and re-arranging the inequality gives

$$F_{pre} r > m_2 g r_{gy} \quad . \tag{4.A.8}$$

As defined in Section 4.2, the pretension force F_{pre} is given by

$$F_{pre} = \rho V g - mg = (m_w - m)g \quad . \tag{4.A.9}$$

in which ρ is water density, $V = \frac{4}{3}\pi r^3$ is the volume of spherical buoy, $m_w = \rho V$ is the mass of water displaced by the submerged spherical buoy.

Substituting Equation (4.A.9) into Equation (4.A.8) gives the stability condition

$$\frac{r_{gy}}{r} < (\frac{m_w - m}{m_2}) \quad . \tag{4.A.10}$$

To conclude, with the condition that the buoy is balanced at its rest pose, the system is capable of maintaining stability during the operation if $0 \leq \varphi \leq \pi/2$, or $\frac{r_{gy}}{r} < (\frac{m_w - m}{m_2})$ for $-\pi/2 \leq \varphi < 0$.

Appendix 4.B

As mentioned in Section 4.3, the hybrid frequency-domain model is built upon the small displacement assumption. In this section, the assumption is justified by presenting the motion amplitude of the SPAMD over the wave frequencies of interest. Figure 4.18 shows the motion amplitude of the SPAMD in surge, heave and pitch. It can be seen that the heave amplitude remains less than 3 m, which means the buoy will not breach the water surface (the top surface of the buoy is 3m below the water surface at its rest pose). Furthermore, the pitch displacement remains less than 10°, which

means the first-order Taylor series expansion applied to Equations (4.9) and (4.12) remains valid [11].

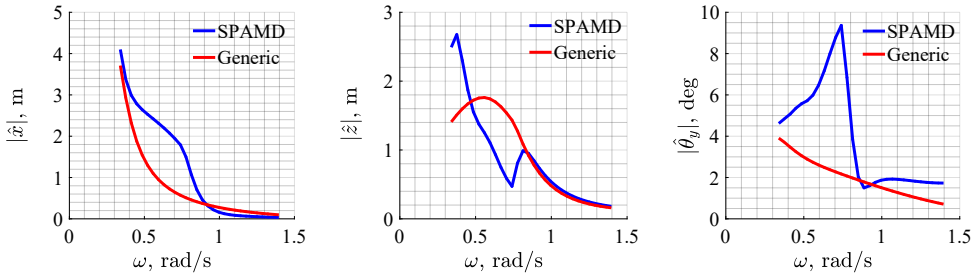

Figure 4.18: The comparison of the motion amplitude between the SPAMD and the generic PA with optimised PTO configuration over the frequency range of interest: (a) surge; (b) heave; (c) pitch.

References

[1] Australian Wave Energy Atlas (2016, accessed 07 June 2016). [Online]. Available: http://awavea.csiro.au/.

[2] Blevins, R. D. (2003). *Applied fluid dynamics handbook*. Krieger Publishing Company.

[3] Evans, D., Jeffrey, D., Salter, S. and Taylor, J. (1979). "Submerged cylinder wave energy device: theory and experiment". In: *Applied Ocean Research* 1.1, pp. 3–12.

[4] Falnes, J. (2002). *Ocean waves and oscillating systems: Linear interactions including wave energy extraction*. Cambridge University Press.

[5] Greenhow, M., Vinje, T., Brevig, P. and Taylor, J (1982). "A theoretical and experimental study of the capsize of Salter's duck in extreme waves". In: *Journal of Fluid Mechanics* 118, 221–239.

[6] Lee, C. H. (1995). *WAMIT Theory Manual*. Massachusetts Institute of Technology, Department of Ocean Engineering.

[7] Linton, C. (1991). "Radiation and diffraction of water waves by a submerged sphere in finite depth". In: *Ocean Engineering* 18.1, pp. 61–74.

[8] Meng, F, Cazzolato, B, Ding, B and Arjomandi, M (2017). *Technical report: Model validation of the submerged spherical point absorber with asymmetric mass distribution*. Tech. rep. University of Adelaide.

[9] Morison, J., Johnson, J. and Schaaf, S. (1950). "The force exerted by surface waves on piles". In: *Journal of Petroleum Technology* 2.05, pp. 149–154.

[10] Nokob, M. H. and Yue, D. K. P. (2012). "The Heave And Pitch Power Output of a Vertical Cylindrical Wave Energy Converter In Finite-Depth Water". In: *The Twenty-second International Offshore and Polar Engineering Conference*. International Society of Offshore and Polar Engineers, pp. 613–620.

[11] O'Neil, P. V. (2011). *Advanced engineering mathematics*. Cengage learning.

[12] Rafiee, A. and Fievez, J. (2015). "Numerical prediction of extreme loads on the CETO wave energy converter". In: *Proceedings of the 11th European Wave and Tidal Energy Conference*. Nantes, France, 09A1–2.

[13] Sergiienko, N., Cazzolato, B., Ding, B. and Arjomandi, M (2016a). "An optimal arrangement of mooring lines for the three-tether submerged point-absorbing wave energy converter". In: *Renewable Energy* 93, pp. 27–37.

[14] Sergiienko, N., Cazzolato, B., Ding, B. and Arjomandi, M. (2016b). "An optimal arrangement of mooring lines for the three-tether submerged point-absorbing wave energy converter". In: *Renewable Energy* 93, pp. 27–37.

[15] Srokosz, M. (1979). "The submerged sphere as an absorber of wave power". In: *Journal of Fluid Mechanics* 95.04, pp. 717–741.

[16] Yurchenko, D. and Alevras, P. (2018). "Parametric pendulum based wave energy converter". In: *Mechanical Systems and Signal Processing* 99, pp. 504 –515.

Chapter 5

A sensitivity study on the effect of mass distribution of a single-tether spherical point absorber

As analysed in the previous chapter, the efficiency of a single-tether submerged spherical point absorber in monochromatic waves can be significantly improved by using a buoy with asymmetric mass distribution. The resulting motion coupling between the surge and heave motion allows the energy arising from surge motion to be transferred to the PTO unit via the single tether. Therefore, the SPAMD is able to achieve energy harvesting efficiencies similar to equivalent multi-tether devices for some wave frequencies, which is three times that of the generic single-tether device.

The modal analysis conducted in the previous chapter also indicates that the SPAMD can not always achieve the three times efficiency improvement in monochromatic waves for all the wave frequencies of interest, which implies the optimal motion coupling is sensitive to the frequency. As the motion coupling is generated by the asymmetric mass distribution, this chapter is designed to provide answers to the following research questions: *1. How does the mass distribution of a spherical buoy affect the performance of a single-tether point absorber? 2. How efficient is the SPAMD in typical sea sites?*

This chapter consists of the following published journal article:
Meng, F., Cazzolato, B. S., Li, Y., Ding, B., Sergiienko, N. and Arjomandi, M. (2019). "A sensitivity study on the effect of mass distribution of a single-tether spherical point absorber". ***Renewable Energy*** **141, pp. 583 -**

595.

The article in its published format is available at `https://doi.org/10.1016/j.renene.2019.03.149`.

Statement of Authorship

Title of Paper	A sensitivity study on the effect of mass distribution of a single-tether spherical point absorber
Publication Status	☑ Published ☐ Accepted for Publication ☐ Submitted for Publication ☐ Unpublished and Unsubmitted w ork w ritten in manuscript style
Publication Details	Meng, F., Cazzolato, B. S., Li, Y., Ding, B., Sergiienko, N. and Arjomandi, M. (2018). "A sensitivity study on the effect of mass distribution of a single-tether spherical point absorber". *Renewable Energy* 141, pp. 853 – 859.

Principal Author

Name of Principal Author (Candidate)	Fantai Meng
Contribution to the Paper	Developed the idea and concepts, developed the mathematical model, wrote the code of simulations and optimisations, interpreted the results, wrote the manuscript and acted as a corresponding author.
Overall percentage (%)	75%
Certification:	This paper reports on original research I conducted during the period of my Higher Degree by Research candidature and is not subject to any obligations or contractual agreements with a third party that would constrain its inclusion in this thesis. I am the primary author of this paper.
Signature	Date 21/8/19

Co-Author Contributions

By signing the Statement of Authorship, each author certifies that:

i. the candidate's stated contribution to the publication is accurate (as detailed above);

ii. permission is granted for the candidate in include the publication in the thesis; and

iii. the sum of all co-author contributions is equal to 100% less the candidate's stated contribution.

iv.

Name of Co-Author	Benjamin S. Cazzolato
Contribution to the Paper	Helped in developing ideas and parametric optimisation algorithm, encouraged to perform the power assessment of the mechanism, supervised the work, helped in interpretation of obtained results, and provided a critical revision of the manuscript.
Signature	Date 21/8/19

Name of Co-Author	Ye Li
Contribution to the Paper	Helped in developing ideas and interpretation of obtained results, and provided a critical revision of the manuscript.
Signature	Date 2019.8.21

Name of Co-Author	Nataliia Sergiienko		
Contribution to the Paper	Supervised the work, helped in interpretation of obtained results, and provided a critical revision of the manuscript.		
Signature		Date	21/08/2019

Name of Co-Author	Boyin Ding		
Contribution to the Paper	Supervised the work, helped in interpretation of obtained results, and provided a critical revision of the manuscript.		
Signature		Date	21/8/19

Name of Co-Author	Maziar Arjomandi		
Contribution to the Paper	Supervised the work, helped in interpretation of obtained results, and provided a critical revision of the manuscript.		
Signature		Date	21/08/2019

Please cut and paste additional co-author panels here as required.

A sensitivity study on the effect of mass distribution of a single-tether spherical point absorber

F. Meng, B. S. Cazzolato, Y. Li, B. Ding, N. Y. Sergiienko, M. Arjomandi

Abstract

In previous work, a single-tether submerged spherical point absorber with asymmetric mass distribution (SPAMD) was proposed to enable harvesting wave energy induced by the surge and heave motion of the buoy. By taking advantage of the motion coupling arising from the asymmetric mass distribution of the buoy, the SPAMD was found to be up to three times more efficient than a generic single-tether point absorber (with uniform mass distribution buoy) under regular waves. For motion-coupled systems like the SPAMD, the mass distribution is a significant factor that governs the kinematics and the efficiency of the device. Therefore, in this paper, a 3DOF (surge, heave and pitch) spectral-domain model considering viscous drag was developed, to investigate the sensitivity of the mass distribution on the power output of the SPAMD in irregular waves. The aim of the sensitivity study is to provide a guideline for the wave energy industry when designing such devices. At the end of this paper, the yearly mean power output of the SPAMD with optimal mass distribution was assessed at three test sites near Yeu Island (France), Perth (Australia) and Sydney (Australia). It was found that in such sea sites, the SPAMD was at least 1.5 times more efficient than the generic single-tether point absorber, indicating that the SPAMD might have a significant commercial potential. Furthermore, for the three sites investigated, the performance of the SPAMD was found to be relatively tolerant to non-optimal PTO configuration, implying that sea-state specific tuning is unnecessary.

5.1 Introduction

With the concerns of global warming and environmental pollution brought on by the burning of fossil fuels, renewable energy is regarded as a significant resource to generate clean electricity. Among the many types of renewable energy, ocean wave energy is one of the commercially viable renewable resources. As the ocean covers the 71% of earth surface, the worldwide potential of ocean wave energy is estimated to be 3.7 Terawatts [7]. Furthermore, electricity generation by using ocean wave energy is more continuous than

solar and wind energy, because ocean wave energy is available more than 90% of year, while solar and wind only have 20%-30% availability [16].

Currently, many conceptual designs of wave energy converter (WEC) have been developed and tested in the hope of commercialising ocean wave energy exploitation. The point absorber (PA) with one or multiple power take-off devices (PTO) is one of the promising WECs, drawing attention from both academic and industrial fields. Point absorbers convert the ocean wave energy into the mechanical energy of the oscillating buoy which in turn drives the coupled PTO. One advantage of point absorber is that it can extract energy from the near-field incident wavefronts by interacting with the incident waves, resulting in a relative capture width (RCW) greater than one [5].

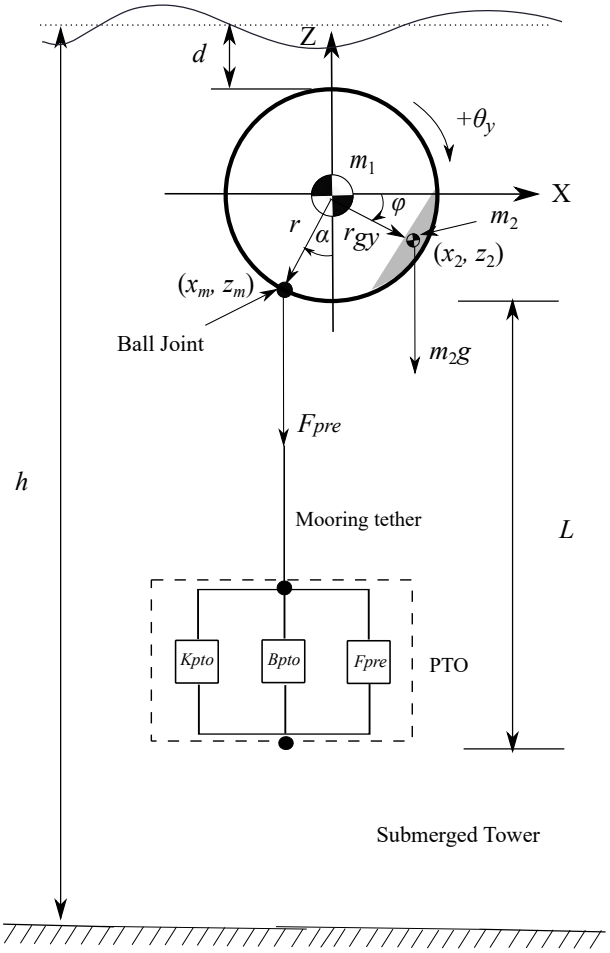

Figure 5.1: Schematic of the SPAMD in the vertical XZ-plane (approximately to scale).

To ensure a PA operates efficiently when deployed at individual sites, the geometry of the buoy is generally regarded as a crucial parameter for optimisation in the design of the PA. This is because the buoy geometry determines the hydrodynamic characteristics of the fluid-structure interaction. For example, Pastor and Liu [15] tested two floating buoys with various bottom shapes, drafts and diameters in the sea states occurring near Gulf of Mexico, to demonstrate that a conical buoy with a 2 m draft and 6.5 m diameter has the best performance in the defined sea site. On the other hand, some studies treat the geometry optimization as a multi-objective problem which includes the cost of manufacturing the buoy, the requirement on the strength of the mooring system and the effectiveness of the control algorithm. For example, Kurniawan and Moan [10] optimised the dimension of a floating cylindrical PA to achieve maximum power output and minimum surface area of buoy in an effort to reduce the cost of the buoy.

For wave energy converters with asymmetric mass distribution (e.g. Edinburgh Duck [4], Bristol Cylinder [13] and Solo Duck [17]), the mass distribution of a buoy is a factor that governs the system performance and thus needs to be considered in optimisation. For example, Cruze and Salter [4] investigated positioning the off-centred rotational axis on the cylindrical Edinburgh Duck, to vary the moment of inertia of the device for maximising the power output in monochromatic waves. However, there is no study systematically investigating the impact of the mass distribution of the buoy on the system performance.

In the previous work by the authors [6, 14], the design concept of a spherical point absorber with asymmetric mass distribution (SPAMD) was introduced. The SPAMD utilizes motion-coupling of the asymmetric mass distribution of the buoy to enable the single-tether PA to absorb power induced by its surge and heave motion. The power output of the SPAMD [14] is also impacted by the mass distribution of the device, however the impact is yet to be quantified. For the current paper, a sensitivity study of the impact that the mass distribution has on the average power output of the SPAMD was conducted, with the aim to understand the correlation between the mass distribution and the performance of the SPAMDs. Furthermore, in this study, the SPAMD with optimal mass distribution is benchmarked against a generic single-tether PA on the basis of the yearly mean power outputs at three test sites: Yeu island (France), Perth (Australia) and Sydney (Australia).

The structure of the paper is as follows. In Section 5.2, the SPAMD system was introduced, together with the definitions of the mass distribution, PTO and sea states for power output assessment. In Section 5.3, a 3DOF spectral-domain model of the SPAMD is derived to provide a computationally efficient

tool for evaluating the power performance of the SPAMD for optimisation in irregular waves. In Section 5.4, the sensitivity of the buoy's mass distribution is studied by using the spectral-domain model. In Section 5.5, the yearly mean power output of the SPAMD with optimal mass distribution is assessed at various test sites.

5.2 Description of the system

As shown in Figure 5.1, the SPAMD consists of a spherical buoy with asymmetric mass distribution (a spherical hull m_1 and an offset mass m_2). An idealised linear PTO is connected to the buoy via a mooring tether with the length of L at rest. It is assumed that the PTO consists of a linear spring with stiffness, K_{pto}, a linear damper with damping coefficient, B_{pto}, and a pretension force, F_{pre}, that balances the net buoyancy of the buoy. The incident waves propagate along the positive X-axis and only excite the SPAMD in surge, heave and pitch. As discussed in the previous work [14], the mooring tether length is an important tuning parameter for the SPAMD as it governs the natural frequency of the system in surge. In order to investigate the performance of the SPAMD with various mass distributions over a wide range of frequencies, the sea should be sufficiently deep to allow a long tether length for low wave frequencies, such as the water depth h = 60 m in this work. Furthermore, to achieve the desired tether length in the defined water column, the SPAMD is anchored on a submerged tower. The buoy at rest has a constant submergence depth $d_s = 3$ m (from the top of the buoy to the water surface). As the submerged structure might significantly increase the cost of project, it is recommended to implement the SPAMD system near-shore in practice. This sensitivity study, which is analysed for deep water, remains valid for near-shore sites because the mass distribution only determines how motion modes become coupled and therefore it is independent from the hydrodynamics.

5.2.1 Mass distribution

According to Lee [11], for a 3DOF (i.e., surge, heave and pitch) spherical buoy with an additional offset point mass m_2, the mass matrix with respect to the geometric centre of the buoy is given by

$$\mathbf{M} = \begin{pmatrix} m_1 + m_2 & 0 & m_2 z_2 \\ 0 & m_1 + m_2 & -m_2 x_2 \\ m_2 z_2 & -m_2 x_2 & I_{yy} \end{pmatrix} , \tag{5.2.1}$$

where the total mass of the buoy is $m = m_1 + m_2$, the total moment of inertia is $I_{yy} = I_1 + I_2 = \frac{2}{3}m_1r^2 + m_2r_{gy}^2$ (r_{gy} is the offset distance, as shown in Figure 5.1), the location of the offset mass m_2 is (x_2, z_2).

From Equation (5.2.1), it can be seen that the mass distribution is affected by three factors: the total mass m, the ratio of spherical hull mass m_1 to the offset mass m_2 and the mass offset coordinates (x_2, z_2). Therefore, four independent parameters are correspondingly defined in this work, namely weight-to-buoyancy ratio m/m_w (where m_w is the mass of displaced water), the mass ratio m_1/m_2 and the mass offset position (r_{gy}, φ). In Section 5.4, sensitivity studies on these parameters are conducted to investigate the impact of the mass distribution on the power output of the SPAMD.

5.2.2 Power take-off configuration

As mentioned previously, the PTO comprises a spring-damper mechanism (K_{pto} and B_{pto}). It is assumed that the averaged power output of the SPAMD is equal to the power consumed by the PTO damper, given by

$$P = \frac{1}{2}B_{pto}(\Delta\dot{L})^2 \quad , \tag{5.2.2}$$

where the $\Delta\dot{L}$ is the PTO elongation velocity. The corresponding average PTO loading (including dynamic and static components) is given by,

$$F_{pto} = -K_{pto}\Delta L - B_{pto}\Delta\dot{L} - F_{pre} \quad . \tag{5.2.3}$$

5.2.3 Sea states

In this work, the irregular sea states used a Modified Pierson-Moskowitz spectrum (ITTC [9]), with the wave spectral density function given by

$$S_f(\omega) = \frac{A_f}{\omega^5}\exp\left(-\frac{B_f}{\omega^4}\right) \quad , \tag{5.2.4}$$

with three parameters A_f, B_f and T_1 given by

$$A_f = \frac{4\pi^3 {H_s}^2}{T_1^4} \quad , \tag{5.2.5}$$

$$B_f = \frac{691}{T_1^4} \quad , \tag{5.2.6}$$

$$T_1 = 2\pi\frac{M_0}{M_1} \quad , \tag{5.2.7}$$

where ω is the wave frequency in the spectrum, H_s is the significant wave height, M_n is the nth moment of the frequency spectrum.

The spectra were linearly discretised into $n = 100$ sample frequencies from 0.02 rad/s to 2 rad/s ($\Delta\omega$=0.02 rad/s). The complex wave elevation of the jth sampled frequency is given by

$$\hat{A}_m(\omega_j) = \sqrt{2S_f(\omega_j)\Delta\omega}e^{i\Psi_j} \quad , \tag{5.2.8}$$

where the initial wave elevation phase Ψ_j of the jth sampled frequency was randomly chosen between 0 to 2π, to simulate the random process of the irregular wave elevation.

5.3 Spectral-domain modelling

In this section, a spectral-domain model was developed to enable a computationally efficient tool for conducting a sensitivity study (see Section 5.4) and power output assessment for various sea sites (see Section 5.5). The spectral-domain model was originally created as a probabilistic method to estimate the dynamics of ships in irregular waves [19]. Folley and Whittaker [8] then introduced this modelling method in their WEC study to accelerate the assessment of mean power output of a WEC under irregular sea states. The spectral-domain model is proven to be as accurate as the equivalent time-domain model for estimation of the WEC power output even in the presence of nonlinear effects [8].

In the spectral-domain model, assuming that the response to irregular waves can be separated into an array of orthogonal single-frequency responses, the resulting total power output is calculated by the principle of superposition [8], given by

$$P_{total} = \sum_{j=1}^{n} P_j \quad , \tag{5.3.1}$$

in which P_j is power output to the jth frequency component of irregular waves. According to Equation (5.2.2), P_j is given by

$$P_j = \frac{1}{2}B_{pto}|\Delta\hat{\dot{L}}_j|^2 \quad , \tag{5.3.2}$$

in which, as shown in the previous work by the authors [14], the complex PTO elongation velocity $\Delta\hat{\dot{L}}_j$ arising from the motion of the SPAMD excited by the jth frequency component of the irregular waves can be derived as

$$\Delta\hat{\dot{L}}_j = \mathbf{J}^{-1}\hat{\mathbf{x}}_j \quad , \tag{5.3.3}$$

where the inverse Jacobian matrix $\mathbf{J}^{-1} = (0, 1, r\sin(\alpha))$ converts the buoy's velocities in the Cartesian space $\hat{\dot{\mathbf{x}}} = (\hat{\dot{x}}, \hat{\dot{z}}, \hat{\dot{\theta}}_y)^{\mathbf{T}}$ into the PTO elongation velocity, in which $\hat{\dot{x}}$ is the complex surge velocity, $\hat{\dot{z}}$ is the complex heave velocity and $\hat{\dot{\theta}}_y$ is the complex pitch velocity.

For given array of $\Delta\hat{L}_j$ (j = 1, 2, 3, ..., n), the resulting root-mean-square PTO loading (including dynamic and static components) under irregular waves is given by

$$\hat{F}_{pto,irregular} = \sqrt{\frac{1}{2}\sum_{j=1}^{n} |\hat{F}_{pto,j}|^2} \quad , \tag{5.3.4}$$

where the $\hat{F}_{pto,j}$ is the average PTO loading of the jth frequency component, as given by Equation (5.2.3).

From the previous work by the authors [14], the equation of motion in the frequency-domain is given by

$$\hat{\mathbf{x}}_j = [i\omega_j(\mathbf{M} + \mathbf{A}(\omega_j)) + (\mathbf{B}(\omega_j) + \mathbf{B}_{pto} + \mathbf{D}) + \mathbf{K}_{pto}/i\omega_j]^{-1}\hat{\mathbf{F}}_{exc}(\omega_j) \quad , \tag{5.3.5}$$

where $\mathbf{M}$ is the mass matrix of the asymmetric mass buoy, given by Equation (5.2.1):

$$\mathbf{A}(\omega_j) = \begin{pmatrix} A_x(\omega_j) & 0 & 0 \\ 0 & A_z(\omega_j) & 0 \\ 0 & 0 & 0 \end{pmatrix} \quad , \tag{5.3.6}$$

$$\mathbf{B}(\omega_j) = \begin{pmatrix} B_x(\omega_j) & 0 & 0 \\ 0 & B_z(\omega_j) & 0 \\ 0 & 0 & 0 \end{pmatrix} \quad , \tag{5.3.7}$$

are the hydrodynamic added mass matrix and the hydrodynamic damping coefficient matrix respectively, which were calculated by using the expressions in [12], and are shown in Figure 5.2;

$$\mathbf{B}_{pto} = \begin{pmatrix} 0 & 0 & 0 \\ 0 & B_{pto} & B_{pto} r\sin(\alpha) \\ 0 & B_{pto} r\sin(\alpha) & B_{pto}(r\sin(\alpha))^2 \end{pmatrix} \quad , \tag{5.3.8}$$

$$\mathbf{K}_{pto} = \begin{pmatrix} \frac{F_{pre}}{L} & 0 & -\frac{F_{pre} r\cos\alpha}{L} \\ 0 & K_{pto} & K_{pto} r\sin\alpha \\ -\frac{F_{pre} r\cos\alpha}{L} & K_{pto} r\sin\alpha & \begin{bmatrix} F_{pre} r\cos\alpha \\ -m_2 g r_{gy}\sin\varphi \\ +\frac{F_{pre}(r\cos\alpha)^2}{L} \\ +K_{pto}(r\sin\alpha)^2 \end{bmatrix} \end{pmatrix} \quad , \tag{5.3.9}$$

are PTO damping matrix and PTO stiffness matrix respectively;

$$\hat{\mathbf{F}}_{exc}(\omega_j) = \begin{pmatrix} \hat{F}_{exc,x}(\omega_j) \\ \hat{F}_{exc,z}(\omega_j) \\ 0 \end{pmatrix} = \begin{pmatrix} \hat{A}_m(\omega_j)\hat{f}_{exc,x}(\omega_j) \\ \hat{A}_m(\omega_j)\hat{f}_{exc,z}(\omega_j) \\ 0 \end{pmatrix} \quad , \tag{5.3.10}$$

is the wave excitation force vector, in which the excitation force coefficients $\hat{f}_{exc,x}(\omega)$ and $\hat{f}_{exc,z}(\omega)$ were calculated by using the expressions in [12] (the results are shown in Figure 5.2); and

$$\mathbf{D} = \begin{pmatrix} D_x \\ D_z \\ 0 \end{pmatrix} = -\rho C_D S \begin{pmatrix} \sqrt{\frac{1}{\pi}\sum_{j=1}^{n} |\hat{\dot{x}}_j|^2} \\ \sqrt{\frac{1}{\pi}\sum_{j=1}^{n} |\hat{\dot{z}}_j|^2} \\ 0 \end{pmatrix} \quad , \tag{5.3.11}$$

is the quasilinear drag force coefficient vector, in which ρ is the water density, C_D is the viscous drag coefficient ($C_D = 0.18$ for the $1 \times 10^6 < Re < 5 \times 10^6$ [3]) and S is the nominal cross-section area of the spherical buoy ($S = \pi r^2$). For a smooth spherical buoy, the viscous drag coefficient in pitch is negligible.

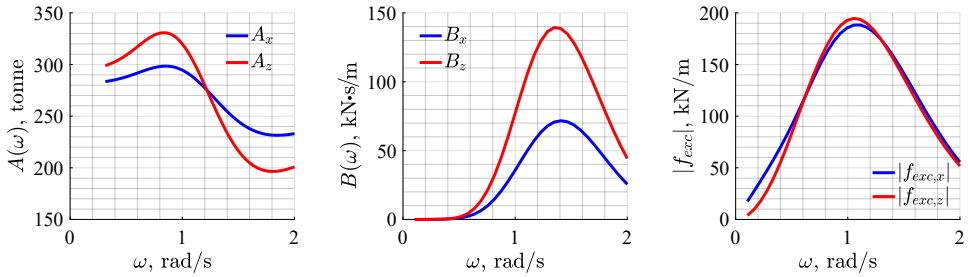

Figure 5.2: Hydrodynamic coefficients for the defined operating environment: (a) added mass $A(\omega)$; (b) radiation damping coefficient $B(\omega)$; (c) excitation force coefficient f_{exc}.

As D_x and D_z are the functions of the velocity response of all discretised frequencies, the spectral-domain model must be solved numerically. Folley and Whittaker [8] recommend the use of an iterative solver with an initial guess of system response to successively update the numerical solution until the predefined convergence termination criteria is met. Figure 5.3 shows a flowchart that determines the D_x and D_z and maximises the power output using the spectral-domain model for a particular mass distribution configuration, which can be summarised as the following procedure:

- **Step 1**: Initialise the hydrodynamic coefficients and the quasilinear drag force coefficients (D_x and D_z). The initial values of drag force coefficients are usually set to zero.

- **Step 2**: Build a spectral-domain model using the coefficients obtained from Step 1.

- **Step 3**: Search optimal PTO configuration (K_{pto}, B_{pto} and L) which results in maximum power output P, with the assistance of optimisation function *fmincon* in MATLAB, subjected to the motion constraint condition $\sqrt{\frac{1}{2}\sum_{j=1}^{n}|\hat{z}_j|^2} \leq 3$ m which ensures the buoy remains fully submerged. In order to tune the system to be resonant in surge for the wave frequency of interest, the optimal nominal tether length L is allowed to vary from 1 to 9 times the buoy's radius ($r \leq L \leq 9r$). The PTO stiffness K_{pto} and the PTO damping coefficient B_{pto} were constrained to be positive values.

- **Step 4**: Check if the deviation of current power output P is less than 0.1% in comparison with the value in the previous iterations. Additionally, the variance of the quasilinear drag force coefficients D_x and D_z should be less than 1% in comparison with the value in the previous iterations. If so, the iteration ceases and the whole optimisation stops; if not, the system response is solved to update the quasilinear drag force coefficients, and then next iteration commences.

5.4 Sensitivity study on mass distribution

In this section, a sensitivity analysis was performed to investigate the influence of the weight-to-buoyancy ratio (m/m_w), mass ratio (m_1/m_2) and mass-offset position (φ and r_{gy}) on the power output of the SPAMD separately. Considering the feasibility in manufacturing the SPAMD, the weight-to-buoyancy ratio was restricted to $0.3 \leq m/m_w \leq 0.6$ and the mass ratio $1/3 \leq m_1/m_2 \leq 3$. Table 5.1 lists the starting values and the range of the mass distribution parameters in the sensitivity studies. The mass distribution used in the previous work of the authors [6, 14] was used as an initial starting point.

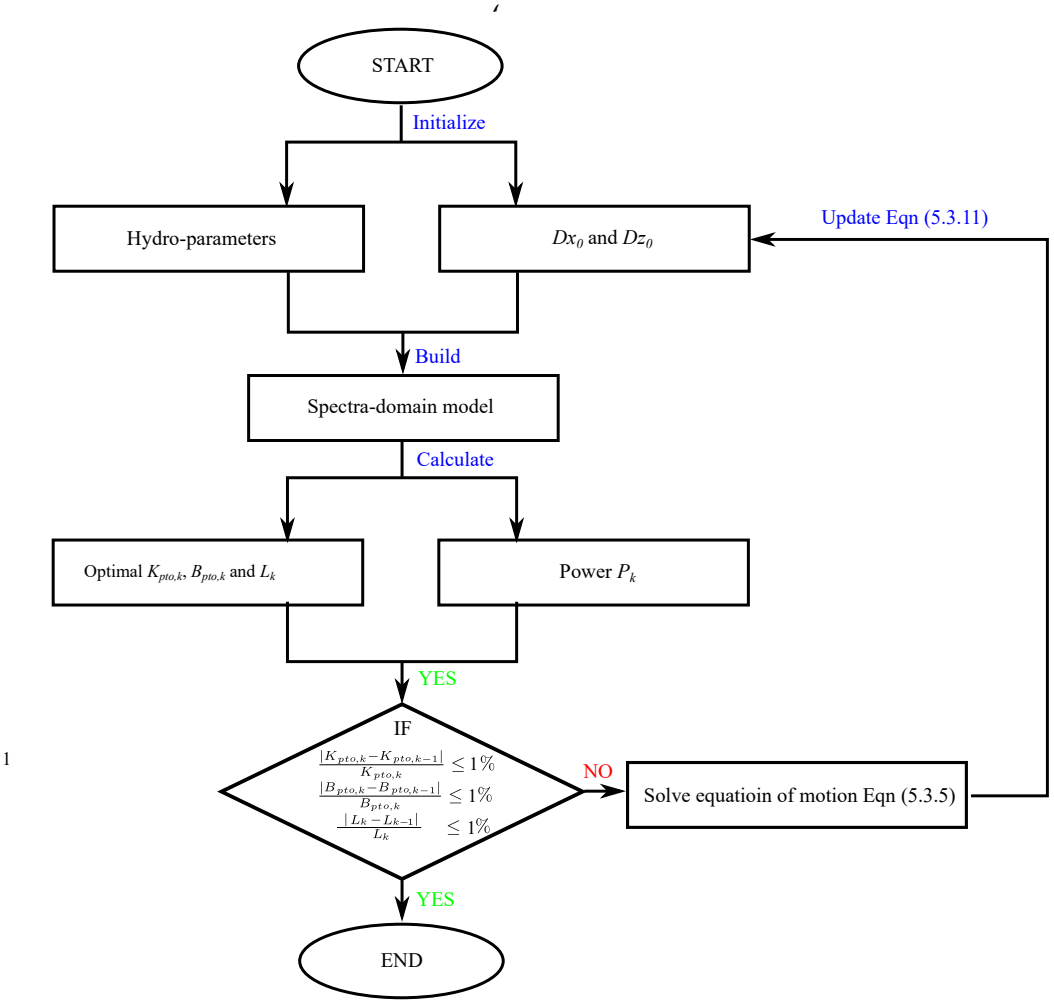

Figure 5.3: Flow chart for determining optimal PTO configuration and calculating the power output from the spectral-domain model.

Table 5.1: Fundamental mass distribution parameters of the sensitivity studies

	weight-to-buoyancy ratio	**Mass ratio**	**Mass-offset position**	
	m/m_w	m_1/m_2	φ (°)	r_{gy} (m)
Starting value used in [14]	0.5	1	30°	4.5
Parameter range	0.3, 0.4, 0.5 and 0.6	1/3, 1/2, 1, 2 and 3	−180 to 180	0 to 5

5.4.1 The relationship between weight-to-buoyancy ratio and power

The influence of the weight-to-buoyancy ratio m/m_w on the power output of the SPAMD was investigated first. The weight-to-buoyancy ratio was varied between four discrete values (0.3, 0.4, 0.5 and 0.6), while the mass ratio and the mass-offset position remained fixed at their starting values.

Figure 5.4 compares the power output between the SPAMDs with various weight-to-buoyancy ratios versus monochromatic wave periods from 4.5 to 18.5 s, under optimal spring-damper control at each wave period. The optimal PTO configuration (stiffness K_{pto}, damping coefficient B_{pto} and nominal tether length L) for monochromatic waves was found by using the algorithm presented in the previous work [14]. The curves of P_A and P_B illustrate the theoretical maximum power absorption of a 3DOF point absorber, without considering viscous drag effect. The derivation of P_A and P_A can be found in Ref [18]. It can be seen that at small wave periods ($T < 8$ s) the lightest buoy ($m/m_w = 0.3$) is up to 1.5 times more efficient than the heaviest one ($m/m_w = 0.6$), however the power output of the lightest buoy decreases rapidly as the wave period increases and the heaviest buoy shows better performance at large wave periods ($T >$10 s).

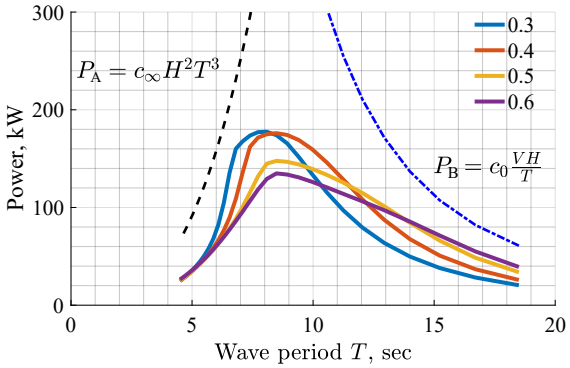

Figure 5.4: Power output comparison among the SPAMDs with weight-to-buoyancy ratios of 0.3, 0.4, 0.5 and 0.6, over the monochromatic wave period ranging from 4.5 to 18.5 s. The PTO configuration (stiffness, damping coefficient and tether length) were optimised for each wave period. P_A and P_B are the theoretical high-frequency and low-frequency limits of power absorption for a 3DOF (i.e., surge, heave and pitch) point absorber in the absence of viscous losses.

The weight-to-buoyancy ratio has limited impact on the absorption bandwidth of the SPAMD. The absorption bandwidth is defined as the normalised

frequency range where the absorbed power remains within the 50% of its peak value. Figure 5.5 shows the non-dimensional power output of the SPAMDs with various weight-to-buoyancy ratios in monochromatic waves of wave height H = 1 m. The PTO configurations were chosen such that the SPAMDs were tuned to be resonant in surge and heave for the peak power period T = 8.5 s). No motion constraints are implemented. The results in Figure 5.5 show that the absorption bandwidth of the SPAMD is almost independent of the weight-to-buoyancy ratio. However, the weight-to-buoyancy ratio m/m_w = 0.5 and 0.6 can lead to an additional peak for ω/ω_0 = 0.7 and 0.6 respectively, which is caused by an additional motion coupling between the heave and pitch motion. As evident in Figure 5.6, the SPAMD with m/m_w = 0.6 has the second largest heave and pitch displacements for ω/ω_0 = 0.75. Considering the SPAMD is an under-actuated system, large weight-to-buoyancy ratios should be avoided in design because the additional motion coupling might significantly degrade the controllability of the system.

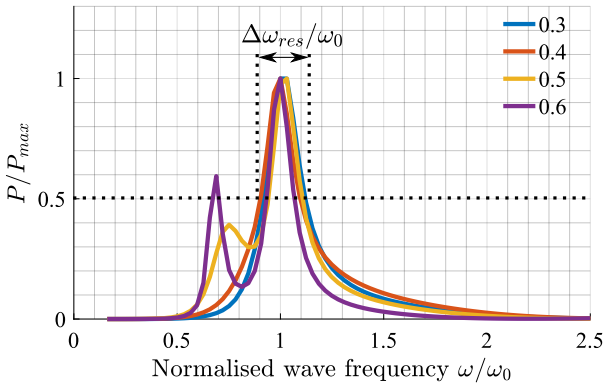

Figure 5.5: Absorption bandwidth of the SPAMDs with various weight-to-buoyancy ratios in monochromatic waves of wave height H = 1 m. The SPAMDs are tuned to reach resonance at the wave period of 8.5 s (ω_0 = 0.739 rad/s). Note that no motion constraints are implemented.

The power comparison of the SPAMDs with various weight-to-buoyancy ratios has also been conducted for irregular waves. Figure 5.7 compares the power output between the SPAMDs with predefined weight-to-buoyancy ratios over a range of irregular sea states of significant wave height H_s = 1 m. It can be seen that the overall trend is consistent with the monochromatic waves in Figure 5.4: the lightest buoy (m/m_w = 0.3) outperforms the heaviest buoy (m/m_w = 0.6) at small peak wave periods (T_p <8 s), with up to 1.9 times improvement in power; while at large peak wave periods (T_p >10 s), the heaviest buoy is slightly more productive.

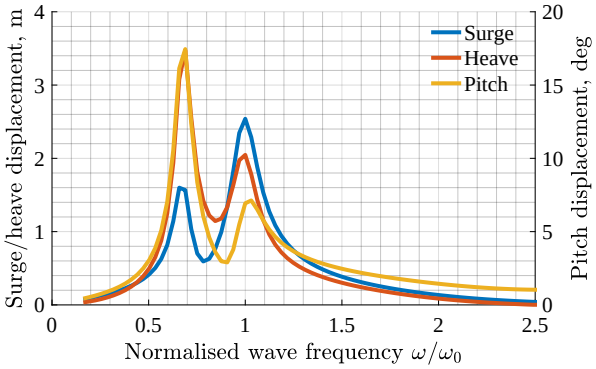

Figure 5.6: Displacements of the SPAMD with weight-to-buoyancy ratio m/m_w =0.6 in monochromatic waves of wave height H = 1 m. The SPAMDs are tuned to reach resonance at the wave period of 8.5 s (ω_0 = 0.739 rad/s). Note that no motion constraints are implemented.

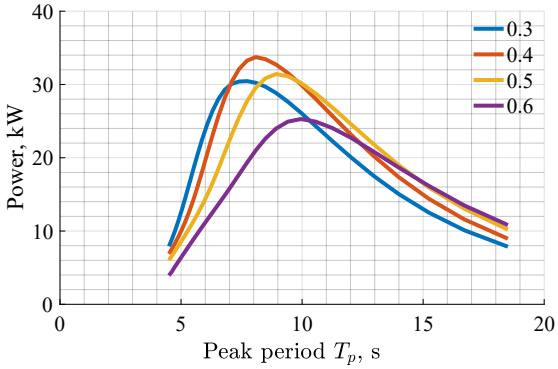

Figure 5.7: Power output comparison among the SPAMDs with weight-to-buoyancy ratios of 0.3, 0.4, 0.5 and 0.6 for irregular waves, over the peak wave period ranging from 4.5 to 18.5 s. The PTO configuration (stiffness, damping coefficient and nominal tether length) was optimised for each peak period.

Although the light buoy exhibits power improvement for small peak wave periods, such gain in the average power output is also associated with a considerable increase in the PTO loading, which is likely to result in an increase of the total system cost. Figure 5.8 compares the corresponding PTO loading amplitudes (including dynamic and static PTO loadings) under the irregular sea states. The lightest buoy requires up to 1.6 times the PTO force than the heaviest buoy over the pre-defined peak wave periods, mainly because the PTO of the lightest buoy needs to provide extra pretension force (as illustrated by the dash lines in Figure 5.8) to keep the buoy submerged. Therefore, it is not recommended to employ the weight-to-buoyancy ratio less than 0.3 for the design of the SPAMD. In addition to the amplitude of PTO force, the power-to-force ratio is also of interest as it is a proxy for the cost of the PTO facility per kW. From Figure 5.9, it has been observed that the heavy buoys tend to achieve the larger power-to-force ratio for large peak periods, indicating the SPAMD with heavy buoy might be more economic when operating in these particular sea states. In contrast, the light buoys might have a significant economic advantage for small peak periods.

Considering the economy and the cost of the system are out of the scope of this paper, the weight-to-buoyancy $m/m_w = 0.4$ was chosen to achieve the greater power production for the rest of the sensitivity study (see Figure 5.7). Furthermore, the system with $m/m_w = 0.4$ can be more controllable than the larger weight-to-buoyancy ratios (see Figure 5.5).

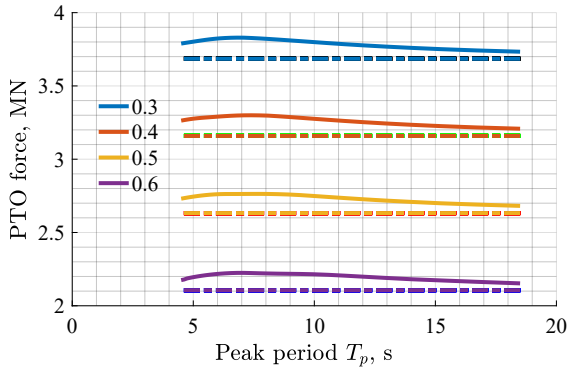

Figure 5.8: PTO loading comparison among the SPAMDs with weight-to-buoyancy ratios of 0.3, 0.4, 0.5 and 0.6 for irregular waves, over the peak wave period ranging from 4.5 to 18.5 s. Solid lines represent the sum of dynamic and static PTO loading for various weight-to-buoyancy ratios, and the dash lines represent the static PTO loading. The PTO configuration (stiffness, damping coefficient and nominal tether length) was optimised for each peak period.

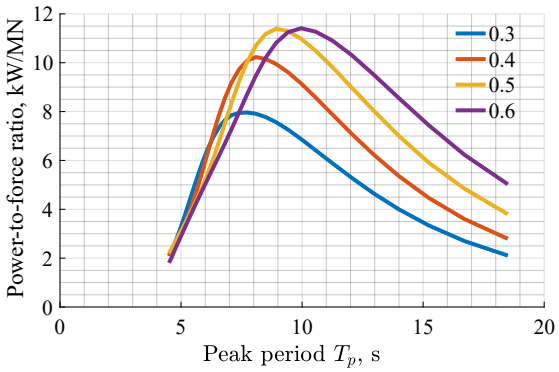

Figure 5.9: Power-to-force ratio comparison among the SPAMDs with weight-to-buoyancy ratios of 0.3, 0.4, 0.5 and 0.6 for irregular waves, over the peak wave period ranging from 4.5 to 18.5 s. The PTO configuration (stiffness, damping coefficient and nominal tether length) was optimised for each peak period.

5.4.2 The influence of mass ratio on power

The influence of mass ratio on the power output of the SPAMD was investigated by varying the mass ratio m_1/m_2 between 1:3, 1:2, 1:1, 2:1 and 3:1, whilst fixing weight-to-buoyancy ratio to 0.4 (determined from the previous subsection) and mass-offset position to the starting value.

Figure 5.10 compares the power output between the SPAMDs with various mass ratios over the monochromatic wave periods of interest. It can be seen that the heavy offset mass (i.e., m_1/m_2 = 1:1, 1:2 and 1:3) can lead to a maximum of 1.7 times (average 1.5 times) power improvement in comparison with the light offset mass (i.e., m_1/m_2 = 2:1 and 3:1) for the monochromatic wave periods $T < 7$ s, while the SPAMDs with light offset mass have only average 5% gain in the average power output for intermediate period waves (7 s $< T <$ 9 s). When the monochromatic wave period further increases, the average power output of the SPAMDs start to converge. Therefore, the mass ratio mainly influences the average power output of the SPAMD for low monochromatic wave periods.

The mass ratio has little impact on the absorption bandwidth of the SPAMD. Similar to Figure 5.5, Figure 5.11 shows the non-dimensional power output of the SPAMDs with various mass ratios in monochromatic waves of wave height H = 1 m. For the mass ratios investigated in this study, the resulting absorption bandwidths are almost identical, indicating the control algorithm of the SPAMD is independent of the mass ratio of the buoy.

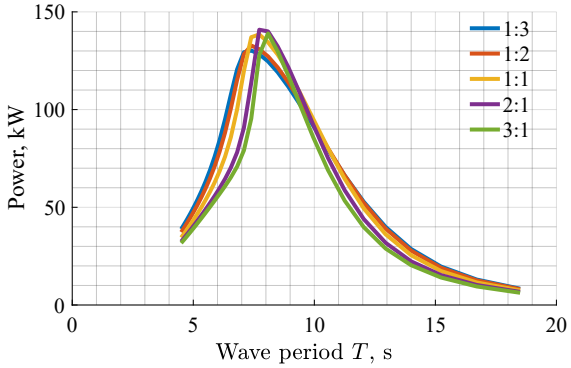

Figure 5.10: Power output comparison among the SPAMDs with mass ratios of 1:3, 1:2, 1:1, 2:1 and 3:1, over the monochromatic wave period ranging from 4.5 to 18.5 s. The PTO configuration (stiffness, damping coefficient and tether length) is optimised for each wave period.

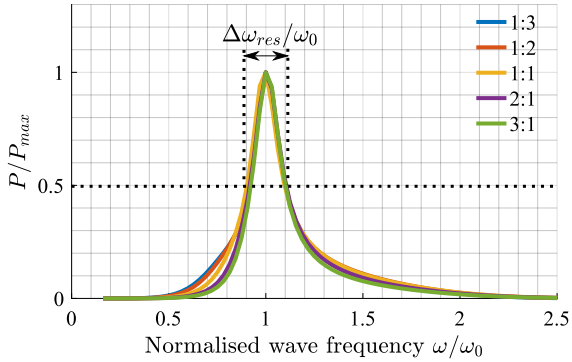

Figure 5.11: Absorption bandwidth of the SPAMDs with various mass ratios in monochromatic waves of wave height H = 1 m. The SPAMDs are tuned to reach resonance at the wave period of 8 s (ω_0 = 0.790 rad/s).

The performance of the SPAMDs with various mass ratios over the peak wave periods of interest is shown in Figure 5.12. In this figure, it can be seen that the configurations with the heaviest offset mass slightly outperform the buoys with lighter offset masses. This can be explained using the power curves for regular waves in Figure 5.10, where the buoys with heavy offset mass deliver more power at small wave periods. Another interesting observation is that the PTO loading is insensitive to the mass ratio of the buoy, as shown in Figure 5.13.

In conclusion, the mass ratio of the buoy has a limited impact on the absorption bandwidth, average power output and PTO loading of the SPAMD.

Therefore, a mass ratio of unity was used for the subsequent sensitivity study, as it shows similar power performance to low mass ratios but is relatively more feasible in terms of manufacturing.

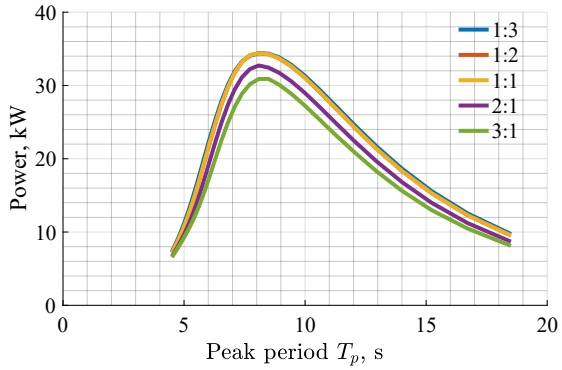

Figure 5.12: Power output comparison among the SPAMDs with mass ratios of 1:3, 1:2, 1:1, 2:1 and 3:1 for irregular waves, over the peak wave period ranging from 4.5 to 18.5 s. The PTO configuration (stiffness, damping coefficient and tether length) was optimised for each peak period.

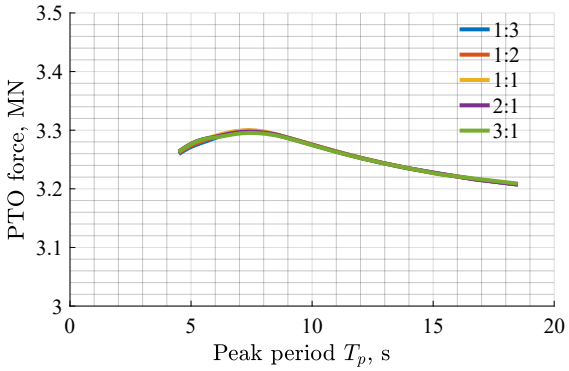

Figure 5.13: PTO loading comparison among the SPAMDs with mass ratios of 1:3, 1:2, 1:1, 2:1 and 3:1 for irregular waves, over the peak wave period ranging from 4.5 to 18.5 s. The PTO configuration (stiffness, damping coefficient and nominal tether length) was optimised for each peak period.

5.4.3 The influence of mass offset position on power

In this section, influence of the mass-offset position on the average power output of the SPAMD was investigated, whilst fixing m/m_w =0.4 and m_1/m_2 =1:1. The starting value of mass offset position is r_{gy} = 4.5 m and $\varphi = 30°$.

The sensitivity of the power output of the SPAMD on mass offset radius r_{gy} and angle φ were investigated. Figure 5.14 shows the power output of the SPAMDs with $\varphi = 30°$ and various mass offset radii (r_{gy} varied from 0 m (generic buoy) to 5 m (offset mass is on the surface of the buoy) over seven different offset radii) over the monochromatic wave periods of interest. It can be seen that the power output of the point absorber can be considerably improved in comparison to the generic PA even when the mass m_2 is offset from the centre of the buoy by only 1.5 m. Furthermore, the power improvement of the SPAMD converges at $r_{gy} > 2.5$ m, after which the gain in power does not grow as the offset radius r_{gy} increases.

In contrast, the power output of the SPAMD is very sensitive to the offset angle φ. Figure 5.15 shows the power output of the SPAMDs with r_{gy} = 4.5 m and various φ ($90° < \varphi < -90°$ over seven discrete angles) over the monochromatic wave periods of interest. It can be concluded that the power output of the SPAMD continuously increases as the mass-offset position moves from the upper hemisphere of the buoy ($\varphi = -30°$ and $-60°$) to the lower hemisphere ($\varphi = 30°$ and $60°$). For the offset angle $\varphi = 60°$, the SPAMD shows up to 2.3 times power improvement in comparison with the case of $\varphi = \pm 90°$. The poor performance when the m_2 is offset vertically is because the surge and heave motion are barely coupled, as seen from Equation (5.2.1). As a result, the SPAMD with vertically offset m_2 has almost identical power output as the generic PA shown in Figure 5.14.

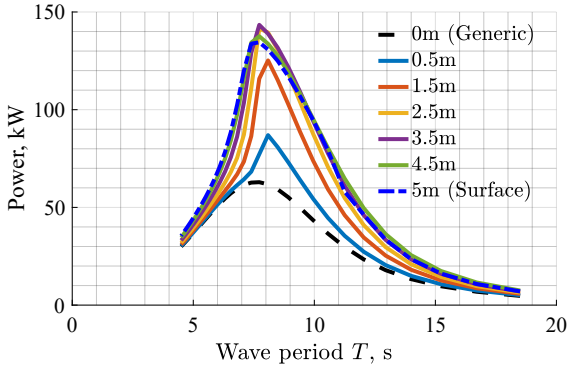

Figure 5.14: Power output comparison of the SPAMDs with a fixed mass offset angle ($\varphi = 30°$) and various mass offset radius (r_{gy} = 0 m, 0.5 m, 1.5 m, 2.5 m, 3.5 m, 4.5 m and 5 m) over the monochromatic wave periods of interest. The PTO configuration (stiffness, damping coefficient and tether length) was optimised for each wave period. The weight-to-buoyancy ratio is 0.4 and the mass ratio is 1:1.

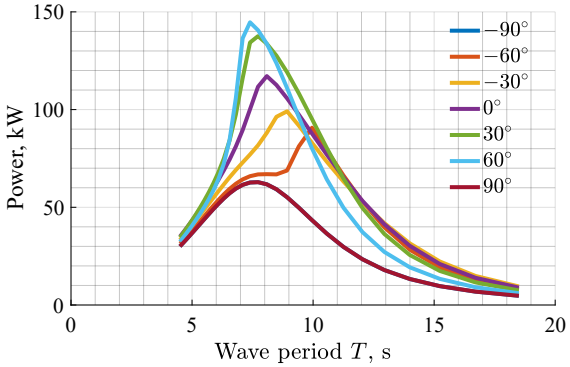

Figure 5.15: Power output comparison of the SPAMDs with a fixed mass offset radius (r_{gy} = 4.5 m) and various mass offset angles over the monochromatic wave periods of interest. The PTO configuration (stiffness, damping coefficient and tether length) was optimised for each wave period. The weight-to-buoyancy ratio is 0.4 and the mass ratio is 1:1.

For irregular waves, the performance of the SPAMD determined for the mass-offset positions reflects the trends consistent with the regular wave results. Figure 5.16 shows the variance in the average power output of the SPAMD for two irregular waves with the peak periods T_p = 9 s and T_p = 13 s, which represent the most likely peak periods of the targeted test sites in the subsequent power assessment. The spherical buoy was gridded by 10 discrete mass-offset radii r_{gy} from 0 to 4.5 m ($\Delta r_{gy} = 0.5$ m), and 24 discrete mass-offset angles φ from $-180°$ to $180°$ ($\Delta\varphi = 15°$). The colour in the grids represents the power output of the SPAMD for corresponding mass offset. Note that the power output of the generic single-tether PA is also illustrated for r_{gy} = 0 m. It can be seen that the improvements are distributed symmetrically about the Z axis, and a vertical mass-offset position would lead to a zero gain in power output. For the peak period $T_p = 9$ s (see Figure 5.16a), the optimal mass-offset positions on the right hemisphere are found within the sector of 3.5 m $< r_{gy} <$ 4.5 m and $0° < \varphi < 30°$, demonstrating 2.2 times power output improvement with respect to the generic single-tether PA. For the peak period $T_p = 13$ s (see Figure 5.16b), the optimal mass-offset positions on the right hemisphere are found within the sector of 4 m $< r_{gy} <$ 4.5 m and $-30° < \varphi < 0°$, yielding 2 times power output improvement in comparison to the generic single-tether PA.

Unlike the weight-to-buoyancy ratio, the power improvement by optimising the mass-offset position is not associated with a considerable increase in PTO loading. Figure 5.17 compares the PTO loading for various mass offset

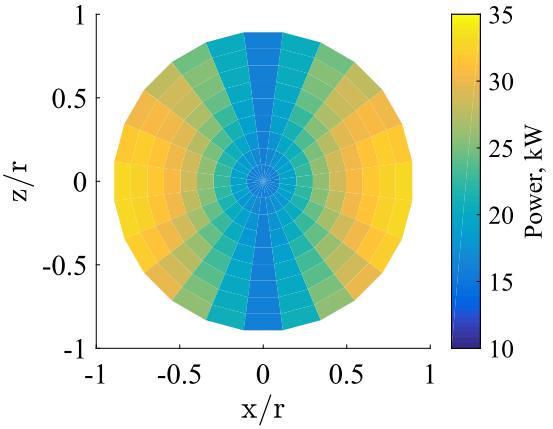

(a)

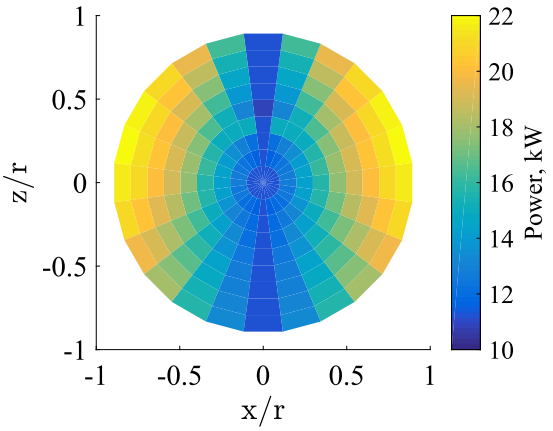

(b)

Figure 5.16: Polar plot of the average power output of the SPAMD for various mass-offset positions for the irregular waves with the peak period: (a) T_p = 9 s; (b) T_p = 13 s. The weight-to-buoyancy ratio is 0.4 and the mass ratio is 1:1. The PTO configuration (stiffness, damping coefficient and tether length) was optimal for each mass offset position. Note that the average power output of the generic PA (r_{gy} = 0 m) are 14 kW and 11 kW for T_p = 9 s and 13 s.

positions when the peak periods $T_p = 9$ s and 13 s. Considering the PTO pre-tension force is 3.15 MN, the variance of PTO loading caused by the different mass-offset positions is negligible, which means optimising the mass-offset position might be more cost-effective than targeting the weight-to-buoyancy ratio.

5.5 Yearly mean power output with optimal mass distribution

In this section, the yearly mean power output of a SPAMD with the optimal mass distribution was benchmarked against a generic single-tether PA of the same size and mass for three sites: Yeu Island in France, and Perth and Sydney in Australia. Figure 5.18 shows the probability of the sea state occurrence matrix of the three test sites. As mentioned in Section 5.2, it was assumed that all the sea states have a Modified Pierson-Moskowitz spectrum. The assessment of yearly mean power output of the SPAMD was conducted in three steps, namely determining the optimal mass distribution, optimising PTO configuration for each sea state and calculating yearly mean power output.

5.5.1 Determining the optimal mass distribution

From Figure 5.18, it can be seen that the most likely peak periods T_p in the test sites are 9 s (Yeu and Sydney sites) and 13 s (Perth site). Therefore, the optimal mass distributions were determined according to the peak periods of 9 s and 13 s. Considering the extremely high computational workload for optimising the mass distribution parameters as well as corresponding PTO configurations, an optimisation loop was created to iteratively search the optimal mass distributions. In this loop, the mass distribution parameters are optimised serially and iteratively until the power output converges, as shown in Figure 5.19.

Table 5.2 lists the resulting optimal mass distribution and tether length used for power assessment. It is interesting to note that the optimal mass distribution found by the optimisation loop is similar to that found in the sensitivity study (see Section 5.4.3), which enhances the confidence on the results of mass distribution optimisation.

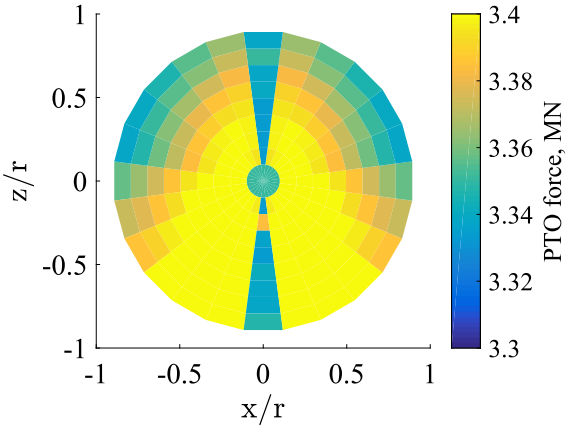

(a)

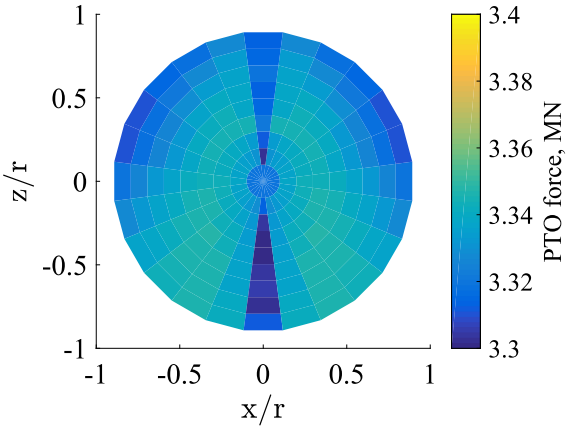

(b)

Figure 5.17: Polar graph of the PTO loading of the SPAMD for various mass-offset positions for the irregular waves with peak wave period (a) T_p = 9 s; (b) T_p = 13 s. The weight-to-buoyancy ratio is set to 0.4 and the mass ratio is 1:1. The PTO configuration (stiffness, damping coefficient and tether length) was optimised for each mass offset position. Note that the PTO loading of the generic PA (r_{gy} = 0 m) are 3.35 MN and 3.33 MN for T_p = 9 s and 13 s respectively. Note that the power output is insensitive to the mass-offset position when it is vertically displaced from the geometric centre, and therefore presents an ill-conditioned problem. This results in noisy PTO force estimates for such cases.

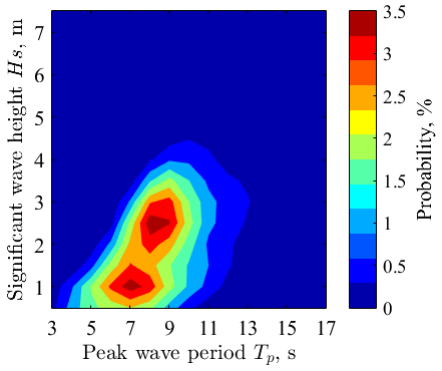

(a)

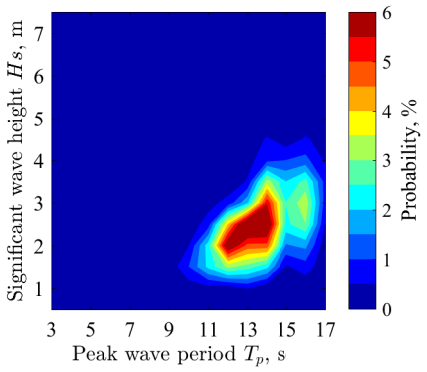

(b)

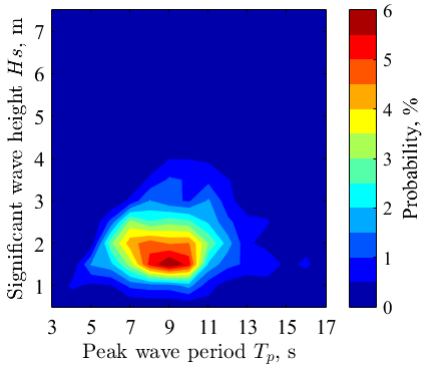

(c)

Figure 5.18: The probability of sea state occurrence of three test sites, which is obtained from real sea measurement: (a) Yeu Island (Location: 059°00, 000′ N - 003°66, 000′ W) [2]; (b) Perth site (Location: 033°50, 000′ S - 114°80, 000′ E) [1]; (c) Sydney site (Location: 034°00, 000′ S - 152°50, 000′ E) [1].

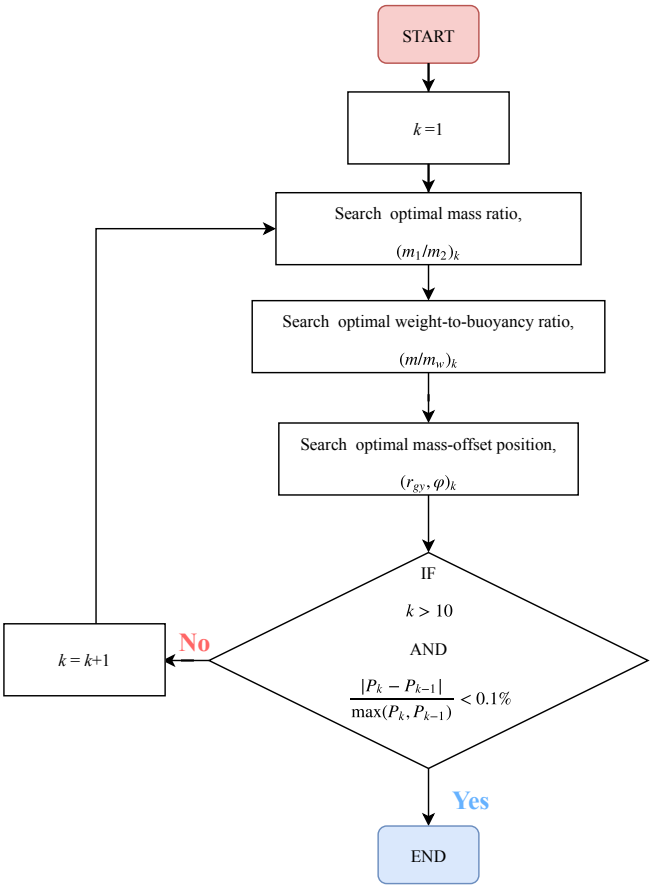

Figure 5.19: Flowchart of optimising mass distribution of the SPAMD for yearly mean power assessment.

5.5.2 Optimising PTO configuration for each sea state

In this assessment, the impact of optimal spring-damper control on the yearly mean power of the SPAMD was also investigated. The SPAMD was divided into two classes: one class with optimal spring-damper control for each sea state (denoted as SPAMD$^{\text{opt}}$); and the other class with a fixed spring-damper control (denoted as SPAMD$^{\text{fixed}}$). Specifically, for the SPAMD$^{\text{opt}}$, the PTO stiffness K_{pto} and damping coefficient B_{pto} were optimised for each sea state; while for SPAMD$^{\text{fixed}}$, the PTO stiffness K_{pto} and damping coefficient B_{pto} were fixed to the optimal settings for the peak period T_p = 9 s (Yeu and Sydney sites) and 13 s (Perth site). For the generic PA (denoted as Generic), its PTO stiffness and damping coefficient was optimised for every sea state.

Since it is not feasible to adjust the mooring tether length L to accommodate varying sea states in practice, the tether length was fixed in this

Table 5.2: Optimal mass distribution for power assessment at test sites

		Yeu Island	**Perth site**	**Sydney site**
Mass distribution	m/m_w	0.4	0.4	0.4
	m_1/m_2	1:1	1:3	1:1
	r_{gy} and φ	4.5 m, -15°	4.5 m, 0°	4.5 m, -15°
Tether length	L	9.24 m	16.26 m	9.24 m

assessment. For the SPAMDs (i.e., SPAMD$^{\text{opt}}$ and SPAMD$^{\text{fixed}}$), the tether length was set as the optimal length for the peak period T_p = 9 s (Yeu and Sydney sites) and 13 s (Perth site), as shown in Table 5.2. For the generic PA, its tether length was fixed to 14 m because the power output of the generic PA is relatively insensitive to the tether length.

5.5.3 Calculating yearly mean power output

The yearly mean power output of the SPAMDs and the generic PA were calculated by multiplying the sea state occurrence matrix (see Figure 5.18) with the power absorption matrices (see Figure 5.20). Table 5.3 compares the resulting yearly mean power output of the SPAMD$^{\text{opt}}$, the SPAMD$^{\text{fixed}}$ and the Generic at the chosen test sites. From Table 5.3, it can be seen that the yearly mean power output of the SPAMD$^{\text{opt}}$ is slightly greater than the SPAMD$^{\text{fixed}}$ as expected, which implies that there is little benefit to implementing an optimal spring-damper control for each sea state if the tether length is non-optimal. Furthermore, the power output of the SPAMD$^{\text{opt}}$ is as much as 1.6 times the Generic, which indicates the SPAMD with optimal mass distribution is likely to more economically competitive than the generic single-tether PA.

Table 5.3: The yearly mean power output comparison between the SPAMD$^{\text{opt}}$, SPAMD$^{\text{fixed}}$ and Generic buoy for three test sites

		Yeu Island	**Perth site**	**Sydney site**
SPAMD$^{\text{opt}}$		100.0 kW	80.4 kW	97.2 kW
SPAMD$^{\text{fixed}}$		96.5 kW	77.1 kW	94.0 kW
Generic		65.6 kW	50.4 kW	62.3 kW
q factor	$\frac{\text{SPAMD}^{\text{opt}}}{\text{SPAMD}^{\text{fixed}}}$	1.04	1.04	1.03
	$\frac{\text{SPAMD}^{\text{opt}}}{\text{Generic}}$	1.53	1.60	1.56

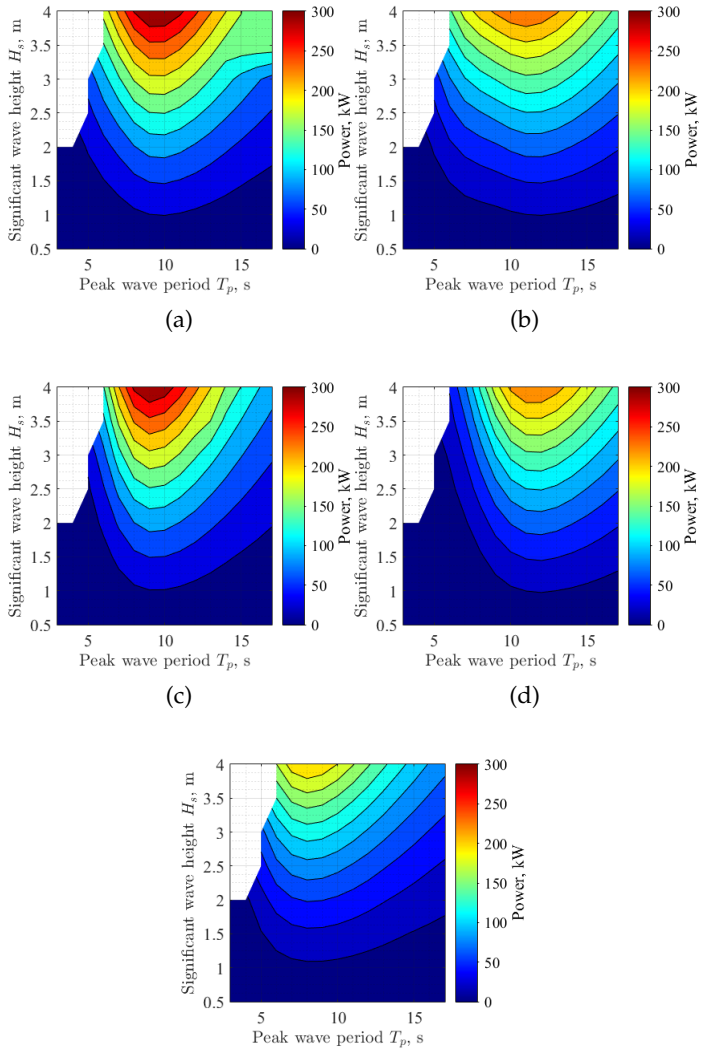

Figure 5.20: Power matrix of: (a) the SPAMD^{opt} with optimal mass distribution for Yeu and Sydney sites; (b) the SPAMD^{opt} with optimal mass distribution for Perth site; (c) the SPAMD^{fixed} with optimal mass distribution for Yeu and Sydney sites; (d) the SPAMD^{fixed} with optimal mass distribution for Perth site; (e) the Generic buoy.

5.6 Conclusion

In this paper, a sensitivity study of mass distribution on the average power output of a submerged spherical point absorber with asymmetric mass distribution (SPAMD) in regular and irregular waves was conducted. The mass distribution of the buoy is determined by three parameters: weight-to-buoyancy ratio, mass ratio and mass-offset position. It was found that the buoy with low weight-to-buoyancy ratio is more productive at small wave periods. However, the gain in power output is also associated with the increase of PTO loading, which might increase the cost of energy production. The mass ratio of the buoy has a limited impact on the power output and the PTO loading of the SPAMD. The mass-offset position was found to have the greatest impact on the power production of the SPAMD, with the optimal position doubling power production compared to the generic buoy. The PTO loading is relatively insensitive to the mass-offset position.

Finally, the yearly mean power output of the SPAMD with optimal mass distribution was compared with the generic single-tether PA at three test sites (Yeu Island, Perth and Sydney). The results showed that the optimal mass distribution of the SPAMD can lead to at least 53% more power in comparison with the generic single-tether PA, which suggests that the SPAMD might be more competitive in the wave energy industry. Furthermore, the impact of optimal spring-damper control on the yearly mean power of the SPAMD was also investigated. It was found that the SPAMD does not require optimal spring-damper control for each sea state to improve the yearly mean power output if the nominal tether length is fixed, which means a sea-state dependant control system might not be essential when the SPAMD is deployed in practice.

Future work will focus on verifying the power output improvement of the SPAMD with presence of nonlinearities in a 3D numerical wave tank (NWT).

Acknowledgment

This research is supported by China Scholarship Council (CSC), Australian Research Council (ARC) Linkage Grant (LP130100117) and the Research Training Program (RTP).

References

[1] Australian Wave Energy Atlas (2016, accessed 07 June 2016). [Online]. Available: http://awavea.csiro.au/.

[2] Babarit, A, Hals, J, Kurniawan, A, Muliawan, M, Moan, T and Krokstad, J (2011). "The NumWEC Project Selection: Numerical Estimation of Energy Delivery from a Selection of Wave Energy Converters". In: *Statkraft, Trondheim, Norway*.

[3] Blevins, R. D. (2003). *Applied fluid dynamics handbook*. Krieger Publishing Company.

[4] Cruz, J. and Salter, S. H. (2006). "Numerical and experimental modelling of a modified version of the Edinburgh Duck wave energy device". In: *Proceedings of the Institution of Mechanical Engineers, Part M: Journal of Engineering for the Maritime Environment* 220.3, pp. 129–147.

[5] Cruz, J. (2007). *Ocean wave energy: current status and future prespectives*. Springer Science and Business Media.

[6] Ding, B, Sergiienko, N, Meng, F, Cazzolato, B, Hardy, P and Arjomandi, M (2019). "The application of modal analysis to the design of multi-mode point absorber wave energy converters". In: *Ocean Engineering* 171.11, pp. 603–618.

[7] Falnes, J. (2007). "A review of wave-energy extraction". In: *Marine Structures* 20.4, pp. 185 –201.

[8] Folley, M. and Whittaker, T. (2010). "Spectral modelling of wave energy converters". In: *Coastal Engineering* 57.10, pp. 892 –897.

[9] ITTC (2002). "Guidelines: Testing and Extrapolation Methods: Resistance-Uncertainty Analysis, Example for Resistance Test". In: *ITTC Recommended Procedures and Guidelines, Procedure 7.5-02-02* 2.

[10] Kurniawan, A. and Moan, T. (2012). "Multi-objective optimization of a wave energy absorber geometry". In: *Proceedings of 27th International Workshop on Water Waves and Floating Bodies, Copenhagen, Denmark*.

[11] Lee, C. H. (1995). *WAMIT Theory Manual*. Massachusetts Institute of Technology, Department of Ocean Engineering.

[12] Linton, C. (1991). "Radiation and diffraction of water waves by a submerged sphere in finite depth". In: *Ocean Engineering* 18.1, pp. 61 –74.

[13] Lucas, J. (2011). "Dynamics of a horizontal cylinder oscillating as a wave energy converter about an off-centred axis". In: *Ph.D. thesis, The University of Edinburgh, 2011*.

[14] Meng, F., Ding, B., Cazzolato, B. and Arjomandi, M. (2019). "Modal analysis of a submerged spherical point absorber with asymmetric mass distribution". In: *Renewable Energy* 130, pp. 223 –237.

[15] Pastor, J. and Liu, Y. (2014). "Power absorption modeling and optimization of a point absorbing wave energy converter using numerical method". In: *Journal of Energy Resources Technology* 136.2, p. 021207.

[16] Pelc, R. and Fujita, R. M. (2002). "Renewable energy from the ocean". In: *Marine Policy* 26.6, pp. 471 –479.

[17] Salter, S. H. (1989). "World progress in wave energy–1988". In: *International Journal of Ambient Energy* 10.1, pp. 3–24.

[18] Sergiienko, N., Cazzolato, B., Ding, B., Hardy, P. and Arjomandi, M. (2017). "Performance comparison of the floating and fully submerged quasi-point absorber wave energy converters". In: *Renewable Energy* 108, pp. 425–437.

[19] St Dinis, M. and Pierson Jr, W. J. (1953). *On the motions of ships in confused seas*. Tech. rep. New York University Bronx School of Engineering and Science.

Chapter 6

Nonlinear hydrodynamics analysis of a submerged spherical point absorber with asymmetric mass distribution

It has been demonstrated in the previous chapters that a submerged spherical buoy with an asymmetric mass distribution can be up to three times more efficient than a generic one for regular waves and up to 1.5 times for irregular waves. However, all the analysis and relevant conclusions on the SPAMD have been performed using linear potential theory models, leading to uncertainty in the performance of the SPAMD when nonlinear hydrodynamics begin to dominate. In order to investigate the effect of the nonlinear hydrodynamics on the performance of the system, a nonlinear hydrodynamic analysis is presented in this chapter, focusing on the motion trajectory and power production to provide some insights into the following research questions:
1. How does motion trajectory reflect the efficiency of multi-mode point absorbers?
2. How do nonlinear hydrodynamics compromise the efficiency of multi-mode point absorbers?

This chapter consists of the following journal article under review:
Meng, F., Rafiee, A., Ding, B., Cazzolato, B. S. and Arjomandi, M. (2019). "Nonlinear hydrodynamics analysis of a submerged spherical point absorber with asymmetric mass distribution". Accepted by Renewable Energy.

Statement of Authorship

Title of Paper	Nonlinear hydrodynamics analysis of a submerged spherical point absorber with asymmetric mass distribution
Publication Status	☐ Published ☑ Accepted for Publication ☐ Submitted for Publication ☐ Unpublished and Unsubmitted w ork w ritten in manuscript style
Publication Details	Meng, F., Rafiee, A., Ding, B., Cazzolato, B. S., and Arjomandi, M. (2019). "Nonlinear hydrodynamics analysis of a submerged spherical point absorber with asymmetric mass distribution". Accepted by Renewable Energy.

Principal Author

Name of Principal Author (Candidate)	Fantai Meng		
Contribution to the Paper	Developed the idea and concepts, developed the numerical models, wrote the code of simulations, interpreted the results, wrote the manuscript and acted as a corresponding author.		
Overall percentage (%)	75%		
Certification:	This paper reports on original research I conducted during the period of my Higher Degree by Research candidature and is not subject to any obligations or contractual agreements with a third party that would constrain its inclusion in this thesis. I am the primary author of this paper.		
Signature		Date	21/8/19

Co-Author Contributions

By signing the Statement of Authorship, each author certifies that:

i. the candidate's stated contribution to the publication is accurate (as detailed above);

ii. permission is granted for the candidate in include the publication in the thesis; and

iii. the sum of all co-author contributions is equal to 100% less the candidate's stated contribution.

Name of Co-Author	Ashkan Rafiee		
Contribution to the Paper	Helped in developing the computational fluid dynamic model by using OpenFOAM toolbox, discussed the results, and provided a critical revision of the manuscript.		
Signature		Date	29/8/2019

Name of Co-Author	Boyin Ding		
Contribution to the Paper	Supervised the work, helped in interpretation of obtained results, and provided a critical revision of the manuscript.		
Signature		Date	28/8/19

Name of Co-Author	Benjamin S. Cazzolato		
Contribution to the Paper	Supervised the work, helped in interpretation of obtained results, and provided a critical revision of the manuscript.		
Signature		Date	27/8/19

Name of Co-Author	Maziar Arjomandi		
Contribution to the Paper	Supervised the work, helped in interpretation of obtained results, and provided a critical revision of the manuscript.		
Signature		Date	27/08/2019

Please cut and paste additional co-author panels here as required.

Nonlinear hydrodynamics analysis of a submerged spherical point absorber with asymmetric mass distribution

F. Meng, A. Rafiee, B. Ding, B. S. Cazzolato, M. Arjomandi

Abstract

In previous work, a frequency-domain model was developed from linear potential theory to investigate the oscillation modes and efficiency of a single-tether 3 degree-of-freedom submerged spherical point absorber with asymmetric mass distribution (SPAMD). It was found that the trajectory of the device has a strong correlation with the performance of the wave energy converter. Specifically, the SPAMD can generate unique circular trajectories under long waves, producing up to 3 times power that of a generic single-tether point absorber (PA). However, this conclusion might not be valid for large buoy displacements due to increased nonlinear hydrodynamic effects (e.g. surface piercing, overtopping water, and vortex shedding). In this study, the trajectory of the SPAMD was analysed to determine the dominant nonlinear hydrodynamic effect that degrades the performance of a fully submerged system. The analysis was conducted in a numerical wave tank experiment (NWT), based on the Navier-Stokes equation and using the computational fluid dynamic toolbox OpenFOAM and the open-source library OLAFLOW for wave generation and absorption. The results obtained from NWT experiments show that surface piercing has the largest negative impact on the system's performance, which compromises the efficiency of the SPAMD by modifying the trajectory and dissipating energy. As a result, the efficiency of the SPAMD significantly decreases for long waves when surface piercing is most likely to occur, which implies that submerged point absorbers are less efficient than the floating ones in this scenario. Furthermore, although the performance of the SPAMD was significantly compromised due to the effect of surface piercing, the resulting power improvement in comparison to the submerged generic point absorber was still considerable for some wave periods.

6.1 Introduction

As a clean and renewable energy resource, ocean wave energy is regarded as an important contributor in the future energy mix. The potential of worldwide

wave energy resource is estimated to be the same level as the annual electricity demand (∼2 TW) [2]. To harvest the energy from ocean waves, a large amount of wave energy converters (WECs) have been proposed, which can be roughly categorised into oscillating water columns, overtopping devices, wave activated bodies and submerged pressure differential devices [23]. Accurate modelling of a wave energy converter plays a significant role in the prototype development as it is required for evaluating survivablity of WECs under extreme wave loadings [13], optimising power absorption efficiency [17], assessing power production [24], system identification [1] and real-time model-based control [25].

The WEC models developed from linear potential theory such as Cummins' model [7, 29] are generally used to estimate the small response of buoys subjected to regular and irregular waves of small amplitude. For a small wave elevation and motion amplitude of buoy, the boundary conditions in fluid-structure interaction are linearised to derive the first-order hydrodynamics. These simplifications provide a computationally efficient approach to simulate the motion of WECs under small wave excitation. However, as many WECs are tuned to operate close to resonant condition or survive in energetic sea states, neglecting nonlinear hydrodynamics in the fluid-structure interaction leads to overestimates of the response of system [16, 28].

Certain nonlinear effects are neglected as a result of the linear approximation of the Froude-Krylov force and radiation-diffraction force. In potential theory, the Froude-Krylov force is the integral of the dynamic pressure over the mean wetted surface. For small wave elevation and buoy motion, it is assumed that the pressure given by Bernoulli's equation can be approximated as a linear format [32]. Furthermore, the hydrostatic force/moment of floating devices is usually simplified as a linear function of the heave displacement of the buoy, which is only suitable for buoys with constant waterplane or small heave displacement. Therefore, when the system operates near its resonant condition, the buoy's response estimated by linear model tend to significantly deviate from the actual value due to the nonlinear effects [6, 16]. Some modifications have been made to improve the accuracy of WEC models in the case of large motion. Giorgi et al. [12] applied the exact nonlinear Froude-Krylov force to the equation of motion by integrating the linearised incident wave pressure over the instantaneous wetted surface of buoy. Based on the former work, Merigaud et al. [22] further improved the nonlinearity estimate of the Froude-Krylov force by using a weak-scatter approximation of the boundary value problem. To address the nonlinear radiation and diffraction problem, Gilloteaux [11] employed a Taylor series to approximate high-order radiation and diffraction forces acting on the WEC prototype SEAREV, resulting in a

satisfactory model that agrees well with corresponding experimental results when the device is at resonance. However, there are additional hydrodynamic nonlinearities beyond the capability of potential wave theory to model, such as wave breaking, surface piercing, vortex shedding and green water effect caused by water overtopping. These nonlinearies can only be solved by using a fully nonlinear numerical approach.

Computational fluid dynamics, based on the Navier-Stokes equations (NS-based CFD) is one of the most widely used numerical methods for studying complex nonlinear hydrodynamics in fluid-structure interaction problems. For example, Sjökvist and Göteman [30] utilised a NS-based CFD model to estimate the peak wave loading on a floating PA caused by water overtopping; Rafiee and Fiëvez [28] identified the viscous drag coefficient of the CETO prototype by using a NS-based CFD model; Chen et al. [5] examined the impact of wave height on mooring cable tension in extreme sea states. Although NS-based CFD generally requires significant computational resource, it is becoming increasingly feasible and essential for high-fidelity tests of a WEC design.

In the previous work by the authors [21], a 3DoF (i.e., surge, heave and pitch) single-tether submerged point absorber with asymmetric mass distribution (SPAMD) was proposed to address the deficiency of a submerged generic PA in harvesting wave energy predominantly via heave. The equation of motion was developed from linear potential theory, with the consideration of viscous drag effect (i.e. the quasi-nonlinear model in this text). According to Falnes [9], a good point absorber should be a good wave maker that can perfectly destruct the incident waves by using radiated waves caused by its surge and heave motion (see Figure 6.1). Therefore, the trajectory of the SPAMD tends to be circular under optimal passive control when the system is excited by monochromatic waves, which has been also observed from other multi-DoF systems such as the Bristol cylinder [8].

In this study, trajectory analysis is presented to identify the dominant nonlinear hydrodynamics that degrade the performance of the SPAMD. Specifically, a trajectory reference which represents the estimated performance of the system was initially generated by using a quasi-nonlinear model for various wave conditions. From this baseline, the most dominant nonlinear hydrodynamics can be identified when the trajectory in the numerical wave tank experiment significantly changes. A 3D numerical wave tank (NWT) was developed using the open source CFD toolbox OpenFOAM, to conduct trajectory and power analysis of the SPAMD in small and large monochromatic waves, according to the nonlinear hydrodynamics induced by the large motion of the buoy. This paper is organised as follows. In Section 6.2, the

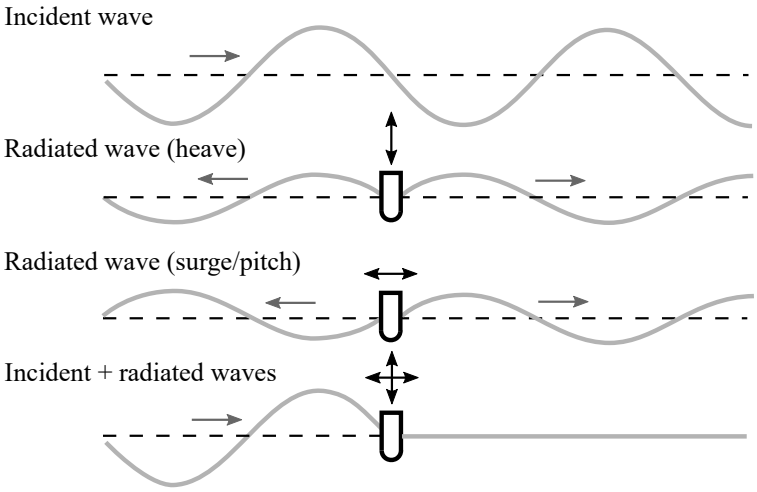

Figure 6.1: Schematic of incident waves cancelled by a 2D buoy, adapted from [9].

system of the SPAMD is briefly introduced, with the parameters used for the mass distribution of the buoy and power take-off device. In Section 6.3, the equation of motion is developed from Cummins' model with consideration of viscous drag (referred to as the quasi-nonlinear model in this paper), and the Navier-Stokes equations (referred to as NS-based CFD model) respectively. In Section 6.4, the set-up of NWT is detailed, together with evidence of mesh convergence and NWT validation against a small scale wave basin experiment undertaken by the Australian Maritime College [3]. In Section 6.5, the trajectory and power analysis of the SPAMD are conducted, as well as the study on efficiency improvement between the generic PA and the SPAMD over five typical wave periods and three wave heights.

6.2 Device description

As mentioned in Section 6.1, the SPAMD utilises the motion coupling achieved by an asymmetric mass distribution of the buoy, to address the deficiency observed with a single-tether PA in harvesting wave energy predominantly in heave. The surge and pitch motion of the SPAMD can drive the PTO as efficiently as the heave motion. Figure 6.2 illustrates the motions of a single-tether 3DOF SPAMD subjected to plane waves in the vertical XZ plane. The parameters used for the mass distribution and power take-off device (PTO) are briefly introduced in the remainder of this section. A more detailed description of the device can be found in previous studies [20, 21].

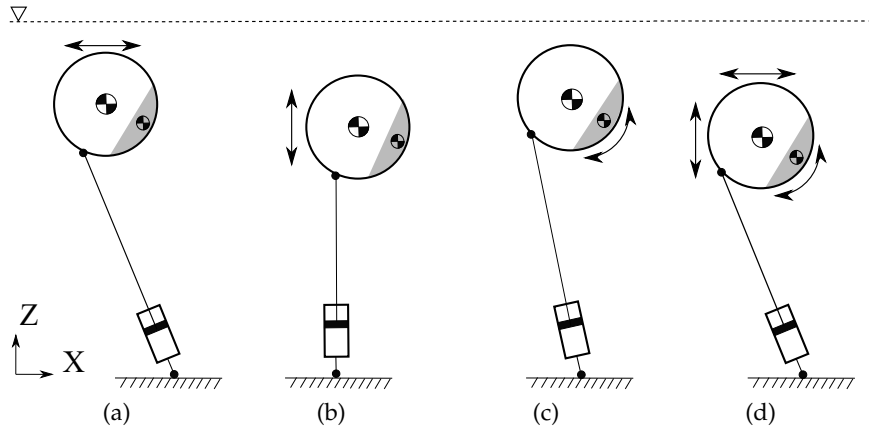

Figure 6.2: Schematic illustrating the motions of a 3DOF SPAMD subjected to plane waves in the vertical XZ-plane: (a) surge motion, (b) heave motion, (c) pitch motion, (d) combined 3DOF motion. The larger centre of mass represents the mass of the solid spherical buoy m_1, the smaller one is the offset point mass m_2. The buoy is fully submerged at rest. The X and Z axes in the bottom left of the figure are only to illustrate the plane and do not relate to the origin of the frame.

6.2.1 Mass distribution

The SPAMD consists of a spherical hull with mass of m_1 and a point mass m_2 offset from the centre of the buoy, as shown in Figure 6.3. Noting that the variables shown in Figure 6.3 are defined in a body-fixed frame. According to Lee [18], the mass matrix of a 3DOF spherical buoy with respect to the geometric centre of the buoy is given by

$$\mathbf{M} = \begin{pmatrix} m_1 + m_2 & 0 & m_2 z_2 \\ 0 & m_1 + m_2 & -m_2 x_2 \\ m_2 z_2 & -m_2 x_2 & I_{yy} \end{pmatrix} \quad , \tag{6.2.1}$$

where the total mass of the buoy is $m = m_1 + m_2$, the total moment of inertia about the geometric centre is $I_{yy} = I_1 + I_2 = \frac{2}{3} m_1 r^2 + m_2 r_{gy}^2$ (r_{gy} is the offset distance, as shown in Figure 6.3), and the location of the offset mass m_2 is (x_2, z_2). The mass distribution parameters employed in this study have been shown to be optimal in the previous work [21], listed in Table 6.1.

6.2.2 Power take-off configuration

The power take-off device consists of a linear spring-damper mechanism to implement complex conjugate control, with tuning parameters of stiffness,

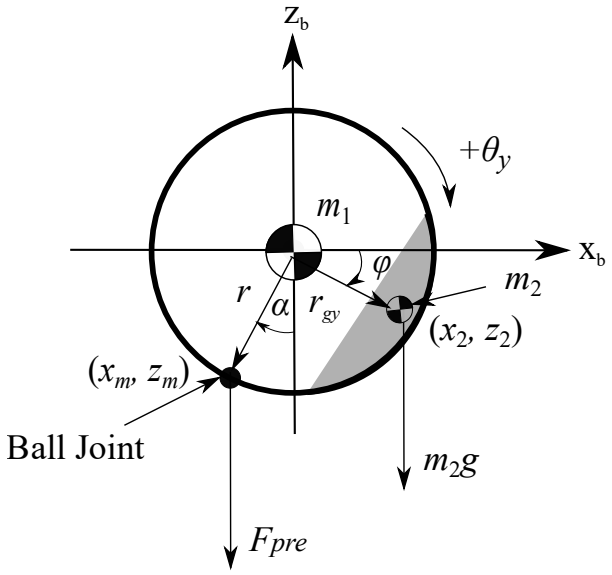

Figure 6.3: Schematic of the mass-offset spherical buoy.

Table 6.1: Parameters of the SPAMD buoy and bathymetry

Description	Parameter	Value/Unit
Mass of spherical hull	m_1	134104 kg
Mass of offset point mass	m_2	134104 kg
Moment of inertia	I_{yy}	5.59×10^6 kg·m^2
Radius of buoy	r	5 m
Mass offset angle	φ	30 deg
Mass offset radius	r_{gy}	4.5 m
Water depth	h	33 m
Submergence depth, (fully submerged, from the top of the buoy to water surface)	d	3 m

K_{pto}, and damping coefficient, B_{pto}. It is assumed that the average power output of the SPAMD is equal to the average power consumed by the PTO damper, given by

$$P_{avg} = \frac{\int_t^{(t+T_s)} B_{pto} |\Delta \dot{L}(t)|^2 dt}{T_s} \quad , \tag{6.2.2}$$

where $\Delta \dot{L}$ is the instantaneous PTO elongation rate, the time period T_s is the sampled time interval after the PA has reached steady-state. This was found to be at least 10 wave cycles.

In this work, the PTO stiffness, K_{pto}, and damping coefficient, B_{pto}, were determined by maximising the response of the quasi-nonlinear model,

without the consideration of motion hard-stop constraints to keep the buoy submerged. Thus, there was the possibility of breaching the water surface for large wave heights, which was simulated in the NWT experiment. Furthermore, as demonstrated in the previous paper by the authors [21], the mooring tether length L is another tuning parameter affecting the efficiency of the SPAMD, which is frequency dependent. To obtain the optimal K_{pto}, B_{pto} and L that maximise the power production of the SPAMD, the quasi-nonlinear model was firstly developed by using the MATLAB-Simulink toolbox *SimMechanics*. The tuning parameters K_{pto}, B_{pto} and L were then optimised by using the optimisation function *fmincon* for given constraint ranges 50 kN/m $\leq K_{pto} \leq 1 \times 10^3$ kN/m, 10 kNm/s $\leq B_{pto} \leq 3 \times 10^2$ kNm/s and 9 m $\leq L \leq 30$ m. The settings of the optimal PTO configuration are detailed in Appendix 6.A.

6.3 Modelling

For a 3DOF single-tether PA with a spring-damper constraint, the equation of motion in the time-domain is given by

$$\mathbf{M}\ddot{\mathbf{x}}(t) = \mathbf{F}_{hydro}(t) + \mathbf{F}_{pto}(t) + \mathbf{F}_{re}(t) \quad , \tag{6.3.1}$$

where the $\dot{\mathbf{x}}(t) = [\dot{x}(t), \dot{z}(t), \dot{\theta_y}(t)]^{\mathrm{T}}$ is the velocity response of the buoy in surge, heave and pitch respectively. The velocities and forces were defined in a global frame, which coincides with the body-fixed frame when the buoy is at rest.

$$\mathbf{F}_{pto}(t) = (-F_{pre} - B_{pto}\Delta\dot{L} - K_{pto}\Delta L(t))\mathbf{T} \quad , \tag{6.3.2}$$

is the PTO control force vector, where F_{pre} is the pretension force that balances the net buoyancy of buoy, K_{pto} is the PTO stiffness, B_{pto} is the PTO damping coefficient, $\mathbf{T}$ is the transformation vector that converts the PTO control force to the Cartesian axes, given by

$$\mathbf{T} = \begin{pmatrix} \sin(\beta(t)) \\ \cos(\beta(t)) \\ r_{dis}(t) \end{pmatrix} \quad , \tag{6.3.3}$$

where $\beta(t)$ is the tether angle with the respect to the vertical direction. $r_{dis}(t)$ is the distance from the centre of the buoy to the mooring line.

$\Delta L(t)$ is the PTO elongation, can be related to the instantaneous buoy motion by

$$\Delta L(t) = \sqrt{(L + z(t) + r\sin(\alpha)\theta_y(t))^2 + (x(t) - r\cos(\alpha)\theta_y(t))^2} - L \quad , \tag{6.3.4}$$

where α is the mooring point angle as shown in Figure 6.3, $x(t)$ and $z(t)$ are the displacement of the buoy in surge and heave in the global frame.

$$\mathbf{F}_{re}(t) = \begin{pmatrix} 0 \\ \rho V(t)g - (m_1 + m_2)g \\ m_2 g r_{gy}\cos(\varphi - \theta_y(t)) \end{pmatrix} \quad , \tag{6.3.5}$$

is the net hydrostatic restoring force vector, which consists of the hydrostatic restoring forces in the heave direction and restoring torque generated by the gravity of the offset mass m_2 in the pitch direction, where $\rho = 1025$ kg/m^3 is the density of water, $V(t)$ is the immersed volume of the buoy and g is the gravitational acceleration. Since the effect of surface piercing is usually modelled by using nonlinear FK force and hydrostatic force [26], in order to investigate the effect of surface piercing, the immersed volume of the buoy $V(t)$ is fixed ($V(t) = V = \frac{4}{3}\pi r^3$) for the quasi-nonlinear model but a time-dependent variable in the CFD model.

$\mathbf{F}_{hydro}(t)$ is the total hydrodynamic force acting on the buoy. In the subsequent Sections 6.3.1 and 6.3.2, the hydrodynamic force $\mathbf{F}_{hydro}(t)$ is determined using linear potential theory for the quasi-nonlinear model and the finite volume method for the NWT experiment/CFD model respectively.

6.3.1 Linear wave theory

Assuming the fluid is incompressible and inviscid and its motion is irrotational, the velocity potential ϕ at an arbitrary position (x, y, z) is given by

$$\phi(x, y, z, t) = \mathrm{Re}\{\hat{\phi}(x, y, z)e^{-i\omega t}\} \quad , \tag{6.3.6}$$

where ω is the wave frequency of the irrotational harmonic motion, $\hat{\phi}(x, y, z)$ is the complex velocity potential, satisfying the Laplace equation throughout the fluid

$$\nabla^2\hat{\phi} = 0 \quad . \tag{6.3.7}$$

For the free water surface boundary condition at z = 0,

$$\frac{\partial \hat{\phi}}{\partial z} + k\hat{\phi} = 0 \quad , \tag{6.3.8}$$

where k is the wavenumber.

For the sea bed boundary condition at z = -h,

$$\left(\frac{\partial \hat{\phi}}{\partial z}\right)_{z=-h} = 0 \quad . \tag{6.3.9}$$

For the mean submerged surface of the buoy S_B,

$$\left(\frac{\partial \hat{\phi}}{\partial n}\right)_{S_B} = u_n \quad , \tag{6.3.10}$$

where $\vec{n}$ is the unit normal on the wetted surface, u_n is the buoy's velocity component nominal to its surface.

The velocity potential $\hat{\phi}$ can be decomposed into the sum of the incident potential $\hat{\phi}_0$, the radiation potential $\hat{\phi}_r$ and the diffraction potential $\hat{\phi}_d$, given by

$$\hat{\phi} = \hat{\phi}_0 + \hat{\phi}_r + \hat{\phi}_d \quad . \tag{6.3.11}$$

Since the buoy is spherical and the surface is assumed to be smooth, the excitation moment in pitch can be neglected. The excitation forces acting on the surface of buoy in surge and heave, $\hat{\mathbf{F}}_{exc}(\omega)$, is given by

$$\hat{\mathbf{F}}_{exc}(\omega) = -i\omega\rho \iint_{S_B} (\hat{\phi}_0 + \hat{\phi}_d)\vec{n}dS \quad . \tag{6.3.12}$$

The added mass matrix $\mathbf{A}(\omega)$ and hydrodynamic damping matrix $\mathbf{B}(\omega)$ which are caused by the motion of buoy are given by

$$\mathbf{A}(\omega) = \mathrm{Re}\{\rho \iint_{S_B} \hat{\phi}_r \vec{n}dS\} \quad , \tag{6.3.13}$$

$$\mathbf{B}(\omega) = \mathrm{Im}\{\omega\rho \iint_{S_B} \hat{\phi}_r \vec{n}dS\} \quad . \tag{6.3.14}$$

The equation of motion Eqn (6.3.1) can be re-written in the time-domain as

$$(\mathbf{M} + \mathbf{A}_\infty)\ddot{\mathbf{x}}(t) + \int_0^t \mathbf{K}(t-\tau)\dot{\mathbf{x}}(t)d\tau = \mathbf{F}_{exc}(t) + \mathbf{F}_{re}(t) + \mathbf{F}_{pto}(t) + \mathbf{F}_{vis}(t) \quad , \tag{6.3.15}$$

where $\mathbf{A}_\infty$ is the added mass matrix for $\omega \to \infty$, $\mathbf{K}(t) = \frac{2}{\pi}\int_0^\infty \mathbf{B}(\omega)\cos(\omega t)d\omega$ is the radiation impulse response function acting as a retardation kernel, $\mathbf{F}_{exc}(t)$ is the inverse Fourier transform of $\hat{\mathbf{F}}_{exc}(\omega)$. In this work, frequency-domain excitation force $\mathbf{F}_{exc}(\omega)$, added mass matrix $\mathbf{A}(\omega)$ and hydrodynamic damping matrix $\mathbf{B}(\omega)$ are calculated by using NEMOH, which is an open-source boundary element method solver (BEM) [27]. Noting that the viscous drag force vector $\mathbf{F}_{vis}(t)$ is also included in Eqn (6.3.15) to model the energy dissipated due to the viscous drag, given by

$$\mathbf{F}_{vis}(t) = -0.5\rho C_D \pi r^2 \begin{pmatrix} |\dot{x}(t)|\dot{x}(t) \\ |\dot{z}(t)|\dot{z}(t) \\ 0 \end{pmatrix} \quad , \tag{6.3.16}$$

where C_D is the viscous drag coefficient (C_D = 0.18 for the $1 \times 10^6 < Re < 5 \times 10^6$) [4]. As the fluid velocity is relatively small compared to the buoy's velocity when the system is at resonance, the fluid velocity is neglected in Eqn (6.3.16) to simplify the computational complexity of the quasi-nonlinear model. It should be noted that for a smooth spherical buoy, the viscous drag coefficient in the pitch direction is negligible.

The time-domain model developed from Eqn (6.3.15) is referred to as the quasi-nonlinear model in this work, and was used to estimate the trajectory references and power output of the SPAMD from the perspective of linear potential theory, to provide a benchmark with the results obtained in the NWT experiment. The quasi-nonlinear model was realised by using the MATLAB-Simulink toolbox *SimMechanics* and solved using the ode45 solver (Runge-Kutta method with variable time step). The validation of the quasi-nonlinear model was presented in a technical report by the authors [19].

6.3.2 RANS model

In Reynold-averaged Navier-Stokes (RANS) model, the total hydrodynamic force $\mathbf{F}_{hydro}$ is given by

$$\mathbf{F}_{hydro} = (p \cdot \vec{n})dS \quad , \tag{6.3.17}$$

where p is the pressure on the surface.

For an incompressible fluid, the continuity equation holds

$$\nabla \cdot \mathbf{U} = 0 \quad , \tag{6.3.18}$$

in which $\mathbf{U}$ is the velocity vector.

The momentum equation can be written as

$$\frac{\partial \rho \mathbf{U}}{\partial t} + \nabla \cdot (\rho \mathbf{U}\mathbf{U}) - \nabla \cdot (\mu_{eff} \nabla \mathbf{U}) = -\nabla p^* - g\mathbf{X}\nabla\rho + \nabla \mathbf{U} \cdot \nabla \mu_{eff} + \sigma\kappa\nabla\delta \quad , \quad (6.3.19)$$

in which ρ is the density of water, μ_{eff} is the effective dynamic viscosity, $p*$ is the pseudo-dynamic pressure [14], g is the gravitational acceleration, $\mathbf{X}$ is the position vector, σ is the coefficient of surface tension, κ is the interface curvature and δ is the indicator phase function varying between 0 and 1, which defines the density of computational cell as

$$\rho = \delta\rho_{water} + (1-\delta)\rho_{air} \quad . \quad (6.3.20)$$

In order to track the interface between air and water, the following advection equation is solved,

$$\frac{\partial \delta}{\partial t} + \nabla \cdot \mathbf{U}\delta + \nabla \cdot \mathbf{U}_c \delta(1-\delta) = 0 \quad , \quad (6.3.21)$$

in which $\mathbf{U}_c$ is the artificial compression term to keep the interface sharp between air and water interface. This is essential to avoid wave dissipation as it travels along the NWT.

The third-party utility OLAFOAM [14] was used to define the boundary conditions and the solver interFoam solves Eqns (6.3.18)-(6.3.21). The PTO was defined as a linear spring-damper type constraint in the *dynamicMeshDict* file used in the OpenFOAM configuration, using the values shown in Appendix 6.A.

6.4 Numerical wave tank

The 3D NWT was used to simulate the response of the SPAMD under monochromatic waves. The dimensions of the NWT are 330 m long (-30 m $\leq x \leq$ 300 m), 100 m wide (-50 m $\leq y \leq$ 50 m) and 43 m high (-33 m $\leq z \leq$ 10 m), in which the water domain ranges from -33 to 0 m in depth and the air domain ranges from 0 to 10 m), as shown in Figure 6.4. Here an active wave generation and absorption are used (within the OLAFLOW library) which eliminates the need of a long relaxation zone for wave generation and absorption.

In this numerical wave tank simulation, a monochromatic plane wave train with first-order or second-order Stokes profile was generated at the inlet of the NWT, according to the determined wave periods and wave heights

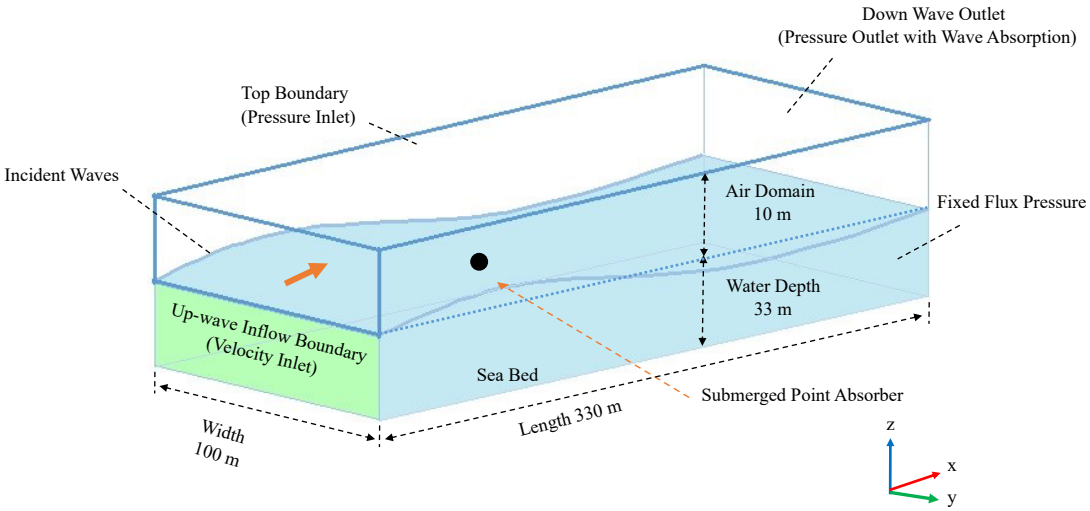

Figure 6.4: Schematic of the numerical wave tank, with key dimensions and boundary conditions.

in Section 6.5. The incident wave train propagates along the positive x-axis and excites the single-tethered PA in surge, heave and pitch. For the two faces of the NWT in XZ plane, the fixed pressure boundary condition was implemented, which allows the water flow in and out of the domain freely. Similar boundary conditions are also applied to the intersection between the water and air. When the incident wave train travels to the end of the NWT, the pressure is artificially truncated to eliminate any wave reflection.

The NWT simulation was conducted on the Phoenix High Performance Computing Cluster of the University of Adelaide. 32 Skylake CPU cores and 64 GB memory were utilised for the cases in subsequent sections.

6.4.1 Mesh generation and resolution

The meshes used in the NWT were created using the OpenFOAM mesh generation utilities. The utility *blockMesh* was used to generate the whole computational domain, while the utility *snappyHexMesh* used to refine the mesh around the water surface and create the shape of the spherical buoy in NWT. A numerical convergence analysis was conducted to determine the sufficient mesh resolution for accurate results.

For the mesh around the water surface, the grid size Δx (along wave propagation) and Δz (along vertical direction) were determined by the incident wave height H and wavelength λ. The numerical convergence analysis starts with $\Delta x = \lambda/20$ and $\Delta z = H/5$ to investigate the impact of mesh resolution on the wave modelling with the absence of the spherical buoy. A

5th order Stokes wave train was produced in the numerical wave tank by using the OpenFOAM toolbox OLAFLOW, with the incident wave height $H = 10$ m and wave period $T = 16$ s. Figure 6.5 compares the normalised wave height H_m/H which is measured at $x = 100$ m versus the number of cells per wavelength and per wave height. It can be seen that the value of the normalised wave height converges at $\Delta x = \lambda/80$ and $\Delta z = H/20$, which agrees with the recommendation given by the International Towing Tank Committee [15] that the horizontal grid size Δx along the wave length should be no greater than $\lambda/40$ and the vertical grid size Δz along the wave height should be less than $H/20$. Figure 6.6 compares the measured wave elevation against the theoretical elevation time series of the sampling point of $x = 100$ m downstream. There is negligible difference between the simulated wave profile and the theoretical profile at the trough. Therefore, the mesh resolution around the water surface was set to be $\Delta x = \lambda/80$ and $\Delta z = H/20$, as shown in Figure 6.7 for the entire analysis.

To accurately model the turbulence around the spherical buoy, five structured prism layers were applied along the surface of the body. The thickness of the first layer was set so that the value of $y+$ was constrained between 30 and 300. Additionally, a set of refined meshes were also applied around the buoy to capture the detail of the flow in the vicinity of buoy. To investigate the appropriate number of cells, a numerical convergence was conducted to test the excitation force of the spherical buoy when fixed, with incident wave height H = 2 m and wave period T = 14 s. Figure 6.8 compares the excitation forces of the fixed spherical buoy versus the number of the refined cells around the surface of buoy, as listed in Table 6.2. It can be seen that the grid with resolution of 40 cm leads to the convergence of excitation force and the resulting excitation forces are identical to that calculated by BEM. Figure 6.9 illustrates the refined dynamic mesh around the buoy with the grid resolution of 40 cm (see Figure 6.9a), and the instantaneous flow field around the structure (see Figure 6.9b).

Table 6.2: Number of cells and resolution of the mesh around the surface of the spherical buoy.

Grid No.	**Number of cells**	**Size of grid on surface (max length)**
1	0.3×10^6	80 cm
2	0.6×10^6	40 cm
3	1.2×10^6	20 cm

The Courant number was restrained to 0.5 in the numerical wave tank ex-

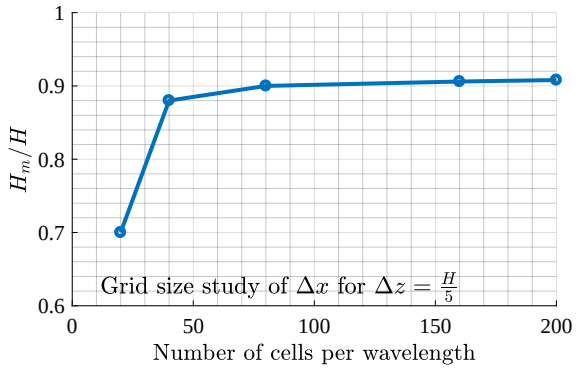

(a)

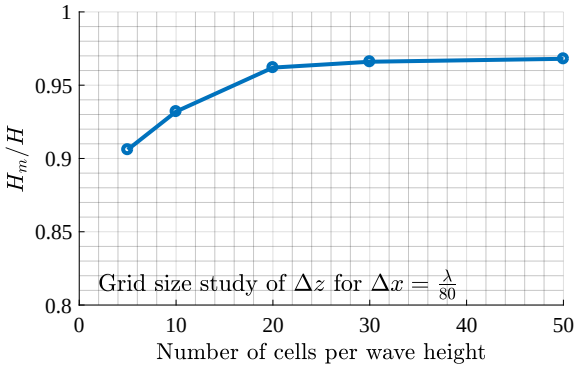

(b)

Figure 6.5: Mesh convergence study for wave dynamics modeling: (a) grid size study of Δx for $\Delta z = H/5$; (b) grid size study of Δz for $\Delta x = \lambda/80$.

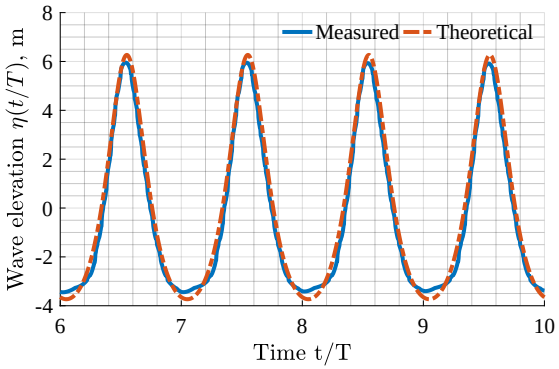

Figure 6.6: Comparison between the measured wave elevation and the theoretical elevation [10] in time series for sampling point at $x = 100$ m downstream.

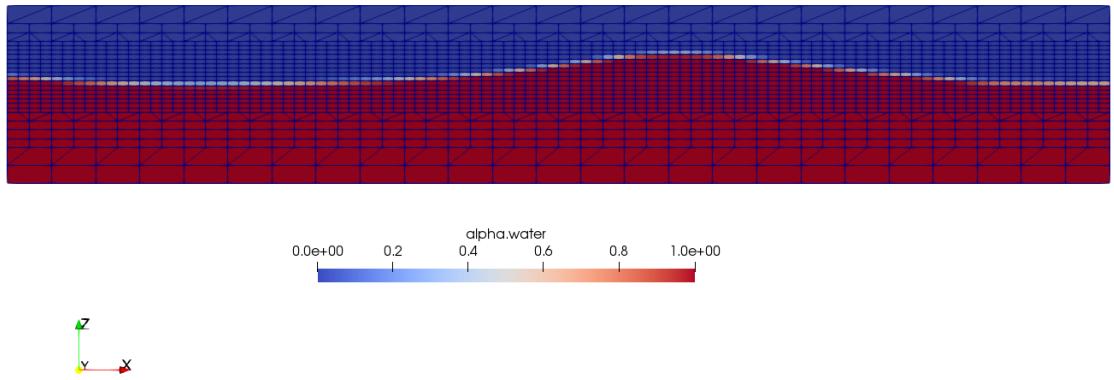

Figure 6.7: Mesh around the water surface in the numerical wave tank.

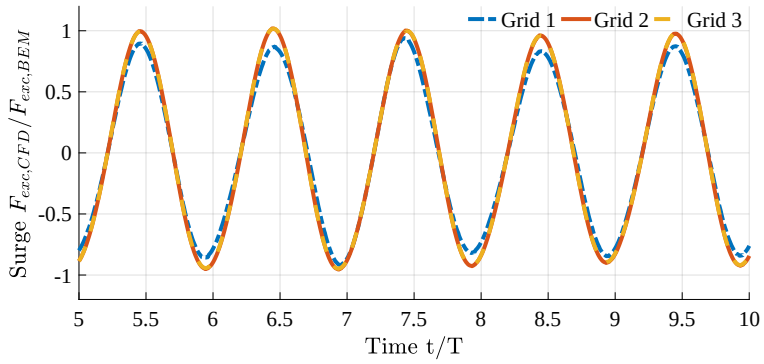

(a)

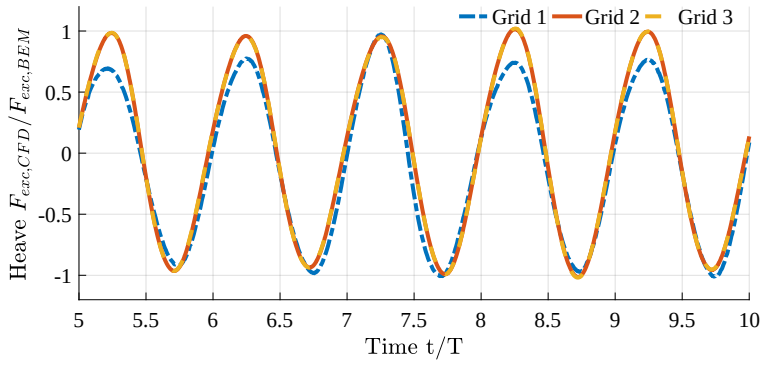

(b)

Figure 6.8: Mesh convergence study for the refined dynamic mesh around the buoy: (a) normalised surge excitation force; (b) normalised heave excitation force.

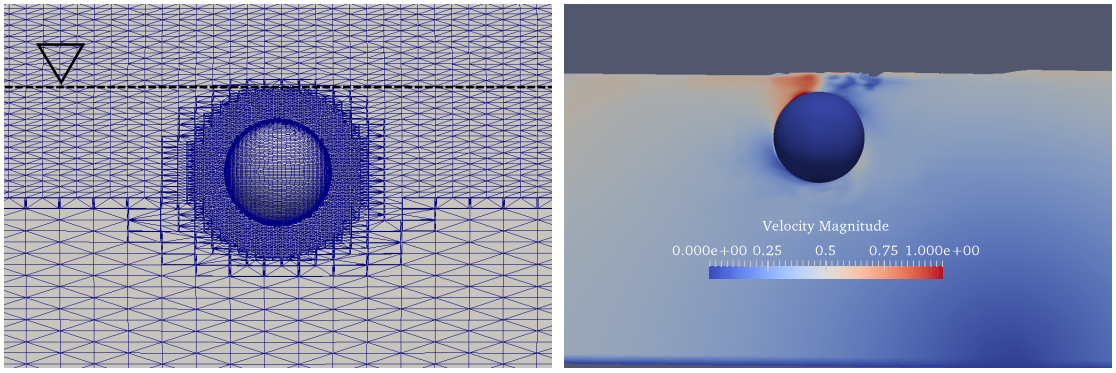

(a) (b)

Figure 6.9: Side-view schematics of (a) refined dynamic mesh around the spherical buoy (the horizontal dashed line represents mean water surface), and (b) the instantaneous flow field around the structure.

periments. Based on the Courant number constraint, flexible time-steps were implemented, with the largest time step being $T/400$, which as suggested in the literature [33].

6.4.2 Validation

The numerical wave tank developed in this work was validated against a small-scale experiment conducted in the wave basin of the Australian Maritime College [3]. For the validation of the diffraction problem, the magnitude of the excitation force coefficient f_{exc} was determined when the buoy was fixed in monochromatic incident waves with wave height of 30 mm over ten sampled frequencies from 0.6 to 1.5 Hz; while for the study of radiation, the magnitude of heave radiation impedance coefficient Z_r was determined when the buoy was forced to oscillate in calm water, with buoy motion amplitude of 30 mm. The detailed fundamental settings of the experiment are listed in Table 6.3. Noting that the same mesh resolution and the size of time step determined in Section 6.4 were applied in this validation.

Figure 6.10 compares the magnitudes of the surge and heave excitation force coefficients of a fixed buoy estimated by the BEM, the CFD model and the small-scale experiment, over the wave frequencies from 0.6 Hz to 1.4 Hz. It can be seen that the results from the BEM deviate slightly from the CFD model and small-scale experiment since the desired incident wave is out of the linear regime. The largest magnitude difference of excitation force coefficients between CFD model and experiment is 15.2 N/m (7.1 % relative

Table 6.3: Physical parameters and the dimensions of the small-scale experiment [3].

Description	Value/Unit
Diameter of buoy	0.25 m
Length of wave basin	15 m
Width of wave basin	4 m
Height of wave basin	1 m
Water depth	0.6 m
Wave height	0.06 m
Wave frequency	0.6 -1.4 Hz over 5 samples

error) in surge and 17.7 N/m (8.9 % relative error) in heave for the wave frequency of 1 Hz, which is consistent with the literature [3].

Figure 6.11 compares the magnitude of heave radiation impedance coefficient of the oscillating buoy estimated by the BEM, the CFD model and the experiment, over the pre-defined wave frequencies. It is found that there is a good agreement between all three models. The largest deviation between the CFD model and experiment is 22.4 (N/m) (6.8 % relative error) for wave frequency of 1.4 Hz, which is consistent with the literature [3].

In summary, the NWT with the applied mesh configuration can reproduce essentially equivalent results to the small-scale experiment for the diffraction and radiation problem.

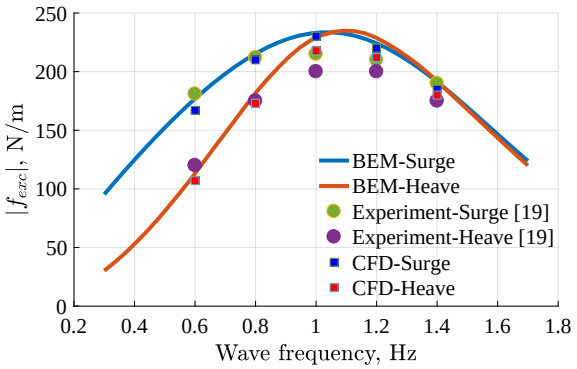

Figure 6.10: BEM, CFD and small-scale experimental [3] excitation force coefficient on stationary spherical buoy.

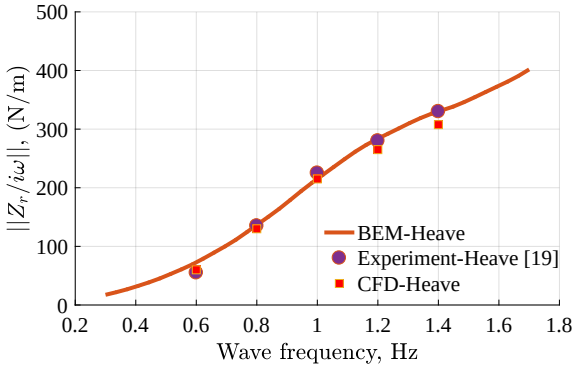

Figure 6.11: BEM, CFD and small-scale experimental [3] heave radiation impedance on an oscillating spherical buoy.

6.5 Results

In this section, the motion trajectory and power output of the SPAMD under nominal wave conditions were investigated by implementing the NWT experiment as described in Section 6.4. The nominal wave condition is defined as regular waves with wave height of 0.5 m, 1 m and 2 m over the wave period of 6 s, 8 s, 10 s, 12 s and 14 s, to provide a fundamental understanding of the relationship between buoy trajectory and power absorption.

6.5.1 Motion analysis

In the previous work done by the authors [20, 21], the efficiency of the SPAMD was found to be highly dependant on the shape of the trajectory of the buoy in Cartesian space. For long waves, such as a wave period of 14 s, the trajectory of the SPAMD tends to be slightly elliptical (see Figure 4.12f) and the resulting efficiency improvement in comparison with the generic spherical buoy is about 3 times; for intermediate wave periods such as 10 s and 12 s, the trajectories approach a horizontal ellipse, resulting in a twofold efficiency improvement; while for short waves with wave periods from 6 s to 8 s, the corresponding trajectories are similar to a vertically aligned ellipse and SPAMD has almost identical power output to the generic symmetric buoys.

Figure 6.12 compares the trajectories of the SPAMD obtained from NWT experiment and quasi-nonlinear model over the pre-defined wave periods (T = 6 s, 8 s, 10 s, 12 s and 14 s) and wave heights (H = 0.5 m, 1 m and 2 m). The shaded area represents the air domain for calm water. It can be seen that surface piercing has the largest negative impact on the system's performance.

When the SPAMD completely operates under water, the trajectories obtained from NWT experiment corresponds closely to the quasi-nonlinear model, even for a large wave height (e.g. the case of 8 s wave period and 2 m wave height). However, when the spherical buoy starts to periodically approach or breach the water surface during its operation, the resulting trajectory differs significantly from the quasi-nonlinear model, even for a small wave height (e.g. the case of 14 s wave period and 0.5 m wave height). This means the surface piercing is the most dominant factor that affects the trajectory of the SPAMD relative to the quasi-nonlinear model trajectory. Figure 6.13 illustrates the dynamic pressure around the surfaces of water and buoy, as well as the particle velocity in the vicinity of the device for wave period of 12 s and wave height of 2 m. It can be observed that an impact occurs when the top of the buoy re-enters the water (see the 5th and 6th frame in Figure 6.13). As a result, the dynamic pressure on the spherical buoy is distributed unevenly: a high dynamic pressure area occurs on the top left of the buoy. This uneven dynamic pressure modifies the trajectory of the buoy from the initial circular motion to the final thin ellipse, as shown in Figure 6.14. Besides the effect of modifying the trajectory, the surface piercing can also dissipate significant energy from the system, which is discussed further in Section 6.5.2.

To conclude, the nonlinear effect caused by surface piercing leads to considerable trajectory changes that might result in most existing model-based controls being invalid. Increasing the PTO damping might be a potential solution to constrain the buoy vertical motion and thus to avoid the surface breaching. However, a heavily damped PTO has the possibility of causing parametric excitation in other directions, adding more uncertainties to the system [31].

6.5.2 Power analysis

As discussed in [21], the trajectory of a multiple-DOF point absorber is generally related to the performance of the device. Therefore, any trajectory deviation from the desired reference trajectory is likely to result in a reduction of power output.

The wave period of 12 s is taken as a case study for power analysis. Figure 6.15 compares the instantaneous power of the device for wave period of 12 s over wave heights of 0.5 m, 1 m and 2 m. For a wave height of 0.5 m, the instantaneous power from NWT experiment matches well with the quasi-nonlinear model and the trajectories are in good agreement. Since the buoy approaches the free water surface for wave height of 1m, the effects of surface piercing starts to affect the trajectory of the buoy, and the resulting

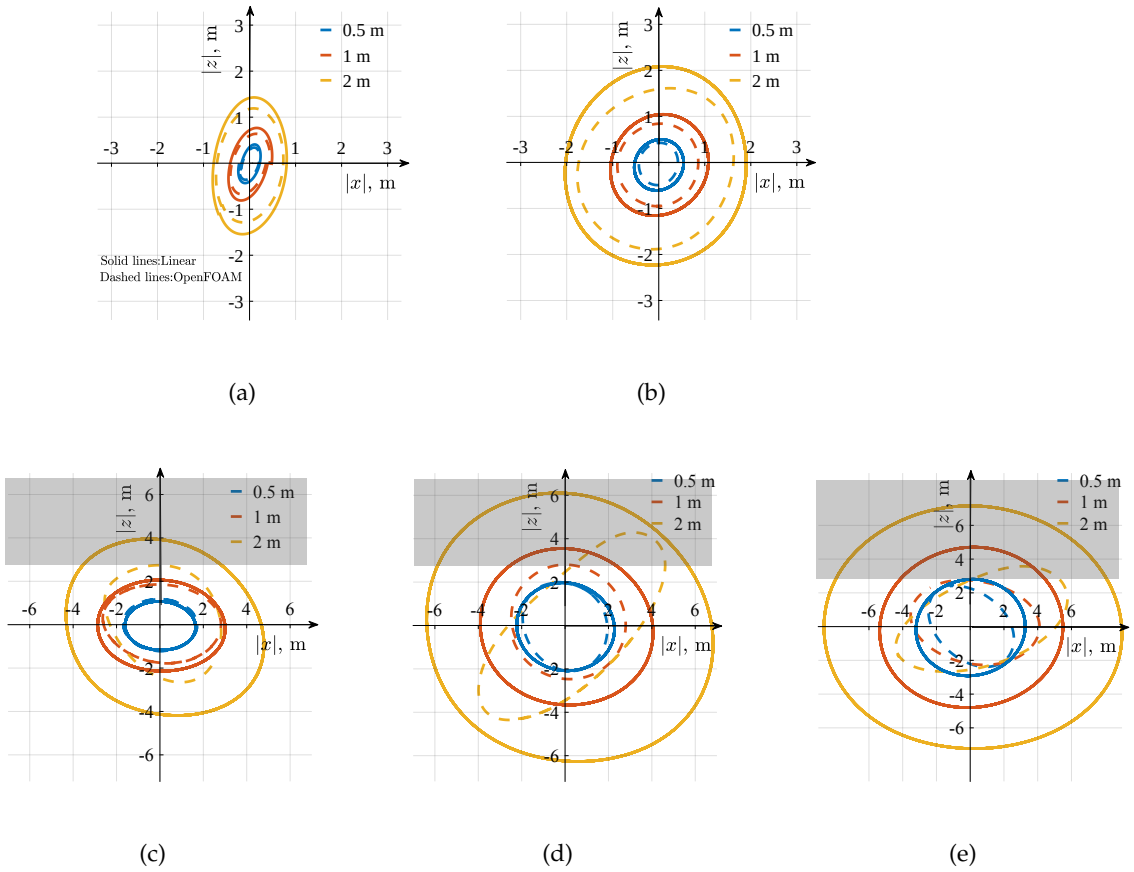

Figure 6.12: Trajectory comparison between the quasi-nonlinear model and the NWT experiment over various wave periods: (a) 6 s; (b) 8 s; (c) 10 s; (d) 12 s; (e) 14 s. The solid lines represent the quasi-nonlinear model. The dashed lines represent the NWT results. The shaded area represents the air domain for calm water.

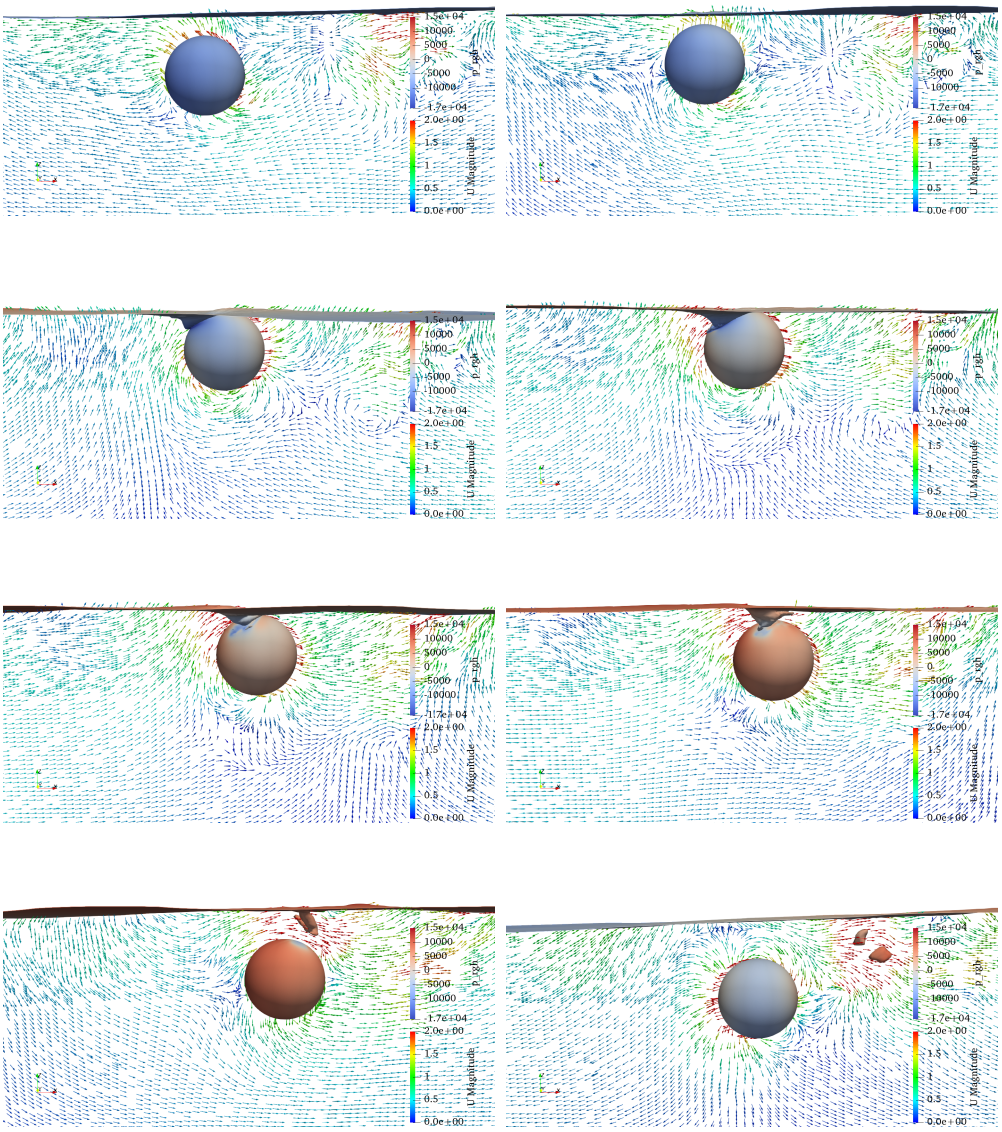

Figure 6.13: Plot of dynamic pressure distribution and water particle velocity vector for a wave period of 12 s and a wave height of 2 m.

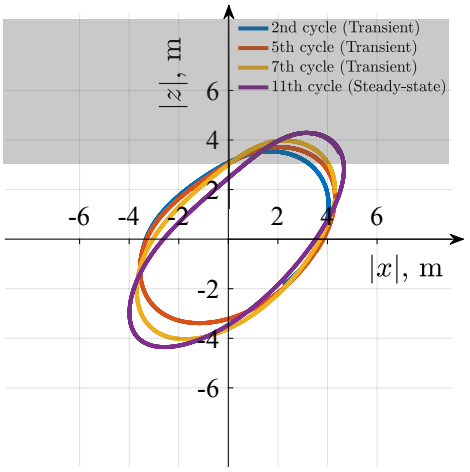

Figure 6.14: Evolution of the trajectory of the SPAMD from transient state to steady-state, under the effect of surface piercing for a wave period of 12 s and a wave height of 2 m.

instantaneous power measured in NWT experiment is compromised by 50% in comparison with the quasi-nonlinear model in each cycle, as shown in Figure 6.15b. When the wave height increases to 2 m, the trajectory of the buoy is modified by the periodic surface piercing. A considerable amount of kinematic energy is dissipated, resulting in average 55% power loss in each cycle and 70% instantaneous power loss when the buoy breaches water surface (highlighted by a green rectangle in Figure 6.15c).

The dynamic PTO loading is also affected by the surface piercing. Figure 6.16 compares the instantaneous dynamic PTO loading of the device for wave period of 12 s over wave heights of 0.5 m, 1 m and 2 m. For a wave height of 0.5 m, the instantaneous PTO loading from NWT experiment is in good agreement with the quasi-nonlinear model (see Figure 6.16a). For a wave height of 1 m, the magnitude of dynamic PTO loading measured from NWT experiment is approximately 70% of the estimate from the quasi-nonlinear model (see Figure 6.16b). As the wave height increases further to 2 m, the difference in dynamic PTO loading between the NWT experiment and quasi-nonlinear model increases to 50%. Noting that as the buoy was decelerated by the surface piercing in the process of breaching water surface, the instantaneous dynamic PTO loading decreases to its negative maximum with a small phase shift (highlighted by a green rectangle in Figure 6.16c).

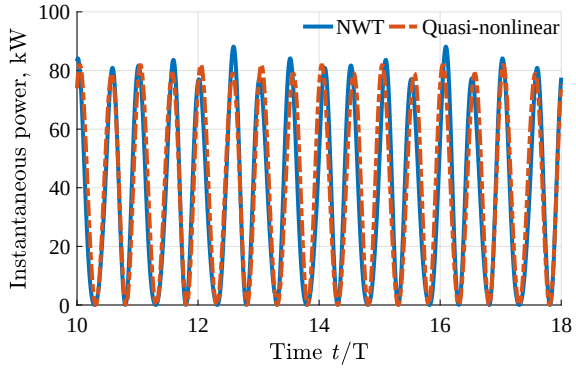

(a)

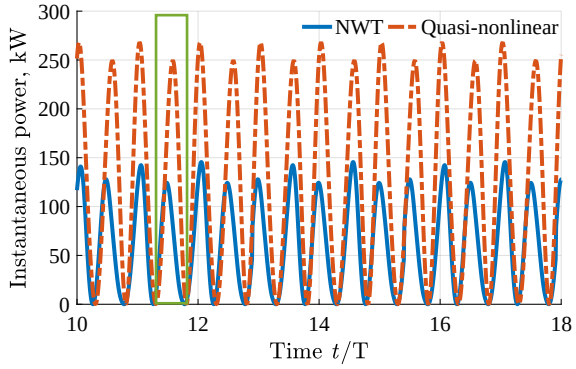

(b)

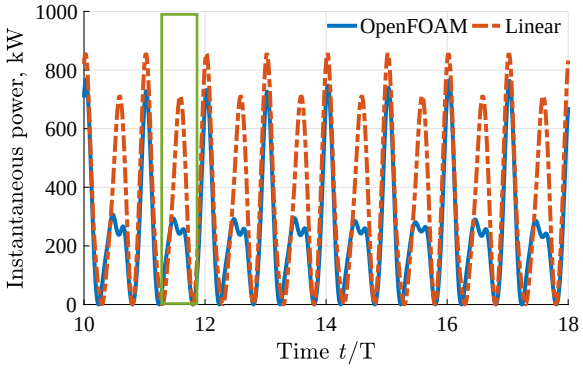

(c)

Figure 6.15: Instantaneous power comparison between the NWT experiment (OpenFOAM) and quasi-nonlinear model (linear potential theory) for wave period of 12 s over wave amplitudes of 0.5 m, 1 m and 2 m : (a) wave height of 0.5 m; (b) wave height of 1 m; (c) wave height of 2 m. Green rectangle represents the half of the cycle when the buoy approaches to the water surface. The instantaneous power obtained from the NWT experiment exhibits a considerable loss when surface piercing happens, unlike the quasi-nonlinear model.

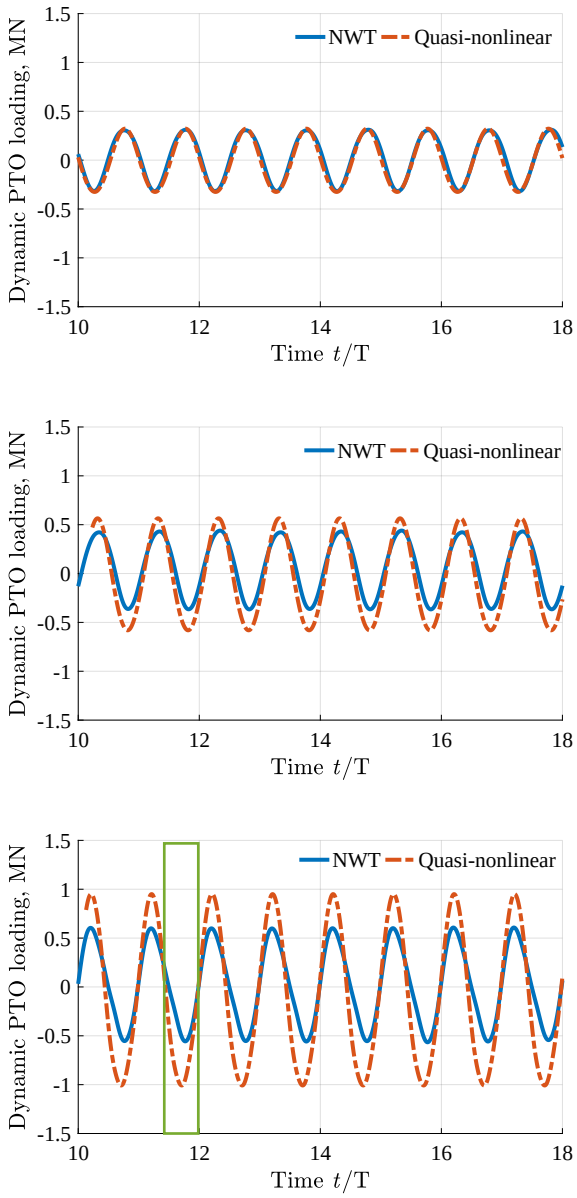

Figure 6.16: Instantaneous PTO loading comparison between the NWT experiment (OpenFOAM) and quasi-nonlinear model (linear potential theory) for a wave period of 12 s over wave amplitudes of 0.5 m, 1 m and 2 m: (a) wave height of 0.5 m; (b) wave height of 1 m; (c) wave height of 2 m.

Figure 6.17 shows the mean power of the SPAMD over pre-defined wave periods and heights. Additionally, the mean power output comparison is also conducted between the SPAMD and a generic PA, with the same physical properties. The efficiency improvement of the SPAMD is quantified by using the q factor, which is defined as the ratio of mean power output of the SPAMD to that of the generic PA. The efficiency improvement in small wave (see Figure 6.17a) reflects the finding in the previous work [21]: for long waves (e.g. T = 14 s), the efficiency improvement of the SPAMD is about 3 times; for intermediate waves (e.g. T = 10 s and 12 s), the SPAMD has twofold efficiency improvement; while for short waves (e.g. T = 6 s and 8 s), SPAMD has almost identical power output to the generic PAs. However, this conclusion is no longer valid when the buoy pierces the surface in large waves. For example, for a wave height of 1 m, the SPAMD has more than twofold efficiency improvement at wave period of 10 s. Since the generic PA can only absorb the wave power arising from its heave motion [21], it needs to have a large heave motion to harvest energy. Consequently, the surface piercing occurs more often for the generic PA compared to the SPAMD (see Figure 6.18b), which leads to dramatic energy loss for the generic PA. It is also interesting to note that when surface piercing occurs for wave height of 2 m, the SPAMD has almost a three-time efficiency improvement for 10 s, although the trajectory of the generic PA is similar to the SPAMD (see Figure 6.18c). This is because the SPAMD can also absorb power from its surge and pitch motion and therefore the instantaneous power is much greater than the generic PA (see Figure 6.19c). In contrast, there was no gain for wave period of 14 s. It is supposed that the SPAMD might have experienced a greater kinematic energy loss in the wave period of 14 s than 10 s and 12 s. The factor that determines the amount of dissipated energy in surface piercing will be studied in future work.

6.6 Conclusion

The trajectory analyses of a submerged spherical buoy were performed in a NWT, to demonstrate that surface piercing caused by large buoy motion can invalidate the models developed from linear potential theory. Specifically, the results from the NWT experiment were compared against a quasi-nonlinear model developed from linear potential theory over five typical wave periods and three typical wave heights.

According to the trajectory analysis, the effect of surface piercing caused by the large motion of the buoy plays an important role in modifying the trajectory of the submerged device. Examples of the wave periods greater

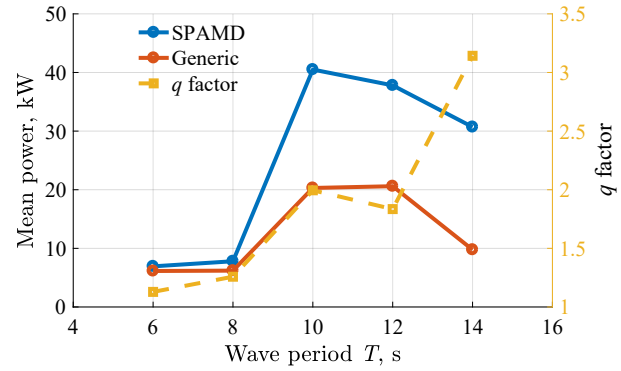

(a)

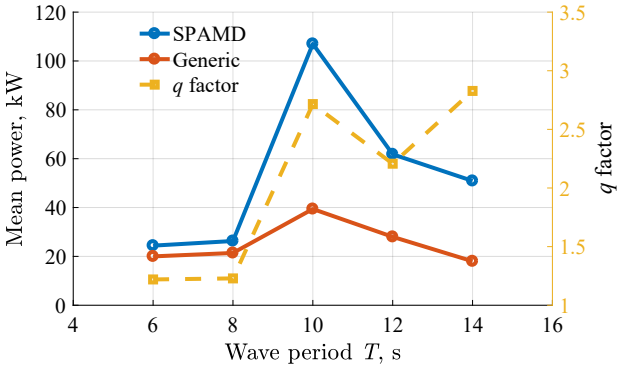

(b)

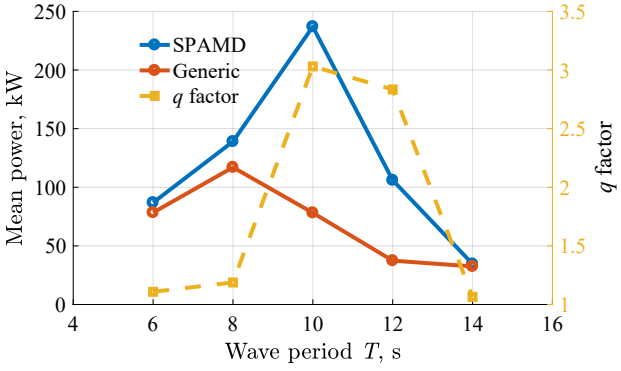

(c)

Figure 6.17: Mean power comparison between the SPAMD and the generic PA obtained from the NWT experiment for various wave heights: (a) 0.5 m; (b) 1 m; (c) 2 m.

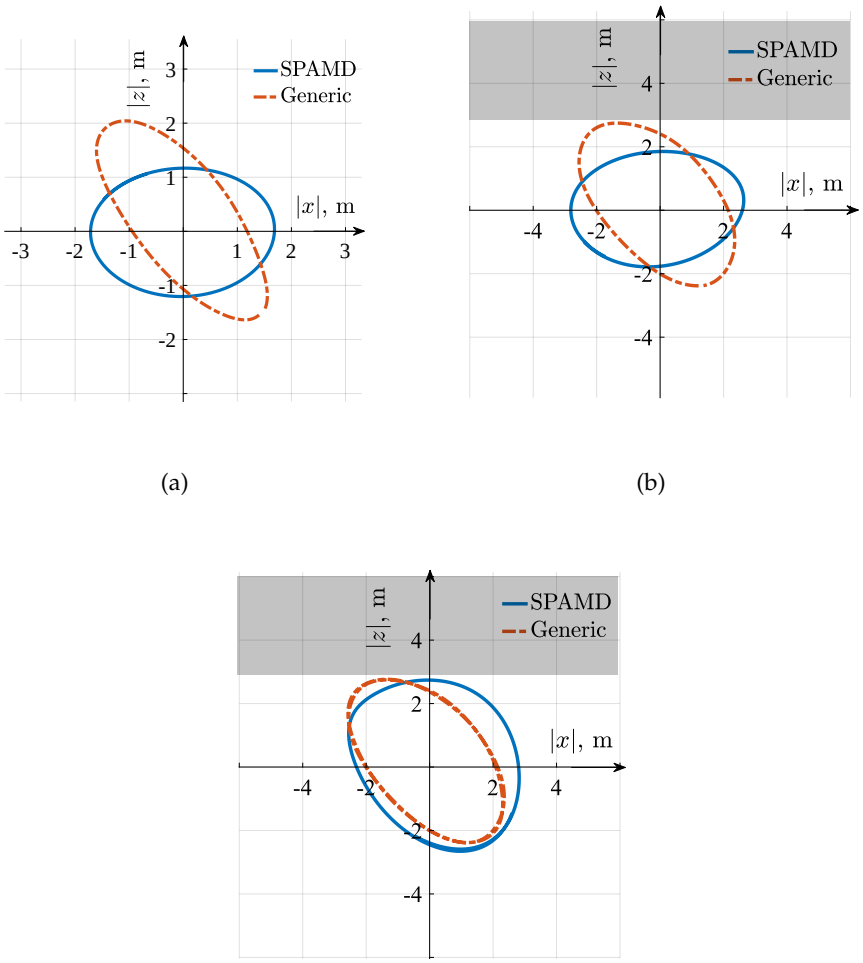

(a) (b)

(c)

Figure 6.18: Trajectory comparison between the SPAMD and the generic PA obtained from the NWT experiment for a wave period of 10 s and various wave heights: (a) 0.5 m; (b) 1 m; (c) 2 m. The shaded area represents the air domain.

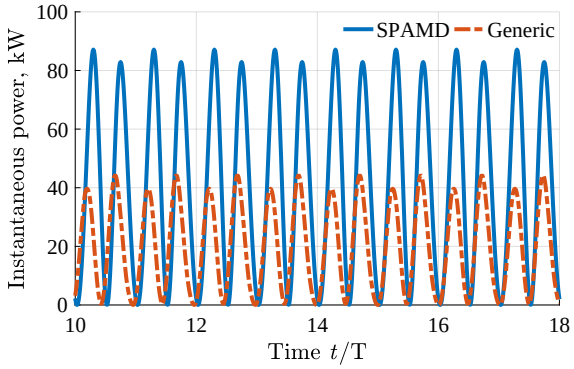

(a)

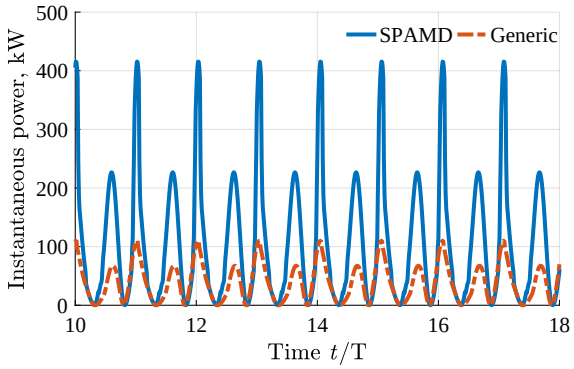

(b)

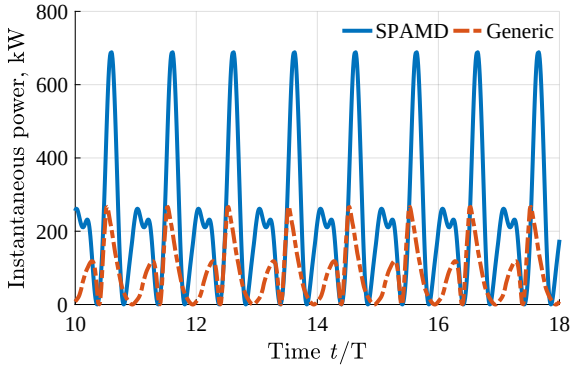

(c)

Figure 6.19: Instantaneous power comparison between the SPAMD and the generic PA obtained from the NWT experiment for wave period of 10 s and various wave heights: (a) 0.5 m; (b) 1 m; (c) 2 m.

than 10 s show that there are considerable trajectory differences between the NWT experiment and the quasi-nonlinear model. The trajectory difference is likely to compromise most existing model-based control laws in practice. Noting that a circular trajectory is known as optimal for only a submerged device, while a floating body is likely to have a different optimal trajectory shape such as ellipse.

For multiple-DOF point absorbers, the trajectory is closely associated with the efficiency of the device. Of the examples investigated, the wave period of 12 s shows that the trajectory change lead to an average 55% instantaneous power loss of the SPAMD for the wave height of 2 m in each wave cycle, in which about 70% of power loss occurred when the buoy breached water surface. Furthermore, the dynamic PTO loading is also affected by the trajectory change. The results show that the magnitude of the PTO loading is half that of the quasi-nonlinear model which does not model surface piercing.

Although the power output of the SPAMD decreases due to surface piercing, the maximum efficiency improvement in comparison to the generic PA was found to be 3 times for all wave heights investigated in this study. It is interesting to note that the effect of surface piercing has a greater negative impact on the performance of the submerged generic PA compared to the SPAMD. This is because the generic buoy predominantly generates power in heave, so anything that restricts heave motion such as surface piercing, will limit power production. Whereas, the SPAMD can also generate power from surge and pitch motion of the buoy, which happens during surface piercing.

Future research should identify the pathway of the considerable kinetic energy dissipation when the buoy breached water surface, whether from turbulence or wave radiation.

Acknowledgment

This research was supported by China Scholarship Council (CSC), Australian Research Council (ARC) Linkage Grant (LP130100117) and the Research Training Program (RTP).

Appendix 6.A

By using the quasi-nonlinear model defined in Eqn (6.3.15), the optimal PTO configuration (K_{pto}, B_{pto} and L) are determined by using the MATLAT optimisation function “fmincon”to maximise the power output of the SPAMD,

for given constraint ranges 50 kN/m $\leq K_{pto} \leq 1 \times 10^3$ kN/m, 10 kNm/s $\leq B_{pto} \leq 3 \times 10^2$ kN·m/s and 9 m $\leq L \leq$ 30 m.

Table 6.4: Optimal PTO configuration for wave height H = 0.5 m.

Wave period (s)	Device	PTO configuration		
		K_{pto} (kN/m)	B_{pto} (kN·m/s)	L (m)
6	SPAMD	683.0	120.7	9
	Generic	637.8	92.5	9
8	SPAMD	236.9	83.9	9
	Generic	372.1	32.8	9
10	SPAMD	156.1	154.6	9
	Generic	231.2	30	9
12	SPAMD	149.6	103.5	14
	Generic	156.9	30	14
14	SPAMD	117.9	51.7	20
	Generic	114.2	30	20

Table 6.5: Optimal PTO configuration for wave height H = 1 m.

Wave period (s)	Device	PTO configuration		
		K_{pto} (kN/m)	B_{pto} (kN·m/s)	L (m)
6	SPAMD	682.3	135.1	9
	Generic	637.8	96.2	9
8	SPAMD	252.9	122.3	9
	Generic	372.1	39.1	9
10	SPAMD	210.1	169.8	9
	Generic	231.2	30	9
12	SPAMD	163.9	79.4	14
	Generic	156.9	30	14
14	SPAMD	120.0	45.6	20
	Generic	114.2	30	20

Table 6.6: Optimal PTO configuration for wave height H = 2 m.

Wave period (s)	Device	PTO configuration		
		K_{pto} (kN/m)	B_{pto} (kN·m/s)	L (m)
6	SPAMD	681.6	151.4	9
	Generic	637.8	102.9	9
8	SPAMD	237.7	149.6	9
	Generic	372.1	48.5	9
10	SPAMD	229.5	158.0	9
	Generic	231.2	32.4	9
12	SPAMD	165.9	78.5	14
	Generic	156.9	30	14
14	SPAMD	120.2	51.4	20
	Generic	114.2	30	20

References

[1] Bacelli, G., Coe, R. G., Patterson, D. and Wilson, D. (2017). "System Identification of a Heaving Point Absorber: Design of Experiment and Device Modeling". In: *Energies* 10.4, p. 472.

[2] Barstow, S., Mørk, G., Mollison, D. and Cruz, J. (2008). "The wave energy resource". In: *Ocean wave energy*. Springer, pp. 93–132.

[3] Bharath, A., Nader, J.-R., Penesis, I. and Macfarlane, G. (2018). "Non-linear hydrodynamic effects on a generic spherical wave energy converter". In: *Renewable Energy* 118, pp. 56–70.

[4] Blevins, R. D. (2003). *Applied fluid dynamics handbook*. Krieger Publishing Company.

[5] Chen, W., Dolguntseva, I., Savin, A., Zhang, Y., Li, W., Svensson, O. and Leijon, M. (2017). "Numerical modelling of a point-absorbing wave energy converter in irregular and extreme waves". In: *Applied Ocean Research* 63, pp. 90 –105.

[6] Clément, A., Babarit, A., Gilloteaux, J.-C., Josset, C. and Duclos, G. (2005). "The SEAREV wave energy converter". In: *6th European Wave and Tidal Energy Conference*, pp. 1–10.

[7] Cummins, W. (1962). *The impulse response function and ship motions*. Tech. rep. DTIC Document.

[8] Davis, J (1990). "Wave energy absorption by the Bristol cylinder: linear and non-linear effects". In: *Institution of Civil Engineers Proceedings Proceedings*. Vol. 89, pp. 317–340.

[9] Falnes, J. (2002). *Ocean waves and oscillating systems: linear interactions including wave-energy extraction*. Cambridge University Press.

[10] Fenton, J. D. (1985). "A fifth-order Stokes theory for steady waves". In: *Journal of Waterway, Port, Coastal, and Ocean Engineering* 111.2, pp. 216–234.

[11] Gilloteaux, J.-C., Bacelli, G. and Ringwood, J. (2007). "A non-linear potential model to predict large-amplitudes-motions: Application to a multi-body wave energy converter". In: *Proceedings of the 22nd International Workshop on Water Waves and Floating Bodies*, pp. 1–10.

[12] Giorgi, G., Penalba, M. and Ringwood, J. (2016). "Nonlinear Hydrodynamic Models for Heaving Buoy Wave Energy Converters". In: *Proceedings of the 3rd Asian Wave and Tidal Energy Conference*. Vol. 1. Singapore, pp. 144–153.

[13] Göteman, M., Engström, J., Eriksson, M., Hann, M., Ransley, E., Greaves, D., Leijon, M. et al. (2015). "Wave loads on a point-absorbing wave energy device in extreme waves". In: *The Twenty-fifth International Ocean and Polar Engineering Conference*. International Society of Offshore and Polar Engineers.

[14] Higuera, P (2015). "Application of computational fluid dynamics to wave action on structures". PhD thesis. University of de Cantabria, Santander, Spain.

[15] ITTC (1999). "CFD User's Guide". In: *International Towing Tank Conference Recommended Procedures and Guidelines*, pp. 1–10.

[16] Iversen, L. C. (1982). "Experimental study of the deviation from linear behaviour for a submerged spherical point absorber". In: *Applied Ocean Research* 4.1, pp. 33–40.

[17] Kalofotias, F. (2016). "Study for the Hull shape of a wave energy converter-point absorber: Design optimization & modeling improvement". MA thesis. University of Twente.

[18] Lee, C. H. (1995). *WAMIT Theory Manual*. Massachusetts Institute of Technology, Department of Ocean Engineering.

[19] Meng, F, Cazzolato, B, Ding, B and Arjomandi, M (2017). *Technical report: Model validation of the submerged spherical point absorber with asymmetric mass distribution*. Tech. rep. University of Adelaide.

[20] Meng, F., Cazzolato, B., Li, Y., Ding, B., Sergiienko, N. and Arjomandi, M. (2019a). "A sensitivity study on the effect of mass distribution of a single-tether spherical point absorber". In: *Renewable Energy* 141, pp. 583 –595.

[21] Meng, F., Ding, B., Cazzolato, B. and Arjomandi, M. (2019b). "Modal analysis of a submerged spherical point absorber with asymmetric mass distribution". In: *Renewable Energy* 130, pp. 223 –237.

[22] Merigaud, A., Gilloteaux, J.-C. and Ringwood, J. V. (2012). "A nonlinear extension for linear boundary element methods in wave energy device modelling". In: *ASME 2012 31st International Conference on Ocean, Offshore and Arctic Engineering*. American Society of Mechanical Engineers, pp. 615–621.

[23] Ocean Energy System. [Online] https://www.ocean-energy-systems.org, accessed 07 Sep 2018.

[24] Pathak, A., Freniere, C. and Raessi, M. (2017). "Advanced computational simulations of water waves interacting with wave energy converters". In: *European Journal of Computational Mechanics* 1, pp. 1–33.

[25] Penalba, M., Mérigaud, A., Gilloteaux, C. and Ringwood, J. (2015). "Nonlinear Froude-Krylov force modelling for two heaving wave energy point absorbers". In: *Proceedings of the 11th European Wave and Tidal Energy Conference*. European Wave and Tidal Energy Conference. Nante, France.

[26] Penalba, M., Giorgi, G. and Ringwood, J. V. (2017a). "Mathematical modelling of wave energy converters: A review of nonlinear approaches". In: *Renewable and Sustainable Energy Reviews* 78, pp. 1188–1207.

[27] Penalba, M., Kelly, T. and Ringwood, J. V. (2017b). "Using NEMOH for modelling wave energy converters: A comparative study with WAMIT". In: *Centre for Ocean Energy Research (COER), Maynooth University, Co. Kildare, Ireland*.

[28] Rafiee, A. and Fiévez, J. (2015). "Numerical Prediction of Extreme Loads on the CETO Wave Energy Converter". In: *Proceeding of 11th European Wave and Tidal Energy Conference*, pp. 1–10.

[29] Ringwood, J. V., Bacelli, G. and Fusco, F. (2014). "Energy-maximizing control of wave-energy converters: The development of control system technology to optimize their operation". In: *IEEE Control Systems* 34.5, pp. 30–55.

[30] Sjökvist, L. and Göteman, M. (2016). "The Effect of Overtopping Waves on Peak Forces on a Point Absorbing WEC". In: *Proceedings of Asian Wave and Tidal Energy Conference, Singapore*. Vol. 1, pp. 11–16.

[31] Tarrant, K. and Meskell, C. (2016). "Investigation on parametrically excited motions of point absorbers in regular waves". In: *Ocean Engineering* 111, pp. 67 –81.

[32] Wolgamot, H. A. and Fitzgerald, C. J. (2015). "Nonlinear hydrodynamic and real fluid effects on wave energy converters". In: *Proceedings of the Institution of Mechanical Engineers, Part A: Journal of Power and Energy* 229.7, pp. 772–794.

[33] Yu, Y. H. and Li, Y. (2013). "Reynolds-Averaged Navier–Stokes simulation of the heave performance of a two-body floating-point absorber wave energy system". In: *Computers & Fluids* 73, pp. 104–114.

Chapter 7

Conclusions and future work

7.1 Overall conclusions

The research presented in this thesis focuses on the study of a spherical point absorber with an asymmetric mass distribution (SPAMD) which is fully submerged and bottom-referenced via a single flexible mooring tether. This new concept utilises the motion coupling created by the asymmetric mass distribution of the buoy, to allow the single-tether device to harvest wave power in surge and heave efficiently. The dynamic equation of motion was developed from linear potential theory in the frequency-domain and the time-domain, with consideration of viscous drag. The power take-off unit was modelled as a spring-damper mechanism whose stiffness and damping coefficient can be tuned to achieve optimal reactive control. The main focus of this research was given to the dynamics of the SPAMD in order to introduce the concept, investigate the working principles, assess the efficiency and annual power output for given sea states, and understand the impact of mass distribution for the design of the system with asymmetric mass distribution.

This research commenced with the conceptual introduction and dynamic analysis of the SPAMD. It was found that the generic single-tether point absorber, which was seafloor referenced, cannot absorb the wave energy arising from the surge motion efficiently. This is because the surge motion of the buoy is only weakly coupled with the power take-off unit. Considering the surge motion can achieve up to two thirds the total capture width, this decoupling significantly degrades the efficiency of the single-tether systems. Unlike previous solutions which use additional PTO units to couple to the surge motion of the system, the SPAMD utilises the motion coupling between surge, heave and pitch motion to transfer the wave power arising from the surge motion via a single tether. As a result, the SPAMD is able to achieve

efficiencies similar to the multi-tether systems for some wave frequencies ($\omega < 0.5$ rad/s), with the same low capital cost of the generic single-tether point absorbers. It should be noted that the performance of the SPAMD is significantly affected by the mooring tether length, which differs from the multi-tether systems which are more affected by tether angles rather than the length of tethers.

The mass distribution of the SPAMD was investigated and defined by three parameters: the weight-to-buoyancy ratio, mass ratio and mass-offset position. It was demonstrated that a buoy with a low weight-to-buoyancy ratio is more productive at small wave periods (that is, high wave frequencies). However, the gain in power output is also associated with an increase in PTO loading, which might increase the capital cost of the plant. The mass ratio of the buoy has a limited impact on the power output and the PTO loading of the SPAMD. The mass-offset position was found to have the greatest impact on the efficiency of power absorption of the SPAMD. The optimal position can result in a maximum three times efficiency improvement compared with the generic buoy for some wave frequencies. The PTO loading is relatively insensitive to the mass-offset position. Finally, the yearly mean power output of the SPAMD with optimal mass distribution was compared with the generic single-tether PA at three test sites (Yeu Island, Perth and Sydney). The results show that the optimal mass distribution of the SPAMD can lead to a minimum of 53% more power in comparison with the generic single-tether PA, which suggests that the SPAMD might be more competitive in the wave energy industry.

The last part of the research focuses on the nonlinear hydrodynamics analysis of the SPAMD to validate the performance of the system for large buoy displacement. Using the numerical wave tank experiment (NWT) developed from Navier-Stokes equations, the trajectory and instantaneous power change of the SPAMD were modelled when the nonlinear hydrodynamics were considered. It was found that the surface piercing caused by the large motion of the buoy plays an important role in modifying the trajectory of the device. As the trajectory is closely associated with the efficiency of the device, the trajectory change is likely to result in a decrease in efficiency of the system. Nevertheless, although the power output of the SPAMD decreases due to the surface piercing, the maximum efficiency improvement in comparison with the generic PA can still be three times for small to intermediate wave heights.

It can be concluded that this thesis provides an insight into the efficiency of the multi-DOF point absorbers. Similar to the terminators such as the Bristol cylinder, the submerged motion-coupled point absorber in this research also has a circular motion when it achieves the highest efficiency

improvement in monochromatic waves. In other words, the efficiency of the multi-DOF point absorber is closely related to the trajectory of the device. Therefore, the trajectory analysis, together with modal analysis, can be employed to understand the efficiency improvement of the proposed WEC design and the deficiency of the generic PAs (see Chapter 4). Furthermore, the application of the trajectory analysis was expended to investigate the negative impact of specific nonlinear hydrodynamics on the performance of the system (see Chapter 6). Specifically, by comparing the trajectory reference corresponding to the maximum efficiency of power absorption, the trajectory change can explain the efficiency compromises of the system due to nonlinear hydrodynamics. Since the trajectory provides another perspective to evaluate the efficiency of the system, it has the potential to be the control reference of multi-DOF point absorbers for wave-by-wave control. Compared with the velocity tracking, the control algorithm based on trajectory reference is able to recover the efficiency of the system from unexpected hydrodynamic events. A relevant study has been launched as an extension of this Ph.D. study.

7.2 Original contributions

The main contributions of this thesis to the field of wave energy are listed below:

1. proposing a new low-cost design of submerged single-tether point absorber that utilises motion coupling to improve efficiency in wave energy absorption.
2. determining the working principles of the motion coupled system by using modal analysis.
3. quantifying the efficiency improvement of the motion coupled single-tether point absorber in comparison with the generic one for regular and irregular waves
4. identifying the impact of the mass distribution on the techno-economic benefit of the motion coupled system
5. highlighting the importance of tuning the mooring tether length for maximising the efficiency of power absorption of the motion coupled system
6. conducting high-fidelity nonlinear hydrodynamic analysis on the motion coupled system by using a Reynold-averaged Navier-Stokes model

7. determining the impact of nonlinear hydrodynamics on the efficiency of power production and control robustness of the motion coupled system.

7.3 Recommendations for future work

The work presented in this thesis explores a low-cost solution to address the power deficiency observed in submerged bottom-referenced single-tether point absorbers. This thesis covers a corresponding analytical model development, parametric sensitivity study, power assessment for various sea states and performance validation under fully nonlinear hydrodynamics. However, in order to achieve commercialisation of the proposed concept, four future studies have been suggested and are detailed in the following sections.

Control system development

Since only simple spring-damper control was employed for the SPAMD in this thesis, it is unknown whether a wave-by-wave control strategy such as model predictive control (MPC) and trajectory-based control can lead to more power production in practice. Noting the SPAMD is an under-actuated system whose controllability is dependent of the instantaneous mooring tether angle, which means the system is nonlinear and time-variant. Therefore, a nonlinear controller is required for the purpose of maximising power production. Furthermore, since a wave-by-wave control usually requires considerable reactive power in each of the control horizons, it is necessary to evaluate the net power production of the SPAMD for various control algorithms.

Small-scale experiments

The analysis presented in this thesis was developed from numerical models, which might lose some important hydrodynamic characteristics. In this respect, a wave flume experiment with the prototype scale between 1:100–1:20 should be ran to validate the power production and estimate the extreme wave loads of the SPAMD for random sea states. Furthermore, as the SPAMD is only symmetrical with the vertical XZ-plane, the system could possibly be unstable in yaw. Therefore, a passive yaw stabiliser may need to be developed and tested via a 6DOF numerical simulation and a small-scale experiment to guarantee the stability of the SPAMD.

Offshore deployment of the prototype

Offshore deployment of the prototype should be systemically optimised in future work. The dimension of the prototype can be one of the key factors that affect the system's performance. For example, a larger buoy tends to have a stronger motion coupling between the surge and heave motion, probably resulting in an improvement in the power absorption bandwidth. Furthermore, the shape of buoy could influence the system dynamic and the efficiency of the PTO to cycle energy, because a shape other than a sphere might introduce significant hydrodynamic coupling. Lastly, the impact of water depth should also be investigated for the offshore deployment. In this thesis, the SPAMD is encouraged to be deployed in shallow water for intermediate to high wave frequencies. However, as the water particle tends to have a greater surge velocity in shallow water, the SPAMD might work more efficiently than in deep water, or require another mass distribution to be optimal.

Array performance

The array performance of the SPAMD should be assessed in order to determine its economic viability as a wave farm. Three research questions need to be answered: (i) how the layout of the SPAMD array affects the power production of the wave farm; (ii) whether the interaction between WECs will degrade the yaw stability of individual devices; and (iii) how to design a control strategy that can achieve the global maximum power output of the SPAMD array.

Furthermore, unlike this thesis, the parameters and quantities presented in the future work should be non-dimensionlised in order to conveniently relate to real-world ones, such as PTO displacement, loading and power.

Appendix A

Numerical simulation of a submerged spherical point absorber with asymmetric mass distribution

Meng, F., Rafiee, A., Cazzolato, B. S., Ding, B., Arjomandi, M., Piper, J., Sergiienko, N., and Hu, Q. (2017). "Numerical simulation of a submerged spherical point absorber with asymmetric mass distribution". In: *Proceedings of the 12th European Wave and Tidal Energy Conference*. Ed. by A. Lewis. Cork, Ireland, pp. 1128-1–1128-8.

Statement of Authorship

Publication Status	Published
Name of Co-author	Fantai Meng
Contribution to the Paper	Developed the CFD model for numerical simulation and analysed the results presented in the paper.
Overall Percentage (%)	75%

Statement of Authorship

Title of Paper	Numerical simulation of a submerged spherical point absorber with asymmetric mass distribution
Publication Status	☑ Published ☐ Accepted for Publication ☐ Submitted for Publication ☐ Unpublished and Unsubmitted w ork w ritten in manuscript style
Publication Details	Meng, F., Rafiee, A., Cazzolato, B. S., Ding, B., Arjomandi, M., Piper, J., Sergiienko, N., and Hu, Q. (2017). "Numerical simulation of a submerged spherical point absorber with asymmetric mass distribution". *Proceedings of the 12th European Wave and Tidal Energy Conference.* Ed. by A. Lewis. Cork, Ireland, pp. 1128-1–1128-8.

Principal Author

Name of Principal Author (Candidate)	Fantai Meng		
Contribution to the Paper	Developed the idea and concepts, developed the numerical models, wrote the code of simulations, interpreted the results, wrote the manuscript and acted as a corresponding author.		
Overall percentage (%)	75%		
Certification:	This paper reports on original research I conducted during the period of my Higher Degree by Research candidature and is not subject to any obligations or contractual agreements with a third party that would constrain its inclusion in this thesis. I am the primary author of this paper.		
Signature		Date	21/8/19

Co-Author Contributions

By signing the Statement of Authorship, each author certifies that:

i. the candidate's stated contribution to the publication is accurate (as detailed above);

ii. permission is granted for the candidate in include the publication in the thesis; and

iii. the sum of all co-author contributions is equal to 100% less the candidate's stated contribution.

Name of Co-Author	Ashkan Rafiee		
Contribution to the Paper	Helped in developing the computational fluid dynamic model by using OpenFOAM toolbox, discussed the results, and provided a critical revision of the manuscript.		
Signature		Date	20/8/2019

Name of Co-Author	Benjamin S. Cazzolato		
Contribution to the Paper	Supervised the work, helped in interpretation of obtained results, and provided a critical revision of the manuscript.		
Signature		Date	21/8/19

Name of Co-Author	Boyin Ding		
Contribution to the Paper	Supervised the work, helped in interpretation of obtained results, and provided a critical revision of the manuscript.		
Signature		Date	21/8/2019

Name of Co-Author	Maziar Arjomandi		
Contribution to the Paper	Supervised the work, helped in interpretation of obtained results, and provided a critical revision of the manuscript.		
Signature		Date	21/08/2019

Name of Co-Author	Jonathan David Piper		
Contribution to the Paper	Supervised the work, helped in interpretation of obtained results, and provided a critical revision of the manuscript.		
Signature		Date	30/8/19

Name of Co-Author	Nataliia Sergiienko		
Contribution to the Paper	Supervised the work, helped in interpretation of obtained results, and provided a critical revision of the manuscript.		
Signature		Date	21/08/2019

Name of Co-Author	Qiuhao Hu		
Contribution to the Paper	Supervised the work, helped in interpretation of obtained results, and provided a critical revision of the manuscript.		
Signature		Date	28/08/2019

Please cut and paste additional co-author panels here as required.

Numerical simulation of a submerged spherical point absorber with asymmetric mass distribution

Fantai Meng*, Ashkan Rafiee†, Benjamin Cazzolato*, Boyin Ding*, Maziar Arjomandi*, Jonathan David Piper*, Nataliia Sergiienko* and Qiuhao Hu‡
*Ocean Wave Energy Research Group, School of Mechanical Engineering,
The University of Adelaide, South Australia, Australia, 5005
E-mail: fantai.meng@adelaide.edu.au
†Carnegie Clean Energy Ltd, Fremantle, WA, Australia, 6160
E-mail: arafiee@carnegiece.com
‡School of Naval Architecture, Ocean and Civil Engineering, Shanghai Jiao Tong University, Shanghai, China, 200240
E-mail: huecu588755@sjtu.edu.cn

***Abstract*—In previous works [1], a single-tethered spherical point absorber with asymmetric mass distribution (SPAMD) was found to be 2-3 times more efficient than a generic single-tethered point absorber (PA) with uniform mass distribution under long-crested waves. However, the hydrodynamics of PAs were modelled using linear potential wave theory that inherently ignores high-order nonlinear effects of wave-body interaction. It is well-known that neglecting such effects has the potential to overestimate the power absorption efficiency of the PAs. In this paper, the efficiency of the PAs were assessed over several wave periods in a numerical wave tank, in which the hydrodynamics were calculated by a Navier-Stokes solver. The tank was originally developed in [2] and then updated for this study. The numerical wave tank was built by using the computational fluid dynamic toolbox OpenFOAM and the open-source library OLAFOAM for wave generation. The results obtained from numerical wave tank experiments show that the SPAMD can be 3 times more efficient than the generic PA, which are consistent with the linear wave theory results, although linear wave theory significantly overestimated the efficiency of the PAs.**

***Index Terms*—spherical point absorber with asymmetric mass distribution (SPAMD), numerical wave tank, non-linear hydrodynamcis, power absorption efficiency**

I. Introduction

Accurately modelling of wave energy converters (WEC) plays an important role in assessing the design of new conceptual WECs. For example, an accurate model can be used to predict the survivability of WECs in extreme sea states [3], analyse and optimise the hydrodynamic features [4], assess power output [5] and system identification [6].

Cummins' equation [7] and the frequency-domain hydrodynamic model [8] are two models widely used for describing the motion of WECs in regular and irregular waves. Both were developed from the linear potential wave theory [9], which is valid when the amplitude of waves are small and the relative motion of the body is small compared to incident wave heights. As the displacement of the free surface and body are sufficiently small, the boundary conditions of free surface and body can be linearised, resulting in the first order Froude-Krylov (FK) force and radiation-diffraction force. Therefore, Cummins' equation provides a computationally efficient way to simulate the motion of WEC. By employing superposition principle, the linear models can also be used to describe the motion of WECs in irregular waves [10] [11]. However, as WECs are usually employed in energetic seas and tuned to operate close to the resonant condition of the WEC, models developed based on linear wave theory are not able to capture the nonlinear effects in wave-body interaction, and therefore overestimate results [2].

A fraction of nonlinear effects results from the linear approximation of the FK force and radiation-diffraction force. In linear potential wave theory, the FK force is calculated by integrating the undistributed static and dynamic pressure over the mean wetted surface. As the wave elevation and buoy's motion are small, the pressure given by the Bernoulli equation can be approximated linearly [12]. Furthermore, the net buoyancy force acting on the point absorber is simplied as a linear function of buoy's heave displacement, which is only applicable for the point absorbers with constant horizontal cross-section area, for example vertical cylindrical point absorbers. As a result, when the point absorber has a large motion amplitude, the buoy's response estimated by linear potential wave theory will have large deviation from the actual value [13], and therefore the power absorption efficiency of the point absorber (PA) will be overestimated. To model the point absorber with large motion amplitude, some researchers developed time-domain models by using partial nonlinear potential to calculate hydrodynamic forces. Giorgi et al. [14] calculated the nonlinear FK force by integrating linearised incident wave pressure over the exact instantaneous wetted surface. Merigaud et al. [15] further improved the nonlinearity of FK force by employing a weak-scatter approximation [16] of the boundary value problem. Additionally, Gilloteaux utilized the Taylor series to estimate the second-order radiation and diffraction forces acting on the prototype SEAREV [17]. It was found that a model with nonlinear FK force and second-order radiation and diffraction forces results in a satisfactory agreement with experimental results in comparison to a conventional Cummins' model when the device is working in resonance. However, additional nonlinearities occurring in extreme sea states such as wave

breaking, surface piercing, vortex generation and green water effect due to water overtopping, can only be modelled by using a fully nonlinear numerical method.

Computational fluid dynamics, based on the Navier-Stokes equation (NS-based CFD) is the most widely used fully nonlinear numerical method employed to solve the complex hydrodynamic nonlinearities in the wave-body interaction problem [18]–[22]. For example, Sjökvist and Göteman [21] utilized NS-based CFD to investigate the peak wave loads caused by water overtopping on a floating PA. Bhinder et al. [22] identified the viscous drag coefficients of a floating WEC by using NS-based CFD simulation. Furthermore, as PAs are designed to be at resonance to work most efficiently, NS-based CFD method could provide an accurate wave loading estimation in this scenario. Whilst NS-based CFD has not been used heavily in the past for WEC analysis because of the computational expense, it is becoming increasingly common and important as the need for fidelity increases.

In this paper, a 3D numerical wave tank (NWT) was developed by using open source CFD toolbox OpenFOAM, aiming to verify the efficiency improvement of the spherical point absorber with asymmetric mass distribution (SPAMD) under typical regular waves, e.g. wave height of 1m ($h = 1$ m) [1]. In Section II, the set-up of NWT is detailed and NWT validation against conventional Cummins' model is presented. In Section III, the comparison of efficiency between the generic PA and the SPAMD over five typical wave frequencies is presented.

II. Numerical wave flume modelling

The 3D NWT is a 330m ($-30\text{m} \leq x \leq 300\text{m}$) long, 100m ($-50\text{m} \leq y \leq 50\text{m}$) wide and 40m ($-30\text{m} \leq z \leq 10\text{m}$) high, with water depth of 30m (see Figure 1). The length of computational domain for such problems strongly depends on the wave generation and absorption methods. It is well understood that in the case of using generation and absorption zones, one would need 1-1.5 times the wave length for each of the zones. However, here an active wave generation and absorption algorithm was used (within the OLAFOAM library) which eliminates the need of a long zone for wave generation and absorption, and hence a total of approximately one wavelength is sufficient for the computation domain. It is worth adding that any longer computational domain does not add any advantage/accuracy to the simulations [23].

The planer waves with the first-order Stokes wave velocity profile enter the NWT via the inlet and propagate along positive x-axis, exciting single-tethered PAs in surge, heave and pitch directions. Fixed pressure boundaries were employed on the two faces of NWT in xz plane, which allows the water flows freely in and out of the domain. When waves reach the outlet of NWT, it is assumed the pressure is truncated, to filter out the additional disturbance caused by wave reflection.

A. Grid generation

The meshes were generated using the OpenFOAM utility blockMesh for the whole computational domain and snappyHexMesh for the finer mesh around buoy, as shown in Figure 2. The total number of cells is 545,433 cells. To be able to model the turbulent structures around the buoy ($30 \leq y+ \leq 300$), five layers of structured prism cells were used in the vicinity of the buoy surface with an expansion rate of 1.2 and the height of first layer of 0.1m. The grid resolution near the free surface of water was also refined with the $\Delta x \approx 0.003\lambda$ (λ is the wavelength) and $\Delta z \approx 0.001h$ (h is the wave height), to be able to simulate the hydrodynamic when the buoy breaches the water surface. As the boundary layers are fine enough to describe the turbulence near buoy surface, no wall function was applied in this study. Mesh convergence testing is presented in Section III-A. In this study, the SST k-ω turbulence model was used, which is a common method for similar problems. Using RANS models (see Section II-C) allows $30 \leq y+ \leq 300$, which eliminates the need for resolving the boundary layer [24]. However, for the wave energy devices driven by diffraction forces, the turbulence is not important in modelling the dynamics of the motion and hence the results are relatively insensitive to the choice of turbulence model and the need to resolve the boundary layer [25].

B. Device description

According to [9], the theoretical capture width of a 3DOF (i.e., surge, heave and pitch) PA can be three times greater than a heave-only PA. It was found that for single-tethered PAs, the heave motion of the buoy strongly couples to the power take-off device (PTO) and therefore this motion can be fully converted to the PTO extension. In contrast, the surge and pitch motions barely couple to the PTO and only a tiny fraction of these motions are converted to useful energy. Therefore, to address the deficiency of single-tethered PAs, the previous study [1] focuses on utilizing a spherical asymmetric mass buoy to couple its surge motion to the linear spring-damper PTO via surge-heave motion coupling or surge-pitch motion coupling. The modal analysis shows that the SPAMD can absorb the energy arising from its surge motion and the efficiency of wave energy capture is significantly improved. Figure 3 illustrates the motions of a 3 degree-of-freedom SPAMD subjected to planer waves in the vertical xz plane.

Table I lists the parameter settings employed for the validation of the NWT experiment against the Cummins' model in Section III-B and the comparison of power absorption efficiency discussed in Section III-C. The settings used in this paper are consistent with the settings used in the previous work [1].

The PTO does not contain any hard-stop motion constraints. The instantaneous power output of the system is equal to the power consumed by the linear PTO damper, given by

$$P(t) = B_{pto}|\Delta\dot{L}(t)|^2 \quad , \tag{1}$$

in which $\Delta\dot{L}(t)$ is the instantaneous tether velocity.

The mean power output from the time t_0 to t_1 is given by

$$P_{mean} = \frac{\int_{t_0}^{t_1} B_{pto}|\Delta\dot{L}(t)|^2 dt}{t_1 - t_0} \quad , \tag{2}$$

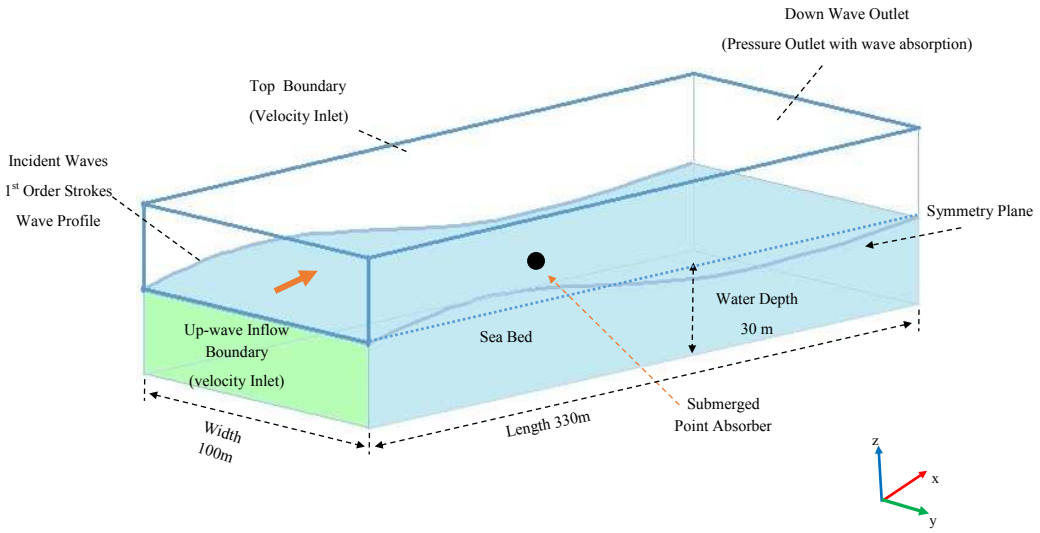

Fig. 1: Schematic of the numerical wave tank, with key dimensions and boundary conditions.

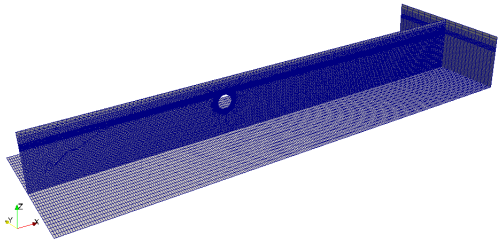

(a)

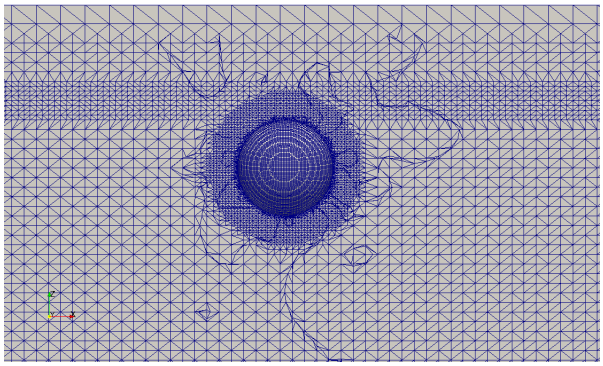

(b)

Fig. 2: The grid resolution used in this study, which is refereed as "medium mesh" in mesh convergence test: (a) the mesh resolution of vertical xz plane, bottom and outlet (b) the mesh near the surface of buoy.

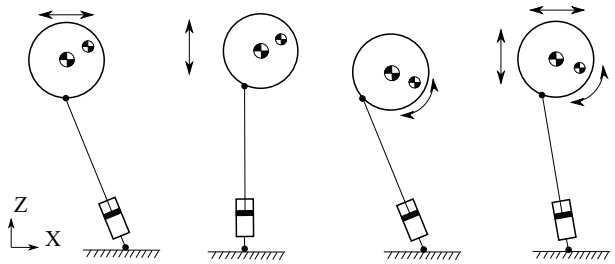

Fig. 3: Schematic illustration of the motions of a 3DOF SPAMD subjected to plane waves in the vertical xz-plane. The larger centre of mass represents the mass of the solid spherical buoy m_1, the smaller one is the offset point mass m_2: (a) surge motion, (b) heave motion, (c) pitch motion, (d) combined 3DOF motions.

TABLE I: Fundamental parameters of the numerical wave tank

Description	Parameter	Value/Unit
Wave periods	T	8, 10, 13, 15, 18 sec
Wave height	h	1m
Water depth	d	30m
Submergence (water surface to buoy's top)	d_s	2m
Weight-buoyancy ratio	δ	0.5
Radius of buoy	r	5m
Tether length	L	18m
PTO stiffness	K_{pto}	1.5×10^5 N/m
PTO damping (for SPAMD)	B_{pto}	1×10^5 Ns/m
PTO damping (for the generic PA)	B_{pto}	0.3×10^5 Ns/m

in which the time period $t_1 - t_0$ is sampled after the PA has reached steady-state, which for this stage was found to be five wave cycles.

In this work, the PTO stiffness K_{pto} and PTO damping coefficient B_{pto} of SPAMD are set to be 150 kN/m and 100 kNs/m,

which are the optimal configuration for Cummins' model at wave period of 13 sec. Similarly the optimal PTO stiffness K_{pto} and PTO damping coefficient B_{pto} were determined in the same way and are 150 kN/m and 30 kNs/m for the generic PA.

C. Numerical method

For the 3D two-phase incompressible flow scenario in this work, the Reynolds-Averaged Navier-Stokes (RANS) equations with specific boundary conditions of wave generation and absorption derived by [26] are employed as the governing equations.

For the continuity equation

$$\nabla \mathbf{U} = 0 \quad , \tag{3}$$

in which $\mathbf{U}$ is the velocity vector.

For the mass conservation equation

$$\frac{\partial \rho \mathbf{U}}{\partial t} + \nabla \cdot (\rho \mathbf{U}\mathbf{U}) - \nabla \cdot (\mu_{eff} \nabla \mathbf{U}) = -\nabla p^* - g\mathbf{X}\nabla\rho + \nabla \mathbf{U} \cdot \nabla \mu_{eff} + \sigma\kappa\nabla\alpha \quad , \tag{4}$$

in which ρ is the density, μ_{eff} is the effective dynamic viscosity, $p*$ is the pseudo-dynamic pressure, g is the gravitational acceleration, $\mathbf{X}$ is the position vector, σ is the coefficient of surface tension, κ is the interface curvature and α is the indicator phase function varying between 0 and 1, which defines the density of computational cell as

$$\rho = \alpha\rho_{water} + (1-\alpha)\rho_{air} \quad . \tag{5}$$

For the air-water phase movement equation

$$\frac{\partial \alpha}{\partial t} + \nabla \cdot \mathbf{U}\alpha + \nabla \cdot \mathbf{U}_c \alpha(1-\alpha) = 0 \quad , \tag{6}$$

in which $\mathbf{U}_c$ is the artificial compression term to keep a sharp air-water interface.

The third-party utility OLAFOAM [27] was used to define the boundary conditions and the solver interFoam solves Eqns (3-6). To maintain a Courant number of smaller than 0.5, an adjustable time step was employed and the maximum time step was set to be smaller than 0.005 sec, especially when PAs were at resonance. The time step convergence testing is shown in Figure 5. The NWT experiment was conducted on the Phoenix high-performance computing (HPC) platform of the University of Adelaide [28]. By using 32 cores on the Phoenix HPC, the solver took 24 hours for 15 wave periods which was sufficiently long for the PA to reach steady-state.

III. Result

Here, NWT results are presented. In Section III-A, the convergence of the mesh and time step used in this study was tested. In Section III-B, the motion response of PAs obtained from NWT experiments were validated against the Cummins' model. In Section III-C, the comparison of power output between the generic PA and the SPAMD was presented.

A. Mesh and time-step convergence testings

Figure 4 compares the motion of the generic PA for a very coarse mesh (20,201 cells), coarse mesh (86,960 cells), medium mesh (545,433 cells) and fine mesh (2,477,590 cells), when the buoy was at resonance at the wave period of 13 sec, during the first 80 sec simulation. The medium mesh was used for all the simulations in this study. The fine mesh is 8 times the number of cells compared to the medium mesh, while the coarse and very coarse mesh have 1/8th and 1/27th the number of cells respectively. It can be seen that the results of the fine mesh, medium mesh and coarse mesh are almost identical, with maximum relative error less than 3% for the peak values of the motions, while the results of the very coarse mesh show considerable relative errors in surge (12.5%), heave (12.5%) and pitch (20.8%) motion. Table II displays the root mean square errors (RMSE) with respect to medium mesh, for the peak values of the surge, heave and pitch motions. The RMSEs in Table II indicates that the results presented in this study is not sensitive to the selected mesh number.

TABLE II: Root mean square errors (RMSE) of the fine mesh, coarse mesh and very coarse mesh with respect to medium mesh, for the peak values of the surge, heave and pitch motions.

RMSE	Surge	Heave	Pitch
Fine mesh	$<$ 0.001 m	$<$ 0.001 m	$<$ 0.001 deg
Coarse mesh	0.006 m	0.092 m	0.09 deg
Very coarse mesh	0.503 m	0.377 m	2.51 deg

Figure 5 compares the motion of the generic PA for a maximum loose time step (ΔT = 0.02 sec), maximum medium time step (ΔT = 0.005 sec) and maximum tight time step (ΔT = 0.0025 sec), when the buoy was resonant at the wave period of 13 sec, during the first 80 sec simulation. The maximum medium time step was used for all the simulations in this study. As shown in Figure 5, the results of the loose time step, medium time step and tight time step are almost identical, indicating that the results presented in this study is not dependent on the selected time step.

B. NWT validation

Figure 6 shows the motion of the generic PA obtained from the OpenFOAM model and from the Cummins' model derived in [29] respectively, at the resonant frequency of the generic PA (T =13 sec). Figure 7 shows the corresponding results on the SPAMD. It can be seen that the surge and pitch response matched well with the Cummins' model, and not surprisingly there was a significant deviation in heave response because the buoy in the Cummins' model is assumed to be submerged all the time. Whereas the heave motion in the CFD was constrained by the submergence depth of the buoy below the water surface (d_s = 2m). When the buoy tries to move out of the water, the net buoyancy will decrease and thus the buoy will be pulled back into the water by the PTO.

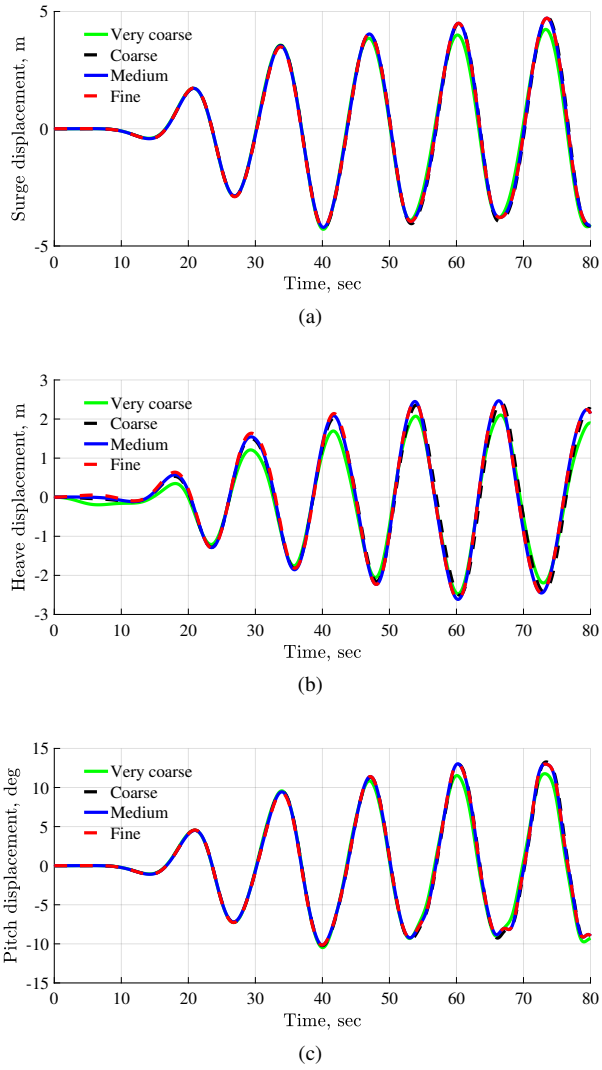

Fig. 4: Time histories of the motion of the generic PA for very coarse, coarse, medium and fine mesh, when the buoy is in resonant at the wave period of 13 sec.

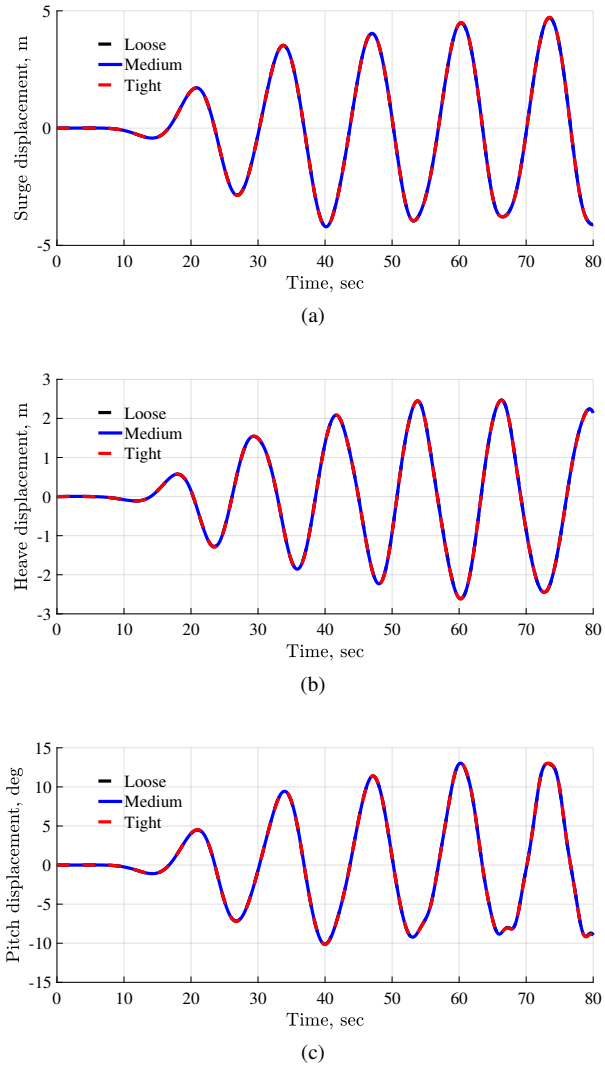

Fig. 5: Time histories of the motion of the generic PA for loose, medium and tight time step, when the buoy is in resonant at the wave period of 13 sec.

C. Power output comparison

In this section, power output was compared between the generic PA and the SPAMD under regular waves of 1m wave height and over several wave periods (T = 8 sec, 10 sec, 13 sec, 15 sec and 18 sec), as shown in Figure 8. Table III lists the mean y+ and mean Reynolds number for the simulation cases of the generic PA and SPAMD. It can be seen that the SST k-ω turbulence model is applicable to such cases with high Reynolds number.

From Figure 8, it can be seen that for the resonant wave frequency of 0.48 rad/sec (T = 13 sec), the power output of the SPAMD was 3 times more than the generic PA, as demonstrated in both Cummins' model simulations and NWT experiments. For the wave frequencies greater than 0.48 rad/sec, although the employed PTO configuration is non-optimal for the wave conditions, the SPAMD was still 2-3

TABLE III: Mean y+ and mean Reynolds number for the simulations of the generic PA and SPAMD, when the wave periods are 8 , 10 , 13 , 15 and 18 sec.

Wave period (sec)		**8**	**10**	**13**	**15**	**18**
Generic PA	y+	182	212	253	244	245
	$\overline{\mathrm{Re}}$ (10^7)	1	1.2	1.9	1.4	0.9
SPAMD	y+	202	228	262	240	243
	$\overline{\mathrm{Re}}$ (10^7)	0.8	1.1	1.6	1.3	0.7

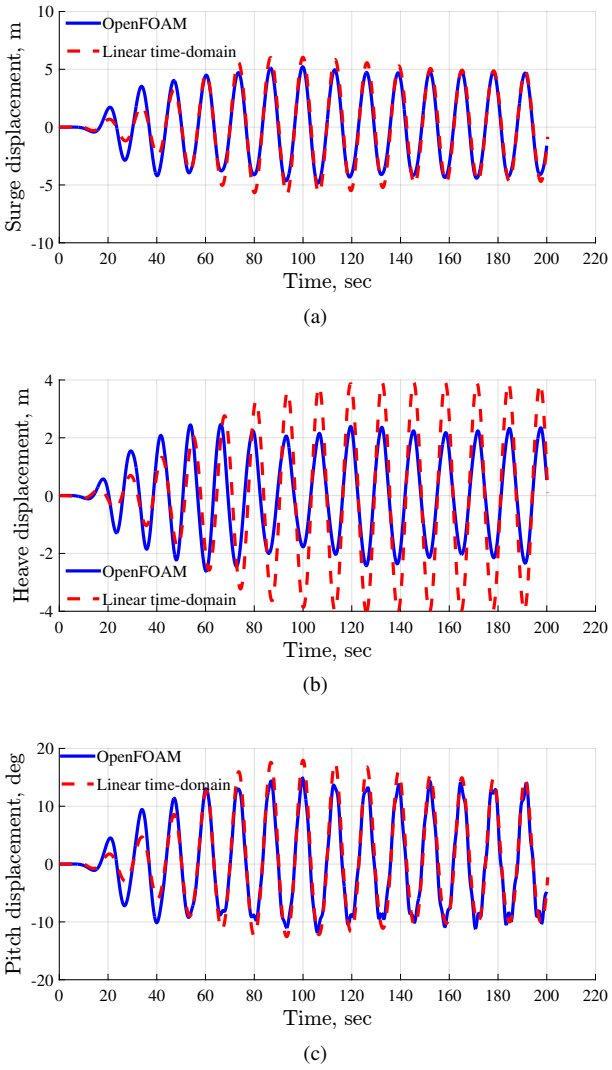

Fig. 6: Response comparison between the OpenFOAM model and the linear time-domain model of the generic PA at wave period of 13 sec (ω = 0.48 rad/sec) and wave height of 1m: (a) surge motion, (b) heave motion, (c) pitch motion.

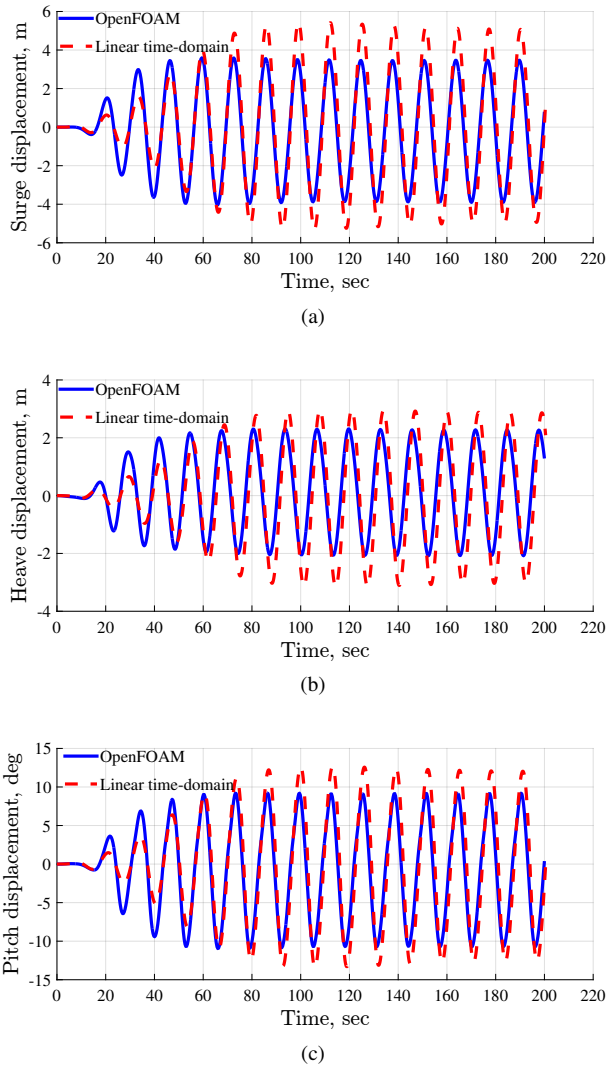

Fig. 7: Response comparison between the OpenFOAM model and the linear time-domain model of the SPAMD at wave period of 13 sec (ω = 0.48 rad/sec) and wave height of 1m: (a) surge motion, (b) heave motion, (c) pitch motion.

times more efficient than the generic PA in terms of power output, which implies that the SPAMD has a wider bandwidth than the generic PA.

The power output of the SPAMD in OpenFOAM model is only half of that estimated from the Cummins' model at wave frequency of 0. 48 rad/sec (T=13 sec). This was because in OpenFOAM model, the heave motion of the SPAMD was constrained by the free water surface, while in the Cummins' solver, the heave motion was not constrained as shown in Figure 9. It was found in [30], the SPAMD works at its optimal efficiency when the trajectory of the buoy is similar to a circle, which implies there are two orthogonal oscillation modes. Constrained by the water surface, the resulting motion trajectory of the SPAMD is flatten and therefore the power absorption efficiency of the system is compromised.

IV. Conclusion

In this paper, the efficiency improvement of SPAMD against the generic PA was assessed in both Cummins' model and the NWT experiments. The results showed that the power output of the SPAMD was still superior to the generic PA under planar regular waves even when nonlinear effects were considered. Additionally, with a fixed PTO configuration, the power absorption efficiency of the SPAMD has a wider bandwidth in comparison to the generic PA. To determine the commercial potential of SPAMD, further investigations need to be conducted in the aspects of techno-economic assessment of SPAMD in irregular waves and the survivability of the system in extreme sea conditions.

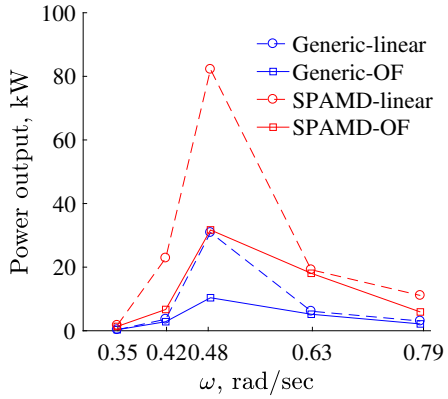

Fig. 8: Power output comparison between the linear time-domain models and OpenFOAM models of SPAMD and generic PA.

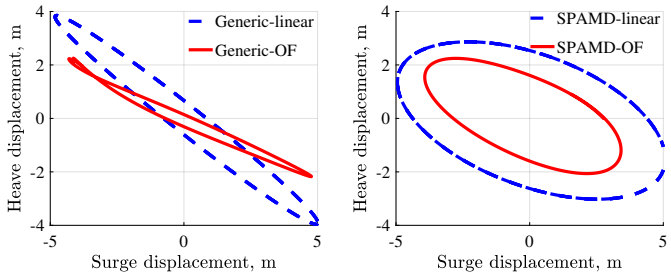

Fig. 9: Schematic illustration of the motion trajectories of generic PA and the SPAMD of their geometry centres at wave period of 13 sec (ω = 0.48 rad/sec): (a) the motion trajectories of generic PA, (b) the motion trajectories of SPAMD.

ACKNOWLEDGMENT

This research is supported by China Scholarship Council (CSC), Australia Research Council (ARC) Linkage Grant (LP13010011F) and the Research Training Program (RTP).

REFERENCES

[1] F. Meng, B. Cazzolato, B. Ding, and M. Arjomandi, "Modal analysis of a submerged spherical point absorber with asymmetric mass distribution," submitted to *Renewable Energy*, 2017.

[2] A. Rafiee and J. Fiévez, "Numerical prediction of extreme loads on the CETO wave energy converter," in *Proceeding of 11th European Wave and Tidal Energy Conference, 09A1-2*.

[3] M. Göteman, J. Engström, M. Eriksson, M. Hann, E. Ransley, D. Greaves, M. Leijon *et al.*, "Wave loads on a point-absorbing wave energy device in extreme waves," in *The Twenty-fifth International Offshore and Polar Engineering Conference*. International Society of Offshore and Polar Engineers, 2015.

[4] F. Kalofotias, "Study for the hull shape of a wave energy converter-point absorber; design optimization & modeling improvement," Master's thesis, University of Twente, 2016.

[5] A. Pathak, C. Freniere, and M. Raessi, "Advanced computational simulations of water waves interacting with wave energy converters," *European Journal of Computational Mechanics*, vol. 1, pp. 1–33, 2017.

[6] G. Bacelli, R. G. Coe, D. Patterson, and D. Wilson, "System identification of a heaving point absorber: Design of experiment and device modeling," *Energies*, vol. 10, no. 4, p. 472, 2017.

[7] W. Cummins, "The impulse response function and ship motions," DTIC Document, Tech. Rep., 1962.

[8] J. V. Ringwood, G. Bacelli, and F. Fusco, "Energy-maximizing control of wave-energy converters: The development of control system technology to optimize their operation," *IEEE Control Systems*, vol. 34, no. 5, pp. 30–55, 2014.

[9] J. Falnes, *Ocean waves and oscillating systems: linear interactions including wave-energy extraction*. Cambridge University Press, 2002.

[10] L. Wang and J. Isberg, "Nonlinear passive control of a wave energy converter subject to constraints in irregular waves," *Energies*, vol. 8, no. 7, pp. 6528–6542, 2015.

[11] M. Folley and T. Whittaker, "Spectral modelling of wave energy converters," *Coastal Engineering*, vol. 57, no. 10, pp. 892–897, 2010.

[12] H. A. Wolgamot and C. J. Fitzgerald, "Nonlinear hydrodynamic and real fluid effects on wave energy converters," *Proceedings of the Institution of Mechanical Engineers, Part A: Journal of Power and Energy*, vol. 229, no. 7, pp. 772–794, 2015.

[13] A. Clément, A. Babarit, J.-C. Gilloteaux, C. Josset, and G. Duclos, "The SEAREV wave energy converter," in *6th European Wave and Tidal Energy Conference*, 2005.

[14] G. Giorgi, M. Penalba, and J. Ringwood, "Nonlinear hydrodynamic models for heaving buoy wave energy converters," in *Proceedings of the 3rd Asian Wave and Tidal Energy Conference*, vol. 1, Singapore, 2016, Conference Proceedings, pp. 144–153.

[15] A. Merigaud, J.-C. Gilloteaux, and J. V. Ringwood, "A nonlinear extension for linear boundary element methods in wave energy device modelling," in *ASME 2012 31st International Conference on Ocean, Offshore and Arctic Engineering*. American Society of Mechanical Engineers, 2012, pp. 615–621.

[16] P. D. Sclavounos, "Nonlinear impulse of ocean waves on floating bodies," *Journal of Fluid Mechanics*, vol. 697, pp. 316–335, 2012.

[17] J.-C. Gilloteaux, G. Bacelli, and J. Ringwood, "A non-linear potential model to predict large-amplitudes-motions: Application to a multi-body wave energy converter." WREC, 2008.

[18] B. Devolder, P. Rauwoens, and P. Troch, "Numerical simulation of a single floating point absorber wave energy converter using OpenFOAM®," in *Progress in Renewable Energies Offshore*. CRC Press, 2016, pp. 197–206.

[19] E. B. Agamloh, A. K. Wallace, and A. Von Jouanne, "Application of fluid–structure interaction simulation of an ocean wave energy extraction device," *Renewable Energy*, vol. 33, no. 4, pp. 748–757, 2008.

[20] Z. Z. Hu, D. Greaves, and A. Raby, "Numerical wave tank study of extreme waves and wave-structure interaction using OpenFOAM®," *Ocean Engineering*, vol. 126, pp. 329–342, 2016.

[21] L. Sjökvist and M. Göteman, "The effect of overtopping waves on peak forces on a point absorbing WEC," in *Proceedings of Asian Wave and Tidal Energy Conference, Singapore*, vol. 1, 2016, pp. 11–16.

[22] M. A. Bhinder, A. Babarit, L. Gentaz, and P. Ferrant, "Assessment of viscous damping via 3D-CFD modelling of a floating wave energy device," in *Proceedings of the 9th European Wave and Tidal Energy Conference, Southampton, UK*, 2011.

[23] P. Schmitt and B. Elsaesser, "A review of wave makers for 3d numerical simulations," in *Marine 2015 6th International Conference on Computational Methods in Marine Engineering*, 2015.

[24] Y.-H. Yu and Y. Li, "Reynolds-Averaged Navier–Stokes simulation of the heave performance of a two-body floating-point absorber wave energy system," *Computers & Fluids*, vol. 73, pp. 104–114, 2013.

[25] Y. Wei, A. Rafiee, A. Henry, and F. Dias, "Wave interaction with an oscillating wave surge converter, Part I: Viscous effects," *Ocean Engineering*, vol. 104, pp. 185 – 203, 2015.

[26] P. Higuera, J. L. Lara, and I. J. Losada, "Realistic wave generation and active wave absorption for Navier–Stokes models: Application to OpenFOAM®," *Coastal Engineering*, vol. 71, pp. 102–118, 2013.

[27] P. Higuera, "Application of computational fluid dynamics to wave action on structures," Ph.D. dissertation, Ph. D. thesis, Univ. de Cantabria, Santander, Spain, 2015.

[28] Phoenix Grant Information. [Online]. Available: https://wiki.adelaide.edu.au/hpc/index.php/Phoenix_Grant_Information.

[29] F. Meng, B. Cazzolato, B. Ding, and M. Arjomandi, "Technical report model validation of the submerged spherical point absorber with asymmetric mass distribution," Tech. Rep., March 2017.

[30] B. Ding, N. Sergiienko, F. Meng, B. Cazzolato, M. Arjomandi, and P. Hardy, “Enhancing the relative capture width of submerged point absorbers,” in preparation for *Ocean Engineering*, 2017.

Appendix B

Study of fully submerged point absorber wave energy converter – modelling, simulation and scaled experiment

Ding, B., da Silva, L. S. P., Sergiienko, N., Meng, F., Piper, J. D., Bennetts, L., Wagner, M., Cazzolato, B. and Arjomandi, M. (2017). "Study of fully submerged point absorber wave energy converter-modelling, simulation and scaled experiment". In: *The 32nd International Workshop on Water Waves and Floating Bodies (IWWWFB)*. Dalian, China.

Statement of Authorship

Publication Status	Published
Name of Co-author	Fantai Meng
Contribution to the Paper	Provided technical support for modelling: helped to derive quasilinear drag coefficients for the frequency-domain model, helped to develop MATLAB code to solve the motion of equation.
Overall Percentage (%)	5%

Statement of Authorship

Title of Paper	Study of fully submerged point absorber wave energy converter-modelling, simulation and scaled experiment
Publication Status	☑ Published ☐ Accepted for Publication ☐ Submitted for Publication ☐ Unpublished and Unsubmitted work written in manuscript style
Publication Details	Ding, B., da Silva, L. S. P., Sergiienko, N., Meng, F., Piper, J. D., Bennetts, L., Wagner, M., Cazzolato, B. and Arjomandi, M. (2017). "Study of fully submerged point absorber wave energy converter-modelling, simulation and scaled experiment". *The 32nd International Workshop on Water Waves and Floating Bodies (IWWWFB)*. Dalian, China. pp. 1 – 4.

Principal Author

Name of Principal Author (Candidate)	Boyin Ding		
Contribution to the Paper	Developed the idea and concepts, developed the numerical models, wrote the code of simulations, design experiment, interpreted the results, wrote the manuscript and acted as a corresponding author.		
Overall percentage (%)	65%		
Certification:	This paper reports on original research I conducted at the University of Adelaide and is not subject to any obligations or contractual agreements with a third party that would constrain its inclusion in this thesis. I am the primary author of this paper.		
Signature		Date	28/8/19

Co-Author Contributions

By signing the Statement of Authorship, each author certifies that:

i. the candidate's stated contribution to the publication is accurate (as detailed above);

ii. permission is granted for the candidate in include the publication in the thesis; and

iii. the sum of all co-author contributions is equal to 100% less the candidate's stated contribution.

Name of Co-Author	Leandro Souza Pinheiro da Silva		
Contribution to the Paper	Helped in obtaining experimental data, helped in interpretation of obtained results.		
Signature	5%	Date	28/08/2019

Name of Co-Author	Nataliia Sergiienko		
Contribution to the Paper	Supervised the work, helped in experimental design, helped in interpretation of obtained results, and provided a critical revision of the manuscript.		
Signature	5%	Date	27/08/2019

Name of Co-Author	Fantai Meng		
Contribution to the Paper	Provided technical support for modelling: helped to derive quasilinear drag coefficients for the frequency-domain model, helped to develop MATLAB code to solve the motion of equation.		
Signature	5%	Date	21/8/19

Name of Co-Author	Jonathan David Piper		
Contribution to the Paper	Helped in interpretation of obtained results, and provided a critical revision of the manuscript.		
Signature	4%	Date	30/8/19

Name of Co-Author	Luke Bennetts		
Contribution to the Paper	Supervised the work, helped in interpretation of obtained results, and provided a critical revision of the manuscript.		
Signature	4%	Date	28/8/2019

Name of Co-Author	Markus Wagner		
Contribution to the Paper	Supervised the work, helped in interpretation of obtained results, and provided a critical revision of the manuscript.		
Signature	4%	Date	29 August 2019

Name of Co-Author	Benjamin Cazzolato		
Contribution to the Paper	Supervised the work, helped in interpretation of obtained results, and provided a critical revision of the manuscript.		
Signature	4%	Date	27/8/19

Name of Co-Author	Maziar Arjomandi		
Contribution to the Paper	Supervised the work, helped in interpretation of obtained results, and provided a critical revision of the manuscript.		
Signature	4%	Date	27/08/2019

Study of fully submerged point absorber wave energy converter - modelling, simulation and scaled experiment

Boyin Ding*, Leandro Souza Pinheiro da Silva, Nataliia Sergiienko, Fantai Meng, Jonathan David Piper, Luke Bennetts, Markus Wagner, Benjamin Cazzolato, Maziar Arjomandi

Ocean Wave Energy Research Group, Faculty of Engineering, Computer and Mathematical Sciences, the University of Adelaide, South Australia, Australia

*boyin.ding@adelaide.edu.au

1. INTRODUCTION

Ocean waves are a huge resource of renewable energy. Wave energy converter (WEC) devices are being developed to optimise capture of this energy. A point absorber (PA), whose dimensions are much smaller than a wavelength, is a typical type of WEC with the main advantage being its insensitivity to wave direction. Examples of operational PA devices are the Carnegie CETO and Wavebob. PAs normally float on the water surface since wave power decreases with increasing submergence depth of the device (Falnes, 2002). However, there is an increasing trend to keep PAs fully submerged in order to increase the survivability of the device under extreme weather conditions. Sergiienko et al. (2017) undertook a systematic comparison study on floating and fully submerged PAs based on numerical simulations, which demonstrates that fully submerged PAs have the potential to capture a large amount of power from surge motion of the buoy component, twice as much as the power captured from heave motion of the buoy, whereas floating PAs capture power purely from heave motion of the buoy. This unique characteristic allows fully submerged PAs to capture the equivalent amount of wave energy to floating devices while maintaining high survivability.

High expenditures arise from manufacturing, installation, maintenance, and testing of the full-scale WECs in the open sea. Therefore, prior to the design and commissioning of the full-scale devices, numerical simulations and scaled experiments in wave tanks are required to prove design and control concepts, as well as to estimate their economic efficiencies. Modelling of hydrodynamics resulting from wave-body interaction is fundamental for the numerical simulation of point absorber WECs. Linear wave theory, based on the assumption of small wave amplitudes, is the most popular method to model hydrodynamics due to its high computational efficiency. The computed hydrodynamics of the PA can then be assembled in the frequency-domain. The resulting frequency-domain model can only be used to simulate the behaviour of the PA under regular wave conditions and does not have the capability to model nonlinearities such as drag forces and nonlinear power-take-off (PTO) forces. Alternatively, the hydrodynamics can be substituted into the Cummins equation (Cummins, 1962), a deterministic solution originally developed to investigate ship dynamics in the time-domain. The resulting time-domain model is able to include nonlinear forces and can be used for simulation under both regular and irregular wave conditions. However, it is more computationally expensive than the frequency-domain model. A spectral-domain model has recently been applied to WECs due to its high efficiency in solving nonlinear hydrodynamic problems. It is a probabilistic model of the system dynamics, which uses a statistical representation of the waves, and when passed through an appropriate transformation function produces a probabilistic estimate of the WEC response (Folley, 2010). The principle advantage of using a spectral-domain model over the conventional Cummins models is that for complex nonlinear systems it is computationally more efficient at providing estimates of power absorption under irregular waves.

In addition to numerical simulation, scaled experiments are also used to quantify the performance of WECs. There are few world-class wave tank testing facilities for WECs around the world. Examples are FloWave at the University of Edinburgh, Scotland; Model Test Basin at the Australian Maritime College, Australia; Ocean Engineering Water Tank at Shanghai Jiao Tong University, China; and Wave Basin at Indian Institute of Technology Madras, India. These facilities are normally developed for testing ship dynamics and offshore structures, and therefore are not always available for the testing of WECs. In addition, these facilities are often expensive to access, which is not affordable for many WEC research groups.

Besides discussing and benchmarking the typical tools for the study of fully submerged point absorber WECs, this paper has two main original contributions. Firstly, the spectral-domain model is applied to a fully submerged PA with numerical validation. Secondly, cost-effective scaled experiments are proposed and investigated for a fully submerged PA within a standard wave flume facility. The methods developed in this work could be applied to study floating PAs and even other types of WECs.

2. MATHEMATICAL MODELLING

In this study, a fully submerged PA is considered and the nonlinear force considered in modelling is the quadratic drag force. The PA dynamic equation takes the following form in the frequency-domain:

$$\Big(j\omega\big(\mathbf{M}+\mathbf{A}(\omega)\big)+\mathbf{B}(\omega)\Big)\hat{\boldsymbol{x}}=\hat{\mathbf{F}}_e(\omega)+\hat{\mathbf{F}}_b+\hat{\mathbf{F}}_{pto}, \tag{1}$$

where $\mathbf{M}$ is the mass matrix of the buoy; $\mathbf{A}(\omega)$ and $\mathbf{B}(\omega)$ are the hydrodynamic added mass and radiation damping matrices, which vary with wave frequency ω; $\hat{\mathbf{F}}_e(\omega)$ is the wave excitation force, which is also frequency dependent; $\hat{\mathbf{F}}_b$ is the net buoyancy force; $\hat{\mathbf{F}}_{pto}$ is the PTO control force; $\hat{\boldsymbol{x}}$ is the buoy velocities in heave, surge, and pitch under the assumption of plane incident waves. The hydrodynamic terms $\mathbf{A}(\omega)$, $\mathbf{B}(\omega)$ and $\hat{\mathbf{F}}_e(\omega)$ can be solved using boundary element solvers (e.g. WAMIT, ANSYS AQWA, NEMOH) for specific buoy shapes. For generic buoy shapes (e.g. sphere and cylinder), the coefficients can be solved using an analytical model developed by Srokosz (1979) and Jiang et al. (2014).

The Cummins equation takes the following form in the time-domain:

$$\big(\mathbf{M}+\mathbf{A}(\infty)\big)\ddot{\boldsymbol{x}}(t)+\int_0^t\mathbf{B}(t-\tau)\,\dot{\boldsymbol{x}}(t)d\tau=\mathbf{F}_e(t)+\mathbf{F}_b(t)+\mathbf{F}_{pto}(t)+\mathbf{F}_d(t), \tag{2}$$

where $\mathbf{A}(\infty)$ is the infinite-frequency added mass matrix ($\mathbf{A}(\omega)$ for $\omega=\infty$); $\int_0^t\mathbf{B}(t-\tau)\,\dot{\boldsymbol{x}}(t)d\tau$ represents the memory effect of the radiation force, which can be approximated as a transfer function and solved by using a Matlab toolbox developed by Perez and Fossen (2009). The wave excitation force time series $\mathbf{F}_e(t)$ can be calculated for both regular waves at a single frequency ω and irregular waves based on wave spectra models. Typical wave spectra models are JONSWAP, Bretschneider and Pierson-Moskowitz; $\mathbf{F}_d(t)$ is the quadratic nonlinear drag force that takes the form $\frac{1}{2}\rho C_d A|\dot{x}|\dot{x}$ on each dimension, where ρ is the density of seawater, C_d is the drag coefficient usually determined from experiments for particular buoy shapes, and A is the cross-sectional area of the buoy perpendicular to the motion direction.

The spectral-domain model is formulated using the same construction as the frequency-domain model and the response of the PA at each wave frequency can be obtained from (Folley, 2010)

$$\Big(j\omega_i\big(\mathbf{M}+\mathbf{A}(\omega_i)\big)+\big(\mathbf{B}(\omega_i)+\mathbf{G}(\omega_i)\big)\Big)\hat{\boldsymbol{x}}_i=\hat{\mathbf{F}}_e(\omega_i)+\hat{\mathbf{F}}_b+\hat{\mathbf{F}}_{pto}, \tag{3}$$

where $\mathbf{G}(\omega_i)$ is the quasilinear drag coefficients linearised from the quadratic nonlinear drag force and takes the form $2C_d\sqrt{\frac{1}{\pi}\sum_i\omega_i^2|x_i|^2}$ on each dimension. The response of the PA at each frequency is dependent not only on hydrodynamic coefficients at that frequency, but also the response of the PA at all frequencies due to the nonlinear force. Total response under irregular waves can then be calculated by superposition of all the wave components. There is no known analytical solution to the spectral-domain model, so an iterative solver has to be used to estimate the response of the PA for the estimation the quasilinear drag coefficients.

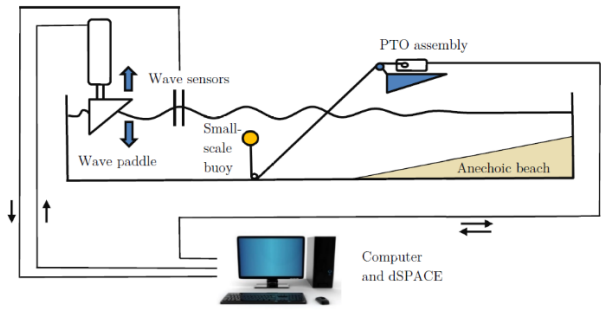

Figure 1. Scaled experiment set-up in the wave flume

Figure 2. Buoy assembly (0.136m diameter sphere)

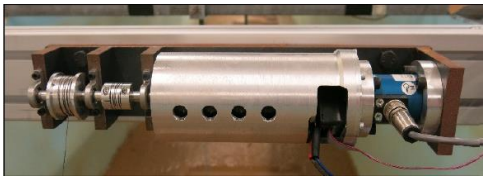

Figure 3. PTO assembly (from left to right: rope spool, shaft coupling, motor-encoder-housing, torque sensor)

3 SMALL-SCALE EXPERIMENT

Figure 1 shows the set-up of the scaled experiment in a standard wave flume facility located in the Chapman lab within the University of Adelaide, which is 32m long, 1.3m wide and 1m deep. A piston-type hydraulic-driven wave paddle is placed at the upstream end of the flume. The up and down motion of the wave paddle generates propagating waves. A perforated anechoic beach sits at the downstream end of the flume, which is used to prevent waves from reflecting back. A fully submerged PA is placed at 5m downstream of the wave paddle, where the generated waves demonstrate the desired regularity. A small boat pulley is placed at the bottom of the flume forming a mooring point. The PA is anchored via a high strength fishing line, which goes through the pulley and rolls on the rope spool within a custom-built PTO system. Six custom-built wave probes are placed around the PA to monitor surrounding wave conditions, two upstream, two downstream, and two at the sides. A DS1104 dSPACE controller is coded via Matlab to control the wave conditions generated by the paddle based on the wave probe readings, as well as control the PTO system to apply desired force on the PA. It also collects data from wave probes, IMU, and motor for post-processing.

Figure 2 shows the buoy assembly of the PA, whose shell is 3D printed from VisiJet M3. The inner space of the buoy shell is used to place an IMU (LORD MicroStrain 3DM-GX4-25) that measures buoy movements and additional weights that allow the change of the net buoyancy and the centre of gravity of the buoy. The shell of the buoy is closed via screw fixation and sealed by double O-rings. The IMU cable exits the buoy shell via a cable gland fixed at the top of the shell. A U tunnel profile is printed at the bottom of the buoy shell, forming an anchoring point for the tether. The dimension of the 3-D printed buoy (0.136m diameter) is 1/73.5 of the full-scale buoy (10m diameter) so that the blockage ratio of the buoy to the flume width is less than 12%. A higher blockage ratio has the risk of modifying the scattering force on the buoy. The ratio (1/73.5) was also chosen considering the similarity of drag coefficients between small/full scales.

Figure 3 shows the PTO assembly that is used to emulate any PTO behaviour. A Maxon RE50 motor drives a rope spool via a shaft coupling and consequently applies PTO force to the PA via pulley-tether coupling. The shafts of the rope spool and motor sit on three rolling-element bearings fixed to the base. The housing of the motor is attached to the base via an aluminium shell and a Lorenz Messtechnik GmbH D-2209 torque sensor. The torque sensor measures the torque applied by the motor. A motor encoder measures the tether displacement. The motor is selected to generate sufficient PTO force to overcome the buoy net buoyancy force and the Coulomb friction force within the PTO assembly, as well as to generate the desired PTO force. Assuming generic linear spring-damper control, the torque command for the motor takes the following form:

$$T_m = -(\rho V - m)g \cdot r + \text{sign}(\dot{\theta}) \cdot c_c + k_{pto} \cdot \theta \cdot r^2 + c_{pto} \cdot \dot{\theta} \cdot r^2, \quad (4)$$

where V is the displaced water due to the buoy; m is the buoy mass; g is the gravitational acceleration; r is the radius of the rope spool; θ is the angular displacement of the motor; c_c is the Coulomb friction coefficient of the PTO assembly; k_{pto} is the scaled PTO spring stiffness; c_{pto} is the scaled PTO damping coefficient. From Eq. 4, it can be seen that the selection of the rope spool radius r compromises the maximum required motor torque and the magnitude of the Coulomb friction torque within the total required motor torque. A current feedback control is applied to track the desired motor torque command calculated from Eq. 4, in order to achieve a desired spring-damper behaviour. Since there is noise within $\dot{\theta}$ arising from differentiating the encoder reading, $\text{sign}(\dot{\theta}) \cdot c_c$ is replaced by a relay function and a low pass filter is applied to remove noise within $\dot{\theta}$ for PTO damping control. The selection of the filter cut-off frequency compromises the phase delay introduced into damping control and the noise attenuation capability.

4. RESULTS

A benchmark study has been undertaken between the modelling methods and the scaled experiment under both regular and irregular wave conditions. Table 1. summarises the full-scale PA and scaled PTO properties.

Table 1. Configuration for the benchmark study

PA property (sphere buoy)	**Values**	**Wave property** (Pierson-Moskowitz spectra used)	**Values**	**PTO property** (for 1/73.5 scale ratio)	**Values**
Water depth	48m	Wave amp (regular)	1.5m	Filter cut-off frequency	50Hz
Buoy radius	5m	Wave period	7, 9, 12s	Relay threshold	eps in Matlab
Submergence depth	8m	Wave height (irregular)	3m	r	15mm
Mass to buoyancy ratio	0.5	Energy wave period	7, 9, 12s	c_c	0.012Nm

Before conducting testing in the wave flume, the buoy was attached to the PTO system without interacting with water to validate the control performance of the PTO system. A decay testing was undertaken by realising the buoy 50mm away from its equilibrium position under spring-damper control. It was evident that the buoy oscillates around its natural frequency $\sqrt{k_{pto}/m}$ and the oscillation decays exponentially almost under the defined PTO damping, c_{pto}. In addition, the hydrodynamic coefficients of the scaled buoy were measured from wave flume experiment, which are similar to the ones computed from linear wave theory, with errors within 20%.

Figure 4 shows the power outputs of the PA resulting from the frequency-domain model (Eq. 1), the time-domain model (Eq. 2) and the scaled experiment under regular wave conditions (power averaged over 16 runs for each wave period, where power in each run averaged over 30 wave periods). The PTO spring and damper were optimised for each wave period subjected to a buoy motion constraint of 3m using the frequency-domain model. The frequency-domain model overestimates the power absorption efficiency of the PA because the nonlinear drag force is not considered. The time-domain model gives much closer results to the experiments, with errors within 10%. Figure 5 shows the power outputs of the PA resulting from the time-domain model (Eq. 2) and the spectral-domain model (Eq. 3) under irregular wave conditions, averaged over 300 peak wave periods (experimental data under irregular waves are still under investigation). The PTO spring and damper were optimised for each energy wave period. The spectral-domain model results match the time-domain model results reasonably well, with errors within 10%.

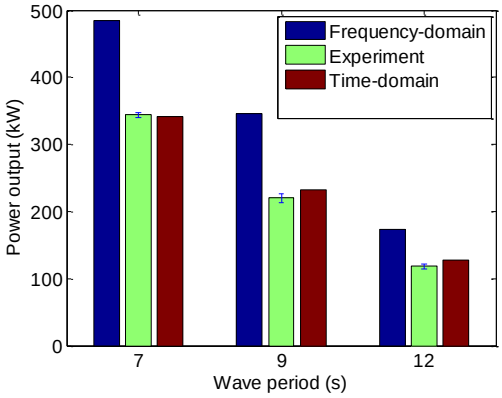

Figure 4. Power outputs under regular waves

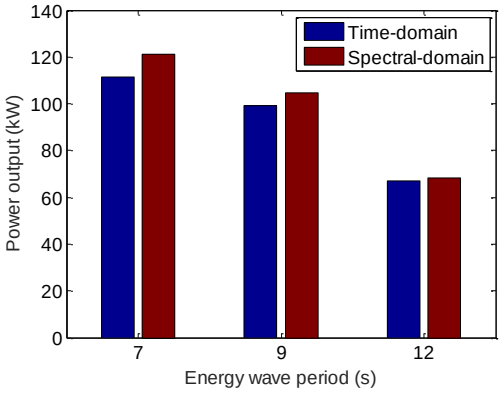

Figure 5. Power outputs under irregular waves

5. CONCLUSION

- We successfully applied a spectral-domain model to fully submerged PA WECs with numerical validation against the conventional time-domain nonlinear model.
- The proposed cost-effective scaled experiment demonstrated high fidelity against the time-domain model, with errors increasing with the increase of wave period. Under long waves, high PTO damping was required to keep the buoy fully submerged, leading to slow tether motion, where the parasitic loss in the PTO assembly cannot be properly compensated.
- More experimental studies are being undertaken to understand the optimal control solution to compensate for parasitic loss within the set-up, especially when the tether motion is slow. One potential solution that will be investigated is the use of dither signals.

REFERENCES

Falnes, J., 2002, Ocean Waves and Oscillating Systems: Linear interactions including Wave-Energy Extraction (Cambridge University Press).

Sergiienko, N.Y. et al., 2017. Performance comparison of the floating and fully submerged point absorber wave energy converters. Renew. Energy, accepted.

Cummins, W.E., 1962. The impulse response function and ship motions. Schiffstechnik, 9, 101-109.

Folley, M. et al., 2010. Spectral modelling of wave energy converters, Coastal Eng. 57, 892-897.

Srokosz, M.A., 1979. The submerged sphere as an absorber of wave power. J. Fluid Mech. 95, 717-741.

Jiang S., 2014. Analytial solution of a wave diffraction problem on a submerged cylinder. J. Eng. Mech. 140, 225-232.

Perez, T. et al., 2009. A Matlab toolbox for parametric identification of radiation-force model of ships and offshore structures. J, Model. Identif. Control, 30, 1-15.

Appendix C

Pseudo-nonlinear hydrodynamic coefficients for modelling point absorber wave energy converters

Schubert, B., Meng, F., Sergiienko, N., Robertson, W., Cazzolato, B. S., Ghayesh, M., Rafiee, A., Ding, B., and Arjomandi, M. (2018). "Pseudo-Nonlinear hydrodynamic coefficients for modelling point absorber wave energy converters". In: *Proceedings of the 4th Asian Wave and Tidal Energy Conference*. Ed. by J. Chen. Taipei, Taiwan, China. pp. 1-10.

Statement of Authorship

Publication Status	Published
Name of Co-author	Fantai Meng
Contribution to the Paper	Helped to develop the LPV and CFD model in the paper
Overall Percentage (%)	10%

Statement of Authorship

Title of Paper	Pseudo-Nonlinear hydrodynamic coefficients for modelling point absorber wave energy converters
Publication Status	☑ Published ☐ Accepted for Publication ☐ Submitted for Publication ☐ Unpublished and Unsubmitted w ork w ritten in manuscript style
Publication Details	Schubert, B., Meng, F., Sergiienko, N., Robertson, W., Cazzolato, B. S., Ghayesh, M., Rafiee, A., Ding, B., and Arjomandi, M. (2018). "Pseudo-Nonlinear hydrodynamic coefficients for modelling point absorber wave energy converters". *Proceedings of the 4th Asian Wave and Tidal Energy Conference*. Ed. by J. Chen. Taipei, Taiwan, China. pp. 1 – 10.

Principal Author

Name of Principal Author (Candidate)	Benjamin W. Schubert		
Contribution to the Paper	Developed the idea and concepts, developed the numerical models, wrote the code of simulations, interpreted the results, wrote the manuscript and acted as a corresponding author.		
Overall percentage (%)	75%		
Certification:	This paper reports on original research I conducted during the period of my Higher Degree by Research candidature and is not subject to any obligations or contractual agreements with a third party that would constrain its inclusion in this thesis. I am the primary author of this paper.		
Signature		Date	26/08/2019

Co-Author Contributions

By signing the Statement of Authorship, each author certifies that:

i. the candidate's stated contribution to the publication is accurate (as detailed above);

ii. permission is granted for the candidate in include the publication in the thesis; and

iii. the sum of all co-author contributions is equal to 100% less the candidate's stated contribution.

Name of Co-Author	Fantai Meng		
Contribution to the Paper	Helped to develop the LPV and CFD model in the paper.		
Signature		Date	21/8/19

Name of Co-Author	Nataliia Sergiienko		
Contribution to the Paper	Supervised the work, helped in interpretation of obtained results, and provided a critical revision of the manuscript.		
Signature		Date	27/08/2019

Name of Co-Author	Will Robertson			
Contribution to the Paper	Supervised the work, helped in interpretation of obtained results, and provided a critical revision of the manuscript.			
Signature			Date	27 AUG 2019

Name of Co-Author	Benjamin Cazzolato			
Contribution to the Paper	Supervised the work, helped in interpretation of obtained results, and provided a critical revision of the manuscript.			
Signature			Date	27/8/19

Name of Co-Author	Mergen Ghayesh			
Contribution to the Paper	Supervised the work, helped in interpretation of obtained results, and provided a critical revision of the manuscript.			
Signature			Date	27/8/19

Name of Co-Author	Ashkan Rafiee			
Contribution to the Paper	Supervised the work, helped in interpretation of obtained results, and provided a critical revision of the manuscript.			
Signature			Date	29/8/2019

Name of Co-Author	Boyin Ding			
Contribution to the Paper	Supervised the work, helped in interpretation of obtained results, and provided a critical revision of the manuscript.			
Signature			Date	28/8/19

Name of Co-Author	Maziar Arjomandi			
Contribution to the Paper	Supervised the work, helped in interpretation of obtained results, and provided a critical revision of the manuscript.			
Signature			Date	27/08/2019

Please cut and paste additional co-author panels here as required.

Pseudo-Nonlinear Hydrodynamic Coefficients for Modelling Point Absorber Wave Energy Converters

Benjamin W. Schubert[#1], Fantai Meng[#2], Nataliia Y. Sergiienko[#3], Will Robertson[#4], Benjamin S. Cazzolato[#5], Mergen H. Ghayesh[#6], Ashkan Rafiee[*7], Boyin Ding[#8], Maziar Arjomandi[#9]

[#]*Ocean Wave Energy Research Group, School of Mechanical Engineering, The University of Adelaide South Australia, Australia, 5005*

[1]benjamin.schubert@adelaide.edu.au

[*]*Carnegie Clean Energy limited, Perth, WA, Australia*

***Abstract*—This study presents dynamic simulation results of two point absorber wave energy converters comparing between linear, pseudo-nonlinear, and CFD models. When modelling wave energy converters, linear assumptions are commonly used to simplify calculations. One such assumption is that the hydrodynamic parameters do not change with pose. This study proposes the inclusion of position and orientation dependence in force estimation, specifically the hydrodynamic terms. A comparison between linear, the proposed pseudo-nonlinear, and CFD models show the effect of the linear assumption for cylindrical and spherical submerged buoys in three degrees of freedom, subject to regular waves. For the case of strong nonlinear hydrodynamic coupling between degrees of freedom, the linear and pseudo-nonlinear models are compared with published literature trends. Accounting for pose dependence of hydrodynamic forces, drag forces, and infinite frequency inertial effects showed trends closer to CFD results but with generally higher motion amplitudes. Significant differences in results for the cylinder are due to the presence of near-surface nonlinear effects that are not captured using linear potential flow solvers. Furthermore, a second order effect was observed in the results, suggesting the proposed method may be well suited to model sufficiently submerged buoys.**

***Index Terms*—Submerged point absorber, nonlinear hydrodynamics, numerical wave tank, wave energy converter, linear parameter varying**

I. Introduction

Wave energy converters (WEC), as a concept, have been developing for over two centuries [1]. As demand for power moves away from fossil-based fuels, research efforts have been intensifying since the 1970s. This enthusiasm has developed into a worldwide interest, leading to a number of technologies employing a variety of different operation principles [2]. Even with large interest globally, most devices are in the research and prototype stage [3]. For this technology to achieve economic viability for large scale energy production, a key area to develop for further study is modelling capability [4].

A common WEC design is a point absorber (PA), which is a device usually insensitive to wave direction. A typical cylindrical submerged point absorber is shown in Fig. 1. To model WECs, efficient and reliable computational methods are essential. Conventional modelling methods include linear boundary element method (BEM) solvers ANSYS AQWA [5], WAMIT [6], and NEMOH [7]. These solvers are used to calculate hydrodynamic parameters which are included in subsequent dynamic simulations. The more computationally intensive numerical wave tank (NWT) CFD approach, such as OpenFOAM or ANSYS Fluent, is becoming increasingly common in the industry. The BEM (also known as potential flow models) and NWT techniques represent linear and nonlinear approaches, respectively [1].

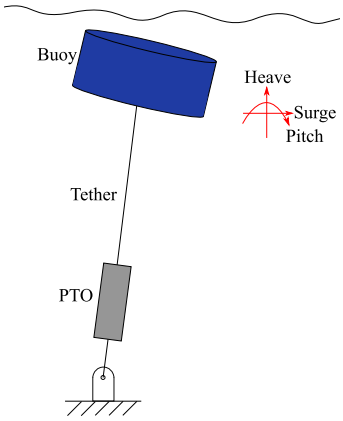

Fig. 1. A schematic of a single tether submerged cylindrical WEC displaying heave, pitch, and surge motions.

Linear BEM solvers provide fast solutions required for design optimisation studies. They do not account for changes in hydrodynamic coefficients as a function of geometric nonlinearities due to changes in pose, as the hydrodynamic coefficients are typically calculated around one position and orientation. Therefore, using results from linear BEM solvers cause the dynamic model to quickly lose accuracy as the motion amplitude of the buoy increases and nonlinearities become dominant [8].

Approaches to capture the nonlinear effects have been attempted previously by using extended linear solving methods,such as varying parameter model of a floating buoy with changing pitch [9]. Other models have involved recalculating the hydrodynamic parameters based on buoy wetted area at each time step for a floating spherical buoy [10] [11] and for a floating cylindrical buoy [11]. These models were constrained to move only in the heave direction. For submerged buoys,

the hydrodynamic parameters have a different dependence on depth and are independent of wetted area, which remains constant. Therefore, it is important to consider how hydrodynamic parameters change with both pitch and heave. Linear models for both floating and submerged buoys generally overestimate motion, and hence power [12], as the motion constraining effects of nonlinearities are ignored. As a whole, comparisons between linear and nonlinear modelling of submerged buoys remains largely unexplored and improvements in the current methods used may be needed to accurately model and rapidly develop these devices.

This paper explores the impact that pose has on the hydrodynamic coefficients and therefore the dynamics of two submerged point absorbers: (i) a cylinder, where coefficients are a function of position and orientation; (ii) a sphere, where coefficients are only a function of position.

Presented in this paper is a comparison between the motion characteristics of linear, pseudo-nonlinear, and fully nonlinear CFD models in three degrees of freedom (DOF) under regular (single frequency) waves. The linear model was constructed using the linear BEM solver NEMOH to find the hydrodynamic coefficients about a nominal position. The linear model does have geometric nonlinearities and drag forces but is referred to as linear in this study to reflect the method of calculating the hydrodynamic properties. The pseudo-nonlinear model used the same solver to find the hydrodynamic coefficients at a grid of points around the motion amplitude to provide linearly interpolated position-dependent hydrodynamic coefficients. Furthermore, the viscous drag force calculation incorporates velocity dependence on drag coefficients and basic orientation dependence. These coefficients and forces were used to investigate the nonlinear dynamics of the PA using MATLAB Simulink. An existing NWT in OpenFOAM was used to compare the linear and pseudo-nonlinear methods against CFD.

The mathematical model is presented in Section II. Included is the governing equation of motion and a description of each constituting term. An overview of typical linear assumptions is also provided for context. Section III discusses the implementation of the pseudo-nonlinear model and the simulation parameters. Section IV presents the results from the linear, pseudo-nonlinear, and CFD models subjected to regular waves. The results and implications on future modelling are discussed in Section V, with concluding remarks given in Section VI.

II. Mathematical Model of WEC

The schematic of the cylindrical buoy used in this study is shown in Fig. 1, with three DOF: surge, heave, and pitch, represented by

$$\mathbf{x} = \begin{pmatrix} \text{Surge} \\ \text{Heave} \\ \text{Pitch} \end{pmatrix} = \begin{pmatrix} x \\ z \\ \theta \end{pmatrix}. \tag{1}$$

Mathematically, the model can be represented by the governing equation, expressed as

$$\mathbf{M}\ddot{\mathbf{x}} = \mathbf{F}_\mathrm{e} + \mathbf{F}_\mathrm{r} + \mathbf{F}_\mathrm{h} + \mathbf{F}_\mathrm{pto} + \mathbf{F}_\mathrm{D} \,, \tag{2}$$

where $\mathbf{M}$ is the mass matrix containing the inertial terms for each DOF, given by

$$\mathbf{M} = \begin{bmatrix} m & 0 & 0 \\ 0 & m & 0 \\ 0 & 0 & I \end{bmatrix} \,, \tag{3}$$

with m being the mass of the buoy and I the moment of inertia about the centre of mass in the pitch direction.

The remaining terms $\mathbf{F}_\mathrm{e}$, $\mathbf{F}_\mathrm{r}$, $\mathbf{F}_\mathrm{h}$, $\mathbf{F}_\mathrm{pto}$, and $\mathbf{F}_\mathrm{D}$, are known as the excitation force, radiation force, hydrostatic or buoyancy force, power take off (PTO) force, and drag force respectively. Each of these terms, as well as how they may be estimated is discussed in the following sections, along with typical assumptions made to model them.

A. Excitation Force

The excitation force, $\mathbf{F}_\mathrm{e}$, from waves acting on the buoy is a function of input wave frequency, wave amplitude, buoy geometry, and buoy pose.

$$\mathbf{F}_\mathrm{e} = \mathbf{F}_\mathrm{e,amp} \sin(\omega t - \boldsymbol{\phi}) \,, \tag{4}$$

where $\mathbf{F}_\mathrm{e,amp}$ is the excitation force amplitude, and $\boldsymbol{\phi}$ is the excitation force phase vector. t represents time, and ω represents the wave frequency. The excitation force is the combination of the diffraction and Froud-Krylov forces [10].

B. Radiation Force

The radiation force, $\mathbf{F}_\mathrm{r}$, is the force applied to the buoy as it radiates waves as a result of motion. Radiation force is commonly represented in the time domain through the Cummins equation [13], given by

$$\mathbf{F}_\mathrm{r} = -\mathbf{A}_\infty \ddot{\mathbf{x}} - \int_0^t \mathbf{K}(t-t')\dot{\mathbf{x}}(t')dt' \,, \tag{5}$$

where $\mathbf{A}_\infty$ is the infinite frequency added mass and $\mathbf{K}$ is known as the memory function. This convolution integral represents the fluid memory affect in which the past state of the fluid effects the current state. In the frequency domain, the radiation force may be described as

$$\hat{\mathbf{F}}_\mathrm{r} = -[\mathbf{B}(\omega) + i\omega\mathbf{A}(\omega)]\hat{\dot{\mathbf{x}}}(i\omega), \tag{6}$$

where $\mathbf{B}(\omega)$ and $\mathbf{A}(\omega)$ is the frequency-dependent radiation damping and added mass respectively. In practice, within simulations, the radiation force is found using a well established method [14], involving constructing transfer functions from radiation damping and added mass with velocity as input and the integral in Equation (5) as the output [15]. For the purpose of these models, transfer functions of order five were found to appropriately fit the data.

C. Hydrostatic and PTO Forces

The hydrostatic force, $\mathbf{F}_\mathrm{h}$, acts only in the heave direction and PTO force, $\mathbf{F}_\mathrm{pto}$, is applied in the direction of the tether. Typically, for submerged buoys, there exists a pretension force provided by the PTO to counteract the hydrostatic force and give an equilibrium position below the surface of the

water [16]. For this study, the PTO force is considered to be a simple spring-damper arrangement,

$$\mathbf{F}_{\text{pto}} = \mathbf{T}(-b\Delta\dot{l} - k\Delta l - |\mathbf{F}_{\text{h}}|) \,, \tag{7}$$

where b and k are the damping coefficients and spring constants of the PTO respectively. The extension of the tether is represented by Δl. These parameters greatly impact the dynamics, and therefore the total power generated by the device. A transform, $\mathbf{T}$, converts the PTO force to the conventional 3 DOF [16].

Both b and k can be optimised for a given frequency wave and buoy [17]. Accordingly, for the purpose of comparing between linear, pseudo-nonlinear, and fully nonlinear CFD, these values will be optimised for each frequency to compare optimal cases. Optimal values are approximately given by the following by assuming tether extension is primarily due to heave motion,

$$b_{\text{opt}} = B_z(\omega) \,, \qquad k_{\text{opt}} = \omega^2(m + A_z(\omega)) \,, \tag{8}$$

where the subscript z refers to the heave direction. In the simulations, the optimal conditions gave large motion amplitudes with part of the buoy breaching the surface. To avoid this, the amplitude was reduced by increasing the damping value while using the optimal PTO stiffness to allow the range of motion to match the sampling grid.

The resonance frequencies of submerged single tether buoys for surge and heave directions are well established [18]. The two resonances approximately overlap when the following stiffness condition is met;

$$k_{\text{pto,overlap}} = \frac{g(\rho V - m)(m + A_z(\omega))}{(l + a)(m + A_x(\omega))} \,, \tag{9}$$

where l is the length of the tether, a is the distance between the tether connection point on the buoy and the center of mass, g is the acceleration of gravity, ρ is the density of water, V is the buoy volume, and A_x and A_z are the added mass in surge and heave, respectively.

When resonances coincide there will be a strong nonlinear coupling between surge and heave. This one-to-one internal resonance condition will be used in this study to demonstrate the impact of including some nonlinearities within the models. The optimal stiffness will be used for comparison with CFD cases to show the impact on weakly nonlinear operating conditions.

To calculate the power generated, PTO nonlinearities are ignored and the simplified equation for instantaneous power is

$$P_{\text{inst}} = b\Delta\dot{l}^2 \,. \tag{10}$$

D. Drag Force

The drag force, $\mathbf{F}_{\text{D}}$, acting on the buoy is modelled as

$$\mathbf{F}_{\text{D}} = -\frac{1}{2}\mathbf{C}_{\text{D}}\rho\mathbf{A}_{\text{D}}|\dot{\mathbf{x}}_{\text{r}}|\dot{\mathbf{x}}_{\text{r}} \,, \tag{11}$$

where $\mathbf{C}_{\text{D}}$ and $\mathbf{A}_{\text{D}}$ are the coefficient of drag and characteristic area respectively, and $\dot{\mathbf{x}}_{\text{r}}$ is the relative velocity of the buoy with respect to the surrounding water. The values for $\mathbf{C}_{\text{D}}$ and $\mathbf{A}_{\text{D}}$ are fixed in the body frame but not the global Cartesian frame and remain approximately constant for a large range of Reynolds numbers [19].

E. Typical Assumptions

The aforementioned forces are complicated to model within the time domain without a number of simplifications and assumptions. Typical assumptions include that:

- the hydrodynamic parameters are independent of buoy pose,
- the coefficients of drag are constant, independent of pitch angle and velocity, the surrounding fluid is stationary, and
- the phase of the excitation force remains constant as the buoy changes surge location.

III. Implementation of Pseudo-Nonlinear Model

In this section, the assumptions listed in Section II-E are addressed in the development of a pseudo-nonlinear dynamic model. Hydrodynamic parameters were introduced in the form of gain-scheduled methods for the excitation force and infinite frequency added mass, and an LPV (linear parameter-varying) system for the radiation force. For the cylinder, these parameters were varied as a function of heave and pitch. For the sphere, only heave was varied as the coefficients are independent of pitch. The viscous drag force was calculated by including velocity dependence in the drag coefficient in the form of Reynolds number calculations. Additionally, for the cylinder, the drag force incorporated pitch dependence by transforming the flow into vector components. For the sphere, the drag force is independent of pitch angle due to symmetry. Excitation force phase change due to motion was implemented as a function of surge, discussed in Section III-C.

A. Hydrodynamic Parameter Position Dependence

Model behaviour is highly dependent on the hydrodynamic parameters ($\mathbf{F}_{\text{e}}$, $\mathbf{B}(\omega)$, $\mathbf{A}(\omega)$). It is therefore critical to investigate the validity of holding these parameters constant for given frequencies as the pose of the buoy changes. Here, the calculation of these parameters was performed using NEMOH, a linear BEM solver [20]. NEMOH provides the amplitude and phase of the excitation force, the hydrodynamic damping, and added mass for a particular buoy at a range of input wave frequencies. To incorporate position dependence, the amplitude and phase of the excitation force and the infinite frequency added mass were calculated through gain-scheduled methods within Simulink. These methods linearly interpolate between a three dimensional lookup table for the cylinder (using heave and pitch), and between a two dimensional lookup table for the sphere (using heave). The radiation force was implemented with an LPV block in Simulink. This block takes an array of state-space models containing a sampling grid, enabling interpolation between models for varying heave and pitch values as required. A block diagram showing the excitation force gain-scheduled method approach is shown in Fig. 2.

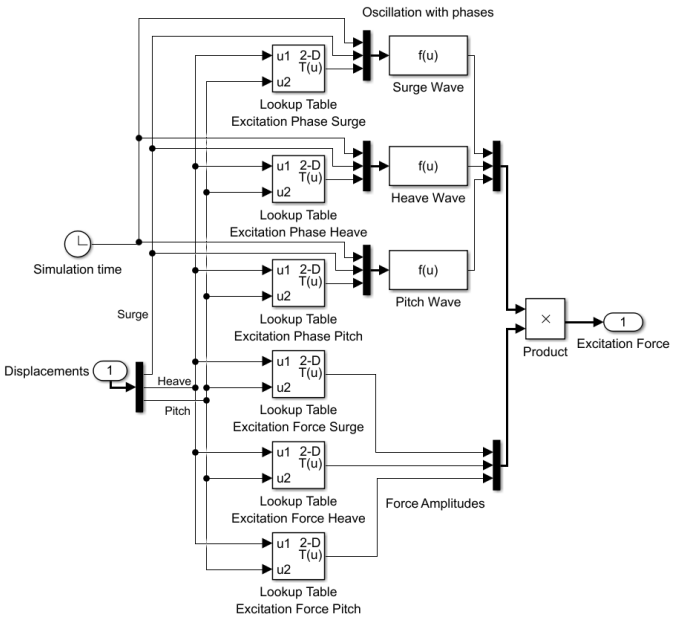

Fig. 2. Block diagram showing the excitation force gain-scheduled method approach. This details the flow of data used to find the interpolated force amplitudes for the cylinder. Force amplitudes for the spherical buoy did not use pitch values.

The range of motion for the cylinder involved varying heave position from -1.5m to 1.5m around the nominal position and pitch angle from $-10°$ to $10°$. For context, geometries of the buoys are provided on Table II. For both DOF, seven different positions and orientations were used, resulting in a sampling grid of 49 different poses. For the spherical buoy, due to symmetry, the pitch angle has no effect. Therefore, only the heave position was varied over the same range as the cylindrical buoy.

To summarise the methodology used for the proposed position-dependent hydrodynamic parameters, the following list shows the step by step procedure.

1) Specify heave and pitch positions
2) Use NEMOH to find $\mathbf{B}(\omega)$, $\mathbf{A}(\omega)$, $\mathbf{F}_{\text{e,amp}}$, and $\boldsymbol{\phi}$
3) Use $\mathbf{B}(\omega)$ and $\mathbf{A}(\omega)$ to create transfer functions describing how each DOF effects the radiation force in another DOF
4) Create a combined state-space for each pose
5) Combine state-space models into state-space array with sampling grid according to heave and pitch positions
6) Use the LPV block in Simulink to implement the state-space array
7) Specify $\mathbf{F}_{\text{e,amp}}$ and $\boldsymbol{\phi}$ into respective arrays and implement in Simulink using the Lookup Table block
8) Specify each element of $\mathbf{A}_\infty$ into respective arrays and implement in Simulink using the Lookup Table block

B. Drag Force Position Dependence

The viscous drag forces acting on the Sphere and Cylinder in the surge and heave directions were approximated through a similar gain-scheduled method. Firstly, the water velocity

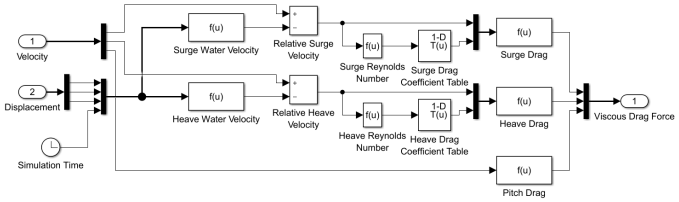

Fig. 3. Block diagram showing the viscous drag gain-scheduled method approach. This details the flow of data used to find the interpolated drag coefficients, and hence drag force amplitudes for the sphere. Force amplitudes for the cylindrical buoy change with pitch and are rotated accordingly.

around the surge and heave positions were found using established theory [17]. The velocity of the buoys relative to the fluid was then used to calculate the Reynolds number at a given time step in each direction. This number was used to find a corresponding drag coefficient based on tabulated data [19]. In the spherical case, no viscous drag torque was modelled in the pitch direction due to symmetry. For the cylindrical buoy, the drag coefficient in the pitch direction was estimated from a previous study with a similar buoy [21]. The cylindrical buoy also has viscous drag forces which are pitch dependent. For an inclined cylinder, as a step towards including position dependence in the viscous drag force, the flow is divided into components in the axial direction of the cylinder, and perpendicular to the axial direction. The forces in the respective directions are found using the previously discussed method to estimate drag coefficients in the rotated reference frame. These forces are then rotated to align with the surge and heave directions. A block diagram showing the flow of data within the pseudo-nonlinear model of the spherical buoy is given in Fig. 3. Though this does not fully capture the nonlinearity of viscous drag, it is expected that this approach is a better representation of drag effects than if the drag coefficient is assumed to be constant and the pitch rotation of the cylinder was ignored.

C. Excitation Force Phase Position Dependence

The excitation force amplitude and phase provided by NEMOH is a description of the force experienced by the buoy at a nominal surge position. Therefore, as the buoy moves in the surge direction, the force experienced by the buoy should reflect this new position. The excitation force is described in Equation (4). The phase change due to surge position (ϕ_{s}) can be represented in the context of the excitation force by

$$\mathbf{F}_{\text{e}} = \mathbf{F}_{\text{e,amp}} \sin(\omega t - \boldsymbol{\phi} + \phi_{\text{s}}) \,, \tag{12}$$

where the phase change from surge is

$$\phi_{\text{s}} = kx \,, \tag{13}$$

and k is the wave number, found as the solution to [22]

$$\omega^2 = gk \tanh(kh) \,, \tag{14}$$

where h is the water depth.

D. Partially-Nonlinear Models from Literature

Previous work has included recalculating the excitation forces at each time step [11] based on the instantaneous wetted area of a floating buoy. This approach still uses a linear model for the radiation force and does not include drag forces. Additionally, the WECs were restricted to oscillate only in the heave direction. A similar study [10] calculated the excitation force at each time step based on instantaneous wetted surface, and uses a second order approximation of the diffraction and radiation force. This model also ignored viscous drag forces, was constrained to move vertically, and only simulated a single regular wave. Such techniques are common in partially-nonlinear models. Nonlinearity in the excitation force is expected to be the most influencial nonlinearity within PA WEC systems [2]. Comparatively, the radiation and diffraction forces require far more computational effort and have less impact on results.

One study, closer to the presented case, uses a Fully Nonlinear Potential Flow model on a submerged cylindrical buoy [23]. The submerged cylindrical buoy is restricted to two DOF, heave and surge. This nonlinear flow model effectively simulated two dimensional NWT results for limited scenarios, involving a small buoy and small wave amplitudes (cylinder with radius of 0.05m, and wave amplitude of 1.7cm). These limitations predispose the simulation to act in a regime in which linear assumptions provide reasonable results. While nonlinear potential flow models show promising results, further research is needed to quantify overall accuracy [2]. Additionally, such models are still computationally expensive compared to linear models [24].

Nonlinearities can have differing results for a change in simulated conditions [25]. One study, on submerged spherical buoys oscillating in the heave direction, showed that a weakly nonlinear model, based on the weak scatterer approximation, predicted lower amplitudes for some frequencies and higher for others [25]. Research in this area seems to indicate that nonlinearties impact models in differing ways and cannot be summarised as a simple increase or decrease compared to the linear model.

Another study which compares linear and nonlinear hydrodynamic parameters for cylinders [26] found that for cylinders close to the surface, the added mass and radiative damping in the heave and pitch directions differ significantly between linear and nonlinear simulations, whereas the surge direction remained relatively unchanged. Also shown in this study was that vortex shedding occurs on the edge of the cylinder, though this nonlinearity is expected to have minimal impact for the case presented. A more influential result seen in this study is the formation of a chute of water as the cylinder oscillates. We expect that this phenomenon could cause significant discrepancy between linear and nonlinear models.

The proposed pseudo-nonlinear method combines the nonlinear relationships present in hydrodynamic parameters as the pose varies, with the computational speed of linear modelling, and in three DOF. For the purpose of this study, the general trend of the responses at varying frequencies will be compared to investigate the degree to which nonlinearities are captured within the proposed model. Additionally, this model applies the same pseudo-nonlinear approach towards quantifying viscous drag effects, a force ignored in previous BEM studies.

E. Simulation Parameters

To compare the performance of each model, some common parameters were selected (Table I). In addition to the simulation parameters, the properties of the buoys and PTOs must be consistent between the respective models. These properties relating to the cylindrical and spherical buoys are presented in Table II.

TABLE I
SIMULATION PARAMETERS

Parameter	**Value**	**Units**
Acceleration of gravity, g	9.81	$\mathrm{m{\cdot}s^{-2}}$
Water density, ρ	1025	$\mathrm{kg{\cdot}m^{-3}}$
Kinematic viscosity of water, ν	1.004×10^{-6}	$\mathrm{m^2{\cdot}s^{-1}}$
Water depth, h	50	m
Submersion depth (buoy top), ds	2.5	m
Wave amplitude, A_w	0.5	m

TABLE II
BUOY PROPERTIES

Property	**Value**	**Units**
Cylinder radius, r_c	5	m
Cylinder height, h_c	5	m
Sphere radius, r_s	5	m
Buoy density, ρ_buoys	0.7ρ	$\mathrm{kg{\cdot}m^{-3}}$

For the linear and pseudo-nonlinear models, the viscous drag can only be approximated from literature values. In the linear case, the drag coefficients are assumed to be constant irrespective of surge and heave position. These coefficients of drag and the corresponding characteristic areas are given in Equations (15) and (16) where $\mathbf{C}_{\mathrm{D,\,c}}$, $\mathbf{A}_{\mathrm{D,\,c}}$, $\mathbf{C}_{\mathrm{D,\,s}}$, and $\mathbf{A}_{\mathrm{D,\,s}}$ are the coefficients of drag for the cylinder, characteristic area of the cylinder, coefficients of drag for the sphere, and the characteristic area of the sphere respectively [21].

$$\mathbf{C}_{\mathrm{D,\,c}} = \begin{pmatrix} 1 & 0 & 0 \\ 0 & 1.1 & 0 \\ 0 & 0 & 0.2 \end{pmatrix}, \mathbf{C}_{\mathrm{D,\,s}} = \begin{pmatrix} 0.5 & 0 & 0 \\ 0 & 0.5 & 0 \\ 0 & 0 & 0 \end{pmatrix} \quad (15)$$

$$\mathbf{A}_{\mathrm{D,\,c}} = \begin{pmatrix} hr_\mathrm{c}^2 & 0 & 0 \\ 0 & \pi r_\mathrm{c}^2 & 0 \\ 0 & 0 & (2r_\mathrm{c})^5 \end{pmatrix}, \mathbf{A}_{\mathrm{D,\,s}} = \begin{pmatrix} \pi r_\mathrm{s}^2 & 0 & 0 \\ 0 & \pi r_\mathrm{s}^2 & 0 \\ 0 & 0 & 0 \end{pmatrix}. \quad (16)$$

In the pseudo-nonlinear case, the drag coefficients for surge and heave are found by interpolating between tabulated results from literature [19], while the pitch drag coefficient is constant.

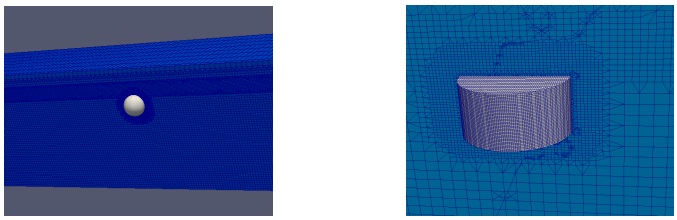

Fig. 4. A broad overview of the NWT is shown with the spherical buoy (left), and the cylindrical buoy mesh within the NWT (right).

For the fully nonlinear case, due to the computational resources required for this type of model, only five test cases were selected based on a distribution of periods. These five test cases, and the corresponding PTO parameters are given in Table III. The optimal PTO stiffness according to Equation (8) was used in these simulations. Test frequencies for the linear and pseudo-nonlinear model range from 0.1 to 2.5 rad/s.

TABLE III
CFD Test Cases

Period (s)	6	8	10	12	14
$K_{\text{pto,cylinder}}$ (MN·m^{-1})	1.07	0.62	0.38	0.25	0.17
$K_{\text{pto,sphere}}$ (MN·m^{-1})	0.79	0.46	0.29	0.20	0.14
$B_{\text{pto,buoys}}$ (MN·s·m^{-1})	0.14	0.14	0.14	0.14	0.14

F. CFD Setup

CFD models are nonlinear models used to simulate fluid structure interaction. They are computationally expensive but can be a powerful tool to acquire accurate simulated results. The CFD model was adapted from previous studies [12], [27]. A broad view of the numerical wave tank and a detailed view of the mesh surrounding the cylindrical buoy can be seen in Fig. 4. This model has been checked for convergence and has been validated against experimental data for spherical buoys.

IV. Results

A. Hydrodynamic results from NEMOH

Hydrodynamic parameters at a range of poses for the cylinder and sphere were found using NEMOH. Representative graphs of the added mass from Equation (6) for the cylindrical buoy at a heave position of 0.5m and varying pitch angles, and the added mass for the spherical buoy at varied heave positions are given in Figs 5 and 6, respectively. Radiation damping of the cylindrical and spherical buoys follow similar trends. Representative excitation forces and phases from Equation (4) are given in Figs 7 and 8 for the cylindrical and spherical buoys, respectively.

These added mass and damping coefficients were used to construct a model of the radiation force for different positions. However, for the spherical buoy, some terms fluctuate about zero due to numerical error or mesh imperfections. Additionally, the pitch-pitch and cross terms were expected to be zero

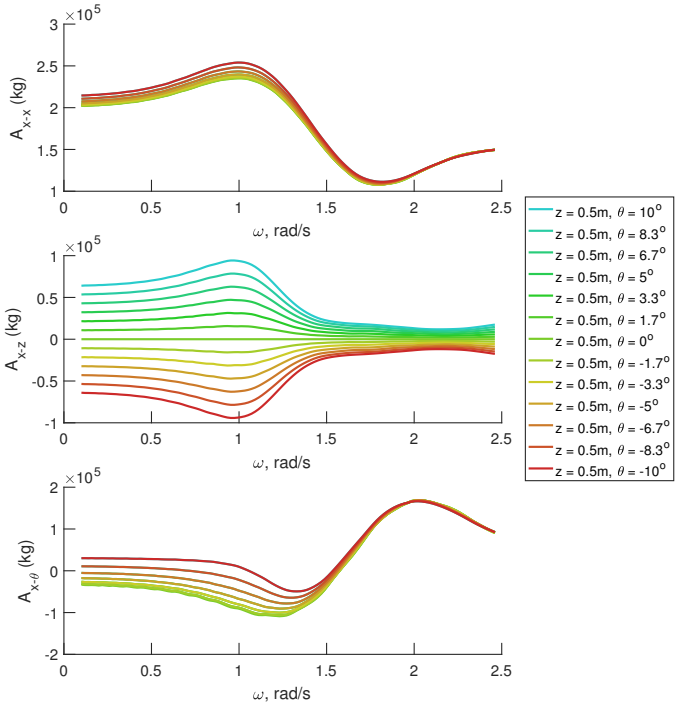

Fig. 5. Representative added mass values for the cylinder at constant surge and heave locations. Shown are the contributions to the added mass in the surge direction due to motions in all three DOF.

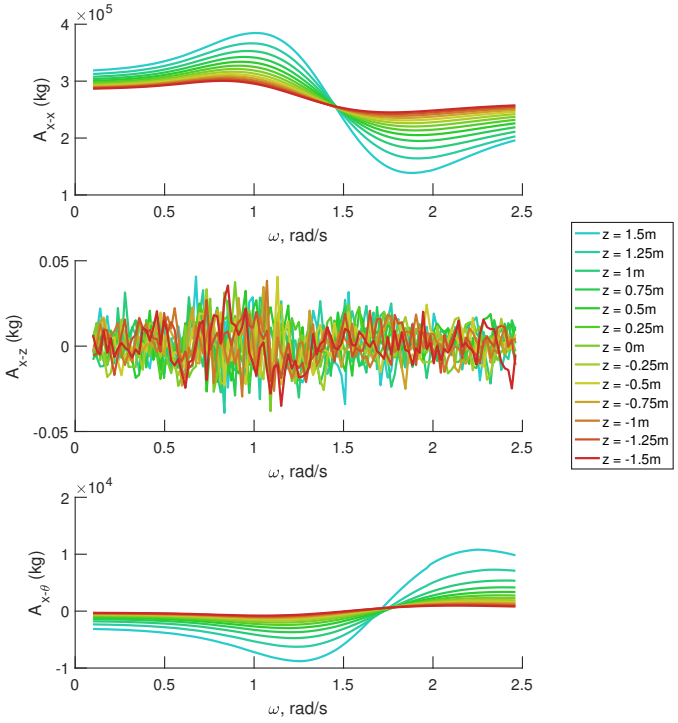

Fig. 6. Added mass values for the sphere at nominal surge location and pitch orientation. Shown are the contributions to the added mass in the surge direction due to motions in all three DOF.

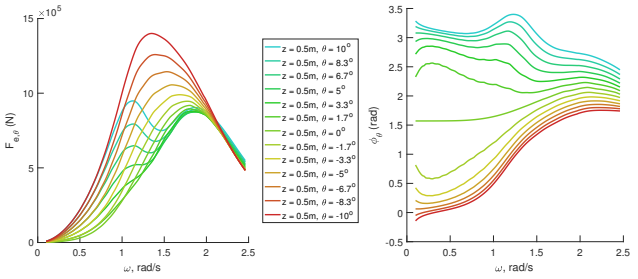

Fig. 7. Representative excitation forces (left) and phases (right) for the cylinder at nominal surge and heave locations. The excitation moment amplitude in the pitch DOF is shown.

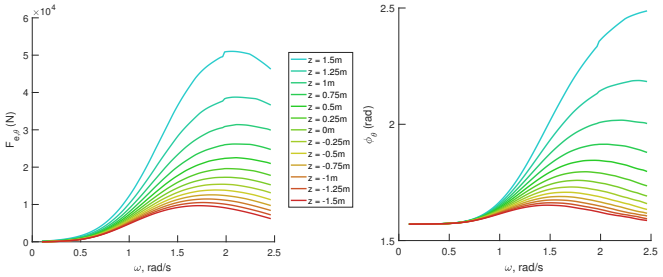

Fig. 8. Representative excitation forces (left) and phases (right) for the sphere at nominal surge location and pitch orientation. The excitation moment amplitude in the pitch DOF is shown.

but were found to be two orders of magnitude lower than surge-surge and heave-heave. These values are likely due to mesh imperfection and were also set to zero for the purpose of this study. Likewise, for the cylinder at the nominal pitch angle, the cross terms were near zero. These quantities were also set to zero in the calculation of transfer functions to prevent numerical artefacts in the radiation forces.

B. Simulation results in regular waves

In order to show the extent of the difference between the linear and pseudo-nonlinear models, the resonance frequency in heave was matched with the resonance frequency in surge using Equation (9). This provides large opportunity for strong nonlinear cross coupling effects. To isolate the effect of the hydrodynamic nonlinearity from viscous drag nonlinearity, the drag coefficient was held constant as with the linear simulations. In another set of simulations, the drag force was calculated according to the pseudo-nonlinear method with varying drag coefficient, (Fig. 9). This figure shows the oscillation amplitude for the cylinder when subjected to regular waves. A similar effect was also seen for the spherical buoy (not shown).

The linear, pseudo-nonlinear, and fully nonlinear models were subjected to simulated regular waves. Under this excitation, the steady state response of the WEC was recorded for each frequency. The mean of each DOF was found and used to center the signal for each DOF. A spectrum was obtained from this time domain signal using a Hamming window and a suitable frequency resolution. The maximum amplitude seen in each simulation was identified. The resulting peak oscillation

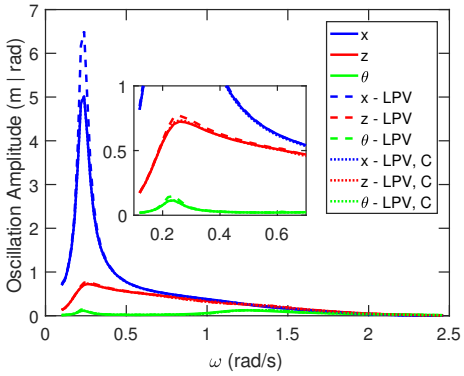

Fig. 9. The peak oscillation amplitude for the linear, pseudo-nonlinear (indicated by LPV), and pseudo-nonlinear with constant drag coefficient (indicated by LPV, C) models when the resonant frequencies in surge and heave are close. Results for the cylindrical buoy are shown.

in three DOF are presented in Figs 10 and 11 for the cylinder and sphere, respectively. The mean position of each buoy subjected to regular waves is shown in Figs 12 and 13 for the cylinder and sphere, respectively.

For practical WEC systems, another aspect to consider is the maximum PTO forces and power generated. The maximum PTO forces and the mean of the power generation were found at each frequency and displayed in Figs 14 and 15 for the cylinder and sphere, respectively.

V. Discussion

The simulated results show a notable difference between the linear and pseudo-nonlinear models. For the strongly coupled case with constant drag coefficients, the linear model and the pseudo-nonlinear models are approximately equivalent with the linear model overestimating and underestimating at different frequency ranges. However, when the drag coefficient is varied as a function of velocity, larger amplitudes are seen. This indicates the constant drag coefficients lead to an overestimate of drag forces. This finding informs the interpretation of subsequent results for the linear, pseudo-nonlinear, and fully nonlinear comparison. That is, larger motion amplitudes are expected for fully nonlinear results due to an overestimate in viscous drag forces in the linear model. Optimal stiffness conditions lead to increased motion amplitudes, which were used to further compare the linear, pseudo-nonlinear, and CFD approaches.

For the optimal stiffness condition, the heave oscillation amplitude of the pseudo-nonlinear model of the cylinder shows an increase around larger amplitudes and is relatively unchanged elsewhere compared to the linear model. A noticeable difference between the results is the change in mean positions about which the buoy oscillates. In both the strongly coupled and optimal stiffness PTO conditions, the pseudo-nonlinear approach resulted in larger displacements for the cylinder than for the spherical buoy. This is expected due to spherical symmetry preventing strong coupling between DOFs. This behaviour arises due to an asymmetric force experienced by the buoy over each oscillation cycle; that is, a net drift

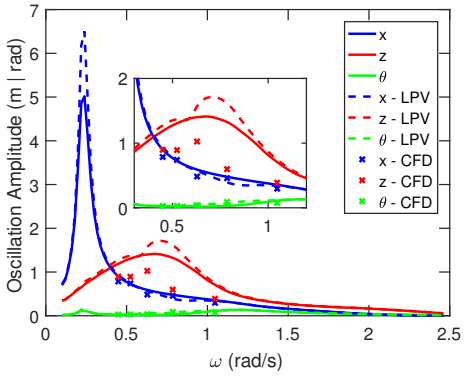

Fig. 10. The peak oscillation amplitude for the cylinder at various excitation frequencies when optimal PTO stiffness is used. The linear, pseudo-nonlinear (indicated by LPV), and fully nonlinear CFD results are shown.

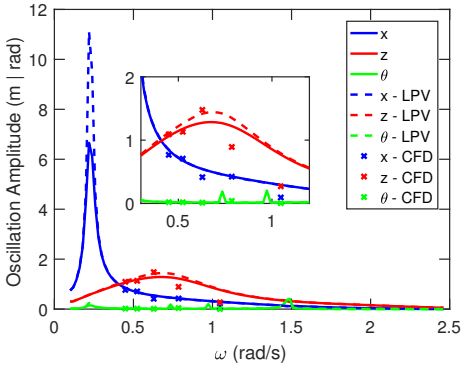

Fig. 11. The peak oscillation amplitude for the sphere at various excitation frequencies when optimal PTO stiffness is used. The linear, pseudo-nonlinear (indicated by LPV), and fully nonlinear CFD results are shown.

force. Drift forces are known to be a second order effect [28]. This behaviour is caused by a phase difference between the heave and surge excitation forces. This phase difference, coupled with the changing position of the buoy, creates a net movement in one direction until the stiffness force of the PTO is large enough to balance this drifting effect. The CFD results show the same bias trend though different peak locations and magnitudes for the spherical buoy. However, the mean position of the cylindrical buoy was clearly over-estimated in the pseudo-nonlinear method. One speculated result of this surge bias is that the tether extension is more coupled with rotation, allowing pitch to have more influence over power generation.

The difference between linear and pseudo-nonlinear oscillation amplitudes may, in part, be due to coupling between the three modelled DOF. This coupling can be seen in the hydrodynamic parameters in Fig. 5 for non-zero pitch angles. For the cylinder, pitch has a large effect on the effective added mass between surge and heave and pitch and heave motions. In the linear system, these cross terms are typically neglected as the pitch angle position is assumed to be zero. Conversely, the amplitude of oscillation of the spherical buoy is relatively unchanged for all DOF. Due to symmetry, the cross terms are zero and a changing heave location does not lead to strong hydrodynamic coupling. Consequently, less change between linear and nonlinear models is expected for spherical buoys.

The CFD results (Fig. 11) demonstrate that the linear model loses accuracy as the motion amplitude increases, agreeing with literature expectation. Results for the pseudo-nonlinear method do not clearly match CFD results but show a closer trend than the linear case, indicating that the LPV method captures some, but not all, nonlinearity in the hydrodynamics acting on the buoy. The trend for the sphere seems to be the peak thinning and a higher peak amplitude. The pseudo-nonlinear model results begin to show the same increase in peak amplitude. The pseudo-nonlinear model of the cylindrical buoy showed two distinct peaks, a large deviation from the linear model. Increased heave amplitudes occurred around the same frequencies as decreased surge amplitudes, indicating some degree of coupling between heave and surge. The CFD results for the cylinder again show that the pseudo-nonlinear results capture trends better than linear counterparts, though with greatly decreased amplitudes. The pseudo-nonlinear method gives larger amplitudes due to asymmetry in excitation forces in heave direction. That is, the exponential trend in excitation force indicates a greater increase for excitation force amplitude above the nominal position than decrease for below (Fig. 8). Therefore, nonlinearity in the excitation force is being captured. However, the motion amplitude is far less in the fully nonlinear CFD model (Fig. 10), indicating there is significant nonlinearity missing which the linear BEM hydrodynamic coefficients do not capture.

Other nonlinear forces acting on the buoy, such as overtopping or slamming, are not able to be modelled with linear BEM solvers. Submerged buoys, however, are away from highly nonlinear surface effects, and the outlined method does more closely approximate the nonlinearity of hydrodynamic forces than the simple linear BEM solver about a nominal position. It is commonly thought that the most influential nonlinearity for PA WEC systems is excitation force [2]. However, these results show that while the inclusion of nonlinearities in the excitation force does impact the results, there are more influential nonlinearties for this system not captured.

Linear BEM solvers are not able to fully capture the radiation forces for cylindrical buoys closer to the surface due to the formation of water jets and vortex shedding [26]. It was noticed that in the CFD simulations, significant vorticity was periodically occurring above the cylinder, indicating the presence of some complex resonance effect present in the column of water above the cylinder. Also, poor sampling grid resolution in the pseudo-nonlinear method and higher order nonlinear forces could be the reason for the discrepancy between pseudo-nonlinear and fully nonlinear results. Furthermore, interpreting the CFD results was made difficult due to the limited number of sampled frequencies. These reasons suggest that the proposed pseudo-nonlinear method is suited towards rapid modelling of submerged WEC devices only if additional improvements can be made which incorporate

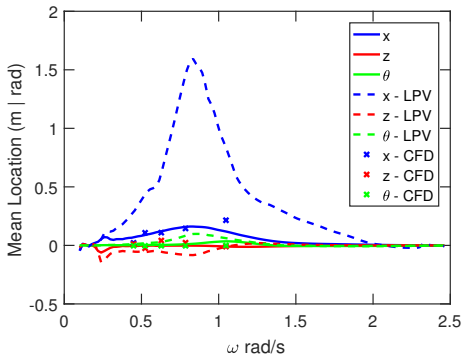

Fig. 12. The mean location for the cylinder at various excitation frequencies when optimal PTO stiffness is used. The linear, pseudo-nonlinear (indicated by LPV), and fully nonlinear CFD results are shown.

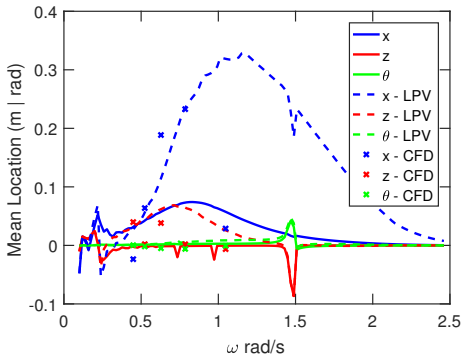

Fig. 13. The mean location for the sphere at various excitation frequencies when optimal PTO stiffness is used. The linear, pseudo-nonlinear (indicated by LPV), and fully nonlinear CFD results are shown.

nonlinear trends as buoys approach the surface. Alternatively, the proposed modelling method may be suited to specific operating conditions, such a sufficient submergence depth, because linear BEM solvers may adequately represent hydrodynamic parameters in particular conditions.

To comprehensively model WEC devices, it is important to accurately model the PTO forces. These forces influence installation cost and power generated. As an indication, the tether forces and power generated for all three modelling methods is provided in Section IV. These results show the pseudo-nonlinear method generally overestimates PTO forces and power generated. It should be emphasised that the viscous drag coefficient for the linear model is held constant and has been shown earlier to be the result of an over-estimated drag coefficient. However, as both the linear and pseudo-nonlinear model overestimate motion at higher frequencies, this is further evidence of the limitation that strong frequency-dependent nonlinearities are not captured using linear BEM solvers. One limitation of this study is that the CFD model was validated only against experimental data of spherical buoys, not cylindrical. Another limitation is that the results present the frequency of maximum oscillation amplitude seen in the response of the WECs when subjected to a regular wave, which does not account for harmonic distortions. Such harmonics were seen in the time domain results of CFD models, and, to a lesser extent, the pseudo-nonlinear model, particularly around natural frequencies.

Though the linear method proposed in this study has significant limitations, there are some benefits to such methods. The primary benefit of the linear and pseudo-nonlinear models is the drastic reduction in simulation time compared to CFD. The pseudo-nonlinear method is marginally more computationally expensive than the linear model. The linear method was able to simulate 2000 seconds in approximately 4 seconds, while the pseudo-nonlinear method took 10–15 seconds, on a standard computer. The CFD model simulated 300 seconds in approximately 2–3 days on a supercomputer. The found results and the potential benefits merit further investigation into the applicability of this modelling technique under a range of operating conditions. If the proposed pseudo-nonlinear model can be shown to capture significant nonlinearities in hydrodynamic forces, it can greatly speed up development of submerged WEC devices.

Further extensions of this research include improving the modelling method of the drag forces in each direction, which could be made more accurate by including drag coefficients of inclined cylinders rather than decomposing the flow direction into components. Furthermore, the resolution of the sampling grid of different positions and orientations may be increased to more adequately represent nonlinear trends in the hydrodynamic parameters. The model could be extended to explore the effect of larger wave amplitudes on submerged buoys. The CFD model could also be used to acquire results from more excitation frequencies to gain a clearer perspective of nonlinear effects over a broad range of operating conditions. Alternatively, the effect of surface nonlinearities in CFD could be further explored by varying the submergence depth. For submerged devices, this pseudo-nonlinear method presents a potential alternative to greatly improving simulation speed from CFD, while capturing some nonlinear behaviours arising from position dependant hydrodynamic parameters.

VI. Conclusion

In this study a linear, pseudo-nonlinear, and fully nonlinear hydrodynamic parameter model for two point absorbers were developed and the corresponding motion and forces were compared. The linear and pseudo-nonlinear models displayed similar motion amplitudes for a spherical buoy and differing amplitudes for a cylindrical buoy. The pseudo-nonlinear model incorporated position dependence into the hydrodynamic parameters and drag forces. The results showed increased nonlinear behaviour and more closely match the trend in the CFD results compared to linear methods. The proposed model demonstrated the ability to capture some higher order nonlinearities such as drift forces and nonlinear trends in excitation forces. The pseudo-nonlinear model showed only a small increase in computation time over the linear model, but showed some basic nonlinear behaviours noticed in the CFD results and matched the trend of the fully nonlinear results. The significant differences between the pseudo-nonlinear and

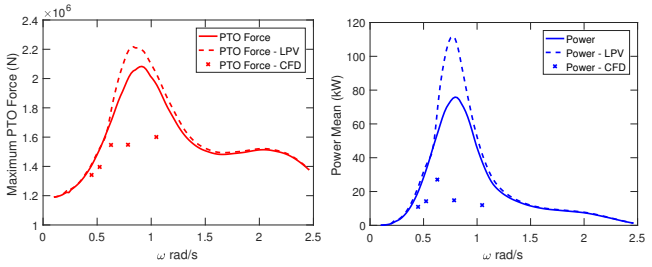

Fig. 14. The maximum PTO force (left) and mean of instantaneous power (right) experienced for each regular wave frequency for the cylindrical buoy.

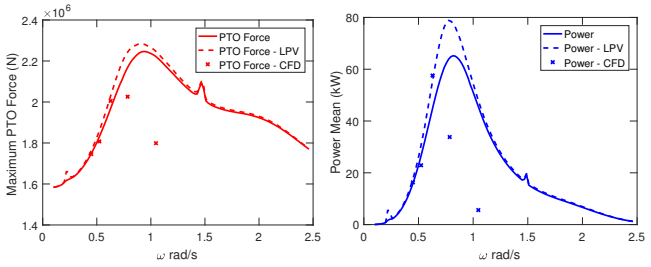

Fig. 15. The maximum PTO force (left) and mean of instantaneous power (right) experienced for each regular wave frequency for the spherical buoy.

fully nonlinear for the cylindrical buoy results suggest that nonlinearity in the hydrodynamic excitation forces are not the most significant nonlinearity for the buoy dynamics, and that the linear potential flow method for calculating hydrodynamic parameters becomes inadequate close to the surface. For the concept of submerged buoys, the results presented demonstrate the applicability of pseudo-nonlinear modelling for rapid simulation compared to fully nonlinear alternatives, and justify further investigation of this method.

Acknowledgement

This work was supported with supercomputing resources provided by the Phoenix HPC service at the University of Adelaide. This research has been supported by the Australian Government Research Training Program Scholarship.

References

[1] J. Cruz, *Ocean Wave Energy*, 1st ed. Springer-Verlag Berlin Heidelberg, 2008.

[2] M. Penalba, G. Giorgi, and J. V. Ringwood, "Mathematical modelling of wave energy converters: A review of nonlinear approaches," *Renewable and Sustainable Energy Reviews*, vol. 78, pp. 1188–1207, Oct. 2017.

[3] P. Hardy, B. Cazzolato, B. Ding, and Z. Prime, "A maximum capture width tracking controller for ocean wave energy converters in irregular waves," *Ocean Engineering*, vol. 121, pp. 516 – 529, 2016.

[4] J. Chozas, "International levelised cost of energy for ocean energy technologies an analysis of the development pathway and levelised cost of energy trajectories of wave, tidal and OTEC technologies," Ocean Energy Systems, Tech. Rep., May 2015.

[5] *AQWA User Manual*, ANSYS, Oct. 2012.

[6] *WAMIT USER MANUAL*, 7th ed., WAMIT Inc., 2016.

[7] A. Babarit, *NEMOH User manual*, Ecole Centrale de Nantes, Jan. 2014.

[8] J. Davidson, S. Giorgi, and J. V. Ringwood, "Linear parametric hydrodynamic models for ocean wave energy converters identified from numerical wave tank experiments," *Ocean Engineering*, vol. 103, pp. 31 – 39, 2015.

[9] A. McCabe, G. A. Aggidis, and T. Stallard, "A time-varying parameter model of a body oscillating in pitch," *Applied Ocean Research*, vol. 28, no. 6, pp. 359–370, 2006.

[10] A. Merigaud, J.-C. Gilloteaux, and J. V. Ringwood, "A nonlinear extension for linear boundary element methods in wave energy device modelling," in *Volume 4: Offshore Geotechnics; Ronald W. Yeung Honoring Symposium on Offshore and Ship Hydrodynamics*. ASME, Jul. 2012.

[11] M. Penalba Retes, A. Mérigaud, J.-C. Gilloteaux, and J. Ringwood, "Nonlinear Froude-Krylov force modelling for two heaving wave energy point absorbers," in *Proceedings of the 11th European Wave and Tidal Energy Conference*. European Wave and Tidal Energy Conference 2015, 2015.

[12] F. Meng, A. Rafiee, B. Cazzolato, B. Ding, M. Arjomandi, J. D. Piper, N. Sergiienko, and Q. Hu, "Numerical simulation of a submerged spherical point absorber with asymmetric mass distribution," in *Proceedings of the 11th European Wave and Tidal Energy Conference*, 2017.

[13] W. Cummins, "The impulse response function and ship motions," David Taylor Model Basin Washington DC, Tech. Rep., 1962.

[14] T. Perez and T. I. Fossen, "A Matlab toolbox for parametric identification of radiation-force models of ships and offshore structures," *Modeling, Identification and Control: A Norwegian Research Bulletin*, vol. 30, no. 1, pp. 1–15, 2009.

[15] R. G. Coe and D. L. Bull, "Nonlinear time-domain performance model for a wave energy converter in three dimensions," in *Oceans-St. John's, 2014*. IEEE, 2014, pp. 1–10.

[16] A. Babarit, J. Hals, M. Muliawan, A. Kurniawan, T. Moan, and J. Krokstad, "Numerical estimation of energy delivery from a selection of wave energy convertersfinal report," *Report, Ecole Centrale de Nantes & Norges Teknisk-Naturvitenskapelige Universitet*, 2011.

[17] J. Falnes, *Ocean waves and oscillating systems: linear interactions including wave-energy extraction*. Cambridge university press, 2002.

[18] F. Meng, B. Cazzolato, B. Ding, and M. Arjomandi, "Modal analysis of a submerged spherical point absorber with asymmetric mass distribution," *submitted to Renewable Energy*, 2017.

[19] R. D. Blevins, "Applied fluid dynamics handbook," *New York, Van Nostrand Reinhold Co., 1984, 568 p.*, 1984.

[20] M. Penalba, T. Kelly, and J. V. Ringwood, "Using NEMOH for modelling wave energy converters: A comparative study with WAMIT," *Centre for Ocean Energy Research (COER), Maynooth University, Co. Kildare, Ireland*, 2017.

[21] N. Y. Sergiienko, B. S. Cazzolato, B. Ding, and M. Arjomandi, "Three-tether axisymmetric wave energy converter: estimation of energy delivery," in *Proceedings of the 3rd Asian Wave and Tidal Energy Conference, Singapore*, 2016, pp. 163–171.

[22] S. Chao Jiang, Y. Gou, B. Teng, and D. Zhi Ning, "Analytical solution of a wave diffraction problem on a submerged cylinder," *Journal of Engineering Mechanics*, vol. 140, no. 1, pp. 225–232, Jan. 2014.

[23] E. Guerber, M. Benoit, S. Grilli, and C. Buvat, "Numerical modeling of fully nonlinear interactions of ocean waves with a submerged moving body," in *Proceedings of the 3rd International Conference on Ocean Energy. Bilbao, Spain*, 2010, pp. 1–6.

[24] L. Letournel, P. Ferrant, A. Babarit, G. Ducrozet, J. C. Harris, M. Benoit, and E. Dombre, "Comparison of fully nonlinear and weakly nonlinear potential flow solvers for the study of wave energy converters undergoing large amplitude motions," in *ASME 2014 33rd International Conference on Ocean, Offshore and Arctic Engineering*. American Society of Mechanical Engineers, 2014, pp. V09BT09A002–V09BT09A002.

[25] L. Letournel, C. Chauvigné, B. Gelly, A. Babarit, G. Ducrozet, and P. Ferrant, "Weakly nonlinear modeling of submerged wave energy converters," *Applied Ocean Research*, vol. 75, pp. 201–222, Jun. 2018.

[26] A. Rafiee and A. Valizadeh, "Nonlinear hydrodynamics of bluff bodies oscillating near freesurface," in *Proceedings of the twenty-eighth International Ocean and Polar Engineering Conference (ISOPE), Sapporo, Hokkaido, Japan*, Jun. 2018.

[27] A. Rafiee and J. Fiévez, "Numerical prediction of extreme loads on the CETO wave energy converter," in *Proceedings of the 11th European Wave and Tidal Energy Conference, Nantes, France*, 2015.

[28] B. W. Kim, S. Y. Hong, and H. G. Sung, "Comparison of drift force calculation methods in time domain analysis of moored bodies," *Ocean Engineering*, vol. 126, pp. 81–91, Nov. 2016.

Appendix D

Enhancing the relative capture width of submerged point absorbing wave energy converters

Ding, B., Sergiienko, N., Meng, F., Cazzolato, B. S., Hardy, P. and Arjomandi, M. (2018). "Enhancing the relative capture width of submerged point absorbing wave energy converters". In: *Proceedings of the 4th Asian Wave and Tidal Energy Conference*. Ed. by J. Chen. Taipei, Taiwan, China. pp. 1-10.

Statement of Authorship

Publication Status	Published
Name of Co-author	Fantai Meng
Contribution to the Paper	Helped to develop the mathematical model of the single-tether point absorber with asymmetric mass distribution, helped in interpretation of obtained results.
Overall Percentage (%)	10%

Statement of Authorship

Title of Paper	Enhancing the relative capture width of submerged point absorbing wave energy converters
Publication Status	☑ Published ☐ Accepted for Publication ☐ Submitted for Publication ☐ Unpublished and Unsubmitted work written in manuscript style
Publication Details	Ding, B., Sergiienko, N., Meng, F., Cazzolato, B. S., Hardy, P. and Arjomandi, M. (2018). "Enhancing the relative capture width of submerged point absorbing wave energy converters". *Proceedings of the 4th Asian Wave and Tidal Energy Conference*. Ed. by J. Chen. Taipei, Taiwan, China. pp. 1-10.

Principal Author

Name of Principal Author (Candidate)	Boyin Ding		
Contribution to the Paper	Developed the idea and concepts, developed the numerical models, wrote the code of simulations, interpreted the results, wrote the manuscript and acted as a corresponding author.		
Overall percentage (%)	70%		
Certification:	This paper reports on original research I conducted at the University of Adelaide and is not subject to any obligations or contractual agreements with a third party that would constrain its inclusion in this thesis. I am the primary author of this paper.		
Signature		Date	27/08/2019

Co-Author Contributions

By signing the Statement of Authorship, each author certifies that:

i. the candidate's stated contribution to the publication is accurate (as detailed above);

ii. permission is granted for the candidate in include the publication in the thesis; and

iii. the sum of all co-author contributions is equal to 100% less the candidate's stated contribution.

Name of Co-Author	Nataliia Sergiienko		
Contribution to the Paper	Helped to develop the mathematical model of the three-tether point absorber, helped in interpretation of obtained results.		
Signature	7.5%	Date	27/08/2019

Name of Co-Author	Fantai Meng		
Contribution to the Paper	Helped to develop the mathematical model of the single-tether point absorber with asymmetric mass distribution, helped in interpretation of obtained results.		
Signature	7.5%	Date	21/8/19

Name of Co-Author	Benjamin Cazzolato		
Contribution to the Paper	Supervised the work, helped in interpretation of obtained results, and provided a critical revision of the manuscript.		
Signature	5%	Date	27/8/19

Name of Co-Author	Peter Hardy		
Contribution to the Paper	Helped in interpretation of obtained results, and provided a critical revision of the manuscript.		
Signature	5%	Date	28/8/19

Name of Co-Author	Maziar Arjomandi		
Contribution to the Paper	Helped in interpretation of obtained results, and provided a critical revision of the manuscript.		
Signature	5%	Date	27/08/2019

Please cut and paste additional co-author panels here as required.

Enhancing the relative capture width of submerged point absorbing wave energy converters

Boyin Ding[1], Nataliia Sergiienko[2], Fantai Meng[3], Benjamin Cazzolato, Peter Hardy, and Maziar Arjomandi

Ocean Wave Energy Research Group, School of Mechanical Engineering, the University of Adelaide
South Australia, Australia, 5005

[1]boyin.ding@adelaide.edu.au

[2]nataliia.sergiienko@adelaide.edu.au

[3]fantai.meng@adelaide.edu.au

***Abstract*— Point absorbing wave energy converters account for 53% of the existing wave energy converter prototype designs. Generally, point absorbers are designed to operate on or just below the water surface, extracting wave power from the heaving motion. In recent years, an increasing amount of attention has been given to fully submerged point absorbers that demonstrate better survivability under storm conditions and capability of extracting wave power from motion in multiple degrees of freedom. This paper investigates three submerged point absorber designs operating in three degrees of freedom: a generic axisymmetric spherical buoy with a single tether power-take-off; and two modified types, one employing an asymmetric mass distribution buoy and the other employing a three tether power-take-off arrangement. Simulations in the frequency domain were used to study the behaviour of the three point absorber designs from the perspectives of dynamic response, power absorption principles and capabilities, and power-take-off requirements. Compared to the generic single tether spherical buoy design, both modified submerged point absorber designs demonstrate considerable improvements in their performance indices (e.g. the relative capture width and the power to PTO force ratio), while exhibit additional challenges in their implementations.**

***Keywords*— Point absorber, submerged wave energy converter, multiple degrees of freedom oscillation, optimal power-take-off**

I. INTRODUCTION

Ocean wave energy has been under the public spotlight over the past few decades for its high energy density, predictability, and consistency. It has shown a great potential to address the increasing global energy demand, with recent estimates suggesting a global wave energy capacity exceeding 2TW [1]. However, wave energy converter (WEC) technologies that extract energy from ocean waves are still in their pre-commercial phase and exhibit great diversity in design, leading to more than one thousand different WEC prototypes in various stage of development [2].

Oscillating point absorbing wave energy converters (PAs), a popular type of WEC designs defined by having geometry smaller than a wavelength, account for 53% of the existing WEC prototypes [3]. PAs are usually designed as axisymmetric buoys which are insensitive to wave direction change [1]. They typically operate offshore in deep water waves with higher energy content than shallow water waves [4]. Budal and Falnes [5], and Evans [6] found that given unconstrained motion, the maximum capture width of the oscillating body does not depend on its size, shape or submergence depth, but is only governed by the mode of motion. An axisymmetric body needs to oscillate in at least two modes, one radiating symmetric waves such as heave and the other radiating antisymmetric waves such as surge, to absorb the maximum available power from waves [7], [8].

Sergiienko et al. [9] compared the power absorption capability of floating and fully submerged PAs under physical motion constraints [9]. Results showed that in comparison with floating PAs, fully submerged PAs generally absorb less power from the heaving mode, but absorb similar amount of power from the combined heaving and surging modes. Furthermore, fully submerged PAs experience less wave excitation force and therefore exhibit higher durability and survivability than floating counterparts. Therefore, a submerged PA operating in multiple degrees of freedom has a potential to resolve the trade-off between power absorption capability and survivability in WEC design.

Buoys are typically submerged in water by a single tether anchored to the seabed (bottom-reference [10]) with a power-take-off (PTO) machinery installed along the tether that converts mechanical power due to buoy oscillation into electricity, as illustrated in Fig. 1(a). Anchored by a tether and excited by a plane wave, the buoy is able to move in three degrees of freedom (3DoF), namely heave, surge and pitch [11]. However, the majority of the wave power is absorbed from the buoy's heave motion arising from the kinematic constraint of the single tether PTO arrangement, where PTO is aligned with the heave motion predominantly. The authors of this paper have previously investigated two submerged PA design variants that are capable of extracting wave energy from the buoy's 3DoF oscillations. The first prototype employs a buoy with asymmetric mass distribution as shown in Fig. 1(b), with the

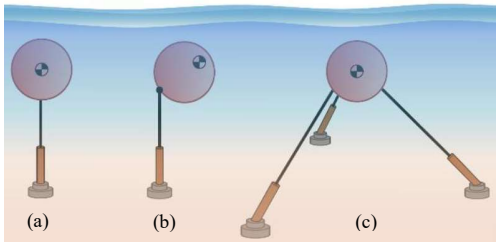

Fig. 1 Tether anchored (bottom fixed) submerged point absorber variants

goal of enhancing dynamic coupling between the buoy's oscillating modes and consequently absorbing power from surge by exploiting the surge-pitch and pitch-heave couplings [12]. The second prototype applies a three-tether PTO arrangement in tripod formation as shown in Fig. 1(c), originally proposed by Srokosz in 1979 [13]. The three-tether PTO can enhance kinematic coupling between the buoy's oscillating modes and the PTO units along the tethers, and therefore more efficiently convert the buoy's 3DoF motion into PTO work [14]-[16]. The two submerged PA variants can absorb 2-3 times more power than the single-tether generic PA in theory [12], [14], however, their engineering characteristics (e.g. optimal design maximising economic efficiency and PTO implementation) remain insufficiently explored for a commercialisation.

This paper conducts a comparison study between the three PA prototypes shown in Fig. 1, in order to better understand their dynamic response, power absorption efficiency, and optimal PTO design requirement, with an effort to provide insights into their engineering merits and economic viability relative to each other. The comparison is undertaken using numerical simulations based on the dynamic models of the PAs in the frequency-domain built upon linear wave theory. The layout of the paper is as follows: Section II describes the systems and their equations of motion, Section III discusses the simulation results and Section IV provides a summary of the results.

II. System Description and Motion Equation

This study considers spherical buoys only for simplicity, particularly for the ease of analysis on a buoy with asymmetric mass distribution as shown in Fig. 2. In order to exclude uncertainties associated with a specific PTO design, it is presumed that the machinery force has linear spring and damper effects proportional to the tether elongation and the rate of change of the tether elongation, respectively. The tether stiffness is assumed to be at least two orders of magnitude higher than the PTO spring stiffness and therefore is regarded as a rigid component in the system. Linear wave theory is used to model the hydrodynamics of the PAs [9], and only monochromatic plane waves are considered. Therefore, the dynamics of the PAs can be simplified to a planar case of 3DoF motion and investigated in the frequency-domain.

A. Equation of Motion for Submerged Point Absorber

An oscillating body excited by a plane incident wave can be modelled based on the Cummins equation [17]:

$$(\mathbf{M}+\mathbf{A}_\infty)\ddot{\mathbf{x}}+\int_0^t \mathbf{K}_{rad}(t-\tau)\dot{\mathbf{x}}(\tau)d\tau=\mathbf{F}_{h/stat}+\mathbf{F}_d+\mathbf{F}_{exc}+\mathbf{F}_{pto}, \quad (1)$$

where the vector $\mathbf{x}$ contains the surge displacement x, heave displacement z and pitch angle θ of the body at its geometrical centre; $\mathbf{M}$ is the mass matrix of the oscillating body; $\mathbf{A}_\infty$ is the hydrodynamic added mass existing at infinite frequency; $\mathbf{K}_{rad}(t)$ is the radiation impulse response function; and $\mathbf{F}_{h/stat}$, $\mathbf{F}_d$, $\mathbf{F}_{exc}$, and $\mathbf{F}_{pto}$ are the hydrostatic, viscous drag, wave excitation and PTO forces exerted on the body in Cartesian space, respectively.

As the buoy is fully submerged, the generalised hydrostatic force is

$$\mathbf{F}_{h/stat}=[0 \quad (\rho V-m)g \quad 0]^{\mathrm{T}}, \quad (2)$$

where ρ is the density of water, m and V are the mass and volume of the buoy respectively, and g is the gravitational acceleration.

The viscous drag forces experienced by the buoy can be written as quadratic functions of the buoy velocity, based on the Morison equation [18]:

$$\mathbf{F}_d=\begin{pmatrix}-0.5\rho C_{Dx}A_x|\dot{x}|\dot{x}\\ -0.5\rho C_{Dz}A_z|\dot{z}|\dot{z}\\ -0.5\rho C_{D\theta}D^4D|\dot{\theta}|\dot{\theta}\end{pmatrix}, \quad (3)$$

where C_{Dx}, C_{Dz}, and $C_{D\theta}$ are the viscous drag coefficients of the buoy along surge, heave and pitch axes respectively, whose values can be found from [19] for various buoy shapes; A_x and A_z are the cross sectional areas of the buoy along surge and heave axes respectively; D is the diameter of the buoy. For the spherical buoy, $C_{Dx}=C_{Dz}$; $C_{D\theta}=0$; and $A_x=A_z=\pi r^2$, where r is the radius of the buoy.

The PTO force exerted on the body is given by

$$\mathbf{F}_{pto}=\mathbf{J}(\mathbf{x})^{-\mathrm{T}}\mathbf{F}_t, \quad (4)$$

where $\mathbf{J}(\mathbf{x})^{-\mathrm{T}}$ is the transpose of an inverse Jacobian matrix $\mathbf{J}^{-1}$ that relates the PTO force in the joint space $\mathbf{F}_t$ (along the tether/s) to the PTO force in the task space $\mathbf{F}_{pto}$ (along the buoy Cartesian coordinates), and is dependent on buoy position. $\mathbf{F}_t$ consists of a static pretension force that overcomes the buoy's hydrostatic force; a spring force proportional to the tether elongation; and a damping force proportional to the rate of change of tether elongation. The forms of $\mathbf{J}^{-1}$ and $\mathbf{F}_t$ are dependent on the specific PA design and will be discussed in more details for each of the PA candidates in later subsections.

Assuming small displacements of the buoy with respect to the tether length, Equation (1) can be linearised at the nominal/rest position of the buoy, $\mathbf{x}_0=[0 \quad 0 \quad 0]^{\mathrm{T}}$, and thus can be written in the following frequency-domain form [10]:

$$\big(\mathbf{M}+\mathbf{A}(\omega)\big)\hat{\ddot{\mathbf{x}}}+\big(\mathbf{B}_{rad}(\omega)+\mathbf{B}_d(\omega)+\mathbf{B}_{pto}\big)\hat{\dot{\mathbf{x}}}+\mathbf{K}_{pto}\hat{\mathbf{x}}=\hat{\mathbf{F}}_{exc}(\omega). \quad (5)$$

For a spherical buoy,

$$\mathbf{A}(\omega)=\begin{pmatrix}a_{11}(\omega) & 0 & 0\\ 0 & a_{33}(\omega) & 0\\ 0 & 0 & 0\end{pmatrix},$$

$$\mathbf{B}_{rad}(\omega)=\begin{pmatrix}b_{11}(\omega) & 0 & 0\\ 0 & b_{33}(\omega) & 0\\ 0 & 0 & 0\end{pmatrix},$$

$$\mathbf{B}_d(\omega)=\begin{pmatrix}b_s(\omega) & 0 & 0\\ 0 & b_h(\omega) & 0\\ 0 & 0 & 0\end{pmatrix},$$

$$\hat{\mathbf{F}}_{exc}(\omega)=\begin{pmatrix}\hat{F}_s(\omega)\\ \hat{F}_h(\omega)\\ 0\end{pmatrix}, \quad (6)$$

where a_{ii} and b_{ii} denote the frequency-dependent hydrodynamic coefficients (added mass and radiation damping respectively) of the buoy at its rest position; b_s and b_h are the frequency and buoy velocity dependent viscous damping

coefficients along surge and heave axes respectively, which are approximated from Equation (3) using Lorentz linearisation [20]; $\hat{F}_s$ and $\hat{F}_h$ represent the wave excitation force along surge and heave axes of the buoy. The superscript $\hat{}$ denotes the complex amplitudes. The hydrodynamic coefficients and the wave excitation forces can be calculated using boundary element solvers such as WAMIT, AQWA and NEMOH for any buoy shapes. For submerged spherical buoys, a_{ii}, b_{ii}, $\hat{F}_s$ and $\hat{F}_h$ can be calculated using an analytical method described in [21]. $\mathbf{M}$, $\mathbf{B}_{pto}$, and $\mathbf{K}_{pto}$ in Equation (5) are dependent on the specific PA design and thus will be discussed in the later subsection for each PA candidate. The hydrostatic force disappears in Equation (5) as it is cancelled by the PTO pretension force.

B. Generic Single Tether Point Absorber

For the generic single tether PA design shown in Fig. 1(a), the PTO force along the tether is

$$F_t = C_{pto} - B_{pto}\Delta\dot{l} - K_{pto}\Delta l, \tag{7}$$

where $C_{pto} = -(\rho V - m)g$ is a pretension (offset) force that counteracts the buoyancy/hydrostatic force along the z-axis; B_{pto} and K_{pto} are the PTO stiffness and damping respectively; Δl is the tether/PTO elongation. The inverse Jacobian matrix of the system $\mathbf{J}^{-1}$ is described in [11] and is not repeated here.

Applying linearisation to the PA system at its nominal/rest position (for more details about the linearisation procedure, please refer to [16]), the following mass and PTO damping and stiffness matrices associated with Equation (5) are obtained:

$$\mathbf{M} = \begin{pmatrix} m & 0 & 0 \\ 0 & m & 0 \\ 0 & 0 & I_{yy} \end{pmatrix},$$

$$\mathbf{B}_{pto} = \begin{pmatrix} 0 & 0 & 0 \\ 0 & B_{pto} & 0 \\ 0 & 0 & 0 \end{pmatrix},$$

$$\mathbf{K}_{pto} = \begin{pmatrix} -C_{pto}/l_0 & 0 & C_{pto}r/l_0 \\ 0 & K_{pto} & 0 \\ C_{pto}r/l_0 & 0 & -C_{pto}r(l_0+r)/l_0 \end{pmatrix}, \tag{8}$$

where I_{yy} is the moment of inertia of the buoy about the pitch (y) axis; r and l_0 denote the radius of the spherical buoy and the nominal tether length at the rest pose of the buoy respectively. Equation (8) shows that the PTO control is directly applied to the heave mode only.

At the nominal position of the buoy, the elongation velocity of the tether/PTO is given by

$$\Delta\hat{\dot{l}} = \mathbf{J}(\mathbf{x}_o)^{-1}\hat{\dot{\mathbf{x}}} = (0 \quad 1 \quad 0)\hat{\dot{\mathbf{x}}}, \tag{9}$$

where $\mathbf{J}(\mathbf{x}_o)^{-1}$ is the inverse Jacobian matrix at the buoy nominal position. The time-averaged absorbed power by the system is then equal to the mechanical power dissipated by the linear PTO damper on the tether:

$$P_a = \frac{1}{2}B_{pto}\left|\Delta\hat{\dot{l}}\right|^2. \tag{10}$$

C. Asymmetric Mass Distribution Point Absorber

The purpose of having an asymmetric mass distribution (AMD) PA as shown in Fig. 1(b) is to enhance dynamic coupling between the oscillating modes of the buoy, with the aim to increase power absorption by the surge mode.

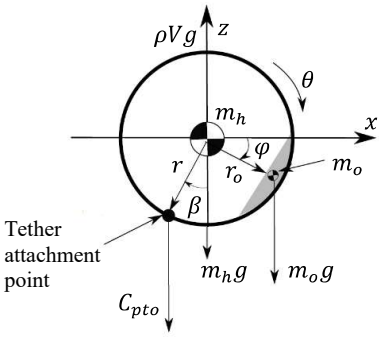

Fig. 2 Schematic showing the x-z plane of a spherical buoy with asymmetric mass distribution at its rest position.

Fig. 2 shows a cross section view of a spherical buoy with asymmetric mass distribution, on the x-z plane that the buoy is symmetric about. A body-fixed coordinate frame is located at the geometric centre of the buoy. The buoy consists of a spherical hull with a radius r and a mass m_h, and an additional mass m_o offset from the geometric centre of the buoy, resulting in an eccentric buoy centre of gravity on the x-z plane. The location of m_o on the x-z plane is defined by the offset distance r_o and the offset angle φ with respect to the positive x-axis. For the buoy to remain at rest in calm water, the PTO pretension (offset) force is given by

$$C_{pto} = -(\rho V - m_h - m_o)g. \tag{11}$$

In addition, in order to balance the torque generated by the offset mass about the geometric centre of the buoy, the tether attachment point is rotated clockwise around the surface of the hull on the x-z plane. The line passing through the geometric centre of buoy and the tether attachment point forms an angle β with respect to the negative z-axis, which can be calculated by solving

$$C_{pto} \cdot r\sin(\beta) = m_o g \cdot r_o \cos(\varphi). \tag{12}$$

A similar linearisation procedure is applied to the AMD PA, as detailed in [16]. The resulting mass, PTO damping and stiffness matrices associated with Equation (5) are given by:

$$\mathbf{M} = \begin{pmatrix} m_h + m_o & 0 & -m_o r_o \sin(\varphi) \\ 0 & m_h + m_o & -m_o r_o \cos(\varphi) \\ -m_o r_o \sin(\varphi) & -m_o r_o \cos(\varphi) & I_{yy,o} \end{pmatrix},$$

$$\mathbf{B}_{pto} = \begin{pmatrix} 0 & 0 & 0 \\ 0 & B_{pto} & B_{pto} r\sin(\beta) \\ 0 & B_{pto} r\sin(\beta) & B_{pto} r^2 \sin^2(\beta) \end{pmatrix},$$

$$\mathbf{K}_{pto} = \begin{pmatrix} -C_{pto}/l_0 & 0 & C_{pto} r\cos(\beta)/l_0 \\ 0 & K_{pto} & K_{pto} r\sin(\beta) \\ C_{pto} r\cos(\beta)/l_0 & K_{pto} r\sin(\beta) & \begin{pmatrix} -C_{pto} r\cos(\beta)\,(l_0 + r\cos(\beta))/l_0 \\ -m_o g r_o \sin(\varphi) + K_{pto} r^2 \sin^2(\beta) \end{pmatrix} \end{pmatrix} \tag{13}$$

Compared with the same matrices for the generic case in Equation (8), $\mathbf{M}$, $\mathbf{B}_{pto}$, and $\mathbf{K}_{pto}$ in Equation (13) exhibit additional couplings (e.g. heave-pitch and surge-pitch) due to the asymmetric mass distribution.

At the nominal position of the buoy (as shown in Fig. 2), the elongation velocity of the tether/PTO is given by

$$\Delta\hat{l} = \mathbf{J}(\mathbf{x}_o)^{-1}\hat{\mathbf{x}} = (0 \quad 1 \quad r\sin(\beta))\hat{\mathbf{x}}. \tag{14}$$

The inverse Jacobian matrix shows that both the heave and pitch modes directly couple to the tether/PTO elongation. The time-averaged absorbed power of the asymmetric mass distribution system is also given by Equation (10).

D. Three Tether Point Absorber

The purpose of having the three-tether PTO arrangement is to enhance kinematic coupling between the oscillating modes of the buoy and the PTO units along the tethers, allowing more efficient conversion of the buoy 3DoF motion into PTO work.

Fig. 3 illustrates a schematic of a three-tether point absorber at its rest pose, where the tethers are equally distributed around the buoy, separated by 120° in the horizontal plane. This configuration makes the system insensitive to wave direction. Tether 1 aligns with the x-z plane, and thus the wave travelling direction, and tethers 2 and 3 are symmetric about the x-z plane. In this paper, it is assumed that all three tethers point towards the geometric centre of the spherical buoy and the PTO units along the three tethers have identical linear characteristics (e.g. pretension force, PTO damping and stiffness). The tether attachment points are located on the surface of the buoy hull. The inclination angle of the tethers with respect to the z-axis, α, plays an important role in this design as it defines the contribution of the surge and heave modes in the total absorbed power, as well as the effects of PTO control on the surge and heave modes. The PTO force along each tether is

$$F_{t,i} = C_{pto}/3\cos(\alpha) - B_{pto}\Delta\dot{l}_i - K_{pto}\Delta l_i, \tag{15}$$

where $C_{pto}/3\cos(\alpha)$ is the pretension (offset) force generated by the PTO unit on each tether. The three PTO units jointly provide a total pretension force C_{pto} along the z-axis that counteracts the buoyancy/hydrostatic force of the buoy.

The three tether PA has a mass matrix identical to the generic single tether PA. Following the linearistion procedure reported in [14], the PTO damping and stiffness matrices for the three tether PA can be derived as shown in Equation (16). Compared with the same matrices for the single tether case in Equations (8) and (13), $\mathbf{B}_{pto}$ and $\mathbf{K}_{pto}$ in Equation (16) demonstrate additional PTO control directly applied to the surge mode, enabled by inclining the tether by α.

$$\mathbf{B}_{pto} = \begin{pmatrix} \frac{3}{2}B_{pto}\sin^2(\alpha) & 0 & 0 \\ 0 & 3B_{pto}\cos^2(\alpha) & 0 \\ 0 & 0 & 0 \end{pmatrix}, \tag{16}$$

$$\mathbf{K}_{pto} = \begin{pmatrix} \left(\frac{3}{2}\sin^2(\alpha)\left(K_{pto} + \frac{C_{pto}}{3l_0\cos(\alpha)}\right)\right) & 0 & C_{pto}r/l_0 \\ & & \\ 0 & \left(3\cos^2(\alpha)\left(K_{pto} + \frac{C_{pto}}{3l_0\cos(\alpha)}\right)\right) & 0 \\ & & \\ C_{pto}r/l_0 & 0 & \frac{-C_{pto}r(l_0+r)(\cos^2(\alpha)+1)}{2l_0\cos(\alpha)} \end{pmatrix}.$$

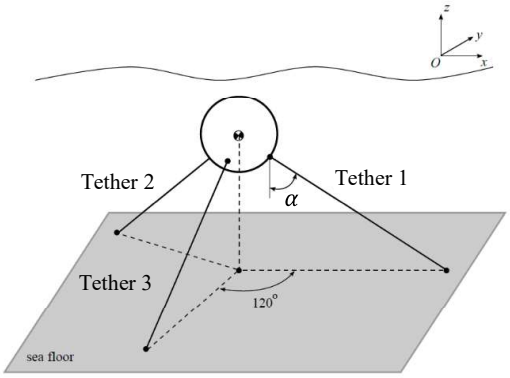

Fig. 3 Schematic showing a three-tether point absorber with a submerged spherical buoy at its rest pose

At the nominal position of the buoy (as shown in Fig. 3), the elongation velocities of the tethers/PTOs are given by

$$\Delta\hat{\boldsymbol{l}} = \begin{pmatrix} \Delta\hat{l}_1 \\ \Delta\hat{l}_2 \\ \Delta\hat{l}_3 \end{pmatrix} = \mathbf{J}(\mathbf{x}_o)^{-1}\hat{\mathbf{x}} = \begin{pmatrix} -\sin(\alpha) & \cos(\alpha) & 0 \\ \sin(\alpha)/2 & \cos(\alpha) & 0 \\ \sin(\alpha)/2 & \cos(\alpha) & 0 \end{pmatrix}\hat{\mathbf{x}}. \tag{17}$$

The inverse Jacobian matrix shows that both the surge and heave modes directly couple to the tether/PTO elongations. The time-averaged absorbed power is equal to the mechanical power dissipated by the three PTO units:

$$P_a = \sum_{i=1}^{3}\frac{1}{2}B_{pto}\left|\Delta\hat{l}_i\right|^2. \tag{18}$$

E. Power Absorption and Optimal Condition

The time-averaged absorbed power can also be calculated in the Cartesian coordinates as the difference between the wave power input into the system and the power radiated and dissipated in water [6]:

$$P_a = \frac{1}{4}\left(\hat{\mathbf{F}}_{exc}^{*}\hat{\mathbf{x}} + \hat{\mathbf{x}}^{*}\hat{\mathbf{F}}_{exc}\right) - \frac{1}{2}\hat{\mathbf{x}}^{*}(\mathbf{B}_{rad} + \mathbf{B}_d)\hat{\mathbf{x}}, \tag{19}$$

where $*$ denotes the conjugate transpose. Furthermore, the total absorbed power can be decomposed into power absorption by the surge and heave modes respectively:

$$P_{a,s} = \frac{1}{4}\left(\hat{F}_s^{*}\hat{x} + \hat{x}^{*}\hat{F}_s\right) - \frac{1}{2}\hat{x}^{*}(b_{11} + b_s)\hat{x},$$
$$P_{a,h} = \frac{1}{4}\left(\hat{F}_h^{*}\hat{z} + \hat{z}^{*}\hat{F}_h\right) - \frac{1}{2}\hat{z}^{*}(b_{33} + b_h)\hat{z}. \tag{20}$$

For a spherical buoy, there is neither excitation torque nor hydrodynamic damping on its rotational axis. Therefore, the power absorption from the pitch mode of the buoy is zero.

Maximum power is absorbed when the velocity of the buoy is unconstrained and equal to:

$$\hat{\mathbf{x}}_{opt} = \frac{1}{2}(\mathbf{B}_{rad} + \mathbf{B}_d)^{-1}\hat{\mathbf{F}}_{exc}, \quad (21)$$

which is the optimal velocity. Equation (21) shows that the buoy optimal velocity is in phase with the excitation force and of optimal amplitude scaled by the damping coefficients [8]. The maximum power available in the surge and heave modes by an axisymmetric body in monochromic waves are:

$$P_{a,s}^{rad} = 2J_t/k,$$
$$P_{a,h}^{rad} = J_t/k, \quad (22)$$

where J_t denotes the power transport per unit width of the wave frontage and k denotes the wavenumber [8]. The superscript rad denotes the power limit of the mode governed by the radiation ability of the mode oscillating at the optimal velocity.

The relative capture width (RCW) is a measure of the efficiency of the WEC device with respect to its size and is given by

$$\text{RCW} = P_a/(2rJ_t). \quad (23)$$

F. Optimisation of Absorbed Power

In order to have a fair comparison of the power absorption capability of the three PAs, it is assumed that all PAs have the same size of buoy and physical constraints, and are located at the same submergence depth but operate under their own optimal PTO configurations, which are wave frequency dependent. Therefore, the optimisation goal is to maximise P_a subject to constraints by seeking the frequency-dependent optimal $\mathbf{B}_{pto}$ and $\mathbf{K}_{pto}$ matrices.

For the single tether PAs, $\mathbf{B}_{pto}$ and $\mathbf{K}_{pto}$ are governed by K_{pto}, B_{pto}, l_0, and C_{pto}, where C_{pto} is set to overcome the hydrostatic force and thus is a fixed value, whilst the other three PTO parameters can be tuned to achieve optimality. l_0 can be physically changed increasing the height of the mooring above the ocean floor, however, a discussion on how specific designs impact on hydrodynamics, and resulting economic viability is out of the scope of the current paper. Substituting Equations (6), (8) and (13) into Equation (5), ignoring all the off-diagonal/coupling terms and comparing with Equation (21), the theoretical optimal values of K_{pto}, B_{pto} and l_0 can be found for the single tether PAs:

$$K_{pto,t} = \big(m + a_{33}(\omega)\big)\omega^2,$$
$$B_{pto,t} = b_{33}(\omega) + b_h(\omega),$$
$$l_{0,t} = C_{pto}/\big[\big(m + a_{11}(\omega)\big)\omega^2\big], \quad (24)$$

where $K_{pto,t}$ and $B_{pto,t}$ achieve the optimal phase (resonance) and amplitude conditions for the decoupled heave mode; $l_{0,t}$ achieves the resonance condition for the decoupled surge mode, implying that for small buoy displacements the surge mode of the bottom-referenced single tether PA is analogous to an inverted pendulum. The theoretical optimal values in Equation (24) do not represent the real optimal values for the systems because dynamic coupling is ignored and physical constraints are not considered. However, they can be used as an initial guess for the PTO optimisation. The optimisation goal for the single tether PAs is then

$$\max\{P_a(K_{pto}, B_{pto}, l_0)\}, \quad (25)$$

subject to the nominal tether length constraint $l_{0,min} \le l_0 \le l_{0,max}$ and the tether elongation (PTO stroke) constraint $|\Delta\hat{l}| \le \Delta l_{max}$.

For the three tether system, $\mathbf{B}_{pto}$ and $\mathbf{K}_{pto}$ are predominantly governed by K_{pto}, B_{pto}, and α. l_0 is determined from the inverse kinematics of the system assuming the tethers are anchored at the sea floor as shown in Figure 3. The optimisation goal for the three tether PA is then

$$\max\{P_a(K_{pto}, B_{pto}, \alpha)\}, \quad (26)$$

subjected to the tether inclination angle constraint $0 \le \alpha \le 90^\circ$ and the PTO stroke constraint $|\Delta\hat{\boldsymbol{l}}| \le \Delta\boldsymbol{l}_{max}$. The initial value of α for optimisation is set to 55° based on the results in [9]. The initial values of K_{pto} and B_{pto} can be obtained from the following equations given known C_{pto}, α, and l_0:

$$\frac{3}{2}\sin^2(\alpha)\left(K_{pto,t} - \frac{C_{pto}}{3l_0\cos(\alpha)}\right) + \frac{C_{pto}}{l_0\cos(\alpha)} = \big(m + a_{11}(\omega)\big)\omega^2,$$
$$B_{pto,t} = 2\big(b_{11}(\omega) + b_s(\omega)\big)/3\sin^2(\alpha_a), \quad (27)$$

which respectively satisfy the optimal phase and amplitude conditions for the decoupled surge mode. We take the priority to tune the system to be optimal in the surge mode because it contains twice power compared to the heave mode for unconstrained buoy motion as shown in Equation (22). Optimisation is implemented using the *fmincon* command in MATLAB Optimisation Toolbox.

G. System Parameters for Simulation

Simulation parameters are listed in Table 1. The buoys for the three PAs are assumed to have the same geometrical shape (sphere), size (radius), and weight (total mass), and are submerged at the same water and submergence depth. The buoy with asymmetric mass distribution has identical hull mass and offset mass, with the offset mass located at a near-optimal location [16]. The buoy hull is assumed to be hollow so that PTO circuits and control instruments can be placed inside. For the single tether PAs, their nominal tether length is constrained between 5m and 50m in optimisation, defined to ensure the fidelity of the optimisation results without taking the feasibility of the specific design into consideration. Maximum PTO stroke of 3m is applied to all systems to prevent the buoy from breaking the water surface, and thus to constrain the problem within the boundaries of linear wave theory. Simulations were run across frequencies between 0.3 and 1.6 rad/s. By default, 0.1m wave amplitude is used unless otherwise stated. PTO optimisation is conducted at each wave frequency for the three PAs, following the procedures discussed in Section II.F.

TABLE I SYSTEM PARAMETERS FOR SIMULATION

Symbol	Value/unit	Description
d_w	50m	Water depth of the sea
h_s	8.5m	Submergence depth from buoy geometric centre to water surface
r	5m	Radius of the spherical buoy
m	2.68×10^5kg	Buoy mass, defined as half of the buoy buoyancy force $m = \rho V/2$

m_h	1.34×10^5kg	Hull mass for the buoy with asymmetric mass distribution
m_o	1.34×10^5kg	Offset mass for the buoy with asymmetric mass distribution
r_o	4m	Offset distance of the offset mass m_o
φ	30°	Offset angle of the offset mass m_o
I_{yy}	4.472×10^6kg.m^2	Moment of inertia of a hollow spherical buoy about its pitch axis, given by $I_{yy} = \frac{2}{3}mr^2$
$I_{yy,o}$	4.383×10^6kg.m^2	Moment of inertia of a hollow spherical buoy with offset mass about its pitch axis, given by $I_{yy,o} = \frac{2}{3}m_h r^2 + m_o {r_o}^2$
$l_{0,min}$, $l_{0,max}$	5m, 50m	Nominal tether length limits for the single tether systems
Δl_{max}	3m	Tether elongation constraint (PTO maximum stroke)
ω	0.3-1.6rad/s	Wave frequency range (regular)
A_w	0.1m	Wave amplitude (regular)

III. Results

This section presents and discusses results categorised into six main aspects that are critical from an engineering perspective: optimal PTO parameters, dynamic response, power absorption, PTO force, power to PTO force ratio, and bandwidth. For convenience, the generic single tether PA, the asymmetric mass distribution PA, and the three tether PA are abbreviated as the *G1T*, the *AMD* and the *3T* respectively.

A. Optimal PTO Parameters

A comparison of the frequency-dependent optimal PTO parameters for the three PAs is shown in Fig. 4. With regard to the G1T, its optimised nominal tether length fluctuates randomly between the defined limits across the wave frequencies (not displayed in the figure) which implies that its power absorption does not depend on the surge (inverted pendulum) mode. This outcome is expected for the G1T given there is no coupling between its surge mode and tether/PTO elongation as evident in Equations (8) and (9). Therefore, the nominal tether length of the G1T is fixed to $d_w - h_s - \mathrm{r} = 36.5$m across the wave frequencies, assuming the tether is anchored to the sea floor level and requires no tower. For the AMD, the optimal nominal tether length decreases sharply with an increase in wave frequency and reaches the lower limit at 0.72rad/s. By comparison, the 3T has its optimal tether inclination angle barely varying across the wave frequencies.

The G1T and the 3T have similar optimal PTO stiffness and damping that smoothly increase across the wave frequencies. The optimal stiffness and damping of the 3T are generally lower than the that of the G1T. In contrast, the AMD demonstrates much larger variations in its optimal PTO stiffness and damping across the wave frequencies, which indicates more challenges in its PTO design and manufacture. The optimal stiffness of the AMD is lower than the optimal stiffness of the G1T for low to medium frequency waves but is higher for high frequency waves. The optimal damping of the AMD is dramatically higher than the optimal damping of the G1T, in particular for low to medium frequency waves, where a peak difference of over one order of magnitude is observed. In the following subsections, results are presented for the PA candidates that operate under the frequency-dependent optimal PTO parameters as shown in Fig. 4, unless otherwise explicitly stated.

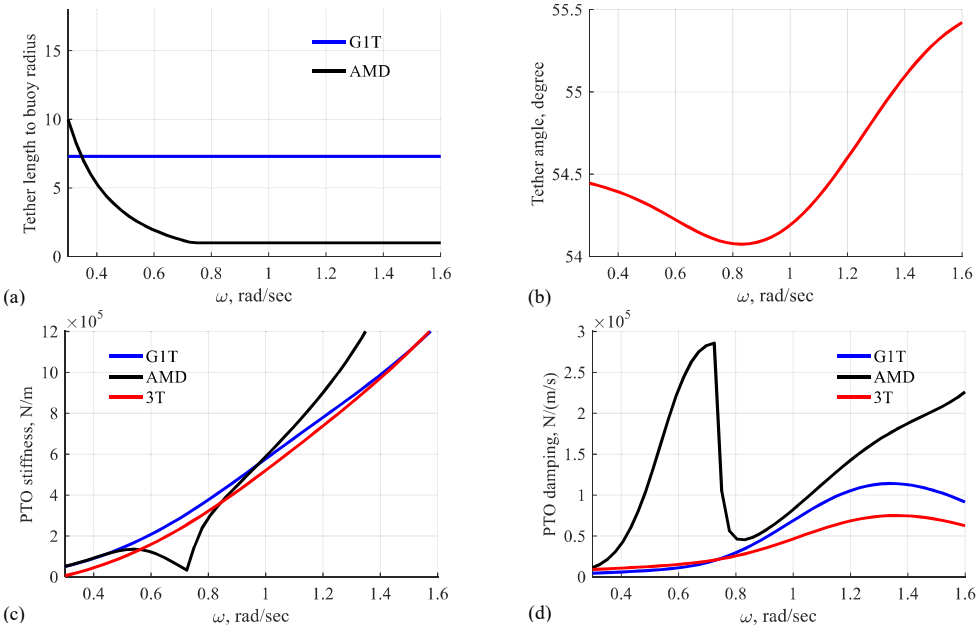

Fig. 4 Comparison of the frequency-dependent optimal PTO parameters for the three PAs: (a) optimal nominal tether length l_0 normalised by buoy radius for the G1T and the AMD; (b) optimal tether inclination angle for the 3T; (c) optimal PTO stiffness K_{pto}; (d) optimal PTO damping B_{pto}.

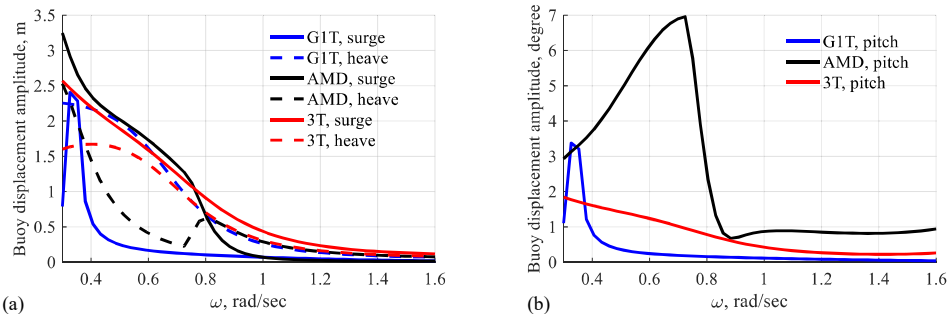

Fig. 5 Comparison of the buoy displacement amplitudes for the three PAs $|\hat{\mathbf{x}}|$ under their optimal PTO configurations: (a) surge displacement $|\hat{x}|$ and heave displacement $|\hat{z}|$; (b) pitch displacement $|\hat{\theta}|$.

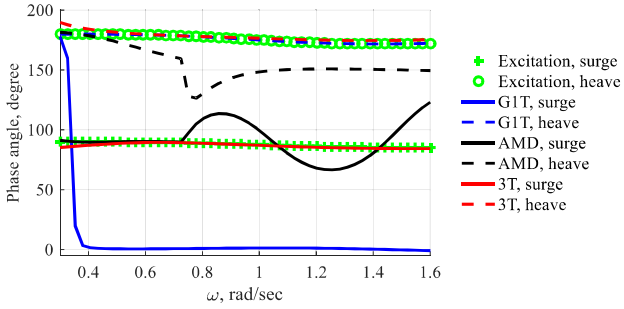

Fig. 6 Comparison between the buoy velocity phases $\angle\hat{\mathbf{x}}$ for the three PAs and the excitation force phases $\angle\hat{\mathbf{F}}_{exc}$

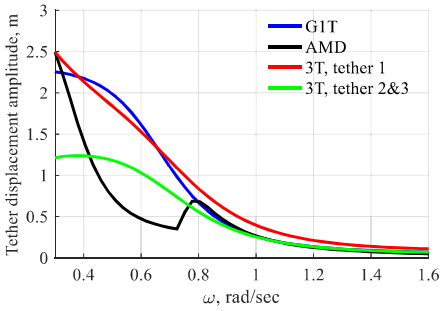

Fig. 7 Comparison of the tether elongation displacement amplitudes $|\Delta\hat{l}_i|$

B. *Dynamic Response*

A comparison of the buoy displacement amplitudes for the three PAs is shown in Fig. 5, while a comparison between the buoy velocity phases for the three PAs and the excitation force phases is shown in Fig. 6.

As was shown in the last subsection, the G1T can only absorb power from heave. Thus, the G1T has the buoy heave velocity in phase with the heave excitation force across the wave frequencies, indicating the buoy heave response reaches its resonance or optimal phase condition as shown in Equation (21), resulting in relatively large heave displacement across the wave frequencies. In contrast, the buoy surge velocity and the surge excitation force are only in phase at a single frequency of 0.3rad/s, and are almost 90° out of phase at other wave frequencies, resulting in a resonance peak at 0.3rad/s in the surge displacement. This is due to the fact that the nominal tether length of the G1T (that governs the surge natural frequency) is fixed across the wave frequencies. The resonance peak in the surge response also induces a peak in the pitch response via the surge-pitch coupling as shown by the stiffness matrix in Equation (8).

In comparison to the G1T, the 3T has both its surge and heave modes tuned to resonance across the wave frequencies, as evident in Fig. 6, where both its buoy surge and heave velocities are in phase with the surge and heave excitation forces across the wave frequencies. This results in relatively large surge and heave displacements across the frequencies. In contrast, the pitch response of the 3T is relatively small across the wave frequencies stabilised by the 3T configuration.

The AMD performance lies between the G1T and the 3T, and its surge and heave modes can only both be tuned to resonance for low frequency waves (below 0.45rad/s), where both the surge and heave displacements are relatively large. Between 0.45rad/s and 0.72rad/s, optimisation tunes the surge mode of the AMD in resonance as the surge mode contains more power than the heave mode. Thus, surge displacement is much larger than the heave displacement in this frequency range. Above 0.72rad/s, the surge (inverted pendulum) mode of the AMD can no longer be tuned to resonance because the nominal tether length reaches the lower limit. As a result, optimisation evaluates the available power in the surge mode and the heave mode to determine their contributions. An intersection between the surge and heave displacement curves at 0.8rad/s indicates that the AMD switches to extract more power from the heave mode. In comparison to the G1T and the 3T, the AMD has higher pitch response below 0.72rad/s because the AMD coverts power from its surge mode into PTO work via surge-pitch and heave-pitch couplings as indicated by Equation (13).

A comparison of the amplitudes of tether elongation displacements is shown in Fig. 7. For the G1T and the AMD, their tether elongation displacements are almost identical to the buoy heave displacements, due to their inverse kinematics at the nominal position of the buoy. The 3T has its first tether oscillating with amplitudes similar as that of the G1T, and its second and third tethers oscillating with amplitudes about two thirds that of the first tether. The AMD requires much less tether elongation than either the G1T or the 3T to absorb maximum power for low to medium frequency waves.

C. Power Absorption

A comparison of the RCWs of the three PAs is shown in Fig. 8. Also shown is the theoretical RCW limits of the heave mode and the combined surge and heave mode. The high frequency RCW limits are defined by the radiation ability of the buoy when operating at optimal velocity given unconstrained motion, calculated from Equations (22) and (23):

$$\mathrm{RCW}_s^{rad} = 2\mathrm{RCW}_h^{rad} = 1/(kr) \quad (28)$$

where the subscripts s and h denote the surge mode and the heave mode respectively. The low frequency RCW limits are defined by the maximum swept volume (MSV) of the buoy, given by the following equation for a submerged sphere:

$$\mathrm{RCW}_s^{msv} = \mathrm{RCW}_h^{msv} = \rho e^{-kh_s} d_{max} V A_w \omega^3/(2rJ_t) \quad (29)$$

where d_{max} denotes the maximum buoy displacement of the corresponding mode [9], and is set as 3m for both the heave mode and the surge mode to be consistent with the tether elongation constraint defined in optimisation.

The G1T has the lowest RCW among the three PAs and converges to the RCW_h^{rad} curve at high frequencies. The 3T has the highest RCW among the three PAs (2-3 times that of the G1T) that converges to the $\mathrm{RCW}_s^{rad} + \mathrm{RCW}_h^{rad}$ curve at high frequencies. The AMD performs between the G1T and the 3T, and has its RCW converge to the 3T curve at low frequencies and to the G1T curve at high frequencies. At low frequencies, the RCWs of the PAs are lower than the RCW_h^{msv} curve and the $\mathrm{RCW}_s^{msv} + \mathrm{RCW}_h^{msv}$ curve. This is because the calculations of the RCW^{msv} limits do not consider the effects of viscous loss. The linearised viscous damping is significantly higher than the radiation damping at low wave frequencies as shown in Fig. 9, which dissipates additional energy in water.

The RCW of each PA is decomposed into the RCWs of the surge mode and the heave mode using Equation (20), with results demonstrated in Fig. 10. The G1T purely absorbs power from its heave mode across the wave frequencies as expected. The 3T absorbs the same amount of power as the G1T from its heave mode and absorbs up to twice the power from its surge mode at high frequencies. The power absorbed by the surge mode and the heave mode of 3T are similar at low frequencies because the surge mode experiences more viscous losses than the heave mode, as shown in Fig. 9. The AMD exhibits power absorption behaviour matching its dynamic response behaviour shown in Fig. 6. For wave frequencies below 0.45rad/s, the power absorbed by the modes of the AMD are equal to those of the 3T. Between 0.45rad/s and 0.72rad/s, the power absorbed by the surge mode of the AMD is equal to that of the 3T, whilst the power absorbed by the heave mode of the AMD is less than that of the 3T. Above 0.72rad/s when the nominal tether length reaches the lower limit, the AMD decreases power absorption from its surge mode and increases power absorption from its heave mode with an increase in wave frequency, and trends towards the G1T at high frequencies.

The power absorption capabilities of the 3T and the AMD are compared under various wave amplitudes but subject to the same tether elongation constraint of 3m, with the q-factors denoting the ratio of the absorbed power by the 3T to the absorbed power by the AMD as shown in Fig. 11. In general, the 3T absorbs more power than the AMD, in particular for very

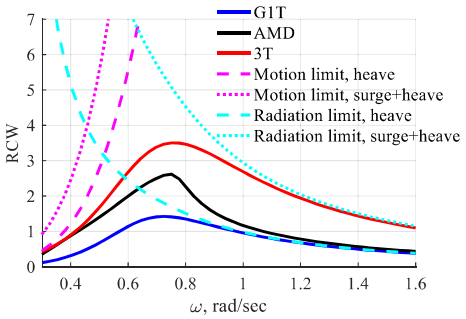

Fig. 8 Comparison of the RCWs of the three PAs (solid lines) and the RCW limits of the heave mode (dashed lines) and the combined surge and heave modes (dotted lines). The RCW limits in magenta and cyan are respectively defined by the maximum swept volume of the buoy and the radiation ability of the buoy given unconstrained motion.

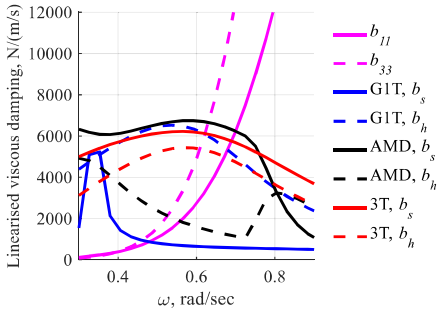

Fig. 9 Comparison of the radiation damping coefficients b_{11} and b_{33} and the linearised viscous damping coefficients b_s and b_h for the three PAs.

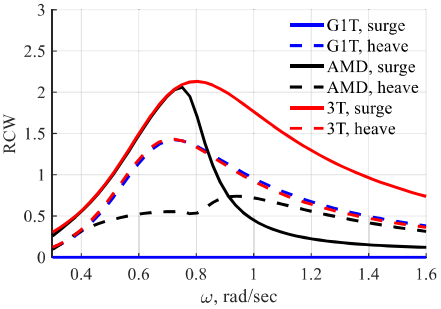

Fig. 10 Comparison of the RCWs associated with the individual modes.

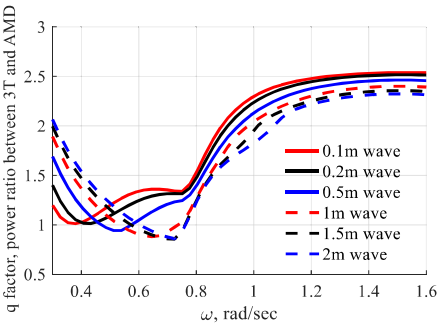

Fig. 11 Comparison of the q factors as an efficiency improvement ratio between power absorption from the 3T and the AMD for various wave amplitudes.

low and high frequency waves. For medium frequency waves, the q-factor decreases with an increase in wave amplitude, to less than unity. This is due to the fact that the 3T requires more tether elongation displacement than the AMD to absorb maximum power from medium frequency waves as evident in Fig. 7. Thus, excited by large waves, the 3T is more likely to reach its tether elongation constraint compared to the AMD.

D. PTO Force

A comparison of the dynamic PTO forces and the net PTO forces for the three PAs are shown in Fig. 12 and Fig. 13 respectively. The dynamic PTO force of the AMD is two to four times lower than that of the G1T at medium wave frequencies between 0.45rad/s and 0.72rad/s. This is because in this frequency range the AMD has lower optimal PTO stiffness and lower tether elongation displacement than those of the G1T, which leads to a significantly lower stiffness force. The average of the dynamic PTO forces on the tethers of the 3T is two to four times lower than the dynamic PTO force of the G1T at frequencies below 0.72rad/s. The dynamic PTO forces on the second and third tethers of the 3T are about two thirds of that on its first tether on average across the wave frequencies. For the three PAs, their net PTO forces are dominated by the pretension forces used to overcome the buoy buoyancy force when excited by small waves. The tethers of the 3T have a pretension force that is 60% of the pretension force of the G1T and the AMD due to the tripod formation of the 3T.

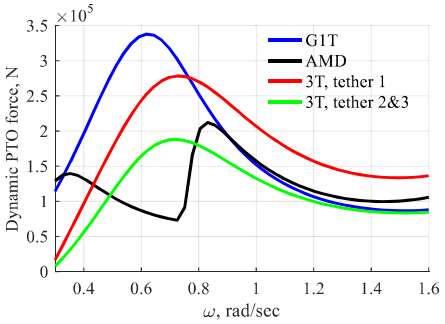

Fig. 12 Comparison of the dynamic (spring and damper) PTO forces

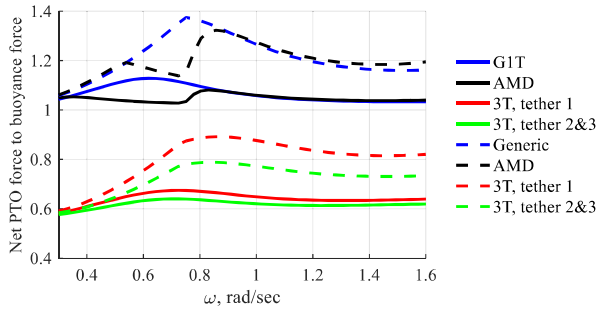

Fig. 13 Comparison of the net PTO force (sum of the PTO dynamic and pretension forces) normalised by the buoy buoyancy force. The solid lines denote results for 0.1m wave amplitude and the dashed lines denote results for 0.5m wave amplitude.

E. Power to PTO Force Ratio

The root mean square (RMS) of the net PTO force relates to the costs of the PTO and the mooring. Therefore, a cost-related performance index of power to PTO force ratio $P_a/F_{t,RMS}$ that indicates the cost of PTO and mooring facility per kW is used to assess the economic viability of the PAs. A comparison of this cost-related index is conducted for two wave amplitudes and across the wave frequencies, with the q-factors that correspond to the increase of $P_a/F_{t,RMS}$ between the PAs as shown in Fig. 14. The AMD has its power to PTO force ratio twofold that of the G1T for low to medium frequency waves that have high occurrence probability in most seas. For the 3T, its power to PTO force ratio is calculated in two ways for comparison: 1) the absorbed power divided by the RMS of the net PTO force on the first tether, assuming that the three tethers share a common PTO circuit and thus the RMS of the highest net PTO force among tethers indicates the whole PTO cost; 2) the absorbed power divided by the sum of the RMS of the net PTO forces on all tethers, assuming that the tethers employ uncoupled PTO units. When having uncoupled PTO units, the 3T has its power to PTO force ratio slightly higher than that of the G1T. However, if the desired PTO forces on the tethers can be achieved by a shared PTO circuit, the 3T has a power to PTO force ratio over three times higher than the G1T.

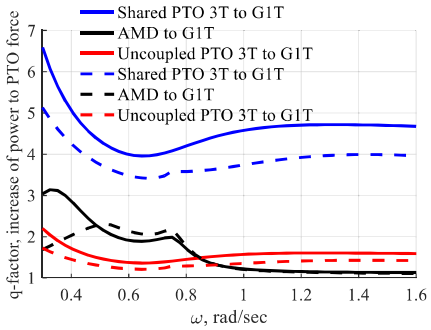

Fig. 14 Comparison of the q factors that correspond to the increase of the power to PTO force ratio between the PAs. The solid lines denote results for 0.1m wave amplitude and the dashed lines denote results for 0.5m wave amplitude.

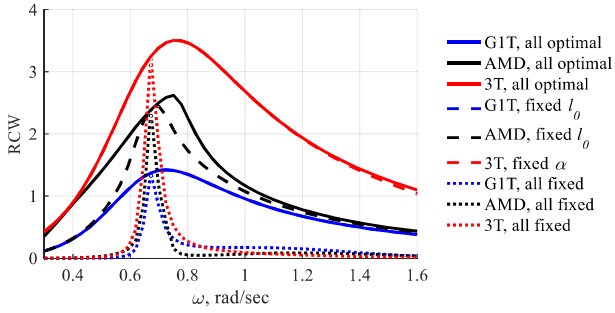

Fig. 15 Comparison of RCWs and bandwidths of the three PAs with: 1) fully optimal PTO parameters – frequency-dependent optimal K_{pto}, B_{pto}, l_0 or α (solid lines); 2) frequency-dependent optimal K_{pto} and B_{pto} but fixed l_0 or α only optimal at 0.67rad/s (dashed lines); 3) fully fixed PTO parameters – fixed K_{pto}, B_{pto}, l_0 or α only optimal at 0.67rad/s (dotted lines).

F. Absorption Bandwidth

Absorption bandwidth of the WEC corresponds to the frequency range where the absorbed power stays within 50% of its maximum value. It indicates the power absorption capability of the WEC in stochastic seas, where the wave frequency and amplitude vary continuously with time. Fig. 15 compares the absorption bandwidth of the three PAs operating with 1) frequency-dependent optimal PTO parameters (as used in the previous subsections); 2) frequency-dependent optimal PTO stiffness and damping but nominal tether length and tether inclination angle fixed to their optimal values for the 0.67rad/s wave; and 3) PTO parameters all fixed to their optimal values for the 0.67rad/s wave. 0.67rad/s (9.4s) wave was selected as it often occurs in sea. Fixing the nominal tether length and the tether inclination angle do not compromise the absorption bandwidth of the G1T or the 3T (about 0.7rad/s). In contrast, fixing the nominal tether length reduces the absorption bandwidth of the AMD from 0.45rad/s to 0.3rad/s. For all the PAs, their bandwidth is significantly reduced (to 0.1rad/s) when their PTO parameters are fully fixed. This implies that adaptive spring-damper control is necessary when the submerged PAs operate at a sea site with a broad wave occurrence spectrum.

IV. Conclusions

This paper conducted a comparison study in the frequency domain between thee submerged PA designs: a generic type as a benchmark and the other two with modified buoy and PTO designs to enhance RCWs. The linearised models for simulation assumed that the displacements of the buoys were small and considered the effects of viscous drag. Constraints were used in PTO optimisation to keep the models within the boundary of linear wave theory.

Results revealed the power absorption mechanisms of the two modified PA designs and compared their engineering characteristics to that of the generic single tether PA from the perspectives of dynamics response, power absorption capability, and PTO design requirements. In comparison to the G1T, the 3T is capable of extracting two to three times power from the combined surge and heave modes across the broad frequency range, given a fixed tether inclination angle set to the optimal value. The economic viability of the 3T largely depends on the feasibility in designing a shared PTO circuit to achieve the desired PTO forces on the three tethers. In contrast, the AMD depends on selecting the appropriate tether length to extract power from the surge mode. It compromises power absorption from the surge and the heave modes for medium frequency waves even if the PTO parameters are tuned to their optimal values. Nevertheless, it still extracts twice the power of the G1T in medium frequency waves. In comparison to the G1T and the 3T, the AMD exhibits larger variations in the optimal PTO parameters across the wave frequencies but demonstrates less requirements for the dynamic PTO force and the tether elongation displacement at medium frequencies. The economic viability of the AMD seems plausible but the costs associated with manufacturing an asymmetric mass distribution buoy and a tower to achieve the desired nominal tether length were ignored in this study. All the three submerged PAs require adaptive control to operate efficiently in stochastic seas. Future work will compare the PAs in stochastic seas in time-domain subject to directional waves.

Acknowledgment

This research was supported by the Linkage Project LP130100117 funded by the Australian Research Council and the Strategic Research Initiative Fund awarded by the Institute for Mineral and Energy Resources at the University of Adelaide.

References

[1] J. Cruz, *Ocean wave energy: Current status and future perspectives*, Green Energy and Technology, Springer Berlin Heieberg, Berlin, 2008.

[2] J. Hayward and P. Osman, "The potential of wave energy," Report, CSIRO, 2011.

[3] International Energy Agency, "Deploying renewables – Best and future policy practice," Report, International Energy Agency, 2011.

[4] B. Drew, A.R. Plummer, and M.N. Sahinkaya, "A review of wave energy converter technology," *In Proc. of the Institution of Mechanical Engineers, Part A: Journal of Power and Energy*, vol. 223, no. 8, pp. 887-902, 2009.

[5] K. Budal and J. Falnes, "A resonant point absorber of ocean-wave power," *Nature*, vol. 256, no. 5517, pp. 478-479, 1975.

[6] D.V. Evans, "A theory for wave-power absorption by oscillating bodies," *Journal of Fluid Mechanics*, vol. 77, no. 1, pp. 1-25, 1976

[7] J.N. Newman, Marine Hydrodynamics, MIT press, 1977.

[8] J. Falnes, *Ocean waves and oscillating systems: Linear interactions including wave-energy extraction*, Cambridge University Press, 2002.

[9] N.Y. Sergiienko, B.S. Cazzolato, B. Ding, P. Hardy, and M. Arjomandi, "Performance comparison of the floating and fully submerged quasi-point absorber wave energy converters," *Renewable Energy*, vol. 108, pp. 425-437, 2017.

[10] A. Babarit, J. Hals, M. Muliawan, A. kurniawan, T. Moan, and J. Krokstad, "Numerical estimation of energy delivery from a selection of wave energy converters – final report," Report, Ecole Centrale de Nantes and Norges Teknisk-Naturvitenskapeige Universitet, 2011.

[11] B. Ding, B.S. Cazzolato, M. Arjomandi, P. Hardy, and B. Mills, "Sea-state based maximum power point tracking damping control of a fully submerged oscillating buoy," *Ocean Engineering*, vol. 126, pp. 299-312, 2016.

[12] F. Meng, A. Rafiee, B. Cazzolato, B. Ding, M. Arjomandi, J. Piper, N.Y. Sergiienko, and Q. Hu, "Numerical simulation of a submerged spherical point absorber with asymmetric mass distribution," *in Proc. of the 12th European Wave and Tidal Energy Conference*, 2017.

[13] M.A. Srokosz, "The submerged sphere as an absorber of wave power," *Journal of Fluid Mechanics*, vol. 95, no. 4, pp. 717-741, 1979.

[14] N.Y. Sergiienko, B.S. Cazzolato, B. Ding, and M. Arjomandi, "An optimal arrangement of mooring lines for a three-tether submerged point-absorbing wave energy converter," *Renewable Energy*, vol. 93, pp. 23-37, 2016.

[15] N.Y. Sergiienko, A. Rafiee, B.S. Cazzolato, B. Ding, and M. Arjomandi, "Feasibility study of the three-tether axisymmetric wave energy converter," *Ocean Engineering*, vol. 150, pp. 221-233, 2018.

[16] F. Meng, B. Ding, B. Cazzolato, and M. Arjomandi, "Modal analysis of a submerged spherical point absorber with asymmetric mass distribution," *Renewable Energy*, accepted pending minor revision.

[17] W.E. Cummins, "The impulse response function and ship motions," Report, DTIC Document, 1962.

[18] J. Morison, J. Johnson, S. Schaaf, "The force exerted by surface waves on piles," *Journal of Petroleum Technology*, vol. 2, no. 5, pp. 149-154, 1950.

[19] R.D. Blevins, *Applied fluid dynamics handbook*, Krieger Publishing Company, 2003.

[20] M. Folley, T. Whittaker, and J. van't Hoff, "The design of small seabed-mounted bottom-hinged wave energy converters," *in Proc. of 7th European Wave and Tidal Energy Conference (EWTEC)*, 2007.

[21] C.M. Linton, "Radiation and diffraction of water waves by a submerged sphere in finite depth," *Ocean Engineering*, vol. 18, no. 12, pp. 61-74, 1991.

Appendix E

The application of modal analysis to the design of multi-mode point absorber wave energy converters

Ding, B., Sergiienko, N., Meng, F., Cazzolato, B. S., Hardy, P. and Arjomandi, M. (2019). "The application of modal analysis to the design of multi-mode point absorber wave energy converters". *Ocean Engineering* 171, pp. 603 - 618.

Statement of Authorship

Publication Status	Published
Name of Co-author	Fantai Meng
Contribution to the Paper	Helped to develop the mathematical model of the single-tether point absorber with asymmetric mass distribution, helped in interpretation of obtained results.
Overall Percentage (%)	10%

Statement of Authorship

Title of Paper	The application of modal analysis to the design of multi-mode point absorber wave energy converters
Publication Status	☑ Published ☐ Accepted for Publication ☐ Submitted for Publication ☐ Unpublished and Unsubmitted work written in manuscript style
Publication Details	Ding, B., Sergiienko, N., Meng, F., Cazzolato, B. S., Hardy, P. and Arjomandi, M. (2019). "The application of modal analysis to the design of multi-mode point absorber wave energy converters". *Ocean Engineering* 171, pp. 603 - 618.

Principal Author

Name of Principal Author (Candidate)	Boyin Ding
Contribution to the Paper	Developed the idea and concepts, developed the numerical models, wrote the code of simulations, interpreted the results, wrote the manuscript and acted as a corresponding author.
Overall percentage (%)	70%
Certification:	This paper reports on original research I conducted at the University of Adelaide and is not subject to any obligations or contractual agreements with a third party that would constrain its inclusion in this thesis. I am the primary author of this paper.
Signature	Date 27/08/2019

Co-Author Contributions

By signing the Statement of Authorship, each author certifies that:

i. the candidate's stated contribution to the publication is accurate (as detailed above);

ii. permission is granted for the candidate in include the publication in the thesis; and

iii. the sum of all co-author contributions is equal to 100% less the candidate's stated contribution.

Name of Co-Author	Nataliia Sergiienko
Contribution to the Paper	Helped to develop the mathematical model of the three-tether point absorber, helped in interpretation of obtained results.
Signature	8% Date 27/08/2019

Name of Co-Author	Fantai Meng
Contribution to the Paper	Helped to develop the mathematical model of the single-tether point absorber with asymmetric mass distribution, helped in interpretation of obtained results.
Signature	7% Date 21/8/19

Name of Co-Author	Benjamin Cazzolato		
Contribution to the Paper	Supervised the work, helped in interpretation of obtained results, and provided a critical revision of the manuscript.		
Signature	5%	Date	27/8/19

Name of Co-Author	Peter Hardy		
Contribution to the Paper	Helped in interpretation of obtained results, and provided a critical revision of the manuscript.		
Signature	5%	Date	28/8/19

Name of Co-Author	Maziar Arjomandi		
Contribution to the Paper	Helped in interpretation of obtained results, and provided a critical revision of the manuscript.		
Signature	5%	Date	27/08/2019

Please cut and paste additional co-author panels here as required.

Ocean Engineering 171 (2019) 603–618

Contents lists available at ScienceDirect

Ocean Engineering

journal homepage: www.elsevier.com/locate/oceaneng

The application of modal analysis to the design of multi-mode point absorber wave energy converters

Boyin Ding*, Nataliia Sergiienko, Fantai Meng, Benjamin Cazzolato, Peter Hardy, Maziar Arjomandi

Ocean Wave Energy Research Group, School of Mechanical Engineering, The University of Adelaide, Adelaide, 5005, Australia

ARTICLE INFO

Keywords:
Point absorber
Submerged wave energy converter
Power absorption by multiple oscillation modes
Modal analysis

ABSTRACT

Point absorbers are one of the most common wave energy converters, which are typically designed to extract power primarily from heave motion. Pure heave motion of an axisymmetric wave energy converter results in a relative capture width limited to a third of the maximum possible. Over the past few decades, an increasing amount of attention has been given to the design of point absorbing wave energy converters operating in multiple oscillation modes, in an attempt to more efficiently extract power from waves. However, it is not a trivial task as wave energy converters operating in multiple modes demonstrate complex coupled vibrational characteristics across several degrees of freedom. This paper addresses this challenge using modal analysis, a modern approach developed for determining, improving and optimising dynamic characteristics of complex engineering systems. Case studies are conducted on three multi-mode submerged point absorber designs, each with distinct modal behaviour to show the generality and efficacy of the approach. Results show that in combination with knowledge of wave power absorption in the frequency-domain, modal analysis can be used as an effective analytical tool to evaluate the vibrational characteristics and the power absorption potential of the multi-mode system, as well as to explore the corresponding working principles and the physical limits of the design.

1. Introduction

Ocean wave energy has been under the public spotlight over the past few decades for its high energy density, predictability, and consistency. It has shown a great potential to address the increasing global energy demand, with recent estimates suggesting a global wave energy capacity exceeding 2 TW (Cruz, 2008). However, wave energy converter (WEC) technologies are still in their pre-commercial phase and exhibit great diversity in design, leading to more than one thousand different WEC prototypes in various stage of development (Hayward and Osman, 2011). Oscillating point absorbers (PA) are a popular type of WEC design defined by having dimensions much smaller than a wavelength and account for 53% of the existing WEC prototypes (International Energy Agency, 2011). PAs are usually designed as axisymmetric heaving buoys which mainly extract power from heave motion regardless of wave direction (Cruz, 2008).

In 1975, 1976, Budal and Falnes (1975), and Evans (1976) found that given unconstrained motion, the maximum capture width of an oscillating buoy does not depend on its size, shape or submergence depth, and is only governed by the mode of motion. An axisymmetric buoy needs to oscillate in at least two modes, one radiating symmetric waves such as heave and the other one radiating antisymmetric waves such as surge or pitch, to absorb the maximum available power from waves (Falnes, 2002). Since then, a number of PA prototypes have been proposed to extract power from multiple modes of motion (multi-mode) (Sergiienko, 2018). A major group of multi-mode PA prototypes employ multiple tethers and power-take-off (PTO) machineries to enhance kinematic coupling between the modes of the buoy (where wave power enters the system) and the PTO machinery (where wave power is either stored or converted to electricity). A typical example is the submerged three tether PA proposed by Srokosz in 1979 (Srokosz, 1979). In contrast, buoys with an asymmetric shape or mass distribution have been employed to enhance dynamic coupling between the modes of the buoy, and thus convert power absorbed by multiple modes into useful PTO work. Typical examples in this category are the Edinburgh duck (Salter, 1974) and the submerged asymmetric mass distribution PA proposed by Meng et al. (Meng et al., 2017). Despite the diversity in the design concepts, multi-mode WECs demonstrate coupled vibrational

* Corresponding author.
E-mail address: boyin.ding@adelaide.edu.au (B. Ding).

https://doi.org/10.1016/j.oceaneng.2018.11.058
Received 27 August 2018; Received in revised form 31 October 2018; Accepted 29 November 2018

characteristics in multiple degrees of freedom (DoFs) which makes them much more complex than their uni-modal counterparts (e.g. heaving buoy). The complexity associated with a specific converter design increases as the number of motion modes and moving parts increase.

Modal analysis is a tool commonly employed for determining, improving and optimising dynamic characteristics of complex engineering systems, and there are numerous applications of modal analysis reported in the literature covering wide areas of engineering, science and technology (He and Fu, 2001). The applications of modal analysis in WEC design optimisation started in the late 1970s, when Newman (1979) and Farley (1982) studied the modal behaviour of floating beam WECs. Taghipour et al. (Taghipour and Moan, 2008) applied the mode expansion method to the investigation of a multi-body WEC array. Recently, Babarit et al. (2017) developed a linear numerical model based on the concept of modal decomposition for analysing the hydroelastic response of flexible electroactive WEC. Nevertheless, to the best knowledge of the authors, few attempts have been made to utilise modal analysis in the design of multi-mode point absorber WECs. Finnegan and Goggins (2012) applied modal analysis to a two-body wave energy converter to transform the coupled equations of motion into uncoupled modal equations, reducing the complexity of the solution for the response amplitude operator in the frequency domain. Meng et al. (2019) used modal analysis to explore the modal behaviour of a submerged asymmetric mass distribution PA with optimal PTO parameters. The two studies mentioned above neither reported the full functionalities of the modal analysis approach nor discussed its true value in solving multi-mode WEC design problems.

This paper addresses the complex design problem of multi-mode WECs by applying modal analysis and well-known theory in wave power absorption. Three multi-mode submerged PA designs are used as examples to illustrate the methodology in order of increasing complexity in the modal behaviour, in an attempt to develop a guideline for the WEC designers to follow. The layout of the paper is as follows: Section 2 describes the fundamental of WEC modelling, wave power absorption in the frequency domain, and modal analysis; Section 3 describes the application of modal analysis on a generic single tether spherical buoy PA, highlighting the procedure, and discussing the outcomes; Sections 4 and 5 escalate the applications to two advanced multi-mode PA designs with more complex modal behaviour and operating principles; Section 6 provides a summary of the results.

2. Fundamental knowledge of wave energy converter properties

2.1. Motion equation for submerged point absorbing wave energy converters

A rigid body oscillating WEC experiences 6DoF motion in the buoy Cartesian coordinates as illustrated in Fig. 1. In general, for an oscillating WEC having axisymmetric buoy that is excited by a plane incident wave travelling along the x-axis, the WEC system can be modelled in 3DoF for analysis: with a surge mode along the x-axis, a heave mode along the z-axis, and a pitch mode about the y-axis. This 3DoF motion equation in the time domain can be written based on the well-known Cummins equation (Cummins, 1962):

$$(\mathbf{M}+\mathbf{A}_{\infty})\ddot{\mathbf{x}}+\int_0^t \mathbf{K}_{rad}(t-\tau)\dot{\mathbf{x}}(\tau)d\tau=\mathbf{F}_{h/stat}+\mathbf{F}_d+\mathbf{F}_{exc}+\mathbf{F}_{pto} \tag{1}$$

where the vector $\mathbf{x}$ contains the surge displacement x, heave displacement z and pitch angle θ of the body at its geometrical centre; $\mathbf{M}$ is the mass matrix of the oscillating body; $\mathbf{A}_{\infty}$ is the hydrodynamic added mass existing at infinite frequency; $\mathbf{K}_{rad}(t)$ is the radiation impulse response function; and $\mathbf{F}_{h/stat}$, $\mathbf{F}_d$, $\mathbf{F}_{exc}$, and $\mathbf{F}_{pto}$ are the hydrostatic, viscous drag, wave excitation and PTO forces exerted on the body in Cartesian space, respectively.

Sergiienko et al. (2017) found that compared with floating converters, fully submerged buoys can more effectively utilise multiple modes of motion to extract power from waves. Therefore, only fully submerged PAs anchored to the sea floor by taut tethers are considered in this study. For a fully submerged buoy, the generalised hydrostatic force is

$$\mathbf{F}_{h/stat}=[0 \quad (\rho V-m)g \quad 0]^{\mathrm{T}} \tag{2}$$

where ρ is the density of water, m and V are the mass and volume of the buoy, respectively, and g is the gravitational acceleration.

The viscous drag forces experienced by the buoy can be written as quadratic functions of the buoy velocity, based on the Morison equation (Morison et al., 1950):

$$\mathbf{F}_d=\begin{pmatrix}-0.5\rho C_{Dx}A_x|\dot{x}-\dot{x}_f|(\dot{x}-\dot{x}_f)\\ -0.5\rho C_{Dz}A_z|\dot{z}-\dot{z}_f|(\dot{z}-\dot{z}_f)\\ -0.5\rho C_{D\theta}D^4D|\dot{\theta}|\dot{\theta}\end{pmatrix} \tag{3}$$

where C_{Dx}, C_{Dz}, and $C_{D\theta}$ are the viscous drag coefficients of the buoy along surge, heave and pitch axes respectively, whose values for various buoy shapes can be found in (Blevins, 2003); A_x and A_z are the cross sectional areas of the buoy along surge and heave axes, respectively; D is the diameter of the buoy; $\dot{x}_f$ and $\dot{z}_f$ are the fluid particle velocities at the position of the geometric centre of the buoy, which are usually assumed to be negligible compared to the buoy velocity. Spherical shape buoys are considered in this study for simplicity. Thus, $C_{Dx}=C_{Dz}$, $C_{D\theta}=0$ and $A_x=A_z=\pi r^2$, where r is the radius of the buoy.

The PTO force exerted on the buoy along buoy Cartesian coordinates is given by

$$\mathbf{F}_{pto}=\mathbf{J}(\mathbf{x})^{-\mathrm{T}}\mathbf{F}_t \tag{4}$$

where $\mathbf{F}_t$ are the forces generated by the PTO machinery installed along the tethers; $\mathbf{J}(\mathbf{x})^{-\mathrm{T}}$ is the transpose inverse Jacobian matrix that maps the PTO forces along the tethers to the PTO forces in buoy Cartesian coordinates. The forms and dimensions of $\mathbf{J}(\mathbf{x})^{-\mathrm{T}}$ and $\mathbf{F}_t$ depend on the specific arrangement of the tethers and the PTO machinery that will be illustrated for each of the three submerged PA designs in later sections.

In order to exclude uncertainties associated with a specific PTO machinery design, it is presumed that the PTO force has linear spring and damping effects proportional to the tether elongation and the rate of change of the tether elongation, respectively. Therefore, the PTO force along each tether consists of a static term for keeping the buoy submerged at its rest position, and the spring and damping terms:

$$F_{t,i}=C_{pto,i}-K_{pto,i}\Delta l_i-B_{pto,i}\Delta\dot{l}_i \tag{5}$$

where C_{pto} is a constant pretension force defined based on the buoyancy force experienced by the buoy and the arrangement of tethers, K_{pto} and B_{pto} are the stiffness and damping coefficients of the PTO machinery along the tether, respectively, Δl is the elongation of the tether, and the subscript i denotes the tether number.

$\mathbf{A}_{\infty}$, $\mathbf{K}_{rad}(t)$ and $\mathbf{F}_{exc}$ are basic hydrodynamics arising from wave-

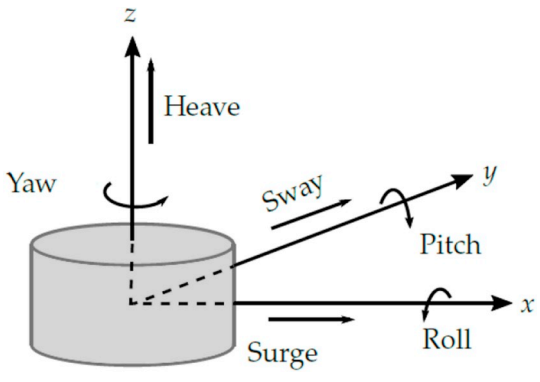

Fig. 1. Six degrees of freedom of the rigid body modes (Sergiienko, 2018).

buoy interaction and are usually solved by linear wave theory that assumes the wave height relative to the wave length and the resulting buoy motion are both small (Pecher and Kofoed, 2017). Therefore, the terms in Equation (1) associated with the fundamental hydrodynamics are linear, which is essential for modal analysis given it is a frequency-domain based approach. In contrast, $\mathbf{F}_d$ and $\mathbf{F}_{pto}$ are non-linear terms which need to be linearised before the time-domain motion equation can be transformed to the frequency domain form for modal analysis. By applying Lorentz linearisation (Folley et al., 2007), the quadratic drag terms in $\mathbf{F}_d$ can be numerically converted to linear viscous damping terms. $\mathbf{F}_{pto}$ contains trigonometric functions of buoy position and can be linearised at the nominal/rest position of the buoy $\mathbf{x}_0 = [0 \;\; 0 \;\; 0]^{\mathrm{T}}$, assuming small displacements of the buoy in Cartesian space with respect to the tether length which is normally the case in deep water. In a shallow water scenario, linearisation of $\mathbf{F}_{pto}$ remains valid subject to the constraint of small magnitudes of wave amplitude and buoy displacement.

After linearisation, Equation (1) can be transformed to the following frequency-domain form (Babarit et al., 2011):

$$(\mathbf{M} + \mathbf{A}(\omega))\hat{\ddot{\mathbf{x}}} + (\mathbf{B}_{rad}(\omega) + \mathbf{B}_d(\omega) + \mathbf{B}_{pto})\hat{\dot{\mathbf{x}}} + \mathbf{K}_{pto}\hat{\mathbf{x}} = \hat{\mathbf{F}}_{exc}(\omega) \tag{6}$$

where the superscript $\hat{\mathbf{x}}$ denotes the complex amplitudes covering the magnitude and phase information of the variables. For a spherical shape buoy,

$$\mathbf{A}(\omega) = \begin{pmatrix} a_{11}(\omega) & 0 & 0 \\ 0 & a_{33}(\omega) & 0 \\ 0 & 0 & 0 \end{pmatrix},$$

$$\mathbf{B}_{rad}(\omega) = \begin{pmatrix} b_{11}(\omega) & 0 & 0 \\ 0 & b_{33}(\omega) & 0 \\ 0 & 0 & 0 \end{pmatrix},$$

$$\mathbf{B}_d(\omega) = \begin{pmatrix} b_s(\omega) & 0 & 0 \\ 0 & b_h(\omega) & 0 \\ 0 & 0 & 0 \end{pmatrix},$$

$$\hat{\mathbf{F}}_{exc}(\omega) = \begin{pmatrix} \hat{F}_s(\omega) \\ \hat{F}_h(\omega) \\ 0 \end{pmatrix}, \tag{7}$$

where ω is the wave frequency; a_{ii} and b_{ii} denote the frequency-dependent hydrodynamic coefficients (added mass and radiation damping respectively) of the buoy at its rest position; b_s and b_h are the linearised frequency-dependent viscous damping coefficients along surge and heave axes, respectively; $\hat{F}_s$ and $\hat{F}_h$ represent the wave excitation force along surge and heave axes of the buoy. The hydrodynamic coefficients and the wave excitation forces can be calculated using boundary element solvers such as WAMIT, AQWA and NEMOH for any buoy shapes. For submerged spherical buoys, a_{ii}, b_{ii}, $\hat{F}_s$ and $\hat{F}_h$ can be solved using an analytical method described in (Linton, 1991). $\mathbf{M}$, , and $\mathbf{K}_{pto}$ in Equation (6) are dependent on the specific PA design and thus will be discussed for each case in later sections. The hydrostatic force disappears in Equation (6) as it is cancelled by the constant PTO pretension force.

After the motion response of the buoy in Cartesian space (e.g. buoy velocity) is solved by Equation (6), the corresponding elongation response of the tethers (e.g. tether elongation velocity) can be obtained:

$$\hat{\Delta \boldsymbol{l}} = \mathbf{J}(\mathbf{x}_o)^{-1}\hat{\dot{\mathbf{x}}}, \tag{8}$$

where $\mathbf{J}(\mathbf{x}_o)^{-1}$ is the inverse Jacobian matrix at the buoy nominal/rest position. The time-averaged power absorbed by the PA, more specifically by the PTO machinery installed along the tethers, is then equal to the mechanical power dissipated by the PTO dampers:

$$P_a = \sum_{i=1}^{n} \frac{1}{2} B_{pto,i} \left| \hat{\Delta l_i} \right|^2, \tag{9}$$

where n denotes the total number of tethers. The time-averaged absorbed power can also be calculated in the buoy Cartesian coordinates as the difference between the wave power input into the system and the power radiated and dissipated in water (Falnes, 2002):

$$P_a = P_{in} - P_{out} = \frac{1}{4}(\hat{\mathbf{F}}_{exc}^{\mathrm{T}*}\hat{\dot{\mathbf{x}}} + \hat{\dot{\mathbf{x}}}^{\mathrm{T}*}\hat{\mathbf{F}}_{exc}) - \frac{1}{2}\hat{\dot{\mathbf{x}}}^{\mathrm{T}*}(\mathbf{B}_{rad} + \mathbf{B}_d)\hat{\dot{\mathbf{x}}}, \tag{10}$$

where the superscript T* denotes the conjugate transpose. Furthermore, the total absorbed power can be decomposed into power absorption by the surge, heave, and pitch modes if only 3DoF motion are considered:

$$P_{a,s} = \frac{1}{4}(\hat{F}_s^*\hat{\dot{x}} + \hat{\dot{x}}^*\hat{F}_s) - \frac{1}{2}\hat{\dot{x}}^*(b_{11} + b_s)\hat{\dot{x}},$$

$$P_{a,h} = \frac{1}{4}(\hat{F}_h^*\hat{\dot{z}} + \hat{\dot{z}}^*\hat{F}_h) - \frac{1}{2}\hat{\dot{z}}^*(b_{33} + b_h)\hat{\dot{z}},$$

$$P_{a,p} = \frac{1}{4}(\hat{F}_p^*\hat{\dot{\theta}} + \hat{\dot{\theta}}^*\hat{F}_p) - \frac{1}{2}\hat{\dot{\theta}}^*(b_{55} + b_p)\hat{\dot{\theta}}. \tag{11}$$

For a spherical buoy, there is neither excitation torque, $\hat{F}_p$, nor radiation damping and linearised viscous damping, b_{55} and b_p respectively, on its rotational axis. Therefore, the power absorbed by the pitch mode of the buoy, $P_{a,p}$, is always zero.

2.2. Theory of wave power absorption

2.2.1. Power limits for regular waves

A body placed in water captures wave energy when it moves in an oscillatory manner and radiates waves in order to counteract the incident wave front. Thus, the maximum amount of power that can be removed from waves is defined by the radiating ability of the body. This limit has been derived in (Budal and Falnes, 1975) and (Evans, 1976) for various motion modes. A well known equation characterising the maximum absorbed power by an axisymmetric body in monochromatic waves is (Falnes, 2002):

$$P_{max}^{rad} = \alpha\frac{J}{k}, \tag{12}$$

where $J = \rho g^2 D(kh)A^2/(4\omega)$ is the wave-energy transport per unit frontage of the incident wave, α is a coefficient that depends on the motion oscillation mode (α= 1 for heave, α= 2 for surge or pitch, and α= 3 when the body oscillates in heave, surge and/or pitch simultaneously), and k is the wavenumber which is obtained by numerically solving $\omega^2 = gk\tanh(kh)$. In the function of J, h is the water depth, A is the wave amplitude, and $D(kh)$ is the depth function which is given by $D(kh) = \tanh(kh) + kh - (kh)\tanh^2(kh)$. In deep water condition where $kh > 1$, k is equal to ω^2/g and $D(kh)$ is equal to 1. Thus, P_{max}^{rad} in Equation (12) depends primarily on the mode of motion and decreases cubically as the wave frequency, ω, increases. It is worth noting that Equation (12) is only valid when the viscous damping loss is not considered in the system.

The actual maximum absorbed power taking linearised viscous damping loss into consideration is obtained when the buoy velocities are (Falnes, 2002):

$$\hat{\dot{x}}_{opt}(\omega) = \frac{1}{2}\hat{F}_s(\omega)/(b_{11}(\omega) + b_s(\omega)), \tag{13a}$$

$$\hat{\dot{z}}_{opt}(\omega) = \frac{1}{2}\hat{F}_h(\omega)/(b_{33}(\omega) + b_h(\omega)), \tag{13b}$$

$$\hat{\dot{\theta}}_{opt}(\omega) = \frac{1}{2}\hat{F}_p(\omega)/(b_{55}(\omega) + b_p(\omega)), \tag{13c}$$

for surge, heave, and pitch modes, respectively. In long period (low frequency) waves with large amplitudes, hydrodynamic damping coefficients are significantly smaller than the excitation force, and thus according to Equation (13) the body should move with extremely high velocities and displacements to approach the maximum power absorption, P_{max}^{rad}. This may not be possible in practice due to the design

constraints associated with the buoy and the PTO machinery. Large PTO damping is usually used in this scenario to constrain the buoy velocity/displacement within the operating limit of the PTO machinery (e.g. PTO maximum stroke defined to protect the machinery from damage), which consequently reduces the absorbed power. Budal (Falnes and Hals, 1959) then showed that the power extraction at low frequencies is limited by the swept volume of the body, which is a collective term for the body physical volume and the maximum motion amplitude of each mode subject to the specific constraints in WEC design. The expression of this low-frequency power limit is strongly dependent on the shape of the buoy, and for a submerged spherical buoy is given by (Sergiienko et al., 2017):

$$P_{max}^{swept} = \rho e^{-kh_s} d_{max} VA\omega^3 \tag{14}$$

for both the surge and heave modes. In Equation (14), h_s denotes the submergence depth of the buoy (from buoy geometric centre to water surface) and d_{max} denotes the maximum buoy displacement of the mode. The P_{max}^{rad} and the P_{max}^{swept} graphs together form the well known Budal diagram (Falnes and Hals, 1959), where viscous damping loss is not considered.

2.2.2. Optimal reactive control

In Equation (13), the optimal condition is defined by the velocity of the buoy in each mode being in phase (resonance) with the excitation force and of optimal amplitude, given by the ratio of the excitation force to the hydrodynamic damping coefficient associated with the mode. This can be achieved by applying optimal reactive control to the PTO machinery. To illustrate the main concept underlying this control strategy, a submerged buoy constrained to move in heave only and subject to reactive PTO control is used as an example. The concept is equally applicable to the other modes such as surge and pitch. The motion equation for a submerged heaving buoy under reactive spring-damper control in the frequency domain can be extracted from Equation (6):

$$(m + a_{33}(\omega))\hat{\ddot{z}} + (b_{33}(\omega) + b_h(\omega) + B_{pto})\hat{\dot{z}} + K_{pto}\hat{z} = \hat{F}_h(\omega). \tag{15}$$

Substituting $\hat{\ddot{z}} = j\omega\hat{\dot{z}}$ and $\hat{z} = -j\hat{\dot{z}}/\omega$ into Equation (15) results in:

$$\left(b_{33}(\omega) + b_h(\omega) + B_{pto} + j\omega m + j\omega a_{33}(\omega) - j\frac{K_{pto}}{\omega}\right)\hat{\dot{z}} = \hat{F}_h(\omega). \tag{16}$$

Comparing Equation (16) with the optimal heave velocity equation in Equation (13b), the following optimal values of the PTO control parameters can be obtained:

$$K_{pto,\,opt} = \omega^2(m + a_{33}(\omega)), \tag{17a}$$

$$B_{pto,\,opt} = b_{33}(\omega) + b_h(\omega), \tag{17b}$$

Equation (17) is usually called optimal reactive control as the PTO spring provides a reactive force, and thus reactive power to the system. It is also often called complex conjugate, or impedance matching, control, as the optimal PTO load impedance is defined as the complex conjugate of the intrinsic mechanical impedance of the buoy (Ringwood et al., 2014):

$$\hat{Z}_{pto,opt}(\omega) = \hat{Z}_h^*(\omega), \tag{18}$$

where $\hat{Z}_{pto,opt}(\omega) = B_{pto,\,opt} - j\frac{K_{pto,\,opt}}{\omega}$, and $\hat{Z}_h(\omega) = b_{33}(\omega) + b_h(\omega) + j\omega(m + a_{33}(\omega))$.

2.3. Modal analysis

2.3.1. Matrix eigenvalue problem for an undamped multiple DoF system

The eigenvalue problem is a commonly encountered problem in engineering and is the basis of modal analysis. The solution of an eigenvalue problem provides important physical meaning to a dynamic system. The general motion equation for the free vibration of an undamped n DoF system is given by:

$$\mathbf{M}\ddot{\mathbf{x}} + \mathbf{K}\mathbf{x} = 0, \tag{19}$$

where $\mathbf{M}$ and $\mathbf{K}$ are the mass and stiffness matrices respectively. Assuming harmonic sinusoidal motion and substituting $\mathbf{x} = \mathbf{\Phi}\sin(\omega t + \phi)$ and $\ddot{\mathbf{x}} = -\omega^2\mathbf{\Phi}\sin(\omega t + \phi)$ into Equation (19) results in:

$$(\mathbf{K} - \omega^2\mathbf{M})\mathbf{\Phi} = 0. \tag{20}$$

The non-trivial solution of Equation (20) is given by:

$$det\,(\mathbf{K} - \omega^2\mathbf{M}) = 0, \tag{21}$$

where *det* is the determinant of the matrix, which can be expanded, forming an nth order polynomial for ω^2. The roots of this polynomial are the eigenvalues of $\mathbf{K}^{-1}\mathbf{M}$, whose square roots are the system natural frequencies $[\omega_1 \;\; \omega_2 \ldots \;\; \omega_n]$. Substituting each eigenvalue or natural frequency into Equation (20), a corresponding eigenvector $\mathbf{\Phi}$ can be derived. Therefore, the system has n eigenvectors $[\mathbf{\Phi}_1 \;\; \mathbf{\Phi}_2 \ldots \;\; \mathbf{\Phi}_n]$, denoting the mode shapes of the system, also referred to as normal modes.

2.3.2. Orthogonality of normal modes

The orthogonality properties of an undamped n DoF system are manifested in the relationship between its spatial and modal models. Mode shapes are orthogonal to each other with respect to system mass and stiffness matrices (He and Fu, 2001):

$$\mathbf{\Phi}_i^T\mathbf{M}\mathbf{\Phi}_j = 0, \;\; \text{for } i \neq j,$$

$$\mathbf{\Phi}_i^T\mathbf{K}\mathbf{\Phi}_j = 0, \;\; \text{for } i \neq j,$$

$$\mathbf{\Phi}_i^T\mathbf{M}\mathbf{\Phi}_i = m_i,$$

$$\mathbf{\Phi}_i^T\mathbf{K}\mathbf{\Phi}_i = k_i, \tag{22}$$

where $\mathbf{\Phi}_i$ and $\mathbf{\Phi}_j$ are the ith and jth eigenvectors/modes, respectively, m_i and k_i are the modal mass and modal stiffness of the ith mode, respectively. This is known as the principle of orthogonality. This principle can be utilised to transform the (usually coupled) spatial model to the uncoupled modal model for an undamped system (He and Fu, 2001). For a system of light damping ($0 < \xi_i$, damping ratio < 0.2 for all modes), the assumption is usually made that the damping matrix satisfies the same modal orthogonality properties as the mass and stiffness matrices (Benaroya, 1998):

$$\mathbf{\Phi}_i^T\mathbf{B}\mathbf{\Phi}_j = 0, \text{ for } i \neq j,$$

$$\mathbf{\Phi}_i^T\mathbf{B}\mathbf{\Phi}_i = b_i, \tag{23}$$

where $\mathbf{B}$ is the damping matrix, and b_i is the modal damping of the ith mode. Under this assumption, a lightly damped n DoF system can be transformed from the original spatial form to the following modal form:

$$\mathbf{\Psi}^T\mathbf{M}\mathbf{\Psi}\hat{\ddot{\mathbf{q}}} + \mathbf{\Psi}^T\mathbf{B}\mathbf{\Psi}\hat{\dot{\mathbf{q}}} + \mathbf{\Psi}^T\mathbf{K}\mathbf{\Psi}\hat{\mathbf{q}} = \hat{\mathbf{N}}_{exc}, \tag{24}$$

where $\mathbf{\Psi} = [\mathbf{\Phi}_1 \;\; \mathbf{\Phi}_2 \ldots \;\; \mathbf{\Phi}_n]$; $\hat{\mathbf{q}}$ denotes the modal displacement defined by $\mathbf{\Psi}^{-1}\hat{\mathbf{x}}$; $\hat{\mathbf{N}}_{exc}$ denotes the modal excitation force defined by $\mathbf{\Psi}^T\hat{\mathbf{F}}_{exc}$. Substituting Equations (22) and (23) into Equation (24), the following decoupled modal model in matrix form is obtained:

$$\begin{pmatrix} m_1 & 0 & \cdots & 0 \\ 0 & m_2 & \ddots & \vdots \\ \vdots & \ddots & \ddots & 0 \\ 0 & \cdots & 0 & m_n \end{pmatrix}\hat{\ddot{\mathbf{q}}} + \begin{pmatrix} b_1 & 0 & \cdots & 0 \\ 0 & b_2 & \ddots & \vdots \\ \vdots & \ddots & \ddots & 0 \\ 0 & \cdots & 0 & b_n \end{pmatrix}\hat{\dot{\mathbf{q}}} + \begin{pmatrix} k_1 & 0 & \cdots & 0 \\ 0 & k_2 & \ddots & \vdots \\ \vdots & \ddots & \ddots & 0 \\ 0 & \cdots & 0 & k_n \end{pmatrix}\hat{\mathbf{q}} = \hat{\mathbf{N}}_{exc}. \tag{25}$$

2.3.3. Application in multi-mode WEC design

To absorb the maximum energy from waves, a multi-mode PA WEC needs to achieve both the phase (resonance) and amplitude optimal conditions for at least two spatial modes: one radiates symmetric waves

such as heave and the other radiates antisymmetric waves such as surge or pitch. The optimal phase condition can be achieved when the natural frequency of the mode is equal to the wave frequency, obtained by re-arranging Equation (17a). The amplitude optimal condition can occur when the PTO damping is equal to the hydrodynamic damping of the mode, as shown in Equation (17b).

The matrix eigenvalue problem defined by Equations (20) and (21) outputs the natural frequencies of a multi-mode PA WEC, ω_i, as well as the corresponding mode shapes represented in the buoy Cartesian coordinates (e.g. $\mathbf{\Phi}_i = [\Phi_{ix} \;\; \Phi_{iz} \;\; \Phi_{i\theta}]^{\mathrm{T}}$ for a 3DoF WEC), which can be used to evaluate the phase optimality of the system modes. A PA WEC is usually lightly damped because it needs to oscillate with waves to extract energy. Thus, the damped spatial model of the PA in buoy Cartesian coordinates as shown in Equation (6) can be transformed to the decoupled modal form as shown in Equation (25) for the ease of evaluating the amplitude optimality of the modes and the controllability of the PA system. Modes that are not utilised or cannot be properly controlled for wave energy extraction should be designed off-resonant with waves to improve the overall durability of the system. Case studies are conducted on three multi-mode WEC designs having representative modal behaviour in the following three sections.

3. Modal analysis on a generic single tether spherical buoy PA

3.1. System description

Fig. 2 shows a generic single tether spherical buoy (to be referred to as G1TSB) PA at its nominal/rest position, where the only tether is vertical and under tension which maintains the positively buoyant buoy fully submerged. The tension is generated by the PTO unit as part of the PTO force shown in Equation (5), and is given by:

$$C_{pto} = -(\rho V - m)g. \tag{26}$$

Fixed system parameters are listed in Table 1. Based on the geometrical dimensions of the buoy, the drag coefficient is $C_{Dx} = C_{Dz} = 0.18$ for $5 \times 10^6 < Re < 1 \times 10^7$ (Blevins, 2003). The parameters that will be tuned by modal analysis are the PTO stiffness K_{pto}, PTO damping B_{pto} and nominal tether length at buoy rest position l_0. During parameter tuning, motion constraints are not considered. The buoy hull is assumed to be hollow so that hydraulic circuits and control instruments can be placed inside. The mass of the buoy is evenly distributed on the buoy hull, resulting in buoy centre of gravity and buoy geometric centre being coincident.

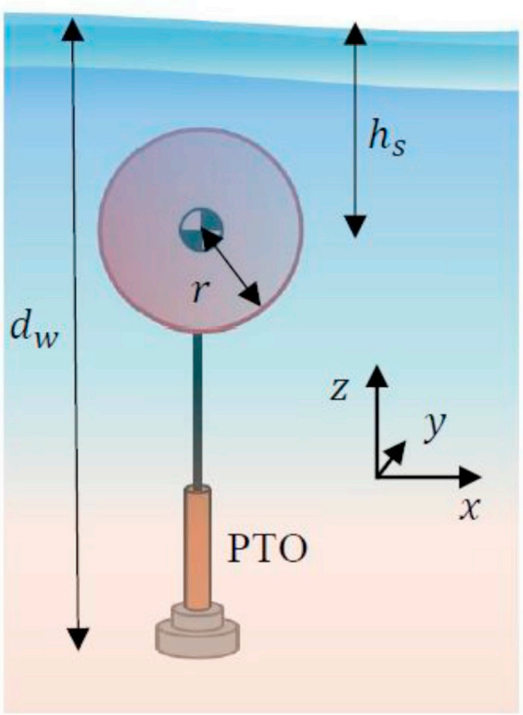

Fig. 2. Generic single tether spherical buoy PA.

3.2. Frequency domain model

A time-domain model of the G1TSB PA system is discussed in detail in (Babarit et al., 2011) and (Ding et al., 2016). Applying linearisation to the system at its nominal/rest position for small waves (refer to (Babarit et al., 2011) for more details about the linearisation procedure), the following mass and PTO damping and stiffness matrices associated with Equation (6) are obtained:

$$\mathbf{M} = \begin{pmatrix} m & 0 & 0 \\ 0 & m & 0 \\ 0 & 0 & I_{yy} \end{pmatrix},$$
$$\mathbf{B}_{pto} = \begin{pmatrix} 0 & 0 & 0 \\ 0 & B_{pto} & 0 \\ 0 & 0 & 0 \end{pmatrix},$$
$$\mathbf{K}_{pto} = \begin{pmatrix} -C_{pto}/l_0 & 0 & C_{pto}r/l_0 \\ 0 & K_{pto} & 0 \\ C_{pto}r/l_0 & 0 & -C_{pto}r(l_0 + r)/l_0 \end{pmatrix}. \tag{27}$$

where there are three unknowns: PTO stiffness K_{pto}, PTO damping B_{pto}, and nominal tether length l_0. In this study, it is assumed that any desired K_{pto} and B_{pto} can be achieved in the PTO design and l_0 can be varied by changing the height of the mooring base above the ocean floor. The corresponding design challenges and economic viability, however, are out of the scope of the paper. At the nominal position of the buoy, the inverse Jacobian matrix of the G1TSB PA is given by:

$$\mathbf{J}(\mathbf{x}_o)^{-1} = (0 \;\; 1 \;\; 0). \tag{28}$$

3.3. Natural frequencies and mode shapes

Substituting the mass and stiffness matrices $\mathbf{M}$, $\mathbf{A}(\omega)$ and $\mathbf{K}_{pto}$ into Equations (20) and (21), the eigenvalue problem for the undamped G1TSB PA system can be solved, for varying nominal tether length l_0 and varying PTO stiffness K_{pto}. The resulting natural frequencies and mode shapes of the system are displayed in Fig. 3, as functions of the nominal tether length and the PTO stiffness. Fig. 3(a) shows two convex surfaces, denoting the natural frequencies of Mode 1 and Mode 3. Mode 1 is surge dominant as can be seen from its mode shapes shown in Fig. 3(b). Mode 2 is pitch dominant as evident in Fig. 3(c). Mode 3 is heave dominant as evident in Fig. 3(d). A graphical representation of Modes 1, 2, and 3 in the buoy Cartesian coordinates is shown in Fig. 4. As the pitch mode does not contribute to power absorption for a spherical buoy, Mode 2 is not shown in Fig. 3(a) for better visualisation of the natural frequencies of Mode 1 and Mode 3. As shown in Fig. 3(a), the natural frequency of Mode 1 increases as the nominal tether length decreases, because the G1TSB PA operating in this surge-dominant mode is analogous to an inverted pendulum under small displacements (see Fig. 4). Therefore, ignoring couplings between the surge and pitch modes in $\mathbf{K}_{pto}$ in Equation (27), the natural frequency of Mode 1 can be approximated as:

$$\omega_1 \approx \sqrt{\frac{(\rho V - m)g}{l_0(m + a_{11}(\omega))}}. \tag{29}$$

On the other hand, the natural frequency of Mode 3 increases as the PTO stiffness increases, and is approximately equal to the natural frequency of a 1DoF heaving PA:

Table 1
Parameters for the generic single tether spherical buoy PA.

Symbol	Value/unit	Description
d_w	50 m	Water depth
h_s	8.5 m	Submergence depth from buoy geometric centre to water surface
r	5 m	Radius of the spherical buoy
m	2.68×10^5kg	Buoy mass, defined as half of the buoy buoyancy force $m = \rho V/2$
I_{yy}	4.472×10^6kg. m^2	Moment of inertia of a hollow spherical buoy about its pitch axis, given by $I_{yy} = \frac{2}{3}mr^2$

$$\omega_3 \approx \sqrt{\frac{K}{(m + a_{33}(\omega))}}. \tag{30}$$

It is evident in Fig. 3(a) that by varying the PTO stiffness, the natural frequency of Mode 3 can reach any value between 0.3 and 1.5 rad/s, the typical wave frequency range, whilst the natural frequency of Mode 1 can only reach up to 0.7 rad/s when the nominal tether length decreases to be less than the buoy radius. The line of intersection of the Mode 1 and the Mode 3 surfaces indicates the wave frequency range where both modes can be tuned to resonance (i.e. optimal phase condition), as well as the required combination of nominal tether length and PTO stiffness.

Wave power is absorbed by the oscillation of the buoy, and then eventually absorbed by the PTO machinery or dissipated in the sea. Therefore, it is critical to consider the coupling between the PTO machinery and the normal modes of the buoy in Cartesian coordinates. The inverse Jacobian matrix can be used to transform the mode shapes in Cartesian coordinates to the contribution of the modes on tether elongation:

$$\varepsilon_i = \mathbf{J}(\mathbf{x}_o)^{-1}\mathbf{\Phi}_i. \tag{31}$$

For the G1TSB PA system, the contribution of its three normal

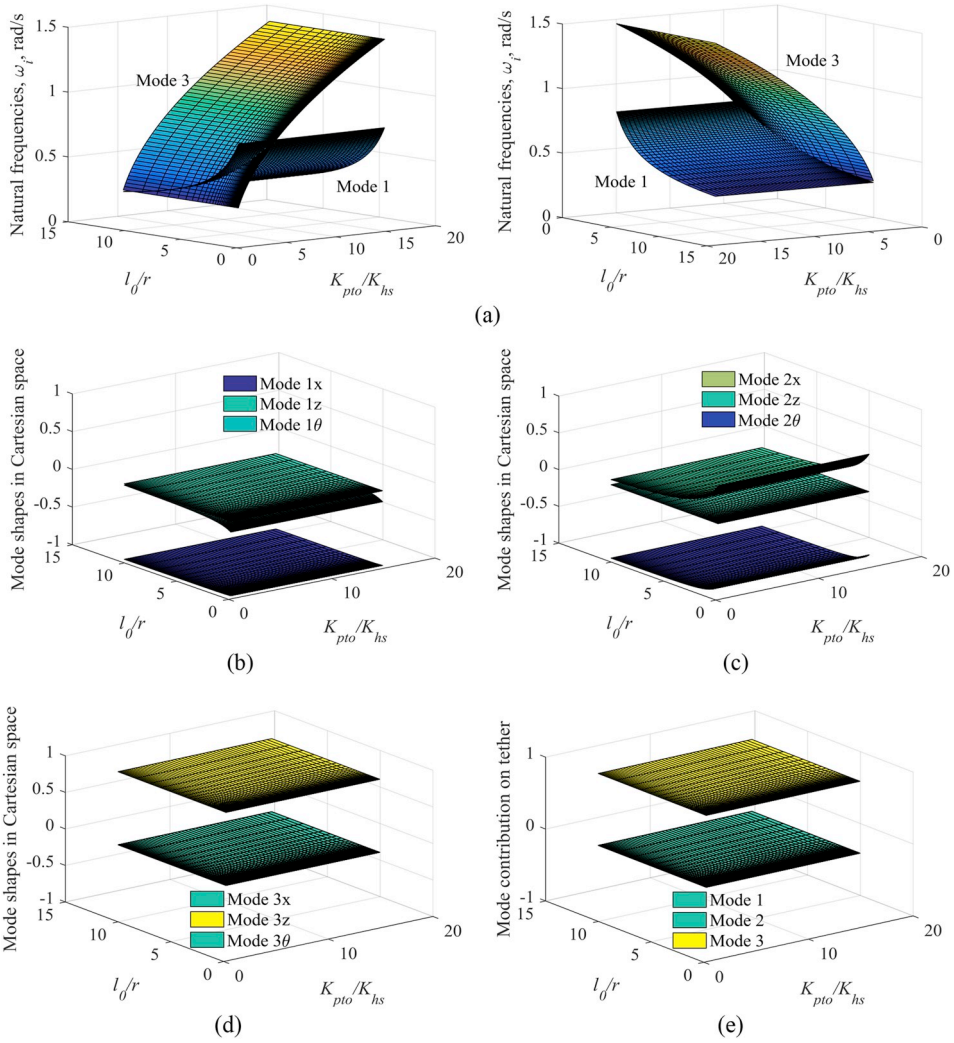

Fig. 3. Eigenanalysis on the generic single tether spherical buoy PA: (a) Natural frequencies of normal modes, ω_i, plotted from two different visual angles; (b) Mode shapes of Mode 1, $\mathbf{\Phi}_1$; (c) Mode shapes of Mode 2, $\mathbf{\Phi}_2$; (d) Modes shapes of Mode 3, $\mathbf{\Phi}_3$; (e) Contribution of normal modes to tether elongation, vs. nominal tether length l_0 (normalised by buoy radius r) and PTO stiffness K_{pto} (normalised by the hydrostatic stiffness of a half-submerged buoy $K_{hs} = \rho\pi r^2$). In subplots (b), (c), (d) and (e), yellow colour indicates value close to 1; green colour indicates values close to 0; and purple colour indicates value close to -1. For an undamped system, its mode shapes are either in phase or 180° out of phase with respect to the spatial modes (e.g. surge, heave, pitch), depending on the sign of the elements of the mode shapes, $\mathbf{\Phi}_i = [\Phi_{ix} \quad \Phi_{iz} \quad \Phi_{i\theta}]^T$. (For interpretation of the references to colour in this figure legend, the reader is referred to the Web version of this article.)

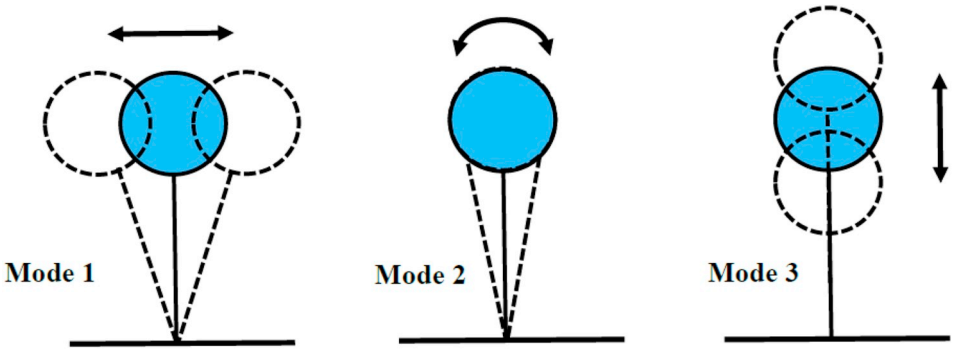

Fig. 4. Graphical representation of Modes 1, 2, 3 in the buoy Cartesian coordinates for the generic single tether spherical buoy PA regardless of wave frequency. Mode 1 oscillates predominantly along surge; Mode 2 oscillates predominantly along pitch; Mode 3 oscillates predominantly along heave.

modes on the single tether is shown in Fig. 3(e). It is evident that only Mode 3 contributes to tether elongation that drives the PTO unit, and therefore actually contributes to PTO power absorption. As Mode 1 and Mode 2 do not contribute to PTO power generation, they should be designed as off-resonant modes to improve the durability of the whole system. In practice, additional modal coupling will occur due to the real nonlinear dynamics of the PA, however, the power arising from these coupling effects are negligible compared to the power in the primary modes.

3.4. Optimality across wave frequencies

For the ease of design in the mooring base, the tether is assumed to be anchored to the sea floor level, and thus $l_0 = d_w - h_s - r = 36.5$ m. At this nominal tether length, the natural frequencies of the G1TSB PA system as a function of PTO stiffness are shown in Fig. 5. By varying PTO stiffness, Mode 3 can be tuned to resonance or optimal phase condition across the wave frequency range, as also observed from the 3D plot shown in Fig. 3(a), whilst the natural frequencies of Modes 1 and 2 remain constant. The natural frequency of Mode 2 is much higher than the wave frequency upper limit and therefore is always an off-resonant mode as desired. The natural frequency of Mode 1 is at the edge of the wave frequency lower limit. Therefore, there is a probability that Mode 1 can reach resonance, in particular at seas sites where very long waves often occur. The natural frequency of Mode 1 can be further reduced by increasing buoy mass as shown in Equation (29).

As shown in Fig. 3, when the nominal tether length is 36.5 m, the mode shapes of the system form a constant matrix regardless of the variation of PTO stiffness:

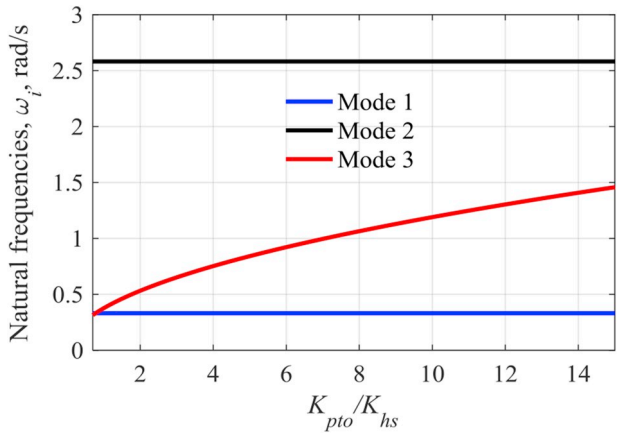

Fig. 5. Natural frequencies of normal modes, ω_i, vs. PTO stiffness K_{pto} (normalised by the hydrostatic stiffness of a half-submerged buoy $K_{hs} = \rho\pi r^2$), when the nominal tether length l_0 is $d_w - h_s - r = 36.5$ m, for the generic single tether spherical buoy PA.

$$\mathbf{\Psi} \approx \begin{pmatrix} -1 & 0.1 & 0 \\ 0 & 0 & 1 \\ 0 & -1 & 0 \end{pmatrix}. \tag{32}$$

The elements of the mode shapes are rounded to one decimal point. Then applying the orthogonality of normal modes described in Section 2.3.2, the motion equation of the G1TSB system given by Equations (6), (7) and (27), can be transformed to the following decoupled modal form:

$$\begin{pmatrix} m + a_{11} & 0 & 0 \\ 0 & I_{yy} & 0 \\ 0 & 0 & m + a_{33} \end{pmatrix} \ddot{\hat{\mathbf{q}}} + \begin{pmatrix} b_{11} + b_s & 0 & 0 \\ 0 & (b_{11} + b_s)/100 & 0 \\ 0 & 0 & b_{33} + b_h + B_{pto} \end{pmatrix} \dot{\hat{\mathbf{q}}} + \begin{pmatrix} -C_{pto}/l_0 & 0 & 0 \\ 0 & -C_{pto} r(l_0 + r)/l_0 & 0 \\ 0 & -C_{pto} r/(5l_0) - C_{pto}/(100 l_0) & 0 \\ 0 & 0 & K_{pto} \end{pmatrix} \hat{\mathbf{q}} = \begin{pmatrix} -\hat{F}_s \\ \hat{F}_s/10 \\ \hat{F}_h \end{pmatrix}, \tag{33}$$

where the scalar numbers arise from the mode shape matrix given by Equation (32). Equation (33) shows that Mode 1 and Mode 2 are not affected by PTO spring, K_{pto}, or damping, B_{pto}, whilst Mode 3 can be reactively controlled by tuning PTO spring and damping to their optimal values as defined in Equation (17).

Since Mode 3 aligns with the heave mode as can be observed from Fig. 3(d), Fig. 4 and Equation (33), the G1TSB PA system can only absorb power from its heave motion, and thus one third of the maximum available wave power with reference to Equation (12) in accordance with Budal, Falnes and Evans (Budal and Falnes, 1975; Evans, 1976). To validate this conclusion made by modal analysis, power absorbed by the surge and heave modes of the reactively controlled system subject to incident waves of 0.1 m amplitude and frequencies between 0.3 and 1.5 rad/s are calculated, with results shown in Fig. 6. The wave amplitude of 0.1 m was selected to meet the conditions of linearised wave assumption used in the modelling, as well as to ensure reasonable unconstrained motion of the buoy across the selected wave frequency range of interests. In this wave frequency range, the selection of 0.1 m wave amplitude results in a wave steepness (wave height to wavelength ratio) of less than 1%. Also shown are the low and high frequency power bounds of the heave mode arising due to the swept volume limit (e.g. $d_{max} = 3$m) and the radiation limit of the buoy, respectively. It can be seen from Fig. 6 that the G1TSB PA system only absorbs power from its heave mode. At low frequencies, the power absorbed by the heave mode is much lower than the power bound associated with swept volume limit because the effects of the viscous drag (which dissipates additional power from the system) were not considered in the calculation of the power bound associated with swept volume limit. The effects of the viscous drag are significant at low wave frequencies but negligible at high wave frequencies (Ding et al., 2018). Thus the power absorbed by the heave mode converges to the power bound associated with the radiation limit at high frequencies, meaning

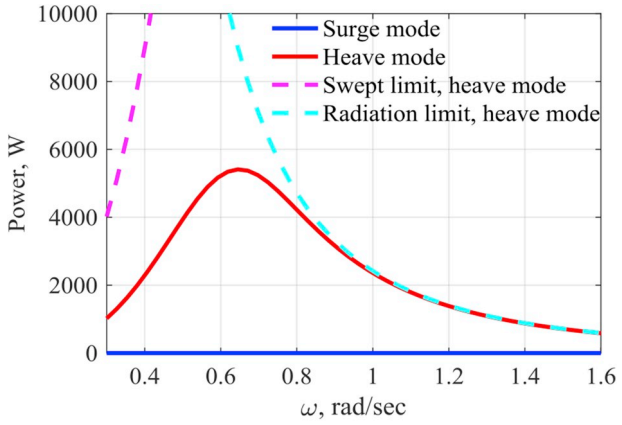

Fig. 6. Power absorbed by the surge (blue solid line) and heave (red solid line) modes of the G1TSB PA system under reactive control subject to incident waves of 0.1 m amplitude and 0.3–1.5 rad/s frequencies; power bound of the heave mode caused by swept volume limit, P_{max}^{swept} for d_{max} = 3 m, (magenta dashed line) defined by Equation (14); power bound of the heave mode caused by radiation limit, P_{max}^{rad} for α= 1, (cyan dashed line) defined by Equation (12). (For interpretation of the references to colour in this figure legend, the reader is referred to the Web version of this article.)

the PA can absorb at most one-third of the wave power.

4. Modal analysis on a three tether spherical buoy PA

4.1. System description

As shown in the previous section, the G1TSB PA system has control authority along its heave mode only and therefore is inefficient for power absorption. Thus, a three-tether spherical buoy (to be referred to as 3TSB) PA system was proposed to enhance kinematic coupling between the oscillating modes of the buoy and the PTO machinery installed along the tethers, enabling more control authority of the modes.

Fig. 7 illustrates a schematic of a 3TSB PA system at its rest pose, where the tethers are equally distributed around the buoy, separated by 120° in the horizontal plane. This configuration makes the system insensitive to wave direction. Tether 1 lies on the x-z plane, and thus the wave travelling direction, and tethers 2 and 3 are symmetric about the x-z plane. In this paper, it is assumed that all three tethers point towards the geometric centre of the spherical buoy and the PTO units along the three tethers have identical linear characteristics (e.g. pretension force

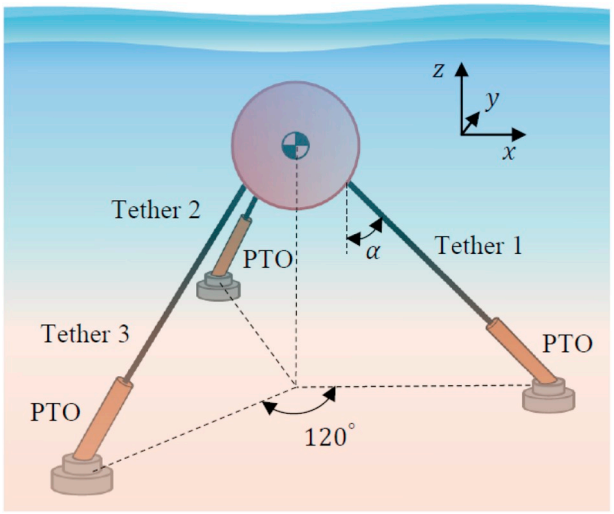

Fig. 7. Three tether spherical buoy PA.

C_{pto}, PTO damping B_{pto} and stiffness K_{pto}). The tether attachment points are located on the surface of the buoy hull. The inclination angle of the tethers with respect to the z-axis, α, plays an important role in this design as it defines the contribution of the surge and heave modes in the total absorbed power, as well as the effects of PTO control on the surge and heave modes (Sergiienko et al., 2018). Due to tether inclination, the pretension force along each tether is given by:

$$C_{pto} = -(\rho V - m)g/(3\cos(\alpha)). \tag{34}$$

The system parameters are kept identical to the ones for the G1TSB PA system as shown in Table 1. Submergence depth of the buoy is fixed during the tuning of the PTO parameters and the tether inclination angle for modal analysis. All three tethers are anchored to the sea floor level and thus the nominal tether length l_0 is a function of the tether inclination angle α between 0 and 90°. Although it is not feasible to have a tether inclination angle of 90° in practice as this results in infinitely long tether length, the purpose is to show the evolution of the PA modal behaviour subject to the variation of tether inclination angle from one extreme condition to the opposite extreme condition.

4.2. Frequency domain model

A time-domain model of the 3TSB PA system is discussed in detail in (Sergiienko et al., 2018). Applying linearisation to the system at its nominal/rest position for small waves (refer to (Sergiienko et al., 2016) for more details about the linearisation procedure), the following mass and PTO damping and stiffness matrices associated with Equation (6) are obtained:

$$\mathbf{M} = \begin{pmatrix} m & 0 & 0 \\ 0 & m & 0 \\ 0 & 0 & I_{yy} \end{pmatrix},$$

$$\mathbf{B}_{pto} = \begin{pmatrix} \frac{3}{2}B_{pto}\sin^2(\alpha) & 0 & 0 \\ 0 & 3B_{pto}\cos^2(\alpha) & 0 \\ 0 & 0 & 0 \end{pmatrix},$$

$$\mathbf{K}_{pto} = \begin{pmatrix} \left(\frac{3}{2}\sin^2(\alpha)\left(K_{pto} + \frac{C_{pto}}{l_0}\right) - \frac{3C_{pto}}{l_0}\right) & 0 & \frac{3C_{pto}r\cos(\alpha)}{l_0} \\ 0 & \left(3\cos^2(\alpha)\left(K_{pto} + \frac{C_{pto}}{l_0}\right) - \frac{3C_{pto}}{l_0}\right) & 0 \\ \frac{3C_{pto}r\cos(\alpha)}{l_0} & 0 & \frac{-3C_{pto}r(l_0+r)(\cos^2(\alpha)+1)}{2l_0} \end{pmatrix}. \tag{35}$$

At the nominal position of the buoy, the inverse Jacobian matrix of the linear 3TSB PA is given by:

$$\mathbf{J}(\mathbf{x}_o)^{-1} = \begin{pmatrix} -\sin(\alpha) & \cos(\alpha) & 0 \\ \sin(\alpha)/2 & \cos(\alpha) & 0 \\ \sin(\alpha)/2 & \cos(\alpha) & 0 \end{pmatrix}. \tag{36}$$

4.3. Natural frequencies and mode shapes

Substituting the mass and stiffness matrices **M**, **A**(ω) and $\mathbf{K}_{pto}$ into Equations (20) and (21), the eigenvalue problem for the 3TSB PA system can be solved, for varying tether inclination angle α and varying PTO stiffness K_{pto}. The resulting natural frequencies and mode shapes of the system are displayed in Fig. 8, as functions of the tether inclination angle and the PTO stiffness. Fig. 8(a) shows two convex surfaces, denoting the natural frequencies of Mode 1 and Mode 3 respectively. Mode 1 is surge dominant as can be seen from its mode shapes shown in Fig. 8(b). Mode 2 is pitch dominant as evident in Fig. 8(c). Mode 3 is heave dominant as evident in Fig. 8(d). A graphical representation of Modes 1, 2, and 3 in the buoy Cartesian coordinates is shown in Fig. 9. As the pitch mode does not contribute to power absorption for a spherical buoy, the natural frequency of Mode 2 is not shown in

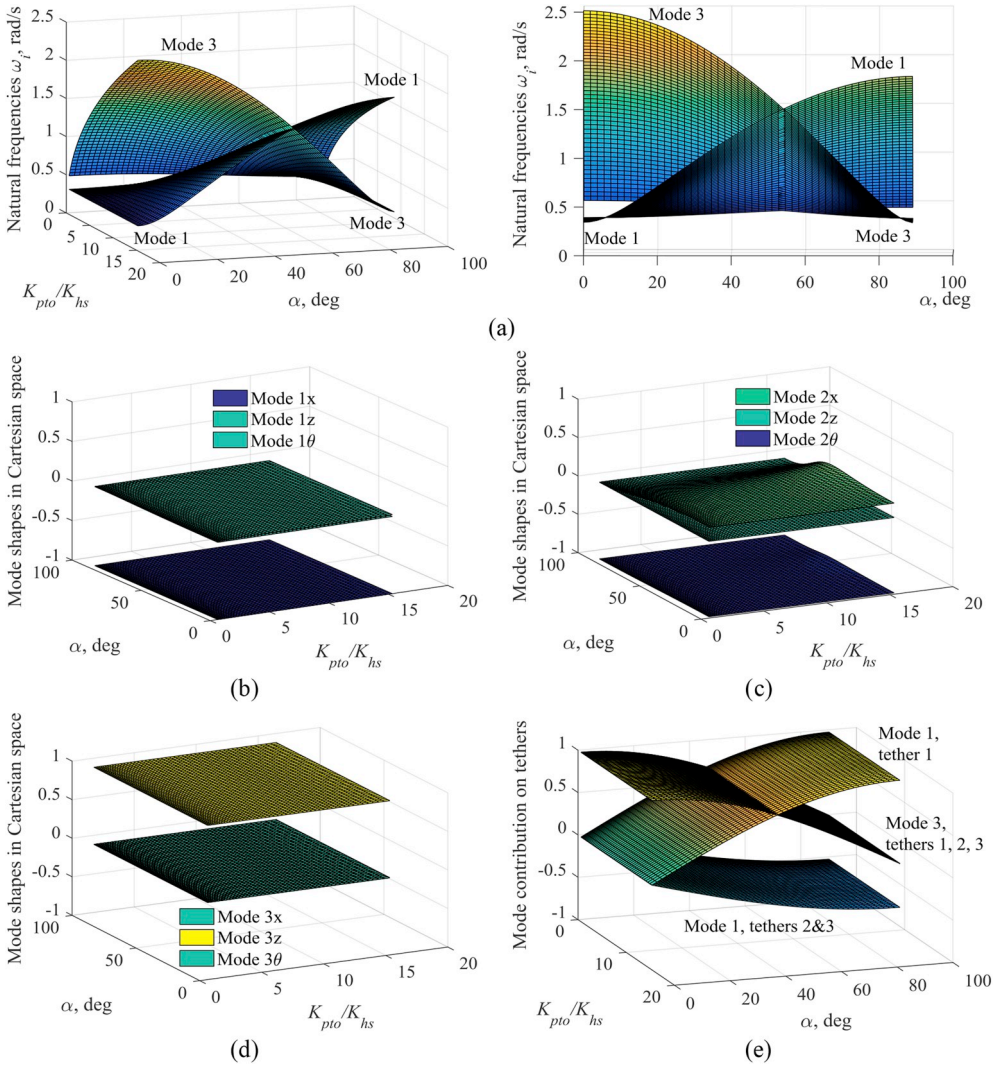

Fig. 8. Eigenanalysis on the three-tether spherical buoy PA: (a) Natural frequencies of normal modes, ω_i, plotted from two different visual angles; (b) Mode shapes of Mode 1; (c) Mode shapes of Mode 2; (d) Modes shapes of Mode 3; (e) Contribution of Mode 1 and Mode 3 to tether elongations, vs. tether inclination angle α in degrees and PTO stiffness K_{pto} (normalised by the hydrostatic stiffness of a half-submerged buoy $K_{hs} = \rho\pi r^2$). In subplots (b), (c), (d) and (e), yellow colour indicates value close to 1; green colour indicates values close to 0; and purple colour indicates value close to -1. (For interpretation of the references to colour in this figure legend, the reader is referred to the Web version of this article.)

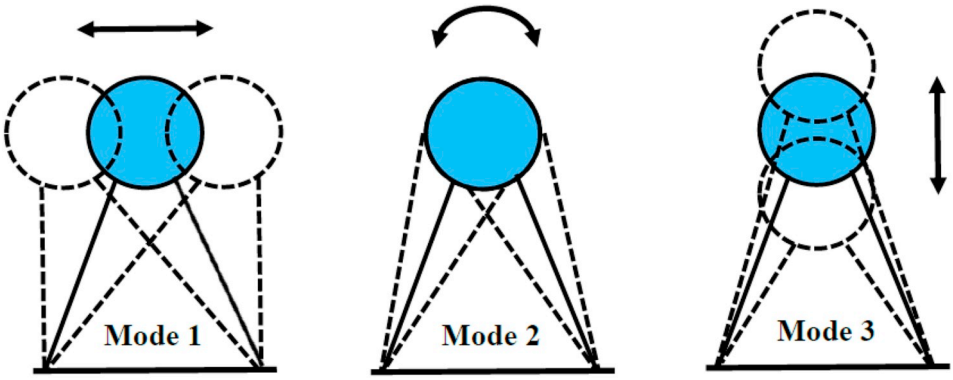

Fig. 9. Graphical representation of Modes 1, 2, 3 in the buoy Cartesian coordinates for the three-tether spherical buoy PA regardless of wave frequency. Mode 1 oscillates predominantly along surge; Mode 2 oscillates predominantly along pitch; Mode 3 oscillates predominantly along heave.

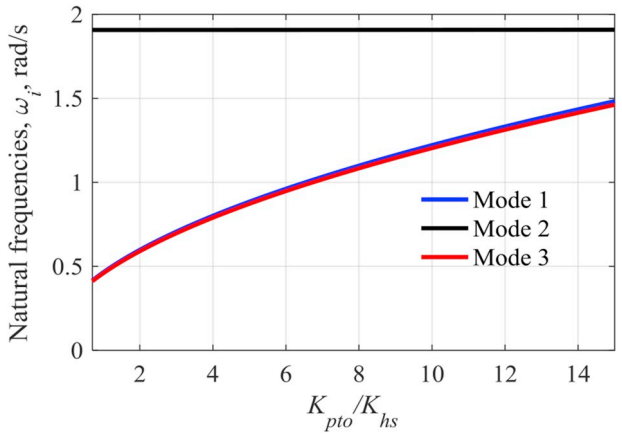

Fig. 10. Natural frequencies of normal modes, ω_i, vs. PTO stiffness K_{pto} (normalised by the hydrostatic stiffness of a half-submerged buoy $K_{hs} = \rho\pi r^2$), when the tether inclination angle α is 54.5°, for the three tether spherical buoy PA.

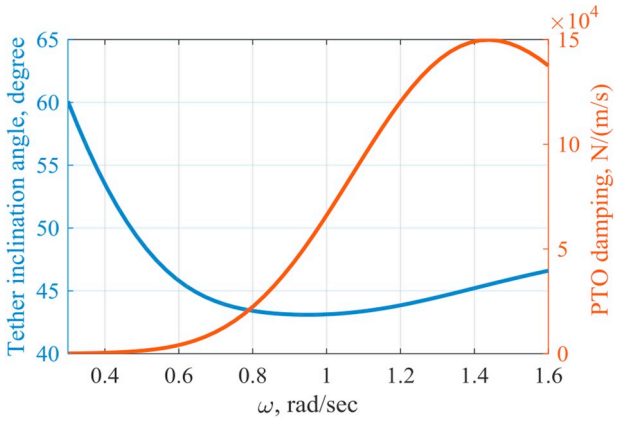

Fig. 11. Tether inclination angle (blue curve) and PTO damping (brown curve) that achieve the optimal amplitude condition for Modes 1 and 3 across the wave frequencies, for the three tether spherical buoy PA. (For interpretation of the references to colour in this figure legend, the reader is referred to the Web version of this article.)

Fig. 8(a). The line of intersection of the natural frequency surfaces of Modes 1 and 3 in Fig. 8(a) indicates that at tether inclination angle of 54.5°, both modes can be simultaneously tuned to resonance (i.e. the optimal phase condition) across the wave frequency range between 0.3 and 1.5 rad/s by varying PTO stiffness. Fig. 10 plots this line of intersection against PTO stiffness. Fig. 8(e) shows the contribution of Mode 1 and Mode 3 to the elongations of the three tethers, mapped from the system mode shapes by the inverse Jacobian matrix. When the tether inclination angle increases from 0 to 90°, the contribution gradually shifts from Mode 3 (heave) dominant (like the G1TSB PA system) to Mode 1 (surge) dominant. At a tether inclination angle of 54.5°, Mode 1 and Mode 3 contribute to approximately equal tether elongations, thus both modes are able to cause considerable PTO power generation.

4.4. Optimality across wave frequencies

As discussed in Section 4.3, Mode 1 (surge-dominant) and Mode 3 (heave dominant) can be simultaneously tuned to resonance across the wave frequency range between 0.3 and 1.5 rad/s, for a tether inclination angle of 54.5° and various PTO stiffness. In contrast, the natural frequency of Mode 2 (pitch-dominant) is insensitive to PTO stiffness and is higher than the usual wave frequency range as shown in Fig. 10, which is ideal as Mode 2 (pitch-dominant) is not necessary for absorbing maximum power from waves.

As shown in Fig. 8, the modes shapes of the system are insensitive to the variations of tether inclination angle and PTO stiffness, hence the mode shape matrix can be approximated by:

$$\boldsymbol{\Psi} \approx \begin{pmatrix} -1 & 0.2 & 0 \\ 0 & 0 & 1 \\ 0 & -1 & 0 \end{pmatrix}. \tag{37}$$

Then applying the orthogonality of normal modes described in Section 2.3.2, the motion equation of the 3TSB PA system can be transformed to the following decoupled modal form:

$$\begin{pmatrix} m+a_{11} & 0 & 0 \\ 0 & I_{yy} & 0 \\ 0 & 0 & m+a_{33} \end{pmatrix} \ddot{\hat{\mathbf{q}}} + \begin{pmatrix} b_{11}+b_s+\frac{3}{2}B_{pto}\sin^2(\alpha) & 0 & 0 \\ 0 & \left(b_{11}+b_s+\frac{3}{2}B_{pto}\sin^2(\alpha)\right)/25 & 0 \\ 0 & 0 & b_{33}+b_h+3B_{pto}\cos^2(\alpha) \end{pmatrix} \dot{\hat{\mathbf{q}}} + \begin{pmatrix} \left(\frac{3}{2}\sin^2(\alpha)\left(K_{pto}+\frac{C_{pto}}{l_0}\right)-\frac{3C_{pto}}{l_0}\right) & 0 & 0 \\ 0 & \left(\frac{-3C_{pto}r(l_0+r)(\cos^2(\alpha)+1)}{2l_0}-\frac{6C_{pto}r\cos(\alpha)}{5l_0}\right) & 0 \\ & \left(-\frac{3}{50}\sin^2(\alpha)\left(K_{pto}+\frac{C_{pto}}{l_0}\right)-\frac{3C_{pto}}{25l_0}\right) & \\ 0 & 0 & \left(3\cos^2(\alpha)\left(K_{pto}+\frac{C_{pto}}{l_0}\right)-\frac{3C_{pto}}{l_0}\right) \end{pmatrix} \hat{\mathbf{q}} = \begin{pmatrix} -\hat{F}_s \\ \hat{F}_s/5 \\ \hat{F}_h \end{pmatrix}. \tag{38}$$

Equation (38) shows that the 3TSB PA system has control authority along all three modes, although Mode 2 is much less controllable than the other two modes. In order to absorb the maximum available power from waves, Mode 1 and Mode 3 are also required to satisfy the optimal amplitude conditions, as shown in the decoupled damping matrix in Equation (38):

$$\begin{aligned} \tfrac{3}{2}B_{pto}\sin^2(\alpha) &= b_{11}+b_s. \\ 3B_{pto}\cos^2(\alpha) &= b_{33}+b_h. \end{aligned} \tag{39}$$

Solving the system of two equations in Equation (39) across the wave frequency range, the frequency-dependent PTO damping and tether inclination angle that result in the optimal amplitude condition for Mode 1 and Mode 3 are obtained, as shown in Fig. 11. The required tether inclination angle varies between 43 and 60°, which conflicts with the previous finding that tether inclination angle should be always fixed at 54.5° to satisfy the optimal phase condition for Mode 1 and Mode 3 across the wave frequency range. Therefore, by having identical PTO characteristics (e.g. spring and damping) on all three tethers, Mode 1 (surge dominant) and Mode 3 (heave dominant) of the 3TSB PA system cannot be simultaneously and optimally controlled except when the

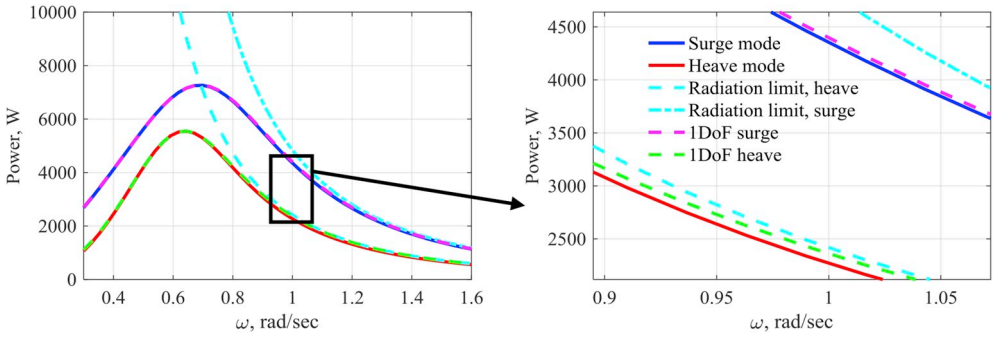

Fig. 12. Power absorbed by the surge (blue solid line) and heave (red solid line) modes of the 3TSB PA system under reactive control, subject to incident waves of 0.1 m amplitude and 0.3–1.5 rad/s frequencies; power bounds of the heave mode (cyan dashed line) and surge mode (cyan dashdot line) caused by radiation limit, P_{max}^{rad} defined by Equation (12); maximum power absorbed by a 1DoF surging buoy (magenta dashed line) and a 1DoF heaving buoy (green dashed line) with identical buoy parameters as the 3TSB PA. The corresponding RAO response of the 3TSB PA can be found in (Ding et al., 2018). (For interpretation of the references to colour in this figure legend, the reader is referred to the Web version of this article.)

system is excited by very low frequency waves. In this case, the determination of the frequency-dependent optimal PTO parameters for the 3TSB PA needs an additional numerical process (e.g. power optimisation), which is discussed in detail in (Ding et al., 2018) and (Sergiienko et al., 2016).

The power absorbed by the surge and heave modes of the reactively controlled system (with the optimised PTO parameters in (Ding et al., 2018)) subject to incident waves of 0.1 m amplitude and frequencies between 0.3 and 1.5 rad/s are calculated, with results shown in Fig. 12. Also plotted are the high frequency power bounds of the heave and surge modes due to the radiation limit of the buoy. In addition, the maximum power absorbed by a 1DoF surging buoy (assuming its PTO perfectly aligns with the surge axis) and a 1DoF heaving buoy with identical buoy parameters as the 3TSB PA are plotted for a benchmark. It is evident that the surge mode and heave mode of the 3TSB PA absorb slightly less power than the combination of a 1DoF surging buoy and a 1DoF heaving buoy, and thus absorb almost the maximum available power from waves. In general, the surge mode absorbs two times more power than the heave mode, except at low frequencies where the surge mode dissipates more power than the heave mode due to higher viscous losses ($b_s > b_h$). The power absorption curves of the surge and heave modes converge to the corresponding power radiation limits at high frequencies, where viscous losses are negligible compared to radiation loss ($b_{11} \gg b_s$ and $b_{33} \gg b_h$). In order to absorb the absolute maximum available power from waves, the 3TSB PA must have distinct PTO characteristics (e.g. spring and damping) on the three tethers.

5. Modal analysis on an asymmetric mass distribution spherical buoy PA

5.1. System description

The 3TSB PA system is almost able to absorb the maximum available power from waves, however its economic viability is governed by the manufacturing costs of the PTO machineries along the tethers. Thus, to reduce the costs associated with PTO machineries, Meng et al. (2017) proposed a single tether asymmetric mass distribution spherical buoy (1TAMDSB) PA, as shown in Fig. 13(a). The concept is to simply shift the buoy's centre of gravity away from its geometric centre to enhance dynamic coupling between the oscillating modes, and thus to provide control authority of all the modes from a single PTO, tether. Fig. 13(b) shows a cross section view of the 1TAMDSB PA system on the x-z plane that the buoy is symmetric about. The buoy consists of a spherical hull with a radius r and a mass m_h, and an additional mass m_o offset from the geometric centre of the buoy, resulting in an eccentric buoy centre of gravity on the x-z plane. The location of m_o on the x-z plane is defined by the offset distance r_o and the offset angle φ with respect to the positive x-axis. For the buoy to remain at rest in calm water, the PTO pretension (offset) force is given by

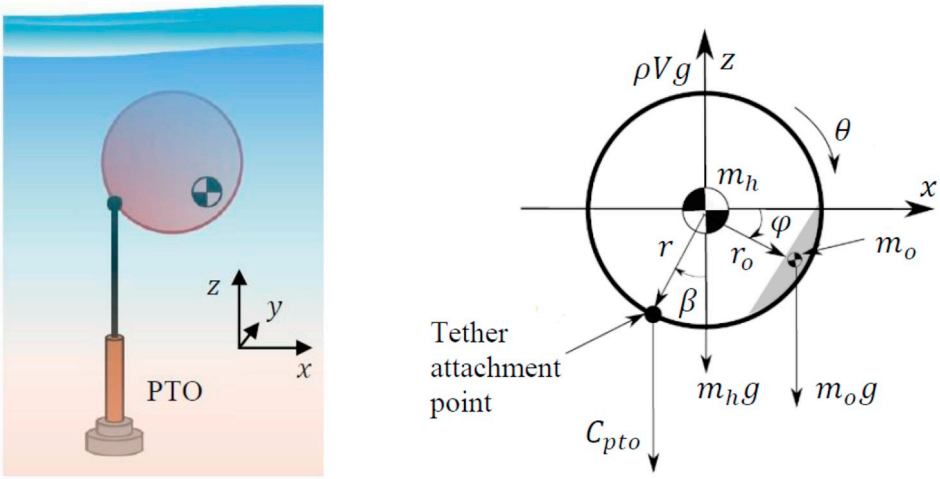

Fig. 13. Single tether asymmetric mass distribution spherical buoy PA (left) and schematic highlighting the buoy variables in the buoy Cartesian coordinates (right).

Table 2
Additional buoy parameters for the asymmetric mass distribution spherical buoy PA.

Symbol	Value/unit	Description
m_h	1.34×10^5kg	Hull mass for the buoy with asymmetric mass distribution
m_o	1.34×10^5kg	Offset mass for the buoy with asymmetric mass distribution
r_o	4 m	Offset distance of the offset mass m_o
φ	30°	Offset angle of the offset mass m_o
$I_{yy,o}$	4.383×10^6kg. m^2	Moment of inertia of a hollow spherical buoy with offset mass about its pitch axis, given by $I_{yy,o} = \frac{2}{3}m_h r^2 + m_o r_o^2$

$$C_{pto} = -(\rho V - m_h - m_o)g. \tag{40}$$

In addition, in order to balance the torque generated by the offset mass about the geometric centre of the buoy, the tether attachment point is rotated clockwise around the surface of the hull on the x-z plane. The line passing through the geometric centre of buoy and the tether attachment point forms an angle β with respect to the negative z-axis, which can be calculated by solving

$$C_{pto} r \sin(\beta) = m_o g r_o \cos(\varphi). \tag{41}$$

The system parameters are kept identical to the ones for the G1TSB and the 3TSB PA systems, except for the ones specific to the 1TAMDSB PA as listed in Table 2. The settings in Table 2 are optimal for the 1TAMDSB PA system subject to low frequency waves, and are used to demonstrate the application of modal analysis in evaluating a tightly coupled multi-mode WEC system.

5.2. Frequency domain model

The linearisation procedure for the 1TAMDSB PA is similar to the one for the G1TSB PA, as detailed in (Meng et al., 2019). The resulting mass, PTO damping and stiffness matrices associated with Equation (6) are given by:

$$\mathbf{M} = \begin{pmatrix} m_h + m_o & 0 & -m_o r_o \sin(\varphi) \\ 0 & m_h + m_o & -m_o r_o \cos(\varphi) \\ -m_o r_o \sin(\varphi) & -m_o r_o \cos(\varphi) & I_{yy,o} \end{pmatrix},$$

$$\mathbf{B}_{pto} = \begin{pmatrix} 0 & 0 & 0 \\ 0 & B_{pto} & B_{pto} r \sin(\beta) \\ 0 & B_{pto} r \sin(\beta) & B_{pto} r^2 \sin^2(\beta) \end{pmatrix},$$

$$\mathbf{K}_{pto} = \begin{pmatrix} -C_{pto}/l_0 & 0 & C_{pto} r \cos(\beta)/l_0 \\ 0 & K_{pto} & K_{pto} r \sin(\beta) \\ C_{pto} r \cos(\beta)/l_0 & K_{pto} r \sin(\beta) & \begin{pmatrix} -C_{pto} r \cos(\beta)(l_0 + r\cos(\beta))/l_0 \\ -m_o g r_o \sin(\varphi) + K_{pto} r^2 \sin^2(\beta) \end{pmatrix} \end{pmatrix} \tag{42}$$

Compared with the matrices for the G1TSB PA in Equation (27), $\mathbf{M}$, , and $\mathbf{K}_{pto}$ for the 1TAMDSB PA in Equation (42) exhibit additional couplings (e.g. heave-pitch and surge-pitch) due to the asymmetric mass distribution.

At the nominal position of the buoy, the inverse Jacobian matrix of the 1TAMDSB PA is given by:

$$\mathbf{J}(\mathbf{x}_o)^{-1} = (0 \quad 1 \quad r\sin(\beta)). \tag{43}$$

5.3. Natural frequencies and mode shapes

Substituting the mass and stiffness matrices $\mathbf{M}$, $\mathbf{A}(\omega)$ and $\mathbf{K}_{pto}$ into Equations (20) and (21), the eigenvalue problem for the 1TAMDSB PA system can be solved for varying nominal tether length l_0 and PTO stiffness K_{pto}. The resulting natural frequencies and mode shapes of the system are displayed in Fig. 14 as functions of the nominal tether length and the PTO stiffness. Fig. 14(a) shows two convex surfaces, denoting the natural frequencies of Mode 1 and Mode 3 respectively, which do not intersect but become extremely close, as shown in the zoomed-in area. This implies that Mode 1 and Mode 3 cannot be simultaneously tuned to resonance through varying the nominal tether length or PTO stiffness. Individually, Mode 1 can be tuned to resonance across the typical wave frequency range, whilst Mode 3 can only be tuned to resonance at frequencies between 0.3 and 0.8 rad/s. The natural frequency of Mode 2 is always higher than the typical wave frequency range, thus, Mode 2 is not considered in this analysis. The mode shapes of the 1TAMDSB PA system vary as the PTO characteristics change. As shown in Fig. 14(b), Mode 1 gradually switches from a heave dominant mode to a surge dominant mode, when the PTO stiffness and the nominal tether length are such that the natural frequencies of Modes 1 and 3 are almost equal. This region of optimality will be herein referred to as “the natural frequency asymptote”. Mode 3 shows a similar but opposite trend to Mode 1, as shown in Fig. 14(c), transitioning from a surge dominant mode to a heave dominant mode. Fig. 14(d) shows the contribution of Mode 1 and Mode 3 to the elongation of the single tether, mapped from the mode shapes by the inverse Jacobian matrix. It is evident that Mode 1 and Mode 3 have nearly equal contributions to the tether elongation near the natural frequency asymptote. The observations from Fig. 12 imply that the optimal combination of nominal tether length and PTO stiffness must exist near the natural frequency asymptote.

The natural frequencies and mode shapes of the 1TAMDSB system are also plotted in 2D in Fig. 15 for a better visualisation. The left subplots are for fixed $l_0/r = 5$ and varying K_{pto}/K_{hs}, while the right subplots are for fixed $K_{pto}/K_{hs} = 6$ and varying l_0/r. For very low wave frequency waves, Mode 1 and Mode 3 can almost be tuned to resonance simultaneously as evident by the tiny gap between the natural frequency surfaces as shown in the zoomed-in area in Fig. 14(a), which can be more clearly observed from Fig. 15(a). When both Mode 1 and Mode 3 operate near resonance, their mode shapes have almost equal Φ_z component and opposite Φ_x component as shown in Fig. 15(b), meaning that the two modes oscillate along the z axis (heave) with equal amplitude and equal phase, and oscillate along the x axis (surge) with equal amplitude but opposite phase, as illustrated in the buoy Cartesian coordinates in Fig. 16. Consequently, Mode 1 and Mode 3 have almost equal contributions to the tether elongation, as shown in Fig. 15(c), similar to the 3TSB PA. When the wave frequency increases, and thus the required natural frequencies of the modes increase, it becomes difficult to tune both modes into resonance, as shown in Figs. 14(a) and Fig. 15(d). In addition, it can be observed from Fig. 15(d), (e) and (f) that the optimal tether length occurring near the natural frequency asymptote is extremely short, as highlighted in the shaded grey regions where $l_0/r < 1$. This generates additional challenges in the practical PA design, and thus a nominal tether length lower limit is introduced for modal analysis (e.g. assuming l_0/r must be greater than 1). This limit further narrows down the wave frequency range within which Mode 1 can be tuned to resonance to between 0.3 and 0.7 rad/s. At the nominal tether length lower limit, Modes 1 and 3

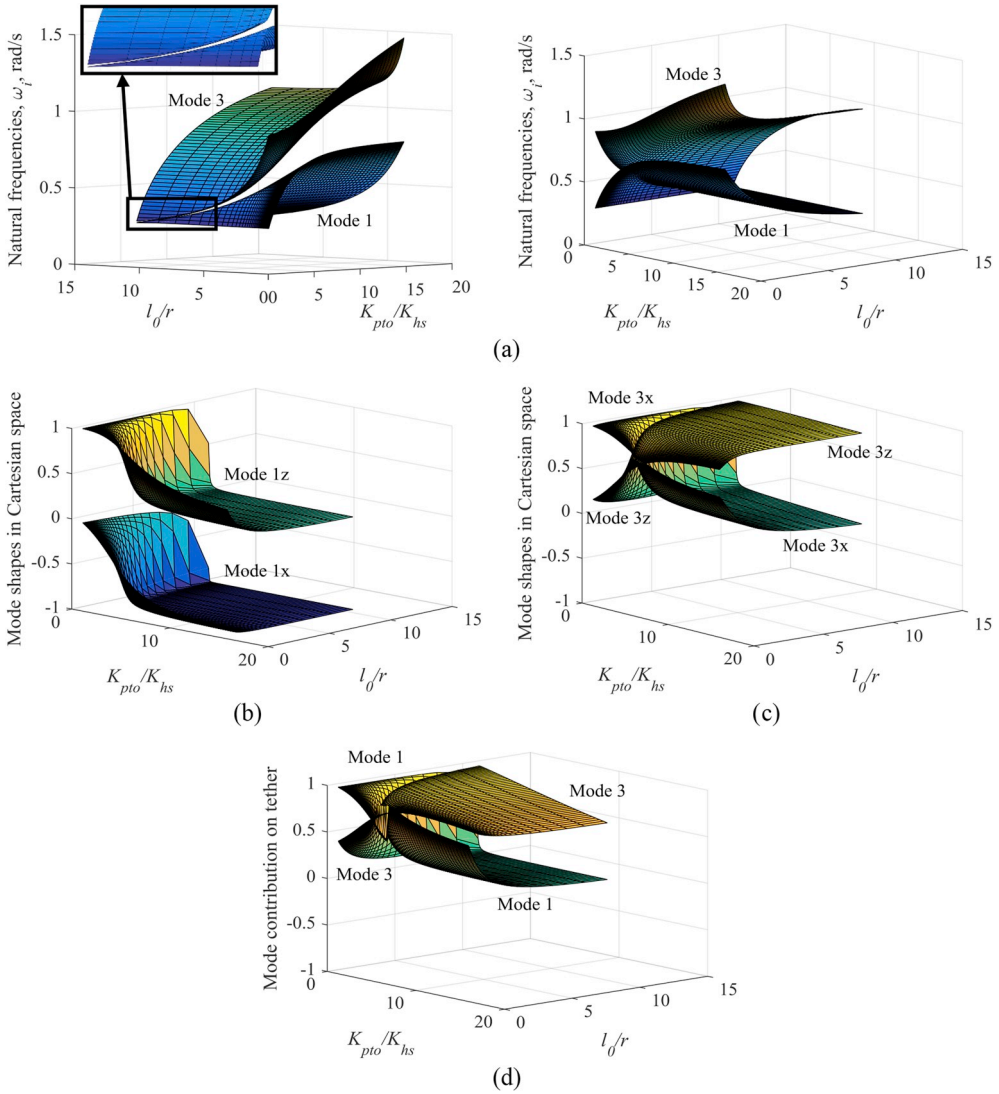

Fig. 14. Eigenanalysis on the single tether asymmetric mass distribution spherical buoy PA: (a) Natural frequencies of normal modes, ω_i, plotted from two different visual angles; (b) Mode shapes of Mode 1; (c) Mode shapes of Mode 3; (d) Contribution of Mode 1 and Mode 3 to tether elongation, vs. nominal tether length l_0 (normalised by buoy radius r) and PTO stiffness K_{pto} (normalised by the hydrostatic stiffness of a half-submerged buoy $K_{hs} = \rho\pi r^2$). In subplots (b), (c), and (d), yellow colour indicates value close to 1; green colour indicates values close to 0; and purple colour indicates value close to −1. (For interpretation of the references to colour in this figure legend, the reader is referred to the Web version of this article.)

start to show surge- and heave-dominant behaviour, as evident in Fig. 15(e), and Mode 3 contributes to more tether elongation than Mode 1, as evident in Fig. 15(f).

5.4. Optimality across wave frequencies

As the wave frequency increases, it is increasingly difficult to simultaneously tune Modes 1 and 3 into resonance, particularly Mode 1 which can only be tuned to resonance for wave frequencies up to 0.7 rad/s given the lower limit is applied to the nominal tether length ($l_0/r \geq 1$). Due to this limit, there is a trend that the mode shapes of Modes 1 and 3 rotate anticlockwise as wave frequency increases, from 45° with respect to the heave and surge spatial modes (as shown in Fig. 16) at very low frequencies to almost aligning with the heave and surge modes at high frequencies:

$$\boldsymbol{\Psi}_{0.4} \approx \begin{pmatrix} -0.7 & 0.2 & 0.7 \\ 0.7 & 0.7 & 0.7 \\ 0 & 0.7 & 0 \end{pmatrix} \rightarrow \boldsymbol{\Psi}_{0.7} \approx \begin{pmatrix} -1 & 0 & 0.3 \\ 0.3 & 0.7 & 1 \\ 0 & 0.6 & 0 \end{pmatrix} \rightarrow \boldsymbol{\Psi}_{1.2} \approx \begin{pmatrix} -1 & 0 & 0 \\ 0 & 0.8 & 1 \\ 0 & 0.5 & 0 \end{pmatrix}. \tag{44}$$

where the subscripts denote the corresponding wave frequency. Again, applying the orthogonality of normal modes, the following decoupled modal forms (without showing Mode 2 for the ease of comparison) are obtained for wave frequencies at 0.4, 0.7 and 1.2 rad/s, respectively.

For ω= 0.4 rad/s,

$$\begin{aligned} &\begin{pmatrix} m + 0.5a_{11} + 0.5a_{33} & 0 \\ 0 & m + 0.5a_{11} + 0.5a_{33} \end{pmatrix} \ddot{\hat{\mathbf{q}}} \\ &+ \begin{pmatrix} 0.5b_{w1} + 0.5b_{w3} + 0.5B_{pto} & 0 \\ 0 & 0.5b_{w1} + 0.5b_{w3} + 0.5B_{pto} \end{pmatrix} \dot{\hat{\mathbf{q}}} \\ &+ \begin{pmatrix} -0.5C_{pto}/l_0 + 0.5K_{pto} & 0 \\ 0 & -0.5C_{pto}/l_0 + 0.5K_{pto} \end{pmatrix} \hat{\mathbf{q}} \\ &= \begin{pmatrix} -0.7\hat{F}_s + 0.7\hat{F}_h \\ 0.7\hat{F}_s + 0.7\hat{F}_h \end{pmatrix}. \end{aligned} \tag{45}$$

For ω= 0.7 rad/s,

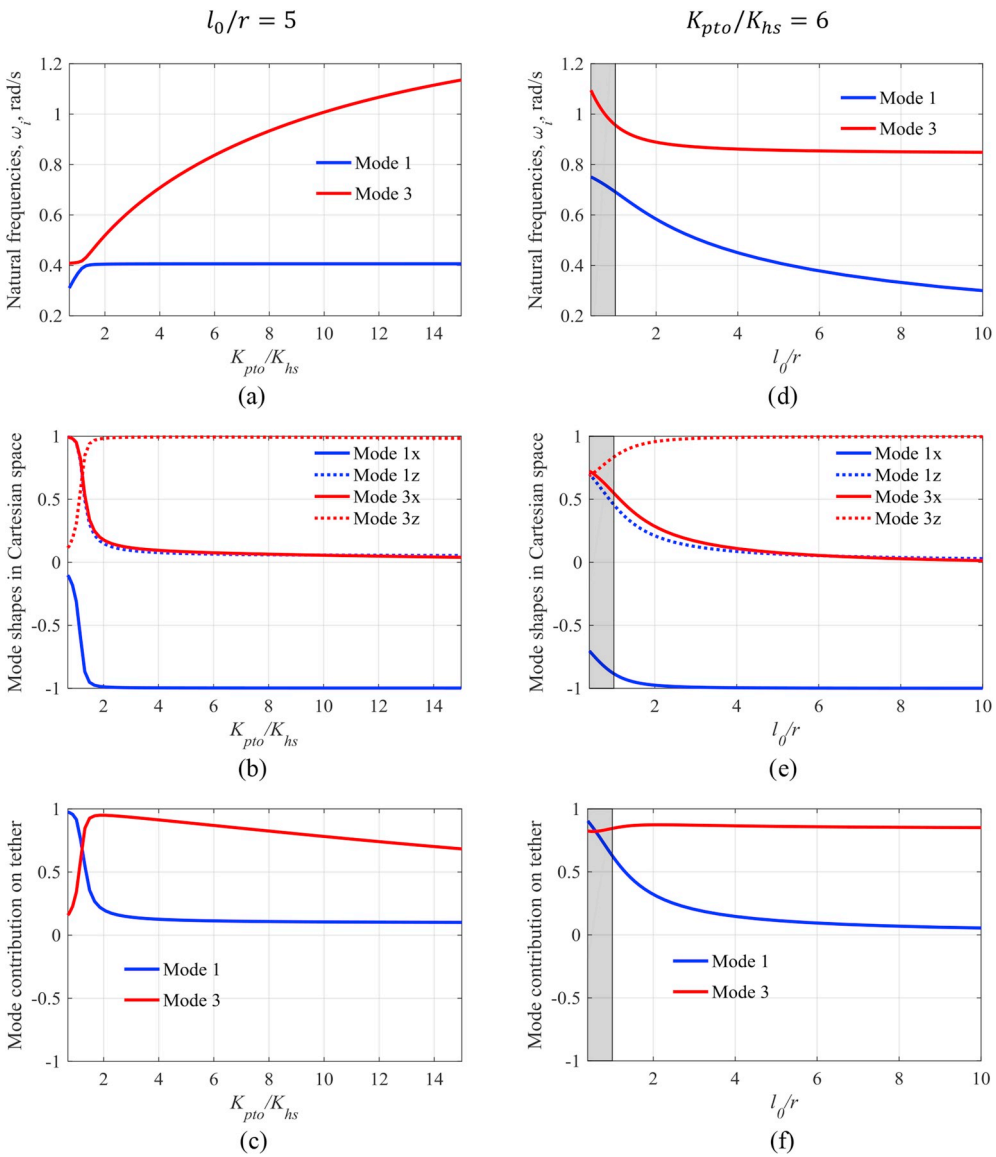

Fig. 15. Eigenanalysis on the single tether asymmetric mass distribution spherical buoy PA: (a), (b) and (c) on the left hand side show the natural frequencies, mode shapes, and contribution of modes to tether elongation, respectively, vs. PTO stiffness K_{pto}, when l_0/r is 5; (d), (e) and (f) on the right hand side show the natural frequencies, mode shapes, and contribution of modes to tether elongation, respectively, vs. nominal tether length l_0, when K_{pto}/K_{hs} is 6. The grey region denotes the impractical case where $l_0/r < 1$

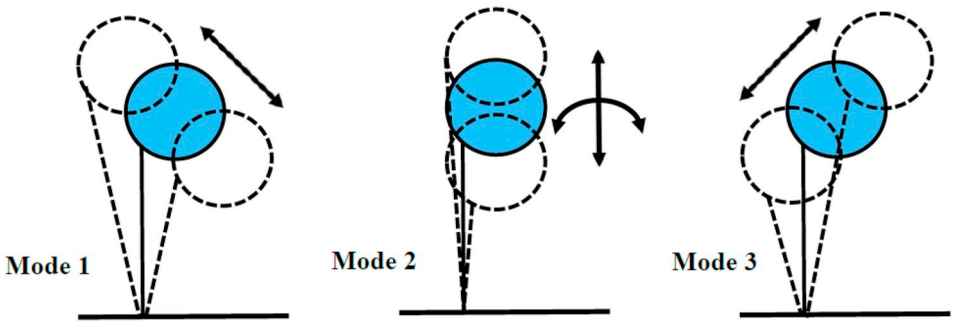

Fig. 16. Graphical representation of Modes 1, 2 and 3 in the buoy Cartesian coordinates for the single tether asymmetric mass distribution spherical buoy PA at the natural frequency asymptote. Mode 1 oscillates predominantly along surge and heave with equal amplitude but opposite phase. Mode 3 oscillates predominantly along surge and heave with equal amplitude and equal phase. Mode 2 oscillates predominantly along heave and pitch with equal amplitude and equal phase. The natural frequency of Mode 2 is much higher than the wave frequency range so Mode 2 barely contributes to power absorption.

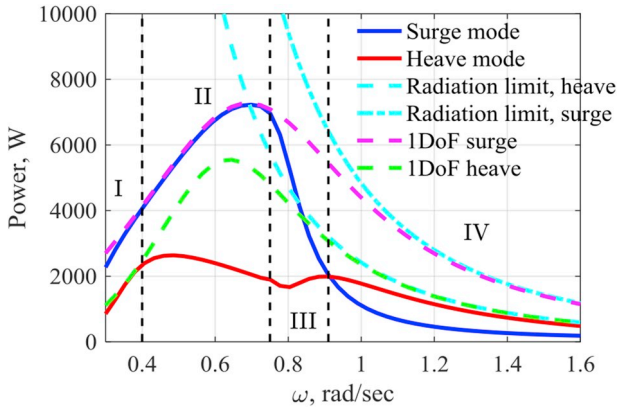

Fig. 17. Power absorbed by the surge (blue solid line) and heave (red solid line) modes of the 1TAMDSB PA system under reactive control, subject to incident waves of 0.1 m amplitude and 0.3–1.5 rad/s frequencies; power bound of the heave mode (cyan dashed line) and surge mode (cyan dashdot line) caused by radiation limit, P_{max}^{rad} defined by Equation (12); maximum power absorbed by a 1DoF surging buoy (magenta dashed line) and a 1DoF heaving buoy (green dashed line) with identical buoy parameters as the 1TAMDSB PA. Black dashed vertical lines divide the frequency-dependent performance of the PA into four regions that have distinct modal behaviour. The corresponding RAO response of the 1TAMDSB PA can be found in (Ding et al., 2018). (For interpretation of the references to colour in this figure legend, the reader is referred to the Web version of this article.)

$$\begin{pmatrix} 1.1m + a_{11} + 0.1a_{33} & 0 \\ 0 & 1.1m + 0.1a_{11} + a_{33} \end{pmatrix}\ddot{\hat{\mathbf{q}}} + \begin{pmatrix} b_{w1} + 0.1b_{w3} + 0.1B_{pto} & 0 \\ 0 & 0.1b_{w1} + b_{w3} + B_{pto} \end{pmatrix}\dot{\hat{\mathbf{q}}} + \begin{pmatrix} -C_{pto}/l_0 + 0.1K_{pto} & 0 \\ 0 & -0.1C_{pto}/l_0 + K_{pto} \end{pmatrix}\hat{\mathbf{q}} = \begin{pmatrix} -\hat{F}_s + 0.3\hat{F}_h \\ 0.3\hat{F}_s + \hat{F}_h \end{pmatrix}. \tag{46}$$

For ω= 1.2 rad/s,

$$\begin{pmatrix} m + a_{11} & 0 \\ 0 & m + a_{33} \end{pmatrix}\ddot{\hat{\mathbf{q}}} + \begin{pmatrix} b_{w1} & 0 \\ 0 & b_{w3} + B_{pto} \end{pmatrix}\dot{\hat{\mathbf{q}}} + \begin{pmatrix} -C_{pto}/l_0 & 0 \\ 0 & K_{pto} \end{pmatrix}\hat{\mathbf{q}} = \begin{pmatrix} -\hat{F}_s \\ \hat{F}_h \end{pmatrix}. \tag{47}$$

where $m = m_h + m_o$, $b_{w1} = b_{11} + b_s$, and $b_{w3} = b_{33} + b_h$. The modal form in Equation (45) shows that at ω= 0.4 rad/s Mode 1 and Mode 3 have almost identical motion equations and are affected almost equally by the PTO control parameters, B_{pto} and K_{pto}, considering round-off errors in the mode shapes used for the transformation. This indicates that Modes 1 and 3 can be simultaneously tuned close to their optimal operating conditions for very low frequency waves, and thus can absorb nearly the maximum available wave power. In contrast, the modal form in Equation (46) for ω= 0.7 rad/s shows two distinct motion equations (as evident by the distinct diagonal terms in the matrices) controlled by the same PTO parameters. Thus a compromise exists in tuning both Modes 1 and 3 to their optimal operating conditions for low to medium frequency waves. For example, it is evident in the modal damping matrix that the PTO damping B_{pto} required to tune Modes 1 and 3 to the optimal amplitude condition exhibits a difference in the order of one magnitude. Mode 1 can absorb more power than Mode 3, as Mode 1 couples more with the surge mode, as evident from the modal excitation force in Equation (46). Therefore, Mode 1 has the priority to be tuned to the optimal operating condition whenever possible for low to medium frequency waves. The modal form in Equation (47) for ω= 1.2 rad/s is almost (to the limit of the round-off errors in the mode shapes for transformation) identical to the modal form of the G1TSB PA system, and thus can only absorb about one third of the maximum available wave power for high frequency waves. The exact frequency-dependent optimal PTO parameters for the 1TAMDSB PA were determined by numerical optimisation, as discussed in detail in (Ding et al., 2018).

The power absorbed by the surge and heave modes of the reactively controlled system subject to incident waves of 0.1 m amplitude and frequencies between 0.3 and 1.5 rad/s are calculated, with results shown in Fig. 17. The optimal PTO parameters determined in (Ding et al., 2018) are adopted. Also plotted are the radiation limit power bounds and the maximum power absorbed by a 1DoF heaving buoy and a 1DoF surging buoy (assuming its PTO perfectly aligns with the surge axis), for a benchmark. It is evident that optimisation results match the conclusions made from modal analysis for the 1TAMDSB PA. At very low frequencies (Region I), the PA absorbs nearly the maximum power from waves similar to the 3TSB PA. Between low and medium frequencies (Region II), the PA can only tune Mode 1 (surge dominant) into the optimal operating condition and therefore can absorb full power from the surge mode and partial power from the heave mode. When the wave frequency further increases (into Region III), the PA can no longer achieve the optimal operating condition for Mode 1 and thus decreases power absorption from Mode 1 while increases power absorption from Mode 3. Finally at high frequencies (Region IV), the PA switches to absorb power from the heave mode dominantly, and thus approaches the performance of the G1TSB PA.

6. Conclusion

This paper introduced the application of modal analysis in the design of multi-mode WECs and used three submerged PA systems with distinct modal behaviour as case studies to illustrate the procedure and the efficacy of the method. The natural frequencies and the mode shapes of normal modes were used to understand the phase condition of the spatial modes of the systems. The decoupled modal form was used to understand the amplitude condition of the spatial modes and the controllability of the systems. Both the phase and the amplitude conditions associated with modes determine the power absorption potential of the multi-mode WEC design. Controllability further suggests the compromise faced in multi-mode control and thus the limit of the proposed design concepts.

Modal analysis provided an in-depth understanding on the three multi-mode submerged PA systems. The single tether generic spherical buoy PA demonstrates an extremely controllable mode (Mode 3, heave-dominant) that contributes to 100% of WEC power absorption, as well as two barely controllable modes (Mode 1, surge-dominant, and Mode 2, pitch-dominant) that should be designed off-resonance to increase system durability. This PA design can only efficiently operate in heave, and this is constrained to absorb one third of the maximum power from the waves. The three tether spherical buoy PA, in contrast, while exhibiting similar modal behaviour (e.g. mode shapes) to the single tether generic spherical buoy PA, shows almost equal control authorities along Mode 1 (surge dominant) and Mode 3 (surge dominant) at the optimal tether inclination angle of 54.5°. Whilst having identical PTO characteristics on all three tethers does not allow the PA to achieve the absolute optimal phase and amplitude conditions for both modes, the three tether spherical buoy PA is able to extract nearly the maximum available power from waves. Finally, the single tether asymmetric mass distribution spherical buoy PA shows complex modal behaviour that is wave frequency dependent due to the nature and physical limits of the design. For very low frequency waves, Modes 1 and 3 are both surge-heave coupled modes, which can be almost simultaneously tuned to optimal, leading to power absorption capability similar to the three tether spherical buoy PA. For low to medium frequency waves, Mode 1 becomes surge-dominant and Mode 3 becomes heave-dominant, which

results a trade-off in tuning both modes close to their optimal. Therefore, Mode 1 (surge-dominant) is optimally controlled as a priority in this wave frequency range as it absorbs more power from waves. For high frequency waves, Mode 1 (surge-dominant) can no longer be tuned to the optimal phase condition, and thus Mode 3 (heave-dominant) is optimally controlled instead, resulting in power absorption performance approaching the single tether generic spherical buoy PA.

In summary, modal analysis was proven to be an efficient analytical approach that can be used to assess and understand the optimality and the limit of the multi-mode PA design in an early conceptual design stage, before more in-depth studies are conducted using time-consuming numerical simulation (e.g. CFD) and fine tuning optimisation under more realistic wave conditions (e.g. larger wave amplitudes and irregular waves) (Li and Yu, 2012; Pastor and Liu, 2014; Rafiee and Fievez, 2015; L Xu et al., 2018). Modal analysis can also be used to assist the interpretation of the optimisation results, which are usually not intuitive for complex multi-mode PA systems operating in several DoFs, particularly in the stage of wave-to-wire development where the system model becomes more complex by involving additional moving parts (e.g. moving components of the PTO transmission system) (Ding et al., 2016). The main limitation of the modal analysis method is that the PA system under investigation must meet the conditions of linear wave theory and small motion assumption for the approach to be accurate. Both these condition are strongly dependent on the system settings and the wave condition. Future work will focus on defining the fidelity region of modal analysis for typical multi-mode PA designs, within which an accurate estimation to the PA behaviour in practice can be achieved by modal analysis. Future work will also attempt to extend the modal analysis approach towards the spectrum domain (Folley and Whittacker, 2010) for the study of WEC systems subject to nonlinear waves and nonlinear system dynamics.

Acknowledgement

This research has been supported by the Australian Commonwealth Research Training Program, Chinese Scholarship Council, Linkage Project LP130100117 funded by the Australian Research Council, and the Strategic Research Initiative Fund awarded by the Institute for Mineral and Energy Resources at the University of Adelaide.

Appendix A. Supplementary data

Supplementary data to this article can be found online at https://doi.org/10.1016/j.oceaneng.2018.11.058.

References

Babarit, A., Hals, J., Muliawan, M., Kurniawan, A., Moan, T., Krokstad, J., 2011. "Numerical Estimation of Energy Delivery from a Selection of Wave Energy Converters – Final Report," Report. Ecole Centrale de Nantes and Norges Teknisk-Naturvitenskapeige Universitet.
Babarit, A., Singh, J., Melis, C., Wattez, A., 2017. A linear numerical model for analyzing the hydroelastic response of a flexible electroactive wave energy converter. J. Fluid Struct. 74, 356–384.
Benaroya, H., 1998. Mechanical Vibration – Analysis, Uncertainties, and Control. Prentice-Hall, Simon & Schuster/A Viacom Company, Upper Saddle River, NJ, USA.
Blevins, R.D., 2003. Applied Fluid Dynamics Handbook. Krieger Publishing Company.
Budal, K., Falnes, J., 1975. A resonant point absorber of ocean-wave power. Nature 256 (5517), 478–479.
Cruz, J., 2008. Ocean Wave Energy: Current Status and Future Perspectives, Green Energy and Technology. Springer Berlin Heidelberg, Berlin.
Cummins, W.E., 1962. The Impulse Response Function and Ship Motions. Department of the Navy – David Taylor Model Basin Report 1661.
Ding, B., Cazzolato, B.S., Arjomandi, M., Hardy, P., Mills, B., 2016. Sea-state based maximum power point tracking damping control of a fully submerged oscillating buoy. Ocean. Eng. 126, 299–312.
Ding, B., Sergiienko, N.Y., Meng, F., Cazzolato, B.S., Hardy, P., Arjomandi, M., 2018. Enhancing the relative capture width of submerged point absorbing wave energy converters. In: Proc. of the 4th Asian Wave and Tidal Energy Conference.
Evans, D.V., 1976. A theory for wave-power absorption by oscillating bodies. J. Fluid Mech. 77 (1), 1–25.
Falnes, J., 2002. Ocean Waves and Oscillating Systems: Linear Interactions Including Wave-energy Extraction. Cambridge University Press.
Falnes, J., Hals, J., 1959. Heaving buoys, point absorbers and arrays. Philosoph. Transact., Roy. Soc. Series A, Math., Phys., Eng. Sci. 370, 246–277 2012.
Farley, F.J.M., 1982. Wave energy conversion by flexible resonant rafts. Appl. Ocean Res. 4 (1), 57–63.
Finnegan, W., Goggins, J., 2012. The structural dynamics of a two-body wave energy converter. In: Proc. Of the 4th International Conference on Ocean Energy.
Folley, M., Whittacker, T., 2010. Spectral modelling of wave energy converters. Coast Eng. 57 (10), 892–897.
Folley, M., Whittaker, T., van't Hoff, J., 2007. The design of small seabed-mounted bottom-hinged wave energy converters. In: Proc. of 7th European Wave and Tidal Energy Conference. EWTEC.
Hayward, J., Osman, P., 2011. "The Potential of Wave Energy," Report. CSIRO.
He, J., Fu, Z., 2001. Modal Analysis. Butterworth-Heinemann, Linarce House, Jordan Hill, Oxford, MA, USA.
International Energy Agency, 2011. "Deploying Renewables – Best and Future Policy Practice," Report. International Energy Agency.
Xu, Q.L., Li, Y., Lin, Z.L., 2018. An improved boundary element method for modelling a self-reacting point absorber wave energy converter. Acta Mech. Sin. 34 (6), 1015–1034.
Li, Y., Yu, Y.H., 2012. A synthesis of numerical methods for modeling wave energy converter-point absorbers. Renew. Sustain. Energy Rev. 16 (6), 4352–4364.
Linton, C.M., 1991. Radiation and diffraction of water waves by a submerged sphere in finite depth. Ocean. Eng. 18 (12), 61–74.
Meng, F., Rafiee, A., Cazzolato, B.S., Ding, B., Arjomandi, M., Piper, J., Sergiienko, N.Y., Hu, Q., 2017. Numerical simulation of a submerged spherical point absorber with asymmetric mass distribution. In: Proc. of the 12th European Wave and Tidal Energy Conference.
Meng, F., Ding, B., Cazzolato, B.S., Arjomandi, M., 2019. Modal analysis of a submerged spherical point absorber with asymmetric mass distribution. Renew. Energy 130, 223–237.
Morison, J., Johnson, J., Schaaf, S., 1950. The force exerted by surface waves on piles. J. Petrol. Technol. 2 (5), 149–154.
Newman, J.N., 1979. Absorption of wave energy by elongated bodies. Appl. Ocean Res. 1 (4), 189–196.
Pastor, J., Liu, Y.C., 2014. Frequency and time domain modeling and power output for a heaving point absorber wave energy converter. Int. J. Energy Environ. Eng. 5, 101.
Pecher, A., Kofoed, J.P., 2017. Handbook of Ocean Wave Energy. Springer Nature Springer International Publishing AG Switzerland.
Rafiee, A., Fievez, J., 2015. Numerical prediction of extreme loads on the CETO wave energy converter. In: Proc. of the 11th European Wave and Tidal Energy Conference.
Ringwood, J.V., Bacelli, G., Fusco, F., 2014. Energy-maximizing control of wave-energy converters: the development of control system technology to optimize their operation. IEEE Contr. Syst. Mag. 34 (5), 30–55.
Salter, S.H., 1974. Wave power. Nature 249 (5459), 720–724.
Sergiienko, N.Y., 2018. "Three-tether Wave Energy Converter: Hydrodynamic Modelling, Performance Assessment and Control," PhD Thesis. the University of Adelaide.
Sergiienko, N.Y., Cazzolato, B.S., Ding, B., Arjomandi, M., 2016. An optimal arrangement of mooring lines for a three-tether submerged point-absorbing wave energy converter. Renew. Energy 93, 23–37.
Sergiienko, N.Y., Cazzolato, B.S., Ding, B., Hardy, P., Arjomandi, M., 2017. Performance comparison of the floating and fully submerged quasi-point absorber wave energy converters. Renew. Energy 108, 425–437.
Sergiienko, N.Y., Rafiee, A., Cazzolato, B.S., Ding, B., Arjomandi, M., 2018. Feasibility study of the three-tether axisymmetric wave energy converter. Ocean. Eng. 150, 221–233.
Srokosz, M.A., 1979. The submerged sphere as an absorber of wave power. J. Fluid Mech. 95 (4), 717–741.
Taghipour, R., Moan, T., 2008. Efficient frequency-domain analysis of dynamic response for the multi-body wave energy converter in multi-directional waves. In: Proc. Of the 18th International Offshore and Polar Engineering Conference.

Appendix F

Comparison of wave-body interaction modelling methods for the study of reactively controlled point absorber wave energy converters

Ding, B., Wuillaume, P., Meng, F., Babarit, A., Schubert, B., Sergiienko, N., Cazzolato, B. (2019). "Comparison of wave-body interaction modelling methods for the study of reactively controlled point absorber wave energy converter". In: *The 34nd International Workshop on Water Waves and Floating Bodies (IWWWFB)*. Newcastle, Australia. pp. 1 - 4.

Statement of Authorship

Publication Status	Published
Name of Co-author	Fantai Meng
Contribution to the Paper	Helped to develop the mathematical model of the single-tether point absorber with asymmetric mass distribution, helped in interpretation of obtained results.
Overall Percentage (%)	10%

Statement of Authorship

Title of Paper	Comparison of wave-body interaction modelling methods for the study of reactively controlled point absorber wave energy converter
Publication Status	☑ Published ☐ Accepted for Publication ☐ Submitted for Publication ☐ Unpublished and Unsubmitted w ork w ritten in manuscript style
Publication Details	Ding, B., Wuillaume, P., Meng, F., Babarit, A., Schubert, B., Sergiienko, N., Cazzolato, B. (2019). "Comparison of wave-body interaction modelling methods for the study of reactively controlled point absorber wave energy converter". *The 34nd International Workshop on Water Waves and Floating Bodies (IWWWFB)*. Newcastle, Australia. pp. 1 - 4.

Principal Author

Name of Principal Author (Candidate)	Boyin Ding		
Contribution to the Paper	Developed the idea and concepts, developed the numerical models, wrote the code of simulations, interpreted the results, wrote the manuscript and acted as a corresponding author.		
Overall percentage (%)	75%		
Certification:	This paper reports on original research I conducted during the period of my Higher Degree by Research candidature and is not subject to any obligations or contractual agreements with a third party that would constrain its inclusion in this thesis. I am the primary author of this paper.		
Signature		Date	28/8/19

Co-Author Contributions

By signing the Statement of Authorship, each author certifies that:

i. the candidate's stated contribution to the publication is accurate (as detailed above);

ii. permission is granted for the candidate in include the publication in the thesis; and

iii. the sum of all co-author contributions is equal to 100% less the candidate's stated contribution.

Name of Co-Author	Pierre-Yves Wuillaume		
Contribution to the Paper	Supervised the work, helped in interpretation of obtained results, and provided a critical revision of the manuscript.		
Signature		Date	27/08/2019

Name of Co-Author	Fantai Meng		
Contribution to the Paper	Helped to develop the mathematical model of the single-tether point absorber with asymmetric mass distribution, helped in interpretation of obtained results.		
Signature		Date	21/8/19

Name of Co-Author	Aurélien Babarit		
Contribution to the Paper	Supervised the work, helped in interpretation of obtained results, and provided a critical revision of the manuscript.		
Signature		Date	27/8/19

Name of Co-Author	Benjamin Schubert		
Contribution to the Paper	Supervised the work, helped in interpretation of obtained results, and provided a critical revision of the manuscript.		
Signature		Date	28/8/19

Name of Co-Author	Nataliia Sergiienko		
Contribution to the Paper	Supervised the work, helped in interpretation of obtained results, and provided a critical revision of the manuscript.		
Signature		Date	27/08/2019

Name of Co-Author	Benjamin Cazzolato		
Contribution to the Paper	Supervised the work, helped in interpretation of obtained results, and provided a critical revision of the manuscript.		
Signature		Date	27/8/19

Please cut and paste additional co-author panels here as required.

Comparison of wave-body interaction modelling methods for the study of reactively controlled point absorber wave energy converter

Boyin Ding[1], Pierre-Yves Wuillaume[2], Fantai Meng[1], Aurélien Babarit[2], Benjamin Schubert[1], Nataliia Sergiienko[1], Benjamin Cazzolato[1]

[1]Ocean Wave Energy Research Group, Faculty of Engineering, Computer and Mathematical Sciences, the University of Adelaide, Australia, boyin.ding@adelaide.edu.au

[2]Ocean Waves and Marine Renewable Energy Group, LHEEA, Ecole Centrale de Nantes - CNRS, France, aurelien.babarit@ec-nantes.fr

1. INTRODUCTION

Ocean waves are a huge resource of renewable energy for utilisation. Wave energy converter (WEC) devices are being developed to enable capture of this energy resource. In the late 1980s, the principle of extraction energy from waves was studied (Falnes, 2007) and it showed that reactive control can increase significantly wave power extraction for a heaving point-absorber. Since then, studies on the control strategies and their implementations have been a focus in the field of wave energy research (Ringwood, 2014).

Majority of the wave energy control studies used linear potential flow theory and Cummins equation as the basis for modelling hydrodynamics arising from wave-body interaction, which is essential for the implementation of control simulation as well as for the formulation of model-based control strategies (Penalba, 2016). Although this simplifies/linearises the control problem as well as speeds up the simulation process, the utilisation of linear solver (which assumes that the wave steepness and body motion are both small) contradicts the large motion arising from the reactively controlled wave energy converter and thus does not ensure the fidelity of the control simulation results in medium to large wave conditions. On the extreme opposite, the Navier-Stokes equation based CFD captures the full nonlinear hydrodynamics in the wave-body interaction problem leading to high fidelity simulation results regardless of the system operational conditions, however, is barely used in the study of wave energy converter control due to its high computational requirement. Compromise between the linear method and the Navier-Stokes solver also exists (Wuillaume, 2019). A typical example is the weak-scatterer potential flow method proposed for seakeeping analysis of ship with forward speed (Pawlowski, 1991), which is formulated based on the assumption that the perturbation wave field generated by the body oscillation is small compared to the incident wave field, such as the free surface conditions can be linearised at the incident wave elevation level. The weak-scatterer method takes into account the unsteady and nonlinear hydrodynamic loads associated with dynamic wave-body interaction as long as the aforementioned assumption is satisfied and that viscosity effects remain negligible. However, it remains questionable if the weak-scatterer method is suitable for solving wave energy converter control problem where large perturbation wave field is expected given the large resonant motion of the body. A further simplified version of the weak-scatterer method is the body-exact potential method that assumes the free surface conditions can be linearised around the mean free surface elevation $z = 0$. This solver was proposed to account for the body motion induced nonlinearities but is only valid when small steepness waves are present. It is a compromise between the weak-scatterer method and the linear method.

The proposed study intends to conduct a comparison study on the aforementioned four wave-body interaction modelling methods in terms of their fidelity in solving the reactive control problem of a submerged point-absorber (PA) WEC.

2. WAVE-BODY INTERACTION MODELLING METHODS

Table 1 summarises the main differences between the four wave-body interaction modelling methods.

1) Navier-Stokes equation (CFD) solver: Navier-Stokes equations are a set of partial differential equations that describe the motion of fluids as a relationship between flow velocity (or momentum) and pressure. For the incompressible sea water, the Navier-Stokes equations can be written in the general form as:

$$\rho\left(\partial\mathbf{u}/\partial t + \mathbf{u}\cdot\nabla\mathbf{u}\right) = -\nabla p + \nabla\cdot(\mu\nabla\mathbf{u}) + \mathbf{f} \tag{1a}$$

$$\nabla \cdot \mathbf{u} = 0 \tag{1b}$$

where $\mathbf{u}$, ρ, p, μ and $\mathbf{f}$ are the velocity vector, density, pressure, dynamic viscosity and external force (e.g. gravity force) and ∇ is the gradient operator. Solving Equation (1) stepwise across the computational domain of the numerical wave tank under boundary conditions and integrating the total stress over the wetted body surface $S_B(t)$ result in the total hydrodynamic force acting on the body (Meng, 2017). The advantage of CFD solvers are that they are not based on any linearisation assumption, take into account the real fluid viscosity, can accommodate turbulence effects and other nonlinear phenomena that may occur during a simulation. However, these benefits come at a cost of high level of complexity and very high computation time relative to linear models. In this study, the OpenFOAM package (e.g. OLAFOAM and interFoam utility) forms the CFD solver (specifically the Reynold-averaged Navier-Stokes model) as described by Meng et al. (2017).

2) Weak-scatterer potential flow (WSP) solver: The potential flow theory was established based on the assumptions that the fluid is irrotational, incompressible and inviscid. Without considering the viscosity and turbulence, the potential flow theory introduced the velocity potential ϕ, the only one scalar function that is necessary to compute the three dimensional fluid velocity. Thus, the velocity potential can be evaluated using a boundary element method and the total pressure can be solved from the Bernoulli's equation (Wuillaume, 2019):

$$p = -\rho\left(\frac{\partial \phi}{\partial t} + \frac{1}{2}\nabla\phi \cdot \nabla\phi + gz\right) \tag{2}$$

where $-\rho gz$ is the hydrostatic pressure. The total dynamic force acting on the body is then calculated by integrating the total pressure over the instantaneous wetted surface of the body $S_B(t)$. Due to the high computational demand associated with the fully nonlinear potential flow method in solving the real varying intersection curves between the free surface and bodies, decomposition of the velocity potential and the wave elevation into incident and perturbed quantities were applied and the weak-scatterer hypothesis was proposed (Pawlowski et al., 1991). It assumed the perturbed quantities are small compared to the incident quantities:

$$\begin{cases} \phi = \phi^I + \phi^P \\ \phi^P = \mathcal{O}(\phi^I) \end{cases}. \tag{3}$$

In this case, the free surface boundary equations are linearised around the known incident free surface elevation $z = \eta^I(x, y, t)$. Thus, the perturbed waves are not required to be meshed which largely reduce computational demand. Due to the free surface conditions, wave breaking cannot be modelled. In this study, the *WS_CN* numerical tool as described in detail by Wuillaume (2019) will be used as the WSP solver.

3) Body-exact potential flow (BEP) solver: The potential flow theory based solver can be further simplified under small wave conditions (e.g. wave steepness, $\epsilon \ll 1$). Thus, the free surface conditions can be linearised around the mean surface elevation $z = 0$. This forces the free surface mesh remain planar, which enables a faster mesh convergence and reduction of computing time. The pressure is integrated over the wetted body surface $S_B(t)$ subject to "body-exact" motion and delimited by the mean wave elevation. In the *WS_CN* numerical tool, an option of linearising the free surface conditions around the mean surface elevation exists and thus the *WS_CN* numerical tool can be configured as the BEP solver for use in this study.

4) Linear potential flow (LP) solver: The potential flow theory based solver can be simplified to its neatest form, by assuming that wave steepness, ϵ, is small and the body undergoes small amplitude motion, A_m. Consequently, the free surface conditions can be linearised around the mean free surface elevation $z = 0$ and the body meshes are fixed at the rest position of the body. This leads to a linearised model, where the perturbed component can be further decomposed into a diffraction component and a radiation component:

$$\begin{cases} \phi = \phi^I + \phi^D + \phi^R \\ \epsilon \ll 1,\ A_m \ll 1 \end{cases}. \tag{4}$$

The elementary problems for these velocity potentials are solved and the total hydrodynamic force is obtained by summing the excitation force and the radiation force. The linearised model can be solved either in the time domain (Cummins, 1962) or in the frequency domain, with hydrodynamic functions/coefficients (e.g. added mass, radiation damping and excitation force) pre-calculated using boundary element solver (e.g. WAMIT, NEMOH, Aquaplus). Surface piercing (e.g. when a fully submerged buoy pierces the free surface) cannot be modelled in this case given the linearised surface and body conditions. In this study, a frequency-domain based linear solver is applied (Ding, 2018).

Table 1. Main differences between the four wave-body interaction modelling methods

	Linear potential flow solver	**Body-exact potential flow solver**	**Weak-scatterer potential solver**	**Navier-Stokes based CFD solver**
Assumption	$\begin{cases}\text{Irrotational and inviscid fluid,}\\ \epsilon \ll 1,\\ A_m \ll 1\end{cases}$	$\begin{cases}\text{Irrotational and inviscid fluid,}\\ \epsilon \ll 1\end{cases}$	$\begin{cases}\text{Irrotational and inviscid fluid,}\\ \phi^P = \mathcal{O}(\phi^I)\end{cases}$	Isotropic fluid
Hydrodynamics decomposition	$\phi = \phi^I + \phi^D + \phi^R$	$\phi = \phi^I + \phi^P$		NA
Meshed free surface	$z = 0$		$z = \eta^I(x,y,t)$	$z = \eta(x,y,t)$
Meshed body surface	$S_B(0)$	$S_B(t)$		
Hydrodynamic force computation	Sum of excitation and radiation forces	Integration of total pressure over the wetted body surface		Integration of total stress over the wetted body surface
Fluid vortices	NO			YES
Wave breaking	NO			YES
Drag force	NO, a Morison-like term $-0.5\rho C_D A\lvert\dot{z}_b - \dot{z}_f\rvert(\dot{z}_b - \dot{z}_f)$ can be added			YES
Surface piercing	NO	YES		
Computational speed	Extremely fast	Medium	Slow	Extremely slow

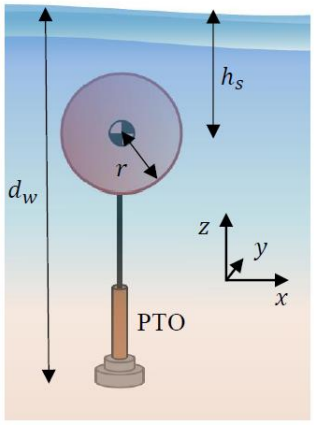

Fig. 1. Submerged heaving PA WEC

Table 2. Parameters for the case studies

Symbol	**Value/unit**	**Description**
d_w	50m	Water depth
h_s	8.5m	Submergence depth from buoy geometric centre to water surface
r	5m	Radius of the spherical buoy
m	2.68×10^5kg	Buoy mass, defined as half of the buoy buoyancy force $m = \rho V/2$

3 CASE STUDIES

Fig. 1 shows the test case, a fully submerged heaving PA WEC with parameters defined in Table 2. A submerged PA was selected since Sergiienko et al. (2018) showed that reactive control plays a critical role in enlarging the absorption bandwidth of this PA system. A spherical buoy was selected to avoid nonlinearities associated with fluid vortices neglected by the potential flow solvers. The power take-off (PTO) was simplified as a combination of a spring, a damper, and a pretension force that counteracts the net buoyancy force. The PA system modelled by the four wave-body interaction methods was tested under regular wave conditions of 0.1m and 1m wave amplitudes and 4 typical wave frequencies, respectively. The PTO spring and damper parameters were optimised in the linear frequency-domain solver so that the PTO damper absorbed power was maximised subject to a body motion constraint of 3m (Ding, 2018). This mitigated the occurrence of surface piercing which was not accounted for by the linear solver. The optimised PTO parameters were then used by all four wave-body interaction models for a comparison. Quadratic damping was considered as an external force in the three potential flow theory based solvers to account for the drag force neglected by the inviscid fluid assumption. Fluid velocity was assumed to be zero in the Morison force computation due to its negligible influence. Lorentz linearisation was used to convert the quadratic Morison equation into a linearised damping for use in the frequency-domain linear solver (Ding, 2018).

4. RESULTS

Fig. 2 shows the RAO and power absorption of the heaving buoy at two wave steepness and four typical wave frequencies, output by the four wave-body interaction models. By the time of abstract submission,

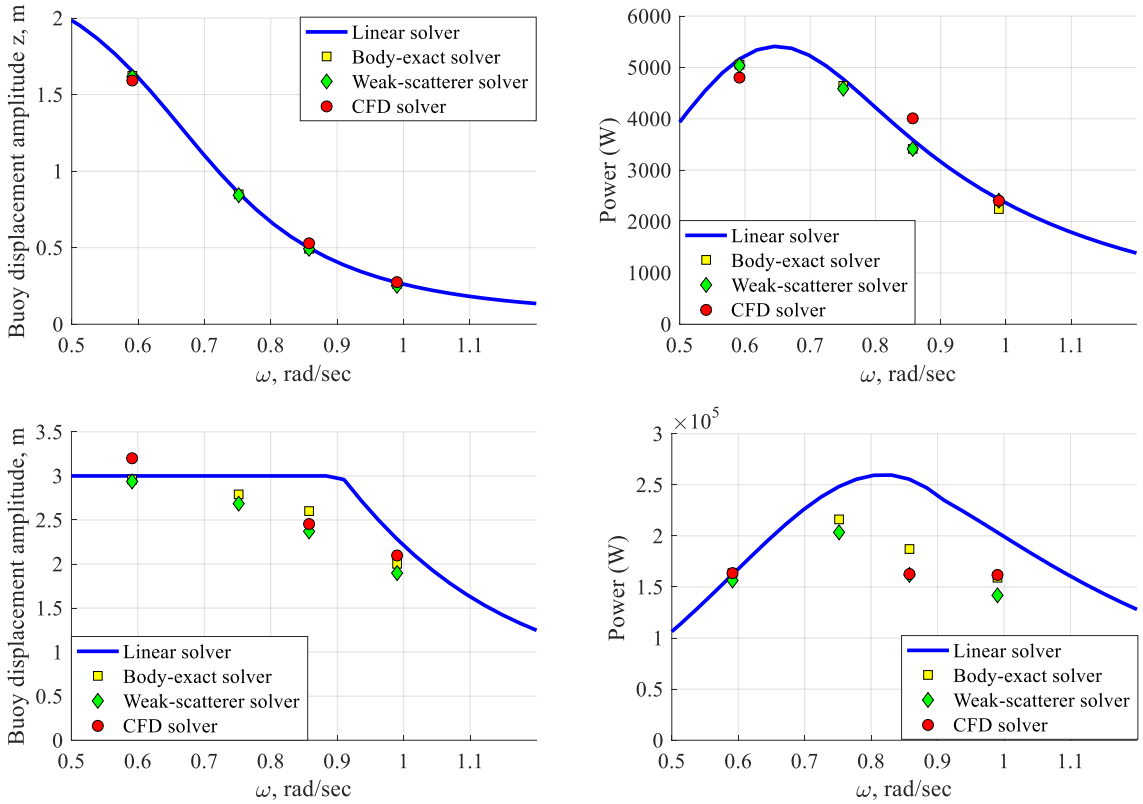

Fig. 2. Buoy heave RAO (left) and power absorption (right) under 0.1m (upper) and 1m (lower) amplitude wave

the CFD solver results at 0.75rad/s had not yet been obtained due to HPC maintenance at the University of Adelaide. At low wave steepness (e.g. 0.1m amplitude), the buoy RAO did not reach the 3m displacement constraint so that the buoy was kept fully submerged during its free motion. In this scenario, the buoy RAO results output by the four solvers reached a good agreement across the frequencies whilst a discrepancy of 14% in the power absorption can be observed between the CFD solver result and the potential flow solver results at 0.85rad/s. The reason behind this discrepancy is under investigation. At high wave steepness (e.g. 1m amplitude), the buoy RAOs were near the 3m displacement constraint, meaning that the buoy moved very closely to the trough of the free surface at its upper stroke so that surface piercing and wave breaking can occur. In this case, both the results output by the BEP solver and the WSP solver diverged from the results of the linear solver (in particular at steeper/higher-frequency waves, with a discrepancy of up to 34%) since buoy motion induced nonlinearities (e.g. those arising from surface piercing phenomenon) became dominant in the system hydrodynamics. The BEP solver and the WSP solver output similar results, with a difference of up to 13%. In general, the WSP solver results were slightly lower than the CFD results, with a discrepancy of up to 8%. The small discrepancy can be attributed to the weak-scatterer hypothesis that disabled the WSP solver from modelling wave breaking. In conclusion, the linear solver showed poor accuracy in modelling reactive control of fully submerged point absorber in high steepness waves, whilst both the BEP solver and the WSP solvers demonstrated acceptable consistency against the CFD solver. More fundamental results (e.g. wave field data and meshing analysis) and new findings are to be shared at the IWWWFB workshop.

REFERENCES

Cummins, W.E., 1962. The impulse response function and ship motions. Schiffstechnik, 9, 101-109.

Ding, B. et al,, 2018, Enhancing the relative capture width of submerged point absorbing wave energy converters, in Proc. of the 4th Asian Wave and Tidal Energy Conference, 9-13 September, Taipei, Taiwan.

Falnes, J., 2007, A review of wave-energy extraction, Marine Structure 20, 185-201.

Meng, F. et al., 2017, Numerical simulation of a submerged spherical point absorber with asymmetric mass distribution, in Proc. of the 2th European Wave and Tidal Energy Conference.

Ringwood, J.V. et al., 2014, Energy-maximizing control of wave-energy converters, IEEE Control System Magazine 34(5), pp. 30-55.

Penalba, M. and Ringwood, J.V., 2016, A review of wave-to-wire models for wave energy converters, Energies 9, 506.

Wuillaume, P.Y., 2019, Numerical simulation of installation operations for offshore wind farms, Doctoral thesis, Ecole Centrale de Nantes.

Pawlowski, J.S. and Bass, D.W., 1991, A theoretical and numerical model of ship motions in heavy seas, SNAME Transactions 99, pp. 319-350.

Sergiienko, N.Y., 2018, Three-tether wave energy converter: hydrodynamic modelling, performance assessment and control, Doctoral thesis, the University of Adelaide.